

Fatigue and Environmentally Assisted Cracking Behavior of Wrought and Additively Manufactured 17-4PH Stainless Steel

A

Dissertation

Presented to

the faculty of the School of Engineering and Applied Science

University of Virginia

in partial fulfillment
of the requirements for the degree

Doctor of Philosophy
in Materials Science and Engineering

by

Trevor Kealoha Shoemaker

August 2022

APPROVAL SHEET

This
Dissertation
is submitted in partial fulfillment of the requirements
for the degree of
Doctor of Philosophy
in Materials Science and Engineering

Author: Trevor Kealoha Shoemaker

This Dissertation has been read and approved by the examining committee:

Advisor: James T. Burns

Committee Member: Ji Ma

Committee Member: Sean R. Agnew

Committee Member: John R. Scully

Committee Member: Xiaodong (Chris) Li

Accepted for the School of Engineering and Applied Science:



Jennifer L. West, School of Engineering and Applied Science

August 2022

Abstract

Additive manufacturing (AM) is an exciting technology that enables production of complex component geometries with just an AM machine and feedstock material. The potential logistical benefits and design freedoms offered by this technology have resulted in a recent explosion of AM research, investment, and utilization. For demanding applications, AM can produce high-strength components by incrementally melting/solidifying metal feedstock to build-up material layer-by-layer. One alloy of interest for metal AM is 17-4PH, a precipitation-hardening martensitic stainless steel. This alloy has been widely used in its traditional, wrought form since the 1940's due to its combination of high-strength and moderate corrosion resistance. These properties have motivated significant microstructural and mechanical properties focused research on "AM" 17-4PH built using the laser powder bed fusion (LPBF) process. However, applications requiring an alloy like 17-4PH typically involve long service lives in aggressive environments. In these situations, failure can be governed by sub-critical environmentally assisted cracking (EAC) modes like corrosion fatigue and stress corrosion cracking (SCC); neither of which have received significant attention in AM 17-4PH research. Critically, EAC is notoriously sensitive to subtle microstructural variations, so AM-induced microstructural features like pores, secondary phases, solidification structures, etc. could be highly detrimental to AM 17-4PH EAC performance. The (i) lack of AM 17-4PH EAC research and (ii) unknown impact of AM-induced microstructural features on EAC performance serve as key knowledge gaps motivating this work.

Wrought 17-4PH can serve as both a benchmark and a baseline for AM 17-4PH. If wrought 17-4PH performance benchmarks can be met or exceeded, then a wide-range of opportunities are opened for AM 17-4PH. Further, careful processing of wrought and AM 17-4PH with similar compositions can allow direct comparison of the two material forms. These assertions and the aforementioned knowledge gaps led to five research objectives guiding this work. (1) Identify processing strategies to strength-match wrought and AM 17-4PH for comparison. (2) Determine the persistent microstructural differences between AM and wrought 17-4PH. (3) Quantify and compare wrought and AM 17-4PH SCC behaviors. (4) Quantify and compare wrought and AM 17-4PH corrosion fatigue behaviors. (5) Link differences in wrought and AM 17-4PH EAC behaviors to their persistent microstructural differences. To meet these objectives, the effects of various heat treatments (i.e., solution anneal, homogenization, hot isostatic press (HIP), peak age, and overage) on the microstructure and mechanical performance of LPBF AM 17-4PH were evaluated. With appropriate heat treatments determined, strength-matched AM and wrought 17-4PH SCC and corrosion fatigue performance was compared via fracture mechanics based crack growth rate testing. Test environments included humidified air (fatigue only) and 0.6M NaCl at various electrochemical potentials. Additionally, a study on the effect of residual stress and its effect on wrought 17-4PH fatigue crack growth

behavior was performed as a supplement. Each of the performance evaluations were complemented by a variety of fractographic and/or crack path analyses to identify mechanisms and microstructural features responsible for the observed fracture behaviors.

Some key conclusions from this work are as follows. AM 17-4PH can be successfully strength-matched to wrought 17-4PH with a range of heat treatments. Of these, the most effective treatment for matching wrought microstructure and strength is two stages of $>1000^{\circ}\text{C}$ treatments followed by an aging heat treatment. Unfortunately, sub-micrometer porosity was persistently present in AM 17-4PH (i.e., in spite of HIP) and plays a critical role in its fracture behavior. This porosity, along with similarly sized oxide-inclusions, was held responsible for AM 17-4PH ductility reductions, degraded SCC performance, and degraded corrosion fatigue performance. These pore-fracture interactions were verified via qualitative morphological examinations, quantitative analysis of pore expansion and spacing, and quantification of microstructural deformation proximate to porosity. In addition to porosity concerns, prior austenite grain (PAG) boundaries in AM 17-4PH were much more susceptible to cathodic electrochemical potentials than wrought 17-4PH. The linkage of degraded AM 17-4PH performance with (1) sub-micrometer scale porosity/inclusions and (2) PAG boundaries constitutes the primary contribution of this work. These key microstructural features in AM 17-4PH can serve to either limit its utilization or act as targets for study/amelioration in future research.

Acknowledgements

There are so many people to whom I owe thanks, but first I need to thank my dissertation advisor, Prof. James Burns. I will always be in your debt for taking me on as a student, supporting me through this process, the countless hours of discussion, and the invaluable mentorship. Your knowledge, work ethic, and leadership will forever serve as a model that I will try to emulate and share with others. Next, I need to thank Zach Harris. You have been with me in the trenches of research since my first day at the University of Virginia. I'll always appreciate the many lessons you've taught me, and I don't know how I would have done this without you. I would also like to thank my dissertation committee members: Prof. John Scully, Prof. Sean Agnew, Prof. Ji Ma, and Prof. Xiaodong Li.

Thanks go to my fellow additive manufacturing student researchers: Lauren Singer, Duane Macatangay, and Mike Roach. It was a ton of fun learning about hydrogen with you, Lauren. Thanks for always being there for my overly pedantic questions. Duane, thank you for graciously teaching me a thing or two about corrosion. And Mike, thanks for being my wingman on this project. I also need to thank the Burns Group members, past and present. Pat Steiner, Adam Thompson, Carly Cocke, Kristyn Ardrey, Luke Brown, Sarah Blust, Alex Jennion, thanks for making it fun to be part of the Burns Ward. Thanks go to the staff at the University of Virginia. Richard White, Tanner Fitzgerald, Sherri Sullivan, Bryana Amador, Tonya Reynolds, Peggy Gibson, Kim Fitzhugh-Higgins, Barry Baber, Kari Werres. I also need to thank the staff at the Commonwealth Center for Advanced Manufacturing, Cameron Gygi, Kyle Snyder, and Rich Martukanitz, for their support in producing the additively manufactured metal in this research. Over at the University of California, Davis, I need to thank Mike Hill and Christine Smudde for their collaboration in the residual stress measurements. And a huge thanks to Michael Majercak over at Majer Precision Engineering, Inc. None of this research would have been possible without your excellent machining work. Thank you, Michael.

Next, I need to acknowledge the United States Air Force STEM+M program for providing me the opportunity to come to the University of Virginia and pursue a Ph.D. Thanks go to my many Air Force colleagues who supported me during this process. I need to thank Mark Thomsen and Larry Butkus for getting me in touch with Prof. Burns; it is hard to imagine where I would be otherwise. Greg Stowe, thanks for sticking with me and supporting me from over in the A-10 Office. Caleb Murphy, Bryce Jolley, and Roger Beal, thank you for being sounding boards during the highs and lows.

This research was funded primarily by the Office of Naval Research under Grant No. N00014-18-1-2427 with Dr. Airan Perez as the Scientific Officer. Additional funding was provided by NASA Space Technology Research Fellowship Grant Number 80NSSC19K1132.

Table of Contents

Abstract.....	i
Acknowledgements	iii
Table of Contents	iv
List of Figures.....	vii
List of Tables	xiii
Chapter 1 - Additive Manufacturing of 17-4PH Stainless Steel	1
1.1 Introduction	1
1.2 Processing and Heat Treatment of 17-4PH	2
1.3 Corrosion Fatigue of 17-4PH	4
1.4 Stress Corrosion Cracking of 17-4PH.....	6
1.5 Knowledge Gaps.....	8
1.6 Research Objectives & Approach.....	9
1.7 Dissertation Overview.....	10
1.8 References	11
Chapter 2 - AM 17-4PH Mechanical Properties and Microstructure	19
2.1 Introduction	19
2.2 Methods.....	20
2.2.1 Materials.....	20
2.2.2 Microstructure Evaluation	22
2.2.3 Mechanical Testing.....	23
2.3 Results.....	24
2.3.1 Microstructure.....	24
2.3.2 Mechanical Properties.....	28
2.3.3 Fractography.....	31
2.4 Discussion	34
2.4.1 Reviewing AM 17-4PH Mechanical Performance.....	35
2.4.2 Choosing an AM 17-4PH Heat Treatment	36
2.4.3 Ductility Reduction in AM 17-4PH.....	38
2.5 Conclusions	40
2.6 Acknowledgements.....	41
2.7 References.....	41
Chapter 3 - Stress Corrosion Cracking Behavior of AM 17-4PH.....	47
3.1 Introduction	47
3.2 Methods.....	48
3.2.1 Materials.....	48

3.2.2 Stress Corrosion Cracking.....	49
3.3 Results.....	51
3.3.1 Mechanical Properties and Microstructure.....	51
3.3.2 Stress Corrosion Cracking Behavior.....	54
3.4 Discussion	63
3.4.1 Decohesion-based Mechanistic Framework for SCC	63
3.4.2 Microstructural Origins of Degraded SCC Performance	67
3.4.3 Implications	74
3.5 Conclusions	75
3.6 Acknowledgements.....	76
3.7 References	76
Chapter 4 - Degradation of Additively Manufactured Metal by Sub-Micrometer Porosity	87
4.1 Introduction	87
4.2 Methods.....	88
4.2.1 Materials.....	88
4.2.2 Environment-Assisted Cracking	89
4.2.3 Crack Wake Analysis.....	89
4.3 Results and Discussion.....	89
4.4 Conclusion.....	95
4.5 Acknowledgements.....	96
4.6 References	96
4.7 Supplemental Figures.....	100
Chapter 5 - Stress Corrosion Crack Wake Deformation in Peak Aged AM 17-4PH.....	104
5.1 Introduction	104
5.2 Materials and Methods.....	104
5.3 Results.....	105
5.4 Discussion	111
5.4.1 H-Assisted Decohesion Framework Review	111
5.4.2 Pore-Crack Interactions.....	111
5.4.3 Intergranular Fracture along PAG Boundaries	114
5.5 Conclusions	115
5.6 Acknowledgements.....	116
5.7 References	116
Chapter 6 - Corrosion Fatigue Behavior of AM 17-4PH.....	117
6.1 Introduction	117
6.2 Methods.....	118
6.2.1 Materials.....	118

6.2.2 Corrosion Fatigue Evaluation	118
6.3 Results.....	119
6.3.1 Fatigue Crack Growth in Humid Air.....	119
6.3.2 Fatigue Crack Growth in 0.6M NaCl.....	122
6.4 Discussion	126
6.4.1 17-4PH Corrosion Fatigue Mechanisms	127
6.4.2 H-Assisted Fatigue & Microstructure Linkages	130
6.4.3 Practical Implications.....	131
6.5 Conclusions	132
6.6 Acknowledgements.....	132
6.7 References	132
Chapter 7 - Fatigue Crack Path Deflection and Residual Stresses in 17-4PH Stainless Steel Rod.....	134
7.1 Introduction	134
7.2 Methods.....	135
7.2.1 Materials.....	135
7.2.2 Fatigue Crack Growth Rate Measurement	136
7.2.3 Residual Stress Measurement	137
7.2.4 Fatigue Crack Growth Rate Simulation	138
7.3 Results & Discussion	140
7.3.1 Microstructure & Mechanical Properties	140
7.3.2 Comparing 17-4PH Rod and Plate Fatigue Responses	141
7.3.3 Interrogating the 17-4PH Rod Fatigue Crack Growth Response.....	144
7.3.4 Residual Stress in 17-4PH Rod.....	150
7.3.5 Implications of this Work.....	154
7.4 Conclusions	155
7.5 Acknowledgements.....	156
7.6 References.....	156
Chapter 8 - Conclusions & Recommendations for Future Work	162
8.1 Key Conclusions.....	162
8.1.1 Processing 17-4PH.....	162
8.1.2 Performance of Wrought and Strength-Matched AM 17-4PH.....	163
8.1.3 Microstructure-Performance Relationships for 17-4PH.....	164
8.2 Recommendations for Future Work.....	165

List of Figures

Fig. 1 | **AM build and specimen geometries.** Laser powder bed fusion with the displayed build plate layout was used to generate stock AM material in two orientations (ZXY, XYZ). The stock material was cut from the plate and two specimen geometries (tension, excess) were excised/machined for evaluation. 21

Fig. 2 | **Evolution of AM 17-4PH microstructure with heat treatment and comparison to wrought 17-4PH.** **a-c**, AM in as-built condition. **d-f**, AM after SA heat treatment. **g-i**, AM after HIP treatment. **j-i**, AM after Hom+SA treatment. **m-o**, AM after HIP+SA treatment. **p-r**, Wrought in SA condition. Microstructures from AM in the YZ plane are shown in (**a**, **d**, **g**, **j**, **m**) and XY plane in (**b**, **e**, **h**, **k**, **n**). Wrought ST and LS planes are shown in (**p**) and (**q**), respectively. Representative high magnification maps are shown for each condition in (**c**, **f**, **i**, **l**, **o**, **r**). Colored regions indicate ferrite & martensite phase grain orientations. Fine black outlines indicate ferrite & martensite grain boundaries while bold outlines indicate PAGBs. 25

Fig. 3 | **Evolution of density and sub-micrometer scale porosity with heat treatment of AM 17-4PH.** **a-e**, Morphology of pores in the as-built (**a**), SA (**b**), HIP (**c**), HIP+SA (**d**), and Hom+SA (**e**) conditions. **f-g**, Quantification of the pore diameter (**f**) and spacing (**g**) distributions across the various AM heat treatment conditions. **h**, Summary of density and pore morphology metrics with wrought density included for reference. Note that “Density” was measured using the Archimedes method and “Percent Density by Area” was calculated using planar image analysis. As-built pore statistics were captured using 7500x magnification images; statistics for all other conditions were captured at 2500x. 27

Fig. 4 | **Hardness variation with aging temperature for AM and wrought 17-4PH.** Vickers microhardness and equivalent Rockwell C hardness variation is shown for 1 h aging heat treatments at various temperatures. Wrought was aged in the SA condition while AM was aged in the Hom+SA, SA, HIP+SA, and HIP conditions. 29

Fig. 5 | **Comparison of stress-strain and work hardening rate behavior for peak aged wrought and AM 17-4PH.** **a-b**, 460°C peak aged AM loaded in X direction versus peak aged wrought. **c-d**, 460°C peak aged AM loaded in Z direction versus peak aged wrought. **e-f**, Peak aged wrought versus hardness matched (500°C aging temperature) AM. Engineering stress-strain curves are shown in (**a**, **c**, **e**) and work hardening rate curves in (**b**, **d**, **f**). Onset of necking, determined by Considère’s criterion, is identified with the circular markers in (**b**, **d**, **f**). 30

Fig. 6 | **Comparison of stress-strain and work hardening rate behavior for overaged wrought and AM 17-4PH.** **a**, Engineering stress-strain curves. **b**, Work hardening rate curves. Onset of necking, determined by Considère’s criterion, is identified with circular markers in (**b**). 31

Fig. 7 | **Tensile fracture morphologies for peak aged AM and wrought 17-4PH.** **a-d**, AM in the SA+460°C/1 h condition. **e-h**, AM in the HIP+460°C/1 h condition. **i-l**, AM in the Hom+SA+460°C/1 h condition. **m-p**, AM in the HIP+SA+460°C/1 h condition. **q-t**, AM in the HIP+SA+500°C/1 h condition. **u-w**, Wrought in the SA+482°C/1 h condition. Fractographs representative of X loading in each condition are shown in (**a**, **e**, **i**, **m**, **q**) and Z loading in (**b**, **f**, **j**, **n**, **r**, **u**). Representative fracture features for each condition are shown in (**c**, **g**, **k**, **o**, **s**, **v**). Dimple morphologies for each condition are shown in (**d**, **h**, **l**, **p**, **t**, **w**). Selected instances of secondary fracture into plane are outlined with red, dashed outlines. Green arrows identify instances of quasi-cleavage. White arrows identify instances of intergranular fracture along PAGBs. 32

Fig. 8 | **Tensile fracture morphologies for overaged AM and wrought 17-4PH.** **a-c**, AM in the HIP+SA+552°C/4 h condition. **d-f**, Wrought in the SA+552°C/4 h condition. 34

Fig. 9 | **Summary of yield strength and ductility data available for LPBF AM 17-4PH.** Pre-aging treatments are defined as follows: “None” indicates as-built material with or without a stress relief heat treatment at 650°C for 1 h. “SA” indicates a $\geq 1000^\circ\text{C}$ treatment. “HIP” indicates ≥ 100 MPa of gas pressure was applied during a $\geq 1000^\circ\text{C}$ heat treatment. “Hom+SA” indicates two stages of $\geq 1000^\circ\text{C}$ heat treatments without elevated pressure. Aging treatments followed pre-aging treatments and are defined as follows: “Peak Aged” indicates a $\leq 500^\circ\text{C}$ heat treatment, typically for 1 h. “Overaged” indicates a $> 500^\circ\text{C}$ heat treatment, typically for 4 h..... 36

Fig. 10 | **Comparison of strength and ductility metrics for peak aged 17-4PH.**..... 37

Fig. 11 | **Relationship between pore spacing and fracture surface dimple spacing in AM 17-4PH.**... 39

Fig. 12 | **AM build and fracture specimen geometries.** Single edge notch tension (SENT) fracture test specimens were machined from two orientations of stock material (ZXY, XYZ) cut from the displayed build plate. 49

Fig. 13 | **AM and wrought 17-4PH grain structure.** **a-b**, AM in the HIP+Peak Age condition. **c-d**, AM in the HIP+SA+Peak Age condition. **e-f** Wrought in the SA+Peak Age condition. Colored regions indicate martensite grain orientations. Grain boundaries are identified with black outlines in (**a,c,e**). Prior austenite grain boundaries are highlighted with the bold, black outlines in (**b,d,f**)..... 52

Fig. 14 | **Pores and particles in AM 17-4PH.** **a**, AM in the HIP+Peak Age condition. **b**, AM in the HIP+SA+Peak Age condition. **c**, Wrought in the SA+Peak Age condition. All images are secondary electron micrographs. White arrows indicate particles protruding out of plane. 53

Fig. 15 | **Inert environment false crack growth rates under rising K for AM and wrought 17-4PH.** **a**, Peak aged 17-4PH. **b**, Overaged 17-4PH. Rising K false crack growth rates were gathered for various forms, heat treatments, and loading orientations of 17-4PH at $dK/dt = 2 \text{ MPa}\sqrt{\text{m/h}}$ in a dry N_2 (inert) environment. Growth rates shown are dcPD artifacts associated with crack tip plasticity and specimen compliance not crack extension. Exponential fit lines for these false growth rates establish resolution limits for aggressive environment tests..... 54

Fig. 16 | **Crack tip blunting resulting from rising K SCC tests with no crack extension.** **a**, HIP+Peak Age AM 17-4PH tested in dry N_2 . **b**, HIP+SA+Peak Age AM 17-4PH tested in 0.6M NaCl at $E_{app} = -0.190 V_{\text{SCE}}$. These are two examples of typical morphologies for 17-4PH fatigue precrack fronts (identified with white arrows) after rising to $K = 30 \text{ MPa}\sqrt{\text{m}}$ at $dK/dt = 2 \text{ MPa}\sqrt{\text{m/h}}$ with no SCC crack extension. Note that the crack extension direction is from left to right and the samples shown were fatigued for further testing after the aforementioned rising K tests. 56

Fig. 17 | **Rising K SCC crack growth rates at a cathodic applied potential for AM and wrought 17-4PH.** **a**, Peak aged 17-4PH. **b**, Overaged 17-4PH. Rising K tests were performed in 0.6M NaCl with a cathodic applied potential ($E_{app} = -1.100 V_{\text{SCE}}$) for various forms, heat treatments, and loading orientations of 17-4PH at $dK/dt = 2 \text{ MPa}\sqrt{\text{m/h}}$ 57

Fig. 18 | **Constant K SCC crack growth rates as a function of applied potential for AM and wrought 17-4PH.** **a**, Peak aged 17-4PH. **b**, Overaged 17-4PH. Constant K SCC crack growth rates were gathered as a function of applied potential in 0.6M NaCl for various forms, heat treatments, and loading orientations of 17-4PH. Where no crack extension was observed, a growth rate of $1 \times 10^{-7} \text{ mm/s}$ with a down arrow is shown. 59

Fig. 19 | **Stress corrosion cracking morphologies for peak aged wrought and AM 17-4PH.** **a**, Wrought in the SA+Peak Age condition at $E_{app} = -1.100 V_{SCE}$. **b**, AM in the HIP+Peak Age condition at $E_{app} = -1.100 V_{SCE}$. **c-d**, AM in the HIP+SA+Peak Age condition at $E_{app} = -1.100 V_{SCE}$ (**c**) and $E_{app} = -0.800 V_{SCE}$ (**d**). All fractographs were gathered from cathodic polarization SCC tests in 0.6M NaCl..... 61

Fig. 20 | **Stress corrosion cracking morphologies for overaged wrought and AM 17-4PH.** **a**, wrought in the SA+Overage condition. **b**, AM in the HIP+SA+Overage condition. Fractographs were both from SCC tests in 0.6M NaCl under cathodic polarization at $E_{app} = -1.100 V_{SCE}$ 61

Fig. 21 | **Intergranular SCC fracture morphologies for wrought and AM 17-4PH.** **a**, AM in the HIP+SA+Peak Age condition. **b**, AM in the HIP+Peak Age condition. **c**, AM in the HIP+SA+Overage condition. **d**, Wrought in the SA+Overage condition. Fractographs were all gathered from cathodic polarization tests in 0.6M NaCl at $E_{app} = -1.100 V_{SCE}$ 62

Fig. 22 | **Postulated variation of grain boundary interface failure stress with stress assisted hydrogen concentration for peak aged 17-4PH.** **a**, Schematic illustration of the primary grain boundary interfaces in 17-4PH. **b**, The postulated response of those interfaces' failure stresses to stress assisted hydrogen concentration ($C_{H\sigma}$) in peak aged 17-4PH. The intergranular (IG) and transgranular (TG) fractographic bases for these postulations are superimposed for reference. 66

Fig. 23 | **Environment assisted cracking in equivalent wrought and AM alloys.** **a-b**, Microstructure for AM (**a**) and wrought (**b**) 17-4PH stainless steel with arrows highlighting porosity in AM. **c**, Environment assisted crack growth kinetics. **d-e**, Fracture surfaces for AM (**d**) and wrought (**e**) corresponding to the conditions in (**c**) with white arrows highlighting porosity. **f-i**, Crack wake grain structure (**f, g**) and deformation (**h, i**) maps for wrought (**f, h**) and AM (**g, i**). White regions indicate the crack paths with primary growth occurring from left to right. Black outlines and colored regions indicate prior austenite grain boundaries and martensite orientations, respectively, in the grain structure maps..... 90

Fig. 24 | **Environment assisted crack path-pore morphological interactions in AM.** **a**, Crack wake with large pores adjacent to the crack path highlighted. **b**, Crack path with split pores along the path highlighted. **c**, Secondary crack extending from a pore. **d**, Crack branch extending from the primary crack path to a pore. **e**, Crack branch extending through a pore. **f**, The primary, active crack tip halted at the end of a test. 92

Fig. 25 | **AM pore morphology proximate to an environment assisted crack path.** **a**, Map of pores (colored by diameter) adjacent to the crack path (black). Note that the pores are replaced by circles and magnified 7x in size for clarity. **b**, Box and whisker plot distributions of pore diameters as a function of distance from the crack path. **c**, Percentage of large outlier pores as a function of distance from the crack path. 93

Fig. 26 | **AM pore-deformation interaction in environment assisted cracking.** **a**, Pore morphology relative to the crack path (black). **b**, Pore morphology relative to the crack path (white), local martensite grain structure (colored), and prior austenite grain boundaries (black). **c**, Pore morphology relative to the local deformation structures (colored) and crack path (white). Equivalent areas of interest (i-v) are bounded with dashed lines in **a-c**. 94

Fig. 27 | **Stress corrosion crack growth rates for peak aged AM and wrought 17-4PH.** Crack growth rate as a function of stress intensity (K) is plotted for AM and wrought 17-4PH at $E_{app} = -0.8, -1.1 V_{SCE}$ in 0.6M NaCl (pH 6.2). The applied stress intensity was initially held constant ($dK/dt = 0 \text{ MPa}\sqrt{\text{m/h}}$) at $K \sim 30 \text{ MPa}\sqrt{\text{m}}$; variation in K occurred as the crack extended. Note that peak aged wrought 17-4PH is not SCC susceptible at $E_{app} = -0.8 V_{SCE}$ 105

Fig. 28 | **Stress corrosion crack path branching in peak aged AM and wrought 17-4PH.** **a**, Wrought, $E_{app} = -1.1 V_{SCE}$. **b**, AM, $E_{app} = -1.1 V_{SCE}$. **c**, AM, $E_{app} = -0.8 V_{SCE}$. Stress corrosion crack wakes are shown for peak aged AM and wrought 17-4PH at $K = 32 \text{ MPa}\sqrt{\text{m}}$ in 0.6M NaCl (pH 6.2) at various applied potentials..... 106

Fig. 29 | **Identification of stress corrosion cracking failure interfaces for peak aged AM and wrought 17-4PH.** **a-b**, Wrought, $E_{app} = -1.1 V_{SCE}$. **c-d**, AM, $E_{app} = -1.1 V_{SCE}$. **d-e**, AM, $E_{app} = -0.8 V_{SCE}$. The stress corrosion crack path is compared for peak aged AM and wrought 17-4PH in 0.6M NaCl (pH 6.2) at various applied potentials. The crack path is shown via backscatter electron images (**a,c,e**) and OIM maps identifying the proximate grain structure (**b,d,e**). OIM coloration indicates grain orientation with fine and bold black outlines identifying martensite and prior austenite grain boundaries, respectively. White and black arrows on the backscatter images indicate transgranular and intergranular fracture, respectively. 107

Fig. 30 | **Stress corrosion crack wake deformation in peak aged AM and wrought 17-4PH.** **a**, Wrought, $E_{app} = -1.1 V_{SCE}$. **b**, AM, $E_{app} = -1.1 V_{SCE}$. **c**, AM, $E_{app} = -0.8 V_{SCE}$. Deformation is quantified and compared via KAM in stress corrosion crack wakes for peak aged AM and wrought 17-4PH in 0.6M NaCl (pH 6.2) at various applied potentials (**a,b,c**). Areas of interest are identified with white arrows in (**c**). For the numbered areas of interest, magnified KAM maps are shown with equivalent backscatter electron images. Black arrows in the backscatter images indicate regions of high deformation. 109

Fig. 31 | **Pore-stress corrosion crack path interaction in peak aged AM 17-4PH.** **a**, $E_{app} = -1.1 V_{SCE}$. **b**, $E_{app} = -0.8 V_{SCE}$. The stress corrosion crack path is shown for peak aged AM 17-4PH in 0.6M NaCl (pH 6.2) at $E_{app} = -1.1, -0.8 V_{SCE}$. Intersections of the crack path with porosity are highlighted with white arrows. 110

Fig. 32 | **Comparison of pore expansion proximate to stress corrosion cracking in peak aged and overaged AM 17-4PH.** The percentage of large, outlier pores (diameter, $D, > 0.6 \mu\text{m}$) is shown as a function of distance from the stress corrosion crack path for two heat treatments (peak age, overage) of AM 17-4PH. All tests were performed in 0.6M NaCl (pH 6.2) at $K = 30\text{-}40 \text{ MPa}\sqrt{\text{m}}$ with $E_{app} = -0.8 V_{SCE}$ or $-1.1 V_{SCE}$,..... 112

Fig. 33 | **Humid air fatigue crack growth rates for AM and wrought 17-4PH.** **a**, Peak aged 17-4PH. **b**, Overaged 17-4PH. Fatigue crack growth rates (da/dN) in humidified air ($\text{RH} > 90\%$) are shown as a function of stress intensity range (ΔK) for multiple loading orientations, forms, and heat treatments of 17-4PH. All data was gathered at a loading frequency (f) of 10 Hz and stress ratio (R) of 0.5..... 120

Fig. 34 | **High ΔK fatigue fracture morphology for AM and wrought 17-4PH.** **a-b**, Wrought in the peak aged (**a**) and overaged (**b**) condition. **c-d**, AM in the peak aged (**c**) and overaged (**d**) condition. Fatigue fracture surfaces shown resulted from humid air conditions at $\Delta K \geq 25 \text{ MPa}\sqrt{\text{m}}$, $R = 0.5$ for the various forms and heat treatments of 17-4PH. 122

Fig. 35 | **Open circuit potential 0.6M NaCl corrosion fatigue crack growth behavior for peak aged AM and wrought 17-4PH.** **a**, Corrosion fatigue crack growth rate as a function of stress intensity range. **b-c**, $\Delta K = 3 \text{ MPa}\sqrt{\text{m}}$ fractography. **d-e**, $\Delta K = 5 \text{ MPa}\sqrt{\text{m}}$ fractography. **f-g**, $\Delta K = 7 \text{ MPa}\sqrt{\text{m}}$ fractography. Fractographs shown are representative of peak aged wrought (**b,d,f**) and additive (**c,e,g**) 17-4PH corrosion fatigue crack growth in neutral 0.6M NaCl (pH 6.2) under free corroding conditions (open circuit potential) at $R = 0.5$ and $f = 10 \text{ Hz}$. White arrows indicate the onset of faceted fatigue fracture. 123

Fig. 36 | **Open circuit potential 0.6M NaCl corrosion fatigue crack growth behavior for overaged AM and wrought 17-4PH.** **a**, Corrosion fatigue crack growth rate as a function of stress intensity range. **b-c**, $\Delta K = 3 \text{ MPa}\sqrt{\text{m}}$ fractography. **d-e**, $\Delta K = 5 \text{ MPa}\sqrt{\text{m}}$ fractography. **f-g**, $\Delta K = 7 \text{ MPa}\sqrt{\text{m}}$ fractography.

Fractographs shown are representative of overaged wrought (**b,d,f**) and additive (**c,e,g**) 17-4PH corrosion fatigue crack growth in neutral 0.6M NaCl (pH 6.2) under free corroding conditions (open circuit potential) at $R = 0.5$ and $f = 10$ Hz. White arrows indicate the onset of faceted fatigue fracture. 124

Fig. 37 | Variation of corrosion fatigue crack growth behavior with applied potential for peak aged AM and wrought 17-4PH. **a**, Fatigue crack growth rate variation with applied potential. **b-c**, $E_{app} = -0.8$ V_{SCE} fractography. **d-e**, $E_{app} = -1.0$ V_{SCE} fractography. **f-g**, $E_{app} = -1.2$ V_{SCE} fractography. Fractographs shown are representative of peak aged wrought (**b,d,f**) and additive (**c,e,g**) 17-4PH corrosion fatigue crack growth in neutral 0.6M NaCl (pH 6.2) at various applied potentials with fixed $\Delta K = 5$ $MPa\sqrt{m}$, $R = 0.5$, and $f = 10$ Hz. White arrows indicate the onset of faceted fatigue fracture. 125

Fig. 38 | Effect of f and ΔK variation on da/dN near the “takeoff potential” for peak aged AM and wrought 17-4PH. **a**, Effect of loading frequency variation. **b**, Effect of stress intensity range variation. All corrosion fatigue crack growth rates shown were gathered in neutral 0.6M NaCl (pH 6.2) with fixed $E_{app} = -0.8$ V_{SCE} and $R = 0.5$ 129

Fig. 39 | Faceted corrosion fatigue fracture morphology for peak aged AM and wrought 17-4PH in cathodic conditions. **a**, Wrought. **b**, Additive. Both fractographs were gathered from corrosion fatigue tests in neutral 0.6M NaCl (pH 6.2) with fixed $E_{app} = -1.2$ V_{SCE} , $\Delta K = 5$ $MPa\sqrt{m}$, and $R = 0.5$ 131

Fig. 40 | Schematic of samples used for residual stress measurement via the slitting method. SENT samples were machined from 17-4PH rod and fatigue tested along the nominal crack path identified in Section A-A. After fatigue testing, a portion of the SENT adjacent to the crack path was excised for use as a slitting sample, instrumented with a strain gage, and incrementally slit via EDM. Strains measured during the slitting process were used to calculate residual stress as a function of crack length (a) normalized by the SENT width (W) (i.e., a/W)..... 138

Fig. 41 | Comparison of 17-4PH rod and plate microstructures. **a-c**, 17-4PH plate microstructure. **d-f**, 17-4PH rod microstructure. Representative microstructure images are shown for 17-4PH plate (**a, b, c**) and rod (**d, e, f**). Grain orientation imaging maps are shown in (**a, b, d, e**) with bold and fine black outlines highlighting the PAG and martensite block boundaries, respectively. The most severe cases of delta ferrite stringers observed in each material form are shown in (**c, f**) with the L direction aligned vertically. 140

Fig. 42 | Comparison of fatigue crack growth rates for 17-4PH rod and plate in humid air. **a**, $R = 0.5$. **b**, $R = 0.7$. Fatigue crack growth rate (da/dN) versus stress intensity range (ΔK) in humid air (>90% RH) for 17-4PH plate and rod are compared at $R = 0.5$ (**a**) and $R = 0.7$ (**b**). Growth rates gathered under shedding or rising ΔK are identified along with the normalized K -gradients (C) used to control load application. 142

Fig. 43 | Comparison of 17-4PH rod and plate fatigue behavior at constant ΔK . **a**, Fatigue crack growth rate versus normalized crack length (a/W). **b**, Fatigue fracture topographies. Growth rates were captured in lab air as a function of a/W at a constant $\Delta K = 9$ $MPa\sqrt{m}$, $R = 0.5$ for 17-4PH rod and plate in the H900 condition (**a**). Topographic height (Z) maps of the fracture surfaces from (**a**) are shown in (**b**). The primary growth region in (**b**) is preceded by EDM notch (0.94 mm) and precrack (0.25 mm) regions. Note also that the 1 mm scalebar in (**b**) only applies to planar dimensions; Z height is exaggerated for clarity..... 142

Fig. 44 | Effect of stress ratio modification on fatigue crack growth in 17-4PH rod. Fatigue crack growth rates are compared at two stress ratios ($R = 0.5, 0.7$) for 17-4PH rod in the H900 condition. Growth rates were captured in lab air as a function of a/W at a constant $\Delta K = 9$ $MPa\sqrt{m}$ 144

Fig. 45 | Effect of crack tip constraint modification on fatigue crack growth in 17-4PH rod. Different levels crack tip constraint were tested by fatigue cracking flat sided and side-grooved SENTs made from

17-4PH rod in the H900 condition. Growth rates were captured in lab air as a function of a/W at a constant $\Delta K = 9 \text{ MPa}\sqrt{\text{m}}$, $R = 0.5$ 145

Fig. 46 | **Comparison of T-stress variation and its effects on fatigue crack growth in 17-4PH rod.** **a**, T -stress distributions via the biaxiality ratio (β) as a function of a/W in pinned-pinned and fixed-fixed SENT loading configurations. **b**, Fatigue crack growth rates versus a/W in pinned-pinned and fixed-fixed SENTs. Published T -stress distributions are compared for two SENT loading configurations (**a**). The effects of these T -stress distribution differences on fatigue crack growth rates were then tested on 17-4PH rod in the H900 condition at a constant $\Delta K = 9 \text{ MPa}\sqrt{\text{m}}$, $R = 0.5$ in lab air (**b**)..... 147

Fig. 47 | **Effect of environment modification on fatigue crack growth in 17-4PH rod.** Fatigue crack growth rates are compared in an inert (Dry N_2 , RH $\sim 0\%$) and benign (Lab Air, RH $\sim 50\%$) environment for 17-4PH rod in the H1025 condition. Growth rates were captured as a function of a/W at a constant $\Delta K = 9 \text{ MPa}\sqrt{\text{m}}$, $R = 0.5$ 148

Fig. 48 | **Effect of heat treatment on fatigue crack growth in 17-4PH rod.** Fatigue crack growth rates are compared for 17-4PH rod in the as-received (AR) condition and heat treated to the H900, H1025, and SA conditions. Growth rates were captured as a function of a/W at a constant $\Delta K = 9 \text{ MPa}\sqrt{\text{m}}$, $R = 0.5$.149

Fig. 49 | **Residual stress and stress intensity in various conditions of 17-4PH rod.** **a**, Residual stresses (σ_{RS}). **b**, Residual stress intensity factors (K_{RS}). Residual stresses and stress intensity factors are shown as a function of a/W for 17-4PH rod in various heat treatment conditions. All residual stresses shown were gathered via the slitting method. 151

Fig. 50 | **Simulated effects of measured residual stresses on fatigue crack growth in 17-4PH rod.** **a**, Simulated heat treatment effect. **b**, Simulated stress ratio effect. Fatigue crack growth rates are simulated using the NASGRO equation with the inclusion of measured residual stress profiles. The simulations attempt to replicate experimental fatigue growth gathered for the 17-4PH rod under various heat treatments (**a**) and applied stress ratios (**b**) at a nominal, constant $\Delta K = 9 \text{ MPa}\sqrt{\text{m}}$ 152

Fig. 51 | **Variation in fracture surface topography induced by heat treatment of 17-4PH rod.** **a**, Fracture surface topographic height (Z) maps. **b**, Fracture surface tilt angle variations. **c**, Fracture surface roughness (Rq) variations. Fatigue fracture surfaces for various conditions of 17-4PH rod (i.e., AR, H900, H1025, SA) were topographically mapped as a function of a/W (**a**). Line profiles traversing across the fracture surface thickness (i.e., B) at various a/W were used to calculate tilt angle (**b**) and roughness variations (**c**). All fatigue cracks shown were grown at a constant $\Delta K = 9 \text{ MPa}\sqrt{\text{m}}$, $R = 0.5$ in lab air. Note that the 1 mm scalebar in (**a**) only applies to planar dimensions; Z height is exaggerated for clarity..... 153

List of Tables

Table 1 Elemental composition of the wrought and AM 17-4PH compared in this study.	22
Table 2 Summary of mechanical properties obtained in this study for AM and wrought 17-4PH. 24	
Table 3 SCC morphologies evaluated as a function of applied potential and 17-4PH form/heat treatment.	60
Table 4 Paris law fits for AM and wrought 17-4PH fatigue crack growth in humid air. A Paris law of the form $da/dN = C(\Delta K)^n$ was fitted to humid air fatigue crack growth rate data ($R = 0.5, f = 10$ Hz) for various forms, loading orientations, and heat treatments of 17-4PH. The units for C are (mm/cycle)/(MPa \sqrt{m}) n . The displayed coefficient of determination (R^2) values are valid in the additive conditions for $3 \text{ MPa}\sqrt{m} \leq \Delta K < 50 \text{ MPa}\sqrt{m}$ and wrought for $3 \text{ MPa}\sqrt{m} \leq \Delta K < 20 \text{ MPa}\sqrt{m}$	121
Table 5 Elemental compositions of the 17-4PH plate and rod used in this study in weight %.	136
Table 6 Heat treatment codes/designations and associated processing parameters used in this study.	136
Table 7 Mechanical properties for selected tempers of the 17-4PH plate and rod used in this study.	141

Chapter 1 - Additive Manufacturing of 17-4PH Stainless Steel

1.1 Introduction

Additive manufacturing (AM) is a growing technology that offers unique benefits when compared to traditional manufacturing processes. In contrast to subtractive and/or formative manufacturing technologies, AM may be used to build up parts layer-by-layer and directly produce complex geometries¹. With feedstock material and an appropriate AM machine, parts that would traditionally take a number of separate processing steps can be produced in a single step. The promise of this technology has resulted in an explosion of its utilization. AM feedstock material annual sales increased from \$71-640 million between 2001 and 2014 with projected sales of \$8 billion by 2025². Though the technology is still in its infancy, major industries are exploring AM for its potential supply chain efficiency benefits^{3,4}. Known colloquially as 3-D printing, additive manufacturing is typically associated with polymers/plastics by the general public, but composites, ceramics, and metals may also be produced using AM technology for demanding applications⁵.

Metallic materials have received significant focus in additive manufacturing research for their combination of high strength, ductility, and, in some cases, corrosion resistance. Traditional Ti-, Ni-, Al-, Mg-, and Fe-based alloy systems are all being explored as AM feedstock materials. Of these systems, Fe-based alloys, steels, are ubiquitous in our society due to their price, strength, ductility, hardness, wide range of achievable microstructures, etc.⁶ As such, study of AM steels is essential. In particular, the 17-4PH alloy, a precipitation hardening martensitic stainless steel, has received significant interest as an AM feedstock material. For applications where a combination of high strength and environmental resistance is required, the precipitation hardened stainless steels like 17-4PH are a typical choice. In such applications, long part lifetime requirements can expand the material demands beyond first order strength and/or ductility requirements to the inclusion of fatigue and/or fracture toughness requirements. Combined with an aggressive environment, fatigue and/or fracture can be accelerated through processes like corrosion, corrosion fatigue, and/or stress corrosion cracking. These time-based failure modes contribute to over 50% of real failures in the aircraft and engineering industry⁷ and are, therefore, a critical aspect of AM research.

To date, AM metals research has largely been focused on AM processing methods, microstructure, and first order strength properties like strength and ductility. Recently, focus has been shifting to second order properties like fatigue/fracture⁸ and corrosion resistance⁹, but the combination of these phenomena,

environmentally assisted cracking (EAC), has received little attention. The following is a dissertation exploring the fatigue and EAC behavior of additively manufactured 17-4PH (AM 17-4PH) by comparison with its traditional, wrought counterpart. Persistent, detrimental microstructural features uniquely introduced through the AM process will be identified through a combination of material processing techniques, microstructure analysis, corrosion fatigue, and stress corrosion cracking testing. The results from this work will break ground on the study of AM 17-4PH EAC behavior and inform future processing changes necessary to improve its EAC performance.

1.2 Processing and Heat Treatment of 17-4PH

Every metallic engineering alloy undergoes a melting and solidification process. If solidified directly into the final desired shape, then the alloy is said to be *cast*. Cast alloys have the advantage of low cost due to minimal processing steps, but the solidification microstructure can result in undesirable material properties. The common alternative to the cast alloy is the *wrought* alloy. Similar to casting, the wrought alloy is first melted and solidified, but into a large ingot rather than the final shape. This ingot is then deformed, “wrought”, into one of a variety of simple shapes like sheet, plate, rod, wire, etc. To facilitate the wrought deformation process, the alloy must undergo thermal and mechanical loads which produces a vastly different microstructure from the solidification microstructure yielded by casting.

The principal process common to all wrought materials is hot working. As the name implies, hot working involves the application of heat (thermal loads) to soften and facilitate the mechanical deformation of a material. Prior to hot working, a cast ingot has a solidification microstructure¹⁰ that typically includes a combination of chemical inhomogeneities, porosity, and large or dendritic grain structures. During hot working¹¹⁻¹³, the cast ingot microstructure undergoes a number of transformations that can result in closure of casting pores, chemical homogenization, recovery, recrystallization, and/or grain refinement. A properly controlled hot working schedule can essentially eliminate the detrimental features of an ingot’s solidification structure to produce a chemically homogenous, fine grained “wrought” microstructure suitable for a wide breadth of applications.

One wrought alloy of great technical interest is 17-4PH stainless steel. As a so-called “precipitation hardening” (PH) martensitic stainless steel, 17-4PH is both corrosion resistant and available at a variety of strengths depending on the precipitation hardening heat treatment. At hot working temperatures, the alloy is austenitic with a low stacking fault energy¹⁴. This allows the hot working process to produce an equiaxed austenitic grain structure of various sizes depending on the working temperature¹⁵. Following hot working, 17-4PH is solution annealed to dissolve copper into the high-strength martensitic matrix that forms upon cooling to room temperature. This dissolved copper is then precipitated via a precipitation hardening (also called aging) heat treatment to further increase the alloy’s strength. Originally developed in the late

1940's¹⁶, 17-4PH is widely used and available in material forms ranging from hot rolled plate or forgings to cold drawn wire.

A relatively new technology for producing material is the additive manufacturing (AM) process¹⁷. Unlike the wrought process where simple shapes are produced and subjected to subtractive processes like machining to make a final shape; additive manufacturing builds up material to produce the final or near-final part geometry. Though many methods are available, a common process for producing metallic AM materials is the laser-powder bed fusion (LPBF) process. Instead of melting and solidifying an ingot, LPBF alloys are melted and solidified as a fine powder by “atomizing” the melt with a media like gas or water. With powder of the desired chemical composition, a laser-equipped machine is used to resolidify the powder layer by layer into a desired shape. Unlike the casting or wrought process, LPBF can directly produce shapes with both complex geometries and high dimensional tolerances. The LPBF process produces material that is unlike cast or wrought and is highly process dependent. Like casting, LPBF produces solidification microstructures, but with orders of magnitude faster cooling rates and complex thermal histories involving melting and re-melting. Additionally, factors like powder morphology, powder atomizing media, build atmosphere, laser energy density, and laser scanning strategy can have profound effects on the underlying microstructure. Some features of interest¹⁸ include textured solidification structures, subgrain “cellular” dislocation structures, varying levels of porosity, and residual stress.

As a well-established wrought alloy, the 17-4PH composition has attracted interest as a potential additively manufactured alloy, hereafter referred to as AM 17-4PH. Though the composition of AM 17-4PH can be held within the bounds of standard¹⁹ 17-4PH, the LPBF process yields a vastly different microstructure from wrought 17-4PH. Rather than a near 100% martensitic structure in the wrought form, AM 17-4PH in the “as-built” condition is primarily a ferritic structure with martensite and/or austenite^{20–28}. Some of the key factors affecting the phase fractions include the powder atomizing media and the atmosphere of the LPBF build chamber. Nitrogen in either case tends to stabilize/promote the formation of austenite^{25,28}. Argon gas is not soluble in iron alloys²⁸, so Ar atomized powders tend to result in minimal austenite content. Unfortunately, the Ar can lead to porosity in the microstructure instead²⁹. In addition to the primary phases, fine Nb carbides are present^{23,24} with some reports of Si or Mn oxide inclusions^{26,30,31}.

The melting process involved in LPBF results in a number of possible microstructure morphologies for AM 17-4PH. The “scanning strategy” can both affect the general shape of the grains and the porosity of the microstructure³². In general, the microstructure is anisotropic. To aid in these describing this anisotropy, an ASTM standard³³ has codified a coordinate system where the build plane may be referred to as the “XY” plane and the additional plane may be referred to as the “XZ” and/or “YZ” plane depending on symmetry of the scan pattern. The XY plane typically reveals a checkerboard patterned grain

morphology following the scanning strategy while the XZ plane is typically a columnar grain structure with the columns aligned approximately with the build (Z) direction. The AM 17-4PH grain morphology is a result of the solidification kinetics involved in LPBF, so unsurprisingly there have been reports of chemical inhomogeneity²⁴ and non-random crystallographic texture^{26,34} in the as-built microstructure.

A key characteristic of wrought 17-4PH is its high strength. The martensitic structure is the first contributor to its strength. In order to attain peak strength, both a “solution” and a “precipitation hardening” (or aging) heat treatment is required³⁵. As previously mentioned, the solution heat treatment is necessary to dissolve the copper in the alloy into solid solution while the aging heat treatment precipitates the copper as a fine dispersion of nanoscale particles to strengthen and/or toughen the material. It has been shown that these heat treatments can be successfully applied to strengthen AM 17-4PH to levels commensurate with traditionally manufactured 17-4PH^{29,36,45,46,37-44}. However, additional “post-process” (i.e., after LPBF) treatments may be desirable. For example, a homogenization heat treatment may be applied to alleviate chemical segregation^{23,24} and/or a hot isostatic press (HIP) heat treatment can alleviate porosity^{47,48} introduced during the LPBF process.

1.3 Corrosion Fatigue of 17-4PH

As a corrosion resistant, high strength alloy, 17-4PH is typically intended for use in high performance applications. In such applications, static overload is only one of several potential failure modes for a material. For components with long service lives undergoing cyclic loading, the fatigue cracking failure mode must be considered. Broadly, fatigue can be considered from a safe-life or a linear elastic fracture mechanics (LEFM) based perspective⁴⁹. The safe-life approach combines the surface-state dominated* fatigue crack nucleation stage with crack propagation which is controlled by bulk microstructure. Conversely, the LEFM approach focuses on crack propagation that is unbiased by surface state effects. With long component lifetimes, evolving surface states complicate the use of safe-life testing for accurate lifing predictions, so fatigue approaches assuming flawed material, so-called damage tolerant analyses⁵⁰, make LEFM-based fatigue crack growth kinetics desirable. In some applications, a corrosive environment may be present that can accelerate the fatigue process and further degrade the service life of a component⁵¹. Therefore, capturing the environment affected fatigue crack growth rate, or corrosion fatigue crack growth rate, in a material is critical.

* Some would argue that low-cycle fatigue (a subset of the safe-life approach) is controlled by crack propagation and, therefore, bulk microstructure. However, the point still holds that the safe-life approach is complicated by the combination of separate crack nucleation and propagation processes.

Corrosion fatigue crack growth results from the combination of cyclic and environmental damage. Under pure cyclic loading, growth of a fatigue crack involves the localized, irreversible accumulation of slip that couples with local tensile stress to result in material separation and, therefore, crack extension⁵². This damage process may be accelerated in the presence of an aggressive environment via a phenomenon broadly described as environmentally assisted cracking (EAC). The EAC phenomenon is a complex mixture of factors and processes⁵³ that can broadly be grouped under stress, material, and environment effects. A material may be composed of different phases, zones of local elemental depletion or enrichment, grain boundary precipitates, and/or elemental segregation to grain boundaries. The interaction of the environment with these heterogeneous microstructural features can then enable and enhance cracking. This EAC process can include local occluded chemistries within a crack, crack tip stress field modified H diffusion, dislocation interactions that lead to crack extension, and eventual fracture of a component. Separating and evaluating these coupled processes is a monumental task that is further impeded by the fact that they occur primarily at the crack tip. So, to date, corrosion fatigue crack growth is primarily characterized through downstream metrics like crack growth rate and upstream phenomena are intimated through post-mortem analyses like fractographic examination. Mechanism-based modeling efforts have been attempted, but are still limited in their predictive capability^{54,55}.

In the literature, lab air^{56,57}, argon gas⁵⁸ (non-aggressive), humidified air⁵⁸ (slightly aggressive), and seawater simulating^{56,59,60} (aggressive) environments have been used to explore the corrosion fatigue crack growth behavior of wrought 17-4PH. Fractography showed that fatigue crack growth in lab air was generally transgranular. Interestingly, argon-oxygen melted (AOM) material exhibited a significant increase in the amount of cleavage features versus vacuum melted (VM) material⁵⁷. Generally, cleavage is a fracture mode associated with poor fracture toughness. In the aggressive seawater environments, the crack growth rate was magnified by a factor of 2 to 5 times versus less aggressive environments, but crack growth rate differences between melting processes (i.e. AOM and VM) were attenuated⁵⁹. It is worth noting that the majority of corrosion fatigue crack growth kinetics captured for 17-4PH are in the Paris-regime ($>1 \times 10^{-5}$ mm/cycle). No investigation of near threshold (i.e., $\sim 1 \times 10^{-7}$ mm/cycle⁶¹) behavior, where environmental effects are expected to be most pronounced, was found to be publicly available.

To date, no corrosion fatigue crack growth data has been published for AM 17-4PH. Fatigue data has been limited to lab air behavior with focus being placed on stress life performance^{29,36,37,44,48,62-64}. In general, the stress life behavior is dominated by surface and near-surface defects on the order of 20-50 μm in size. These defects, introduced during the LPBF process, act as crack nucleation sites and lead to greatly reduced stress lives. However, it has been found that machining the first 0.5 mm from the surface of a LPBF component removed the majority of these defects and greatly improved fatigue life⁶⁴. Such fatigue

characteristics make damage tolerance even more important as LEFM analyses coupled with crack growth kinetics can be used to make life predictions with assumed initial flaws.

In the last couple years, several lab air based fatigue crack growth rate investigations have been published for AM 17-4PH^{29,65,66}. Again, microstructure inhomogeneities and defects have impacted the crack growth in AM 17-4PH. Crack path turning and tortuosity was attributed to brittle delta ferrite phase aligned with the build direction of the LPBF process⁶⁵. Even more extreme crack path deviations, build to build variations, and delamination were attributed to poor fusion between melt layers⁶⁶. However, stage II crack propagation kinetics were largely similar to wrought; this is consistent with the tendency for fatigue crack propagation behavior to be relatively insensitive to microstructure for many steels. The unique crack growth characteristics are largely a result of processing parameters or issues introduced by the LPBF process. The most promising set of fatigue data to date involved modifying the build atmosphere from argon to nitrogen in order to reduce porosity, refine grain size, improve ductility, and ultimately improve fatigue performance²⁹. However, nitrogen addition also results in retained austenite which can reduce the peak strength of 17-4PH³⁵.

1.4 Stress Corrosion Cracking of 17-4PH

Under sustained tensile stress and exposure to an aggressive environment, some materials can undergo a phenomenon called stress corrosion cracking (SCC). This phenomenon is particularly insidious as materials suitable for a wide range of applications may suddenly become prone to SCC failure if exposed to an unsuitable environment. In a similar manner to fatigue, SCC involves crack nucleation and propagation leading to eventual failure. Typical methods⁶⁷ for evaluating SCC behavior involve constant strain, constant load, constant extension rate, or fracture mechanics based load application while a material is exposed to an aggressive environment. Like the safe life method used in fatigue evaluation, many of these methods conflate the surface state dominated crack nucleation stage with the microstructurally dominated crack propagation stage. Stress corrosion cracking is highly sensitive to microstructure-environment interactions that result in a number of possible cracking mechanisms. As such, it is critical to identify and understand these microstructure-environment-mechanism combinations if SCC failure is to be mitigated.

Like corrosion fatigue, stress corrosion cracking falls under the EAC umbrella. Many of the EAC factors and processes previously discussed in the context of corrosion fatigue also apply to stress corrosion cracking. Unlike corrosion fatigue, however, the removal an aggressive environment or replacement with a non-susceptible material completely negates the SCC fracture process. Fatigue can occur in the absence of environment as a purely mechanical process. Therefore, understanding and identifying the underlying environmental mechanisms is core to the study of SCC. For the purposes of this dissertation, only SCC

crack propagation processes will be discussed. This reduction in scope shifts the focus to crack tip processes as opposed to surface dominated crack nucleation processes. At and near the crack tip, chemical/electrochemical reactions and/or their by-products can promote SCC crack growth through a number of proposed mechanisms.

For metallic materials, chemical and electrochemical processes proximate to a crack tip can produce conditions that support stress corrosion crack extension. The geometry of a crack produces an occluded environment that is distinct from the bulk environment. For some environments and material systems, metal cations produced via dissolution at the crack tip support hydrolysis reactions that, in turn, acidify the crack tip. These various reactions and processes can then be buffered by mass transport and either anodic or cathodic polarization of the crack. As anodic reactions can involve the dissolution of the metal substrate into solution as an ionic species, a classical “anodic” mechanism proposed for SCC crack extension is the “film rupture” or “slip-dissolution” model⁶⁸. In this model, it is assumed that the protective passive film at a crack tip is ruptured through slip (brought on by applied stress), then bare metal can be exposed and dissolved anodically resulting in crack extension. In a similar manner, the “corrosion tunnel” model assumes that dissolution results in closely spaced tunnel-like features that eventually promote local ductile fracture and crack extension. Some models center around the rupture and re-growth of the passive layer at a crack tip to either directly extend the crack (“tamish-rupture” model) or promote local cleavage of the metal substrate (“film-induced cleavage” model). In addition to anodic reactions involving damage through direct dissolution, SCC damage can be promoted through hydrogen that is produced by the local occluded chemistry caused by the anodic dissolution process.

For general EAC, the most common routes for hydrogen, H, introduction in liquid environments are through proton reduction in acidic conditions or water reduction at cathodic potentials. Hydrogen can also be introduced in gaseous environments either directly as H₂ gas or indirectly through dissociation of water vapor⁶⁹. With the high stresses at or just ahead of the crack tip, local dilation of the material lattice promotes a high, stress-assisted H concentration, $C_{H\sigma}$, that assists the fracture process and, therefore, crack propagation. The exact mechanism through which H aids fracture is widely debated, but several mechanisms have been proposed. The three most popular of these mechanisms for H assisted damage⁶⁹ are hydrogen enhanced decohesion (HEDE), hydrogen enhanced localized plasticity (HELP), and adsorption induced dislocation emission (AIDE). Disregarding the controversies, combined HELP-HEDE models have been used to describe hydrogen environmentally assisted cracking (HEAC) in high strength alloys⁷⁰⁻⁷². Though their predictive power is limited, these models can serve as useful frameworks for describing the phenomenological observations in HEAC.

For wrought 17-4PH, there is a long record of SCC investigations in a variety of environments using a range of test methodologies. The primary test environments for 17-4PH have included aqueous 3.5% NaCl at a neutral or acidified pH, a salt spray atmospheric environment, or a “sour” H₂S containing liquid environment^{73,74}. Of these, aqueous 3.5% NaCl (~0.6M NaCl) is the most commonly employed since it simulates seawater. Early investigations involving simple U-bend specimens found that 17-4PH is resilient to SCC in neutral 3.5% NaCl under freely corroding conditions⁷⁵ (also called “open circuit potential” or OCP) and salt spray^{76,77}. Later investigations corroborated this resilience to SCC using a fracture mechanics approach⁷⁸ and slow-strain rate tension loading⁷⁹. Cathodically dominant conditions were later evaluated from a fracture mechanics perspective and showed that, depending on the temper, the threshold stress intensity (K_{TH}) could be degraded by up to 75% versus OCP conditions^{80–82}. This cathodic degradation was maximum in peak strength tempers and mitigated somewhat by overaging. Similarly, anodic conditions in acidified 3.5% NaCl promoted lower time to failure, as compared to OCP, in U-bend and constant tension tests though excessively anodic applied potentials gave way to general corrosion/dissolution^{83,84}.

Unlike its wrought counterpart, AM 17-4PH has few published SCC related investigations or even general corrosion related studies. As of a 2021 review⁸⁵, fewer than 5 studies have been published on the general corrosion behavior of AM 17-4PH, all of which were in neutral chloride solutions. In general, porosity has been linked to increased corrosion rates in AM 17-4PH versus wrought^{86,87}, though a homogenization heat treatment²⁴ or reduced sulfur⁸⁸ content in AM pushed the pitting performance closer to wrought. A small number of hydrogen sulfide environment sulfide stress cracking (SSC) tests have been performed on AM 17-4PH in accordance with NACE standards for oil & gas applications⁸⁹. Characterization was limited, but time to failure and allowable crack length requirements set by the standards were not met. A more detailed study examining the hydrogen charged smooth/notched tensile behavior of directly overaged (580°C/4 h, no solution anneal) AM 17-4PH found generally increased susceptibility to H embrittlement in AM versus wrought⁹⁰. However, the AM material was ferritic and lower strength than the martensitic wrought material which limits the utility of the comparison.

1.5 Knowledge Gaps

As a “corrosion-resistant” alloy, understanding the effect of environment on the fracture behavior of AM 17-4PH is critical. Presumably, AM 17-4PH will be chosen for engineering applications based on its apparent combination of high strength and corrosion resistance like its wrought predecessor. These types of engineering applications typically involve long service lives with stringent reliability requirements. Based on the previous discussions, it is clear that the strength aspect of this problem has received focus through mechanical property and microstructural evaluation. The service life aspect is seeing increasing

focus through fatigue evaluations, but study of the effect of environment on the fracture performance of AM 17-4PH is still in its infancy. In particular, knowledge of the environmentally assisted cracking behavior of AM 17-4PH is lacking. The two basic EAC modes, stress corrosion cracking and corrosion fatigue, have yet to be evaluated for AM 17-4PH in any level of detail.

In a similar manner to casting, the additive manufacturing process introduces a number of unique microstructural features and defects into AM 17-4PH. For wrought 17-4PH, casting ingot defects can largely be removed through a thermomechanical processing (i.e., hotworking) schedule. For AM 17-4PH, pure thermal processing is available and necessary to achieve high strength levels. However, geometric constraints preclude the “mechanical” aspect in post-processing treatments of AM components, so many of the defects that are traditionally alleviated via thermomechanical processing will persist. The nature of these persistent microstructural features and their effect on the EAC behavior of AM 17-4PH is currently unknown.

1.6 Research Objectives & Approach

To address the aforementioned knowledge gaps, five research objectives were developed to guide a survey of AM 17-4PH environmentally assisted cracking behavior. A number of assertions undergird these objectives: (i) Additively manufactured 17-4PH may be thermally post-processed to match strength for comparison to its wrought equivalent through stress corrosion cracking, corrosion fatigue, and microstructural evaluations. (ii) Through such evaluations, persistent microstructural features introduced through the additive manufacturing process and detrimental to environmentally assisted cracking performance may be identified for mitigation. (iii) This type of analysis is possible because a well-designed thermal processing schedule combined with similar chemical compositions should yield similar basic microstructural morphologies and phases for wrought and AM 17-4PH. With these assertions, the following research objectives serve as the basis of this dissertation:

1. Identify post-processing heat treatments to match strengths of wrought and additive forms of 17-4PH.
2. Determine persistent microstructural differences between the strength-matched forms of 17-4PH.
3. Quantify SCC behavior using fracture mechanics approaches and fracture morphologies for the two forms of 17-4PH.
4. Quantify corrosion fatigue behavior using fracture mechanics approaches and fracture morphologies for the two forms of 17-4PH.

5. Link persistent microstructural differences to differences in EAC behavior of wrought and AM 17-4PH.

Several themes will be followed to guide these objectives. As previously mentioned, this research is primarily a survey of AM 17-4PH EAC with an emphasis on comparing its behavior to a baseline established by wrought 17-4PH. In a similar manner to an engineer looking to substitute AM 17-4PH for standard wrought 17-4PH, best available practices (i.e., AM processing parameters, established thermal treatments, common strength levels) will be implemented to reach state-of-the-art mechanical properties. As such, the LPBF process will be used to produce the AM material. Further, a linear elastic fracture mechanics approach will be used for the fatigue and fracture evaluations. This LEFM approach supports the aforementioned damage tolerance paradigm, microstructural comparison, and shifts the focus away from surface state effects that could further complicate the study. Finally, microstructural, fractographic, and fracture kinetics data will be synthesized to inform processing changes necessary to improve AM 17-4PH EAC behavior.

1.7 Dissertation Overview

This dissertation is divided into eight chapters. The current chapter has reviewed the state of metal additive manufacturing research for the 17-4PH stainless steel alloy. Critical knowledge gaps for AM 17-4PH in the context of environmentally assisted cracking performance were identified and five research objectives were presented. The remainder of this dissertation will address each of those objectives as follows:

- Chapter 2 will evaluate the effect of post-build heat treatment on the microstructure and mechanical performance of AM 17-4PH. This evaluation will be used to establish heat treatment protocols to strength-match wrought and AM 17-4PH for the remainder of the dissertation.
- In Chapter 3, select heat treatments from Chapter 2 will be applied to rigorously compare the stress corrosion cracking performance of strength-matched AM and wrought 17-4PH.
- Chapter 4 is a focused study on the relationship between porosity, a key microstructural feature in AM metals, and the stress corrosion cracking performance of AM 17-4PH *via* examination of crack wake morphology and deformation.
- Chapter 5 extends the work in Chapter 4 to additional heat treatments of wrought and AM 17-4PH.
- Chapter 6 shifts focus to a comparison of the corrosion fatigue crack growth behavior of wrought and AM 17-4PH.

- Chapter 7 is a supplementary study on the effect of residual stress and other factors on fatigue crack growth behavior via comparison of two forms of wrought 17-4PH.

The dissertation concludes in Chapter 8 by highlighting and synthesizing the key performance metrics and performance-microstructure linkages for 17-4PH that were found throughout the work. With these insights, recommendations are provided for future studies that might aid in understanding and improving the performance of AM 17-4PH.

1.8 References

1. ASTM International. ISO/ASTM 52900:2015(E) Standard Terminology for Additive Manufacturing - General Principles - Terminology. (2016).
2. Bourell, D. L. Perspectives on Additive Manufacturing. *Annu. Rev. Mater. Res.* **46**, 1–18 (2016).
3. Singamneni, S. *et al.* Additive Manufacturing for the Aircraft Industry: A Review. *J. Aeronaut. Astronaut. Eng.* **08**, 1–13 (2019).
4. Sireesha, M. *et al.* A review on additive manufacturing and its way into the oil and gas industry. *RSC Adv.* **8**, 22460–22468 (2018).
5. Gibson, I., Rosen, D., Stucker, B. & Khorasani, M. *Additive Manufacturing Technologies*. (Springer, 2021).
6. Bajaj, P. *et al.* Steels in additive manufacturing: A review of their microstructure and properties. *Mater. Sci. Eng. A* **772**, (2020).
7. Raja, V. S. & Shoji, T. *Stress Corrosion Cracking Theory and Practice*. (Woodhead Publishing, 2011).
8. Zerbst, U. *et al.* Damage tolerant design of additively manufactured metallic components subjected to cyclic loading: State of the art and challenges. *Prog. Mater. Sci.* 100786 (2021). doi:10.1016/j.pmatsci.2021.100786
9. Laleh, M., Hughes, A. E., Xu, W., Gibson, I. & Tan, M. Y. A critical review of corrosion characteristics of additively manufactured stainless steels. *Int. Mater. Rev.* **0**, 1–37 (2020).
10. McGuire, M. *Stainless Steel for Design Engineers*. (ASM International, 2008).
11. Slunder, C. J., Hoenie, A. F. & Hall, A. M. *NASA-SP-5089 Thermal and Mechanical Treatment for Precipitation-Hardening Stainless Steels*. (1967).
12. Semiatin, S. L. Recovery, Recrystallization, and Grain-Growth Structures. in *ASM Handbook*,

Volume 14A Metalworking: Bulk Forming (ASM International, 2005).
doi:<https://doi.org/10.31399/asm.hb.v14a.a0004019>

13. Semiatin, S. L. Evolution of Microstructure during Hot Working. in *ASM Handbook, Volume 14A Metalworking: Bulk Forming* (ASM International, 2005). doi:10.31399/asm.hb.v14a.a0009002
14. Mirzadeh, H., Najafizadeh, A. & Moazeny, M. Hot deformation behaviour of precipitation hardening stainless steel. *Mater. Sci. Technol.* **26**, 501–504 (2010).
15. Mirzadeh, H. & Najafizadeh, A. The rate of dynamic recrystallization in 17-4 PH stainless steel. *Mater. Des.* **31**, 4577–4583 (2010).
16. Hoenie, A. F. & Roach, D. B. *DMIC Report 223 New Developments in High-Strength Stainless Steels.* (1966).
17. Herzog, D., Seyda, V., Wycisk, E. & Emmelmann, C. Additive manufacturing of metals. *Acta Mater.* **117**, 371–392 (2016).
18. Collins, P. C., Brice, D. A., Samimi, P., Ghamarian, I. & Fraser, H. L. Microstructural Control of Additively Manufactured Metallic Materials. *Annu. Rev. Mater. Res.* **46**, 63–91 (2016).
19. ASTM International. ASTM A693-16 Standard Specification for Precipitation-Hardening Stainless and Heat-Resisting Steel Plate, Sheet, and Strip. (2016).
20. Facchini, L. *et al.* Metastable austenite in 17-4 precipitation-hardening stainless steel produced by selective laser melting. *Adv. Eng. Mater.* **12**, 184–188 (2010).
21. Murr, L. E. *et al.* Microstructures and properties of 17-4 PH stainless steel fabricated by selective laser melting. *J. Mater. Res. Technol.* **1**, 167–177 (2012).
22. Rafi, H. K., Pal, D., Patil, N., Starr, T. L. & Stucker, B. E. Microstructure and Mechanical Behavior of 17-4 Precipitation Hardenable Steel Processed by Selective Laser Melting. *J. Mater. Eng. Perform.* **23**, 4421–4428 (2014).
23. Cheruvathur, S., Lass, E. A. & Campbell, C. E. Additive Manufacturing of 17-4 PH Stainless Steel: Post-processing Heat Treatment to Achieve Uniform Reproducible Microstructure. *JOM* **68**, 930–942 (2016).
24. Stoudt, M. R., Ricker, R. E., Lass, E. A. & Levine, L. E. Influence of Postbuild Microstructure on the Electrochemical Behavior of Additively Manufactured 17-4 PH Stainless Steel. *Jom* **69**, 506–515 (2017).
25. Meredith, S. D., Zuback, J. S., Keist, J. S. & Palmer, T. A. Impact of composition on the heat

- treatment response of additively manufactured 17–4 PH grade stainless steel. *Mater. Sci. Eng. A* **738**, 44–56 (2018).
26. Sun, Y., Hebert, R. J. & Aindow, M. Effect of heat treatments on microstructural evolution of additively manufactured and wrought 17-4PH stainless steel. *Mater. Des.* **156**, 429–440 (2018).
 27. Vunnam, S., Saboo, A., Sudbrack, C. & Starr, T. L. Effect of powder chemical composition on the as-built microstructure of 17-4 PH stainless steel processed by selective laser melting. *Addit. Manuf.* **30**, 100876 (2019).
 28. Lass, E. A., Zhang, F. A. N. & Campbell, C. E. Nitrogen Effects in Additively Manufactured Martensitic Stainless Steels : Conventional Thermal Processing and Comparison with Wrought. *Metall. Mater. Trans. A* **51**, 2318–2332 (2020).
 29. Nezhadfar, P. D. *et al.* Improved high cycle fatigue performance of additively manufactured 17-4 PH stainless steel via in-process refining micro-/defect-structure. *Addit. Manuf.* **36**, 101604 (2020).
 30. Sun, Y., Hebert, R. J. & Aindow, M. Non-metallic inclusions in 17-4PH stainless steel parts produced by selective laser melting. *Mater. Des.* **140**, 153–162 (2018).
 31. Hsu, T. H. *et al.* Microstructure and property of a selective laser melting process induced oxide dispersion strengthened 17-4 PH stainless steel. *J. Alloys Compd.* **803**, 30–41 (2019).
 32. Lashgari, H. R., Xue, Y., Onggowarsito, C., Kong, C. & Li, S. Microstructure, Tribological Properties and Corrosion Behaviour of Additively Manufactured 17-4PH Stainless Steel: Effects of Scanning Pattern, Build Orientation, and Single vs. Double scan. *Mater. Today Commun.* **25**, 101535 (2020).
 33. ASTM International. ISO/ASTM 52921:2013(E) Standard Terminology for Additive Manufacturing - Coordinate Systems and Test Methodologies. (2013).
 34. Clausen, B. *et al.* Deformation behavior of additively manufactured GP1 stainless steel. *Mater. Sci. Eng. A* **696**, 331–340 (2017).
 35. Ludwigson, D. C. & Hall, A. M. *DMIC Report 111 The Physical Metallurgy of Precipitation-Hardenable Stainless Steels.* (1959).
 36. Carneiro, L., Jalalahmadi, B., Ashtekar, A. & Jiang, Y. Cyclic deformation and fatigue behavior of additively manufactured 17–4 PH stainless steel. *Int. J. Fatigue* **123**, 22–30 (2019).
 37. Nezhadfar, P. D., Shrestha, R., Phan, N. & Shamsaei, N. Fatigue behavior of additively manufactured 17-4 PH stainless steel: Synergistic effects of surface roughness and heat treatment.

- Int. J. Fatigue* **124**, 188–204 (2019).
38. Pasebani, S., Ghayoor, M., Badwe, S., Irrinki, H. & Atre, S. V. Effects of atomizing media and post processing on mechanical properties of 17-4 PH stainless steel manufactured via selective laser melting. *Addit. Manuf.* **22**, 127–137 (2018).
 39. Boyce, B. L. *et al.* Extreme-Value Statistics Reveal Rare Failure-Critical Defects in Additive Manufacturing. *Adv. Eng. Mater.* **19**, (2017).
 40. Hu, Z., Zhu, H., Zhang, H. & Zeng, X. Experimental investigation on selective laser melting of 17-4PH stainless steel. *Opt. Laser Technol.* **87**, 17–25 (2017).
 41. Mahmoudi, M. *et al.* Mechanical properties and microstructural characterization of selective laser melted 17-4 PH stainless steel. *Rapid Prototyp. J.* **23**, 280–294 (2017).
 42. Nezhadfar, P. D., Masoomi, M., Thompson, S., Phan, N. & Shamsaei, N. Mechanical Properties of 17-4 PH Stainless Steel Additively Manufactured under Ar and N₂ Shielding Gas. in *Solid Freeform Fabrication 2018: Proceedings of the 29th Annual International Solid Freeform Fabrication Symposium – An Additive Manufacturing Conference* 1301–1310 (2018).
 43. Salzbrenner, B. C. *et al.* High-throughput stochastic tensile performance of additively manufactured stainless steel. *J. Mater. Process. Technol.* **241**, 1–12 (2017).
 44. Yadollahi, A., Shamsaei, N., Thompson, S. M., Elwany, A. & Bian, L. Effects of building orientation and heat treatment on fatigue behavior of selective laser melted 17-4 PH stainless steel. *Int. J. Fatigue* **94**, 218–235 (2017).
 45. LeBrun, T., Nakamoto, T., Horikawa, K. & Kobayashi, H. Effect of retained austenite on subsequent thermal processing and resultant mechanical properties of selective laser melted 17-4 PH stainless steel. *Mater. Des.* **81**, 44–53 (2015).
 46. LeBrun, T., Tanigaki, K., Horikawa, K. & Kobayashi, H. Strain rate sensitivity and mechanical anisotropy of selective laser melted 17-4 PH stainless steel. *Mech. Eng. J.* **1**, SMM0049 (2014).
 47. Burns, D. E. *et al.* Investigating Additively Manufactured 17-4 PH for Structural Applications. *J. Mater. Eng. Perform.* **28**, 4943–4951 (2019).
 48. Molaei, R., Fatemi, A. & Phan, N. Multiaxial fatigue of LB-PBF additive manufactured 17-4 PH stainless steel including the effects of surface roughness and HIP treatment and comparisons with the wrought alloy. *Int. J. Fatigue* **137**, 105646 (2020).
 49. Stephens, R. ., Fatemi, A., Stephens, R. R. & Fuchs, H. O. *Metal Fatigue in Engineering*. (John

- Wiley & Sons, 2001).
50. Gallagher, J. P., Giessler, F. J., Berens, A. P. & Engle, R. M. *AFWAL-TR-82-3073 USAF Damage Tolerant Design Handbook: Guidelines for the Analysis and Design of Damage Tolerant Aircraft Structures*. (1984).
 51. Milella, P. P. *Fatigue and Corrosion in Metals*. (Springer, 2013).
 52. Chowdhury, P. & Sehitoglu, H. Mechanisms of fatigue crack growth - A critical digest of theoretical developments. *Fatigue Fract. Eng. Mater. Struct.* **39**, 652–674 (2016).
 53. Brown, B. F. *Stress Control Cracking Control Measures*. (National Bureau of Standards, 1977).
 54. Gangloff, R. P. *NASA CR-4301 Corrosion Fatigue Crack Propagation in Metals*. (1990).
 55. Turnbull, A. Modelling of Environment Assisted Cracking. *Corros. Sci.* **34**, 921–960 (1993).
 56. Lin, C.-K. & Lin, C.-P. Corrosion Fatigue Behavior of 17-4PH Stainless Steel in Different Tempers. in *Fatigue and Fracture Mechanics: 33rd Volume, ASTM STP 1417* (eds. Reuter, W. G. & Piascik, R. S.) 598–613 (ASTM International, 2002).
 57. Crooker, T. W., Hasson, D. F. & Yoder, G. R. Micro-Mechanistic Interpretation of Cyclic Crack Growth Behavior in 17-4PH Stainless Steels. in *Fractography—Microscopic Cracking Processes, ASTM STP 600* (eds. Beachem, C. D. & Warke, W. R.) 205–219 (American Society for Testing and Materials, 1976).
 58. Rack, H. J. & Kalish, D. The Strength, Fracture Toughness, and Low Cycle Fatigue Behavior of 17-4 PH Stainless Steel. *Metall. Mater. Trans.* **5**, 1595–1605 (1974).
 59. Crooker, T. W., Bogar, F. D. & Cares, W. R. Effects of Flowing Natural Seawater and Electrochemical Potential on Fatigue-Crack Growth in Several High-Strength Marine Alloys. in *Corrosion Fatigue Technology, ASTM STP 642* (eds. Craig, H. L., Crooker, T. W. & Hoepfner, D. W.) 189–201 (American Society for Testing and Materials, 1978).
 60. Bogar, F. D. & Crooker, T. W. The Influence of Bulk-Solution-Chemistry Conditions on Marine Corrosion Fatigue Crack Growth Rate. *J. Test. Eval.* **7**, 155–159 (1979).
 61. ASTM International. ASTM E647-15e1 Standard Test Method for Measurement of Fatigue Crack Growth Rates. (2015). doi:10.1520/E0647-15E01
 62. Akita, M., Uematsu, Y., Kakiuchi, T., Nakajima, M. & Kawaguchi, R. Defect-dominated fatigue behavior in type 630 stainless steel fabricated by selective laser melting. *Mater. Sci. Eng. A* **666**, 19–26 (2016).

63. Mower, T. M. & Long, M. J. Mechanical behavior of additive manufactured, powder-bed laser-fused materials. *Mater. Sci. Eng. A* **651**, 198–213 (2016).
64. Romano, S., Nezhadfar, P. D., Shamsaei, N., Seifi, M. & Beretta, S. High cycle fatigue behavior and life prediction for additively manufactured 17-4 PH stainless steel: Effect of sub-surface porosity and surface roughness. *Theor. Appl. Fract. Mech.* **106**, (2020).
65. Nezhadfar, P. D. *et al.* Fatigue crack growth behavior of additively manufactured 17-4 PH stainless steel: Effects of build orientation and microstructure. *Int. J. Fatigue* **123**, 168–179 (2019).
66. Yadollahi, A. *et al.* Effects of crack orientation and heat treatment on fatigue-crack-growth behavior of AM 17-4 PH stainless steel. *Eng. Fract. Mech.* **226**, 106874 (2020).
67. Ramamurthy, S. & Atrens, A. Stress corrosion cracking of high-strength steels. *Corros. Rev.* **31**, 1–31 (2013).
68. Jones, R. H. Stress-Corrosion Cracking. in *ASM Handbook, Volume 13A: Corrosion: Fundamentals, Testing, and Protection* (eds. Cramer, S. D. & Covino, B. S.) 346–366 (ASM International, 2003). doi:10.31399/asm.hb.v13a.a0003633
69. Gangloff, R. P. Hydrogen Assisted Cracking of High Strength Alloys. in *Comprehensive Structural Integrity* (eds. Milne, I., Ritchie, R. O. & Karimhaloo, B.) (Elsevier Science, 2003).
70. Lee, Y. & Gangloff, R. P. Measurement and modeling of hydrogen environment-assisted cracking of ultra-high-strength steel. *Metall. Mater. Trans. A Phys. Metall. Mater. Sci.* **38 A**, 2174–2190 (2007).
71. Pioszak, G. L. & Gangloff, R. P. Hydrogen Environment Assisted Cracking of Modern Ultra-High Strength Martensitic Steels. *Metall. Mater. Trans. A Phys. Metall. Mater. Sci.* **48**, 4025–4045 (2017).
72. Harris, Z. D., Guiseva, K., Scully, J. R. & Burns, J. T. On the hydrogen environment-assisted cracking resistance of a compositionally complex Co–Ni–Cr–Fe–Mo–Ti alloy. *Mater. Sci. Eng. A* **802**, 140601 (2021).
73. Bloom, F. K. Stress Corrosion Cracking Of Hardenable Stainless Steels. *CORROSION* **11**, 39–49 (1955).
74. Coseglio, M. S. D. R. Sulphide stress cracking of 17-4 PH for applications in oilfield components. *Mater. Sci. Technol.* **33**, 1863–1878 (2017).
75. Humphries, T. S. & Nelson, E. E. *NASA-TM-X-53910 Stress Corrosion Cracking Evaluation of*

- Several Precipitation Hardening Stainless Steels.* (1969).
76. Slunder, C. J. *DMIC Report 158 Stress-Corrosion Cracking of High-Strength Stainless Steels in Atmospheric Environments.* (1961).
 77. Humphries, T. S. & Nelson, E. E. *NASA TM-78257 Stress Corrosion Cracking Evaluation of Martensitic Precipitation Hardening Stainless Steel.* (1980).
 78. Carter, C. S., Farwick, D. G., Ross, A. M. & Uchida, J. M. Stress Corrosion Properties of High Strength Precipitation Hardening Stainless Steels. *Corrosion* **27**, 190–197 (1971).
 79. Ghosh, R. *et al.* Effect of Heat Treatment Anomaly on the Stress Corrosion Cracking Behavior of 17-4 PH Martensitic Stainless Steel. *Trans. Indian Inst. Met.* **72**, 1503–1506 (2019).
 80. Judy, R. W., Fujii, C. T. & Goode, R. J. *NRL Report 7639 Properties of 17-4PH Steel.* (1973).
 81. Fujii, C. Stress-Corrosion Cracking Properties of 17-4 PH Steel. in *Stress Corrosion—New Approaches* 213–225 (ASTM International, 1976). doi:10.1520/STP28681S
 82. Shahinian, P. & Judy, R. Stress-Corrosion Crack Growth in Surface-Cracked Panels of High-Strength Steels. *Stress Corros. Approaches, ASTM STP 610* 128–142 (1976). doi:10.1520/stp28675s
 83. Dull, D. L. & Raymond, L. A Test Procedure to Evaluate the Relative Susceptibility of Materials to Stress Corrosion Cracking. *Corrosion* **29**, 205–212 (1973).
 84. Prasad Rao, K. & Raja, K. S. Environmental cracking behaviour of the Precipitation hardened stainless steel, 17-4 PH, under applied potential. *Mater. Corros.* **46**, 370–375 (1995).
 85. Schindelholz, E. J., Melia, M. A. & Rodelas, J. M. Corrosion of Additively Manufactured Stainless Steels—Process, Structure, Performance: A Review. *Corrosion* **77**, 484–503 (2021).
 86. Schaller, R. F., Taylor, J. M., Rodelas, J. & Schindelholz, E. J. Corrosion Properties of Powder Bed Fusion Additively Manufactured Stainless Steels. *Corrosion* **73**, 796–807 (2017).
 87. Irrinki, H. *et al.* Effects of powder characteristics and processing conditions on the corrosion performance of 17-4 PH stainless steel fabricated by laser-powder bed fusion. *Prog. Addit. Manuf.* **3**, 39–49 (2018).
 88. Alnajjar, M. *et al.* Influence of microstructure and manganese sulfides on corrosion resistance of selective laser melted 17-4 PH stainless steel in acidic chloride medium. *Corros. Sci.* **168**, 108585 (2020).
 89. Hiebler, F. Investigation of Additive Manufacturing of Components for the Oil and Gas Industry. (Montan Universitat, 2020).

90. Alnajjar, M., Christien, F., Bosch, C. & Wolski, K. A comparative study of microstructure and hydrogen embrittlement of selective laser melted and wrought 17–4 PH stainless steel. *Mater. Sci. Eng. A* **785**, 139363 (2020).

Chapter 2 - AM 17-4PH Mechanical Properties and Microstructure

2.1 Introduction

Before comparing the environmentally assisted cracking (EAC) behavior of wrought and AM 17-4PH, it is first necessary to establish the material processing routes. For wrought 17-4PH, material is available commercially in a variety of forms meeting well-established standards. Further, standard heat treatment protocols are available to provide a wide range of strength and ductility levels. Unlike wrought 17-4PH, AM 17-4PH has no well-accepted processing routes or heat treatment protocols. In the literature, heat treatment protocols have been used to enhance the strength of AM 17-4PH but with varying levels of success¹⁻⁴⁴. To further complicate the AM 17-4PH processing route, the powder choice, machine choice, and machine parameters may greatly influence the final material behavior. Therefore, the first critical task in this research is to establish material processing routes for both AM 17-4PH and wrought 17-4PH. If similar mechanical properties and microstructures are obtained between AM 17-4PH and wrought 17-4PH then root causes for EAC deficiencies in AM 17-4PH may be identified because the number of extraneous differences between the two forms are minimized.

17-4PH is commonly used in one of two conditions: (1) a “peak aged” temper with high strength and moderate ductility or (2) an “overaged” temper with reduced strength but enhanced ductility. As both of these tempers are common in engineering applications, both will be examined. The wrought form of 17-4PH is typically provided in the solution annealed condition, so either of these tempers can be easily obtained with a relatively low temperature “aging” heat treatment. Standard peak aged “H900” (i.e., 900°F/482°C, 1 h aging treatment) and overaged “H1025” (i.e., 1025°F/552°C, 4 h aging treatment) wrought 17-4PH will serve as the baselines for this study.

Additively manufactured 17-4PH requires many more processing decisions, but the aforementioned wrought baseline establishes some targets. By choosing two wrought tempers, two target strength levels of 17-4PH have been established. Additionally, the wrought microstructure is near 100% martensite with small volume fractions of austenite, delta ferrite, NbC carbides, and Cu precipitates (in order of decreasing volume fraction). For a worthy comparison of wrought and additive 17-4PH, it is necessary to mimic these basic strength and microstructure characteristics. This research will utilize the LPBF process, so an appropriate powder, machine, and machine parameter set must be chosen. For the powder, an Ar atomized powder (as opposed to water or N₂ atomized) will be utilized to maximize strength

and minimize retained austenite. For the machine, a common LPBF machine with default parameters will be used to reflect current best practices. Additionally, post-processing heat treatment will be required to transform the typically ferritic AM 17-4PH to martensite and reach desired strength levels. With post-processing, it is also possible to ameliorate some of the defects expected with additive manufacturing. Specifically, the hot isostatic press (HIP) heat treatment may be utilized to minimize porosity and homogenize the microstructure. Following the HIP, solution annealing and aging heat treatments may be applied to dissolve/precipitate Cu, respectively, and meet desired strength levels.

With the aforementioned approach as a guide, the purpose of this chapter is to perform a microstructural and mechanical properties evaluation comparing wrought and AM 17-4PH. The influence of HIP, solution annealing, and aging heat treatments on the microstructure and mechanical properties of peak aged and overaged AM 17-4PH will be identified. Additionally, the effect of high-pressure on porosity will be isolated with an atmospheric pressure homogenization treatment matching the HIP temperature and time profile. Subsequent to heat treatment, a combination of hardness, tensile, fractographic, and microstructural evaluation techniques will be used to identify and compare strength-matched AM and wrought 17-4PH. These results will then be synthesized to identify microstructural feature(s) that might lead to observed deficiencies in AM 17-4PH mechanical behavior.

2.2 Methods

2.2.1 Materials

The wrought and AM forms of 17-4PH were obtained for comparison in this study as follows. The AM material was built using the laser powder bed fusion (LPBF) process with an EOS M290 machine. In accordance with best practices, the built-in machine parameters recommended by EOS for 17-4PH were used⁴⁵. Notable parameters include a 47° hatch rotation angle, 0.11 mm infill hatch distance, 220.1 W infill laser power, 755.5 mm/s infill laser speed, 0.04 mm layer thickness, 80 °C build plate temperature, an argon build atmosphere, and the use of argon-atomized powder (particle size range of 15-45 μm). Two LPBF builds were performed according to the build plate layout in Fig. 1 to produce 21 x 21 x 75 mm stock bars in two orientations. Note that the coordinate system shown conforms to ISO/ASTM 52921⁴⁶, and the stock bars were rotated 11 degrees off axis to aid with powder flow during recoating. Virgin powder was used for the first build and then recycled for use in the second build.

Post-build, the printed bars of stock material were cut from the build plate using electrical discharge machining (EDM) for heat treatment and specimen machining. One stock bar in each orientation was left in the “as-built” condition for characterization. The remainder of the stock bars underwent a series of one or more high-temperature heat treatments. These treatments are designated as “SA” for solution anneal, “HIP” for hot isostatic press, “HIP+SA” for HIP followed by SA, or “Hom+SA” for homogenization

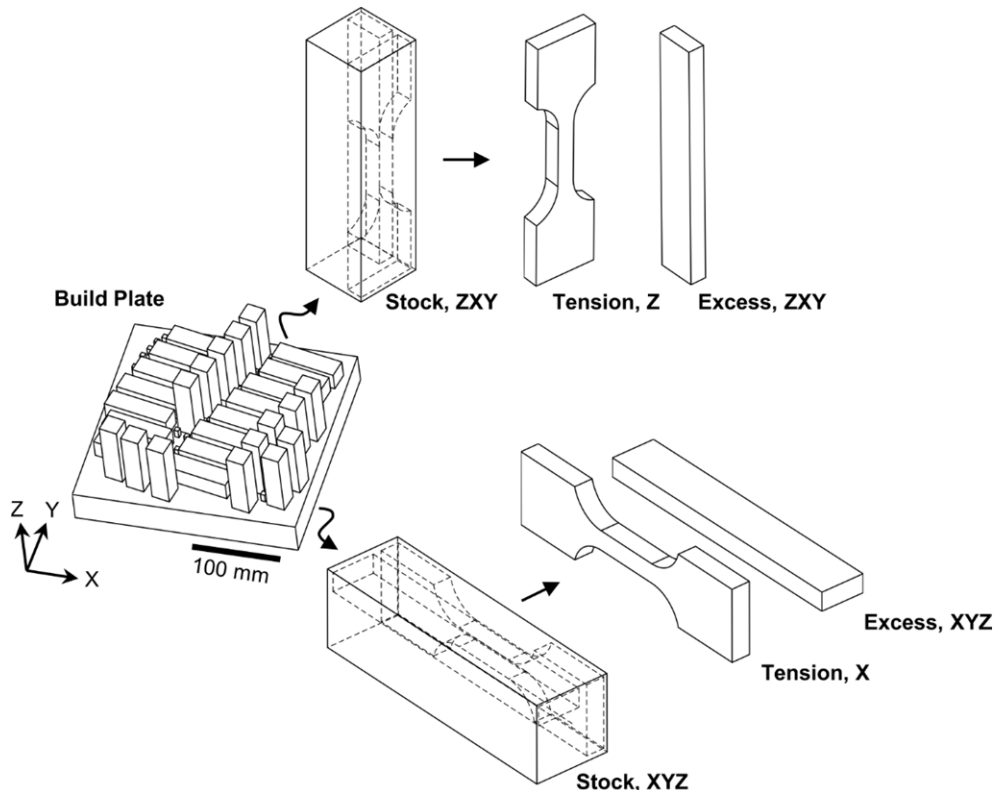


Fig. 1 | **AM build and specimen geometries.** Laser powder bed fusion with the displayed build plate layout was used to generate stock AM material in two orientations (ZXY, XYZ). The stock material was cut from the plate and two specimen geometries (tension, excess) were excised/machined for evaluation.

followed by SA. The SA treatments were conducted in lab air at 1040°C for 0.5 h, followed by air-cooling to ambient temperature. The HIP treatment was performed in argon at a pressure of 100 MPa and temperature of 1125°C for 4 h, followed by furnace-cooling at 310°C/h to 300°C, then air-cooling to ambient temperature. Note that the HIP time, temperature, and pressure were chosen based on recommendations in ASTM F3301⁴⁷ for 4340 and UNS S31603 since specific parameters for 17-4PH were not available. The HIP cooling rate was the standard rate used by the process supplier. The Hom treatment consisted of the same time, temperature, and cooling rate as the HIP - but at atmospheric pressure. The stock bars were wrapped and sealed in 0.05 mm thick 309 stainless steel foil to protect the bars from excessive oxidation during the Hom treatment. Tension and excess specimens were then machined from the stock (Fig. 1), and, if previously heat treated, underwent a low-temperature “peak age” (440-500°C for 1 h, air-cool) or “overage” (552°C for 4 h, air-cool) treatment in lab air for either peak strength or increased ductility, respectively. Throughout the heat treatment and machining processes, build orientations were tracked to differentiate between the various build planes (XY, XZ, YZ) and tensile loading directions (X, Z).

The wrought material was procured as an electric furnace (EF) melted, argon-oxygen decarburized (AOD), and hot-rolled 15.9-mm thick plate produced per ASTM A693⁴⁸ and supplied in the SA condition. Tension and excess specimens were excised from the plate and heat treated in lab air to either a standard peak age (482°C for 1 h, air-cool) or overage (552°C for 4 h, air-cool) condition. Tension specimens were oriented with the loading axis parallel to the longitudinal (L) direction (i.e., the plate rolling direction).

Chemical compositions of the as-supplied wrought and as-built AM material were measured using inductively coupled plasma optical emission spectroscopy (ICP-OES), glow discharge mass spectroscopy (GDMS), and instrumental gas analysis (IGA), see Table 1. Compositions were nominally similar for the wrought and AM materials. All primary alloy elements, reported in wt. %, fell within the ASTM A693⁴⁸ specifications for wrought 17-4PH. Differences were mainly in the trace elements composition, reported in wppm, with the wrought material having significantly more C, N, V, Mo, Co, and W than the AM material. The AM material overall had smaller concentrations of impurities relative to the wrought material except for a significant amount of O within the powder that decreased slightly during the build. Note that the powder composition was measured by the powder supplier while a commercial laboratory (Evans Analytical Group) measured the wrought and AM build material compositions. The apparent increase in Ni and Si from powder to build is most likely due to testing lab variability.

2.2.2 Microstructure Evaluation

Specimens for microstructure evaluation were cut from excess portions of both the wrought and AM materials. The wrought material was examined in the SA condition on the LS and ST material planes, where L, T, and S are the longitudinal, long transverse, and short transverse directions, respectively. The AM material was evaluated on the XY and YZ planes for all pre-aging heat treatment conditions (i.e., as-built, SA, Hom+SA, HIP, HIP+SA). To best represent the mechanical tests, microstructure evaluation planes were sectioned near the center of each stock bar - though macroscale spatial variability in microstructure was not observed in spot-checks. Polished samples were mounted in cold-curing epoxy

Table 1 | Elemental composition of the wrought and AM 17-4PH compared in this study.

Form (wt%):	C	Mn	P	S	Si	Cr	Ni	Cu	Nb	Fe
Wrought	0.041	0.51	0.018	0.001	0.32	15.20	4.85	3.22	0.26	bal.
AM										
Powder	0.020	0.46	< 0.010	< 0.010	0.45	16.32	4.36	4.00	0.29	bal.
Build	0.014	0.42	0.009	0.006	0.53	16.10	4.51	3.73	0.28	bal.
Form (wppm):	Al	Mo	N	O	V	Co	As	Sn	W	
Wrought	10	1600	280	44	510	770	31	53	230	
AM										
Powder	-	100	100	600	-	-	-	-	-	
Build	12	57	140	480	26	260	17	12	7	

resin and initially ground using 320, 600, 800, and 1200 grit SiC papers, followed by polishing with 3, 1, 0.5, 0.25, and 0.1 μm diamond slurries, and finishing with 0.05 μm alumina or colloidal silica suspension.

Orientation imaging microscopy (OIM) was conducted *via* electron backscatter diffraction (EBSD) using a FEI Helios G4 UC FIB/SEM equipped with an Oxford Instruments Symmetry EBSD detector. All samples were degaussed prior to imaging and OIM maps were collected at two different magnifications using an accelerating voltage of 20 keV and probe current of 3.2 nA. Low-magnification maps were completed at 200x/500x using a 0.15 μm step size, while high-magnification maps were performed at 2500x using a 75 nm step size. Inverse pole figure (IPF) maps and parent austenite grain structure were determined from the collected OIM data using the MTeX software package⁴⁹. To determine the parent austenite grain structure, prior austenite grain boundaries (PAGBs) were reconstructed using the approach developed by Nyssonen *et al.*⁵⁰

Pore morphology and material density were evaluated using scanning electron microscopy (SEM) and the Archimedes method⁵¹. Pore evaluations were performed with a FEI Quanta 650 SEM to capture secondary electron (SE) and backscatter electron (BSE) images. The various forms/planes/heat treatments were evaluated at magnifications ranging from 200x to 10,000x. SE image contrast, indicating topographic variation, was used to verify cavernous pores were present. The high contrast provided by BSE imaging was used to capture a set of images for quantitative evaluation of the pore morphology *via* image analysis. A MATLAB circle finding algorithm was then used to process the images and calculate pore diameters, pore spatial distributions, and percent density by area (i.e., 100 - area percent of pores). Volumetric densities were obtained by a commercial laboratory (Evans Analytical Group) using a Dataphysics DCAT 25 tensiometer. The volumetric density samples weighed ≥ 3.0 g and were measured a minimum of three times each to establish a mean and standard deviation density for each material condition.

2.2.3 Mechanical Testing

Hardness testing was used to evaluate the peak aging temperature for wrought and AM 17-4PH. Prior to hardness testing, samples were incrementally polished with 320, 600, 800, and 1200 grit SiC paper. The Vickers micro-hardness was then measured in accordance with ASTM E384⁵² using an applied load of 500 g and a dwell time of 10 s. A minimum of nine measurements were taken to establish a mean and standard deviation hardness. For reference, these micro-hardness values were then converted to the Rockwell C hardness scale in accordance with ASTM E140⁵³.

Tensile stress-strain behavior was evaluated for selected heat treatments of wrought and AM 17-4PH, refer to Table 2. Tension testing was performed on a servohydraulic load frame in accordance with ASTM E8⁵⁴. Samples had a 5 x 5 mm square gage cross-section and 17.8 mm reduced section length. A minimum of two replicate tests (i.e., N = 2) were performed for each heat treated condition and orientation.

Table 2 | Summary of mechanical properties obtained in this study for AM and wrought 17-4PH.

Form	Heat Treatment	Loading Direction	E (GPa)	σ_{YS} (MPa)	σ_u (MPa)	e_u (mm/mm)	e_f (mm/mm)	EL (%)	RA (%)	α	n	N
AM	As-Built	X	214	810	886	0.107	0.419	27.1	67	2.194	13.2	1
		Z	185	793	863	0.103	0.439	24.3	57	1.555	14.9	1
Wrought	SA+482°C/1 h	L	204	1194	1336	0.085	0.410	20.7	59	0.344	19.3	2
		AM	SA+460°C/1 h	X	209	1281	1417	0.060	0.209	14.0	36	0.115
	HIP+460°C/1 h	Z	205	1265	1395	0.039	0.272	12.1	38	0.041	35.7	2
		X	197	1211	1366	0.044	0.186	11.8	30	0.048	29.9	3
	Hom+SA+460°C/1 h	Z	208	1214	1371	0.028	0.147	11.2	34	0.067	26.8	2
		X	196	1254	1407	0.070	0.277	15.7	37	0.112	25.0	2
	HIP+SA+460°C/1 h	Z	204	1269	1406	0.062	0.215	14.3	29	0.111	28.1	2
		X	205	1291	1432	0.059	0.283	15.2	40	0.080	29.4	2
	HIP+SA+500°C/1 h	Z	205	1295	1432	0.040	0.238	12.8	34	0.047	33.9	2
		X	208	1260	1364	0.046	0.290	15.0	44	0.074	37.1	2
Wrought	SA+552°C/4 h	Z	201	1238	1350	0.043	0.257	14.3	40	0.114	32.8	3
		L	207	1059	1110	0.068	0.435	21.4	62	1.136	21.5	2
AM	HIP+SA+552°C/4 h	X	197	1078	1114	0.065	0.335	17.1	49	0.766	28.5	2
		Z	220	1128	1156	0.034	0.299	15.7	45	0.422	45.6	2

Test loads were applied at a constant crosshead displacement rate of 8×10^{-4} mm/s, which corresponded to an initial strain rate of $\sim 1 \times 10^{-4}$ s⁻¹. The engineering strain (e) was calculated using displacement measured with an 8 mm gage length clip-on extensometer. The strains at peak and failure loads were used to determine the uniform engineering strain (e_u) and engineering strain at failure (e_f), respectively. Considères criterion⁵⁵ was used to calculate the true strain at necking and corresponded well with e_u . Modulus of elasticity (E), 0.2% offset yield strength (σ_{YS}), and ultimate strength (σ_u) were calculated through normal means. Strain hardening parameters (n and α) were determined by fitting the Ramberg-Osgood power law equation⁵⁶ to true stress-strain curves. Post-test, elongation to failure (EL) was calculated by dividing the total sample length change, measured using ruler-paper (+/- 0.25 mm), by the aforementioned reduced section length. Fractographic examination was performed using a combination of optical and SEM imaging. Reduction in area (RA) was calculated using optical fractographs. Fractographic features and morphologies were evaluated *via* SEM at magnifications ranging from 20x to 2500x. Fracture dimple spacing was quantified by manually marking 2500x images with approximately 100 dimple centers per condition and using image analysis to gather spacing statistics.

2.3 Results

2.3.1 Microstructure

The microstructures of AM and wrought 17-4PH were first evaluated and compared using EBSD, refer to Fig. 2. For AM, the nominal “as-built” condition consisted of a coarse, ferritic, highly anisotropic structure. Elongated solidification structures are apparent in the YZ plane (Fig. 2a) while a checkboard pattern consistent with the laser-scanning strategy is reflected in the XY plane (Fig. 2b). Similar as-built microstructural morphologies have been reported several times in the literature^{37,57–59} for AM 17-4PH and

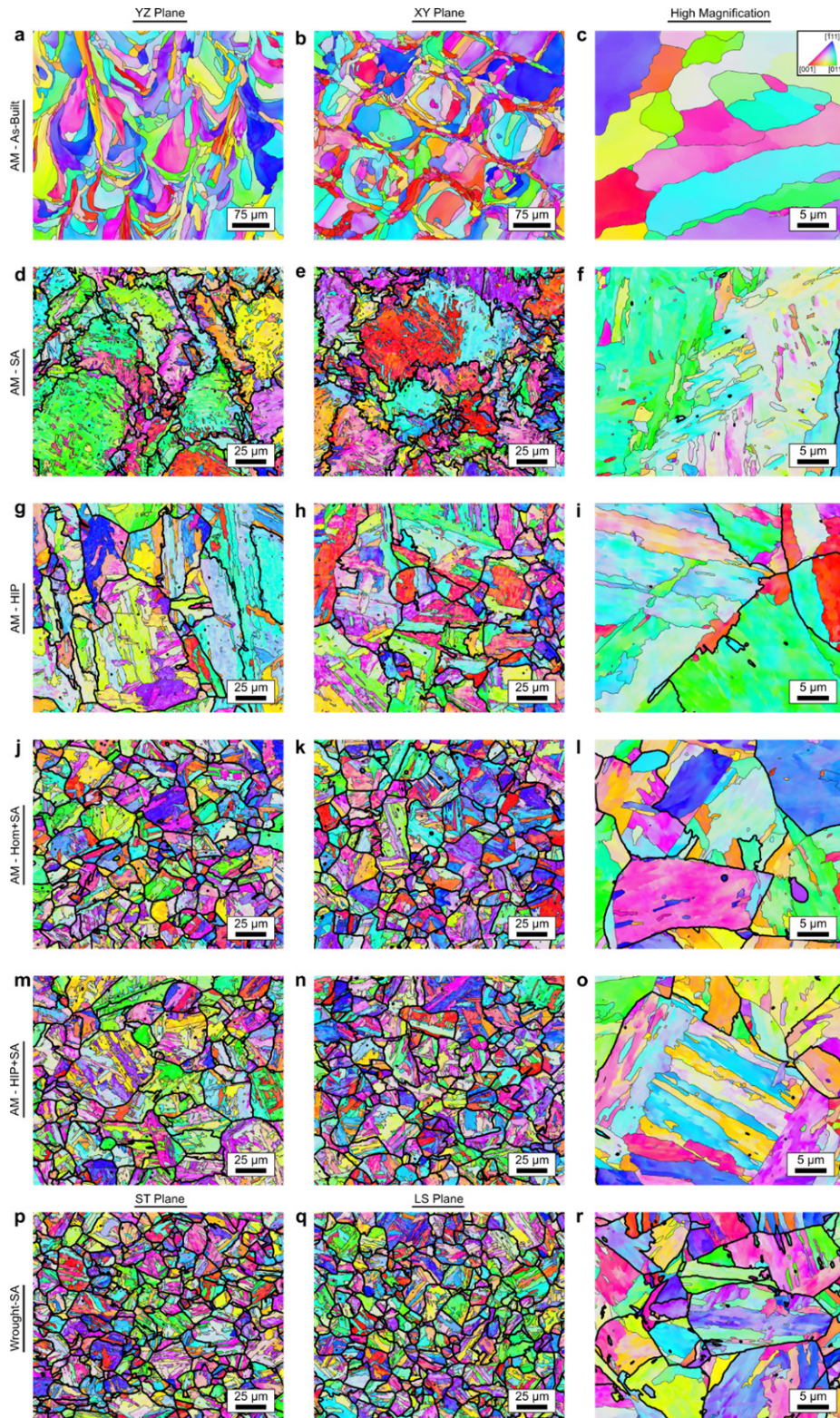


Fig. 2 | Evolution of AM 17-4PH microstructure with heat treatment and comparison to wrought 17-4PH. a-c, AM in as-built condition. d-f, AM after SA heat treatment. g-i, AM after HIP treatment. j-i, AM after Hom+SA treatment. m-o, AM after HIP+SA treatment. p-r, Wrought in SA condition. Microstructures from AM in the YZ plane are shown in (a, d, g, j, m) and XY plane in (b, e, h, k, n). Wrought ST and LS planes are shown in (p) and (q), respectively. Representative high magnification maps are shown for each condition in (c, f, i, l, o, r). Colored regions indicate ferrite & martensite phase grain orientations. Fine black outlines indicate ferrite & martensite grain boundaries while bold outlines indicate PAGBs.

may be considered typical for the build strategy presented by this work. After applying a SA treatment, the coarse, as-built grain structure underwent significant refinement. This refinement is clearest when comparing high magnification grain maps of the two conditions (Fig. 2c,f). Specifically, the globular as-

built structure is replaced by a fine, plate-like structure indicating a martensitic transformation in the SA condition. However, remnants of the coarse, as-built structure still remain apparent. Outlining the prior austenite grain boundaries (PAGBs) in the SA condition continues to reflect elongated grains in the YZ plane (Fig. 2d) with comparably smaller grains in the XY plane (Fig. 2e). This is especially clear when comparing to the equiaxed PAGs in the wrought microstructure (Fig. 2p,q).

The additional time and temperature of the HIP, Hom+SA, and HIP+SA heat treatments produced AM 17-4PH microstructures most comparable to wrought 17-4PH. The HIP produced a rounded PAG and block/packet martensite structure⁶⁰ (Fig. 2g,h,i) comparable to wrought, but the martensite and PAG structures were both coarser in AM. Additionally, slight anisotropy is still present in the HIP condition. The HIP YZ plane PAG structure (Fig. 2g) has a coarser, elongated structures than the XY plane (Fig. 2h), consistent with the as-built and SA conditions. The dual-stage Hom+SA (Fig. 2j,k,l) and HIP+SA (Fig. 2m,n,o) heat treatments produced AM 17-4PH microstructures closely resembling wrought 17-4PH. Equiaxed PAG structures just slightly larger than wrought, martensite block/packet structures, and martensite blocks with similar sizes to wrought were yielded by both of these dual-stage heat treatments. Noting that the Hom+SA treatment has the same time/temperature profile as the HIP+SA treatment, application of pressure during heat treatment had no apparent effect on either the PAG or martensite grain structure evolution of AM 17-4PH. As a final note on the EBSD evaluation, negligible amounts of retained austenite were detected; the primary phase was ferrite/martensite in all conditions of wrought and AM 17-4PH.

The persistent differentiator between AM and wrought 17-4PH was the presence of porosity in AM 17-4PH, refer to Fig. 3. Wrought 17-4PH was found to be fully dense with no indications of porosity. Conversely, pores were present in AM 17-4PH and followed a bi-modal distribution that could be divided into micrometer scale and sub-micrometer scale porosity. At the micrometer scale, porosity was evaluated at 200x magnification and found to be negligible with few pores per image, typically <10 μm in diameter. These larger pores were most evident in the as-built, SA, and Hom+SA conditions, but evaluation was limited in scope. The HIP was generally effective in eliminating pores at the larger length scale. The vast majority of pores were found at the sub-micrometer length scale and are shown for each AM condition in Fig. 3a-e. These sub-micrometer pores underwent clear evolution in size and spacing with the various AM heat treatments starting at a nanometer length scale in the as-built condition.

To evaluate the pore evolution, the diameter and spacing of statistically significant sample sizes of pores (N_{pore}) were quantified for each AM 17-4PH condition (Fig. 3f-g). The sigmoidal shapes of the various empirical cumulative distribution functions shows that the pore diameters (Fig. 3f) and spacings (Fig. 3g) are normally distributed except for the Hom+SA condition that skews to pore diameters larger than 0.2 μm .

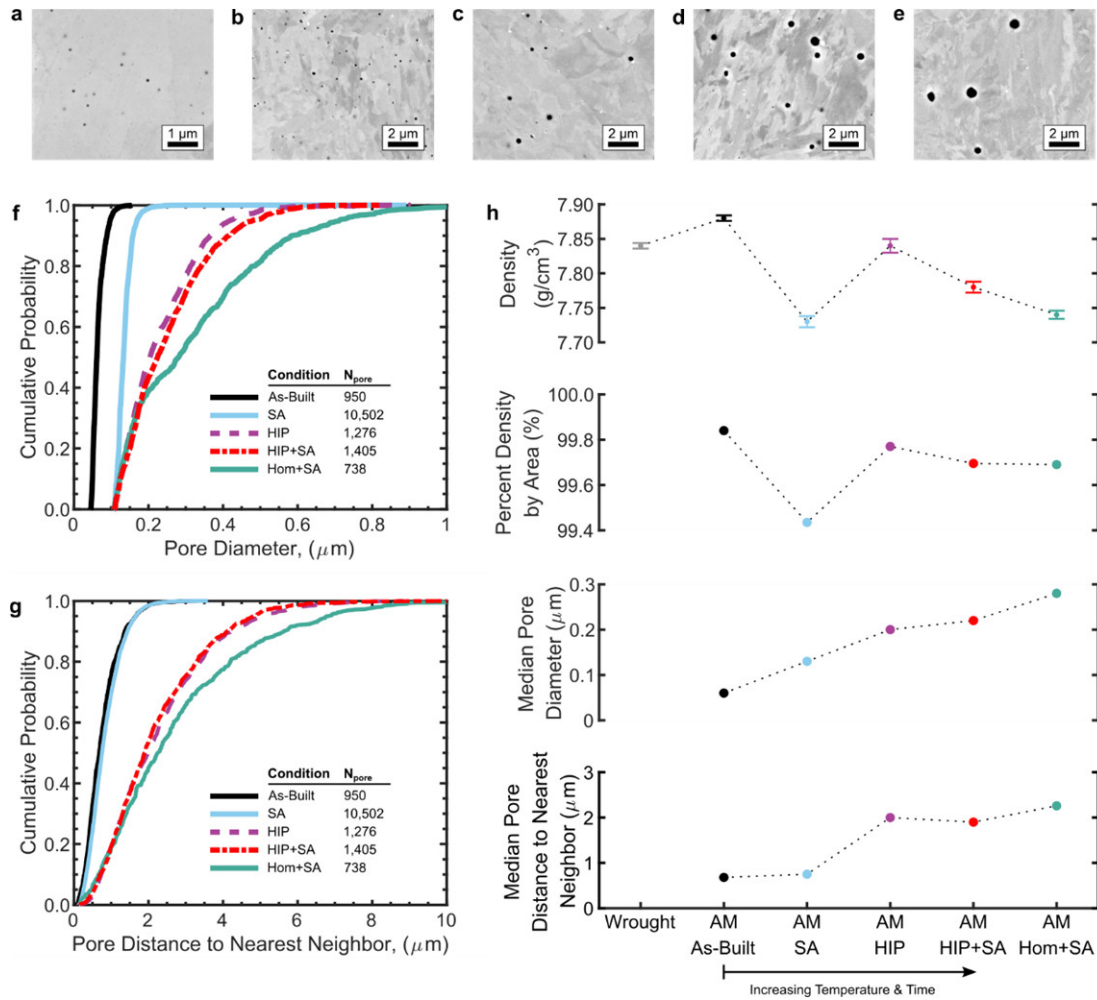


Fig. 3 | Evolution of density and sub-micrometer scale porosity with heat treatment of AM 17-4PH. a-e, Morphology of pores in the as-built (a), SA (b), HIP (c), HIP+SA (d), and Hom+SA (e) conditions. f-g, Quantification of the pore diameter (f) and spacing (g) distributions across the various AM heat treatment conditions. h, Summary of density and pore morphology metrics with wrought density included for reference. Note that “Density” was measured using the Archimedes method and “Percent Density by Area” was calculated using planar image analysis. As-built pore statistics were captured using 7500x magnification images; statistics for all other conditions were captured at 2500x.

The relative differences between the various conditions are best understood by first looking at the pore spacing (Fig. 3g). There are clearly three regimes of pore spacing: (1) as-built and SA, (2) HIP and HIP+SA, and (3) Hom+SA. Regime (1), consisting of no heat treatment and the lowest time at elevated temperature, has the smallest pore spacing. Regime (2) involved applied pressure (HIP) and increased the pore spacing. Regime (3) consisted of the longest applied temperature/time with no applied pressure and resulted in the largest pore spacing. This general spacing increase with time and temperature suggests that a classical coarsening mechanism⁶¹ is present. However, if this were a simple coarsening phenomenon, then conservation of mass might suggest a similar trend in the pore size (i.e., pore spacing increasing as pores

consolidate to larger sizes). Instead, the regime (1) conditions split into two discrete sets of pore sizes, and regime (2) has a clear, though subtle, difference in pore size between the HIP and HIP+SA conditions.

Density measurements were used to clarify these pore size and spacing behaviors, refer to Fig. 3h. Density was measured both by volumetric means (i.e., “Density”) and by quantifying pore area (i.e., “Percent Density by Area”). The density for wrought 17-4PH is shown for a 100% density baseline, but as-built AM 17-4PH, which is clearly less than 100% dense, actually has a higher density than wrought. This may be understood by recognizing that as-built AM 17-4PH has a ferritic (BCC) crystal structure while wrought 17-4PH is martensitic (BCT)⁶². This difference in crystal structure results in ferrite being denser than martensite⁶³⁻⁶⁵. Noting the previously discussed martensitic transformation for the SA conditions, the significant density reduction from as-built to SA is likely due, at least partially, to this crystallographic density difference. The strain involved in the martensitic transformation might also partially explain the expansion of the pores (i.e., reduction in density by area and increase in median pore size) from as-built to SA with no change in pore spacing. However, pore expansion also occurs from the HIP to HIP+SA condition with no ferrite to martensite transformation (i.e., both of these conditions are martensitic). This suggests the presence of mechanism(s) for pore expansion beyond coarsening and crystallographic effects.

The HIP and HIP+SA conditions may be used to identify a third mechanism driving the pore size and density variations. First, the HIP results in the highest AM 17-4PH density, but pores are still present (Fig. 3c) and density is lower than wrought on both the volumetric and area-based metrics (Fig. 3h). This suggests that (1) the pores are filled with an insoluble gas and (2) the gaseous pores respond to applied pressure. With regard to the HIP, the external pressure shrinks the pores and increases density, but the pores still increase in size relative to the as-built and SA conditions due to a classical coarsening mechanism. If pressure is a factor driving pore evolution, then internal pressure should act to expand the pores. For a gaseous pore, a high temperature treatment would increase internal pore pressure, potentially expand the pores, and subsequently reduce density. Indeed, this is exactly the behavior observed when comparing the HIP to the HIP+SA condition (Fig. 3h). Correspondingly, with its lack of applied pressure, the Hom+SA condition results in the largest pore size and the second lowest density.

2.3.2 Mechanical Properties

The results in Table 2 illustrate the need to heat treat AM 17-4PH in order to match wrought 17-4PH strength levels. Though ductility is higher, both the yield strength and ultimate strength of as-built AM 17-4PH are less than 70% of peak aged (SA+482°C/1 h) wrought 17-4PH. This strength difference may be bridged by applying a high-temperature heat treatment to produce a martensitic structure, followed by a low-temperature aging heat treatment to precipitate Cu for enhanced strength. The previous section demonstrated the effects of various high-temperature heat treatments on the microstructure at the

micrometer and sub-micrometer scale, but Cu precipitation occurs on the nano-scale. Rather than directly evaluating the nano-scale microstructure, the effects of these nano-scale precipitates were evaluated through microhardness testing of 17-4PH with 1.0 h aging treatments at various temperatures, refer to Fig. 4. The first takeaway from this hardness study is that both AM and wrought 17-4PH reach peak hardness at approximately 460°C for the 1.0 h aging time. This peak hardness temperature is consistent with manufacturer recommendations for peak aging AM 17-4PH⁴⁵, but inconsistent with the common H900 “peak age” temper for wrought 17-4PH (482°C). The second takeaway is the range of AM hardness values produced by the various high-temperature treatments preceding aging. For a given aging temperature, AM 17-4PH consistently exhibited higher hardness than wrought except for the HIP condition.

With the aforementioned hardness data, AM 460°C and 500°C “peak age” temperatures were chosen for comparison to the common, 482°C peak age wrought temper *via* tension testing, refer to Fig. 5 and Table 2. Consistent with the hardness data, AM generally had higher yield and ultimate strength with the HIP+460°C/1 h condition strength mostly closely matching peak aged wrought. These trends held across loading orientations with little strength anisotropy between X and Z loading. With regard to ductility, all conditions of peak aged AM underperformed relative to peak aged wrought with lower e_u , e_f , EL , and RA . Additionally, the Z loaded AM was generally less ductile than X loaded AM. Noting the generally inverse relationship between strength and ductility, it is not surprising that the higher strength AM tempers were less ductile than wrought. For potentially more comparable ductility, a 500°C/1 h heat treatment with a lower, more comparable hardness/strength match between AM and wrought was evaluated, but the AM ductility deficit persisted (Fig. 5e). To further investigate the mechanical behavior differences between AM and wrought, the work hardening rate (WHR) behavior was evaluated (Fig. 5b,d,f). Interestingly, a better

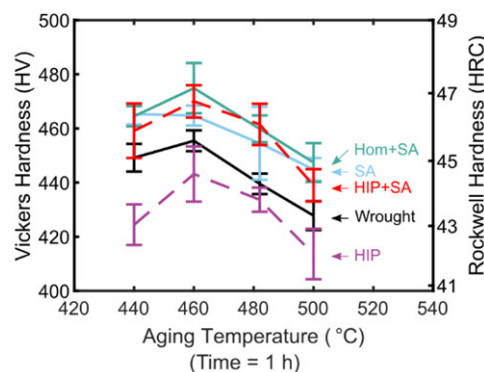


Fig. 4 | **Hardness variation with aging temperature for AM and wrought 17-4PH.** Vickers micro-hardness and equivalent Rockwell C hardness variation is shown for 1 h aging heat treatments at various temperatures. Wrought was aged in the SA condition while AM was aged in the Hom+SA, SA, HIP+SA, and HIP conditions.

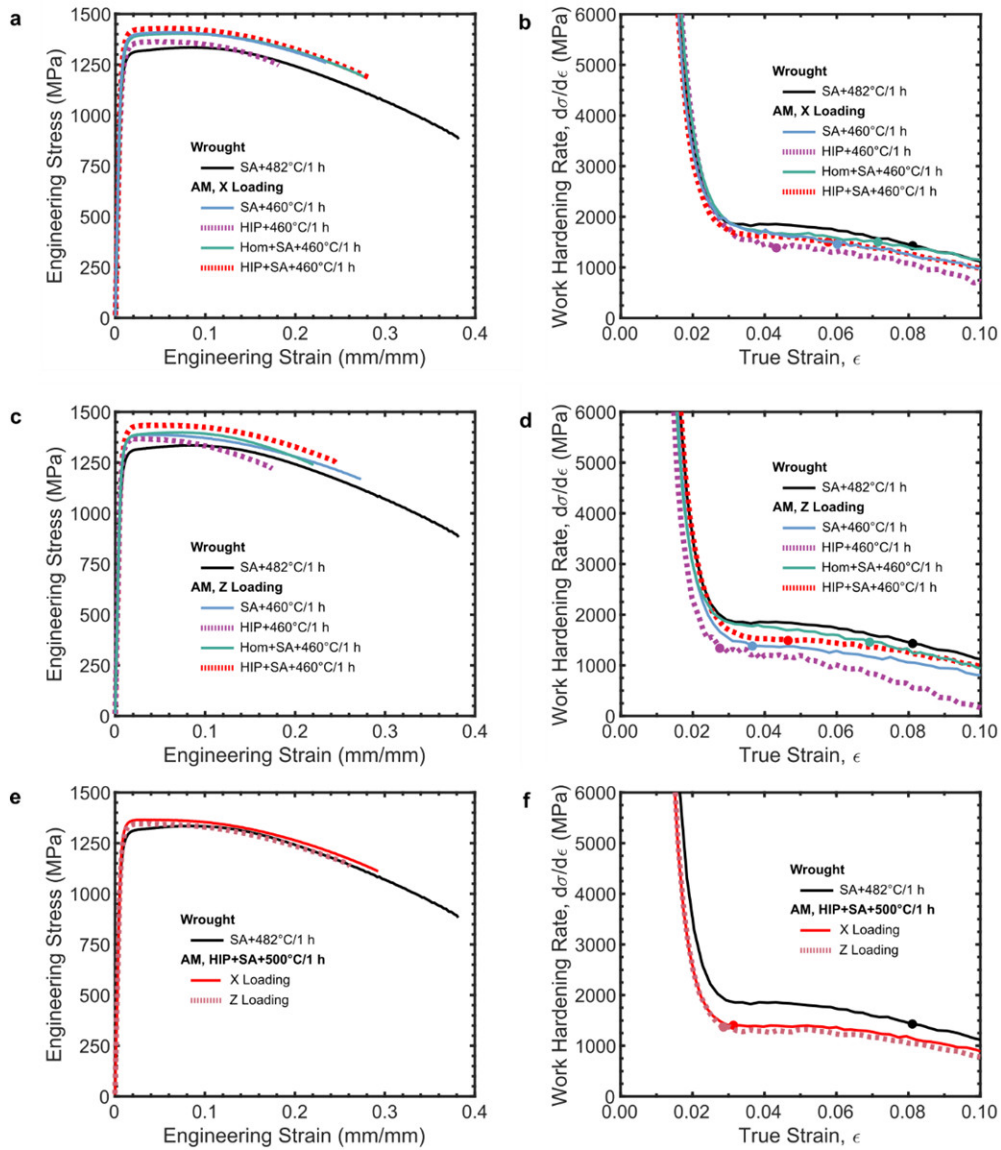


Fig. 5 | **Comparison of stress-strain and work hardening rate behavior for peak aged wrought and AM 17-4PH.** **a-b**, 460°C peak aged AM loaded in X direction versus peak aged wrought. **c-d**, 460°C peak aged AM loaded in Z direction versus peak aged wrought. **e-f**, Peak aged wrought versus hardness matched (500°C aging temperature) AM. Engineering stress-strain curves are shown in **(a, c, e)** and work hardening rate curves in **(b, d, f)**. Onset of necking, determined by Considère's criterion, is identified with the circular markers in **(b, d, f)**.

WHR match occurred between the AM 460°C tempers and wrought than the between wrought and the hardness-matched AM 500°C temper. Specifically, the WHR for the X loaded SA, Hom+SA, and HIP+SA conditions match well to wrought with the highest necking strains. In comparison, the hardness matched AM 500°C temper has a reduced WHR and the lowest necking strain of all peak aged tempers. Note that

these WHR curves are only strictly valid prior to the onset of necking⁵⁵, indicated by circular markers, but $d\sigma/d\epsilon$ is estimated at higher strains for reference.

Tensile behavior of overaged wrought and AM 17-4PH was also compared in Fig. 6 and Table 2. Unlike peak aging, overaging at 552°C for 4 h yielded similar hardness values for both AM in the HIP+SA condition (366-370 HV) and wrought (358-378 HV). This matching carried through to yield and ultimate strength with a maximum difference of 69 MPa between AM and wrought. However, the ductility deficit in AM persisted with reductions across all ductility metrics versus wrought. Also, the WHR is significantly lower in overaged AM than overaged wrought. Interestingly, the relatively isotropic strength behavior in peak aged AM did not hold for overaged AM. The maximum strength difference for X and Z loaded peak aged AM was 22 MPa. Conversely, the strength difference is 42-50 MPa for the two loading orientations of overaged AM. This anisotropy is further magnified by the significant difference in necking strain (near 2-fold) between the two loading orientations (Fig. 6b), though the WHR behavior is otherwise similar.

2.3.3 Fractography

Fractographic examination was performed in order to understand the fracture mechanism differences in AM and wrought 17-4PH and between the various conditions of AM 17-4PH. In the peak aged condition, a wide range of AM fracture morphologies were found that varied across all evaluated heat treatments and by loading orientation, see Fig. 7. With regard to loading orientation, the clearest fractographic differences were present for the SA+460°C/1 h condition and the HIP+SA+500°C/1 h condition. For the former, secondary fracture occurring into plane (red outlines, Fig. 7a,b) seems to follow the as-built grain structure morphology. For example, the X loaded fracture shown in Fig. 7a occurs on the YZ plane; comparison with the corresponding as-built microstructure (Fig. 2a) then illustrates clear

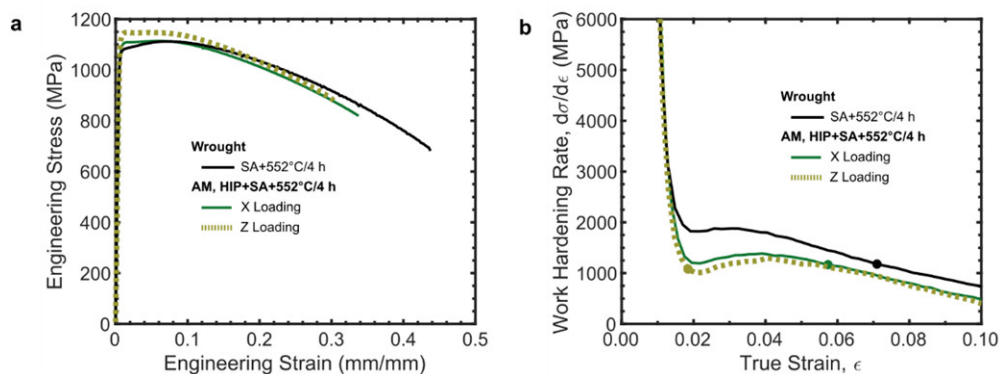


Fig. 6 | Comparison of stress-strain and work hardening rate behavior for overaged wrought and AM 17-4PH. **a**, Engineering stress-strain curves. **b**, Work hardening rate curves. Onset of necking, determined by Considère's criterion, is identified with circular markers in (b).

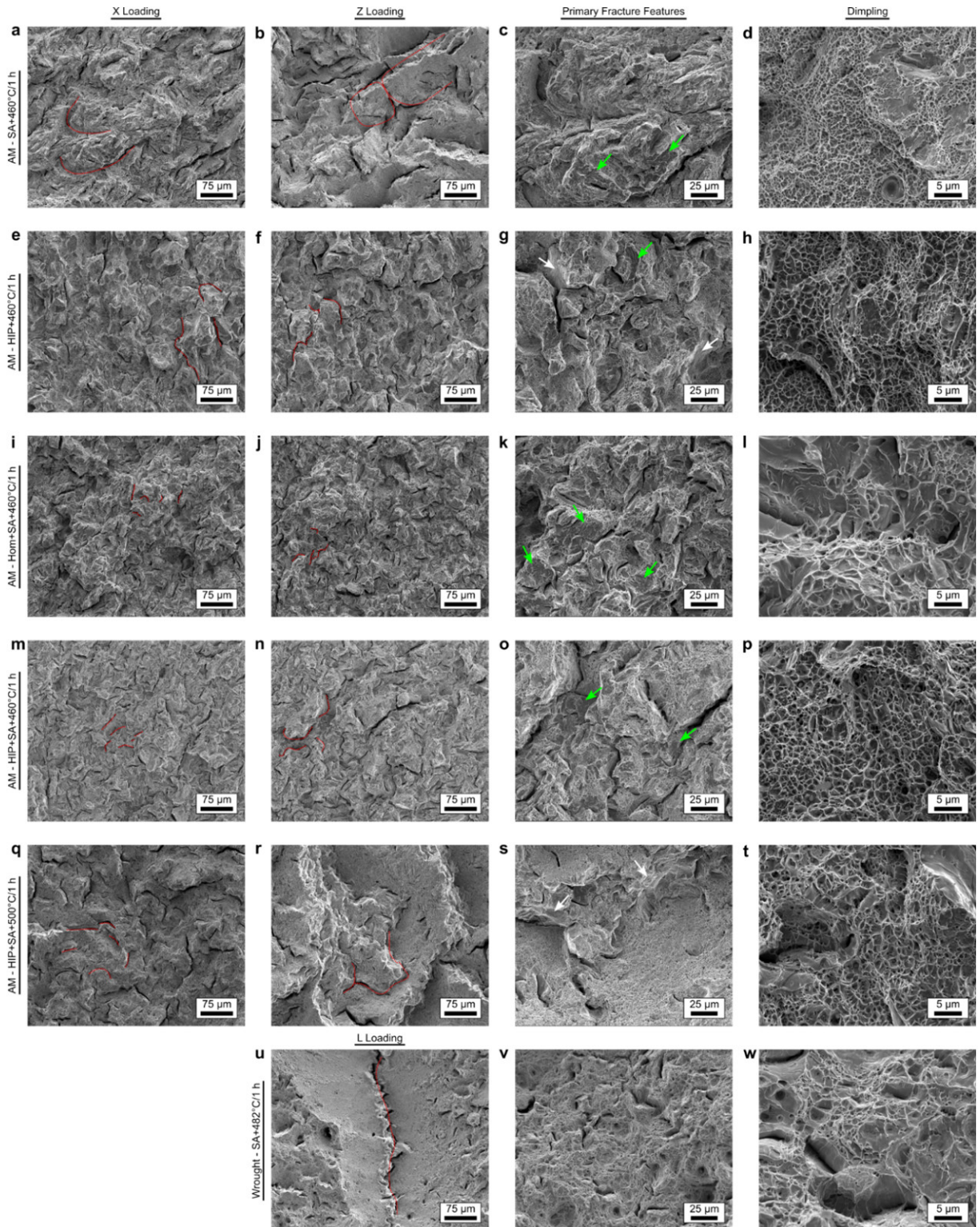


Fig. 7 | Tensile fracture morphologies for peak aged AM and wrought 17-4PH. **a-d**, AM in the SA+460°C/1 h condition. **e-h**, AM in the HIP+460°C/1 h condition. **i-l**, AM in the Hom+SA+460°C/1 h condition. **m-p**, AM in the HIP+SA+460°C/1 h condition. **q-t**, AM in the HIP+SA+500°C/1 h condition. **u-w**, Wrought in the SA+482°C/1 h condition. Fractographs representative of X loading in each condition are shown in (**a**, **e**, **i**, **m**, **q**) and Z loading in (**b**, **f**, **j**, **n**, **r**, **u**). Representative fracture features for each condition are shown in (**c**, **g**, **k**, **o**, **s**, **v**). Dimple morphologies for each condition are shown in (**d**, **h**, **l**, **p**, **t**, **w**). Selected instances of secondary fracture into plane are outlined with red, dashed outlines. Green arrows identify instances of quasi-cleavage. White arrows identify instances of intergranular fracture along PAGBs.

alignment with the grain morphology. The same is true when comparing the Z loaded SA+460°C/1 h XY plane fracture surface (Fig. 7b) to the as-built XY plane (Fig. 2b). This observation suggests that remnants of the as-built microstructure persist after SA as was noted in Section 2.3.1. Loading orientation differences were also apparent for the HIP+SA+500°C/1 h condition, though the origins of the behavior were less clear. In the Z loading orientation, fracture was tortuous with large ledges of secondary fracture (Fig. 7r); conversely, X loading produced a relatively flat fracture surface with fine secondary fractures (Fig. 7q). Across the remainder of the peak aged AM conditions, anisotropic fracture was not apparent. Instead the fracture surface was flat for both loading orientations and decorated with fine secondary fractures (Fig. 7e,f,i,j,m,n). Notably these secondary fractures are roughly on the same scale as the PAGBs identified for each of the corresponding microstructures in Fig. 2 (e.g., HIP microstructure in Fig. 2g versus the HIP+460°C/1 h fracture surface in Fig. 7e).

At higher magnification, the presence of various other fracture morphologies become apparent in peak aged AM 17-4PH, refer to Fig. 7c,g,k,o,s. Depending on the condition, varying levels of quasi-cleavage (QC) and/or intergranular fracture along PAGBs (IG) were present. The clearest cases of IG (white arrows) were present in the HIP+460°C/1 h condition and the HIP+SA+500°C/1 h condition. All conditions with a 460°C aging heat treatment had indications of QC (green arrows), but QC was most prevalent in the Hom+SA+460°C/1 h condition. The only “peak aged” AM condition without significant QC was the HIP+SA+500°C/1 h condition. Notably, QC was most prevalent on the Hom+SA+460°C/1 h condition’s fracture surfaces (Fig. 7k). Sub-micron scale ductile dimpling was present on all peak aged AM conditions (Fig. 7d,h,l,p,t) indicating that fracture was never completely dominated by the brittle IG or QC features. Notably, the dimple size/spacing was uniform for a given pre-aging heat treatment condition (e.g., HIP+SA+460°C/1 h dimpling is similar to HIP+SA+500°C/1 h), but the dimpling morphology varied significantly between the various pre-aging heat treatment conditions (e.g., SA+460°C/1 h dimples are much smaller than Hom+SA+460°C/1 h).

With the various peak aged AM fracture behaviors established, they may now be compared to peak aged wrought. The wrought fracture morphology consisted primarily of ductile fracture and tearing (Fig. 7u,v,w). Secondary fracture was present in wrought (Fig. 7u), but was much larger than AM and followed no grain-scale features. Instead, fracture was dominated by ductile dimpling at a wide range of length scales (Fig. 7v,w). Unlike AM, wrought dimpling was non-uniform in size and distribution with dimples ranging from a sub-micron scale to tens of microns. Also, no indications of IG or QC were present in peak aged wrought. A similar fractographic examination was performed for overaged wrought and AM 17-4PH (Fig. 8). For overaged AM, the fracture surface was flat (a) and consisted of a uniform distribution of ductile dimples with no significant instances of QC, IG, or anisotropic fracture. The overaged wrought fracture

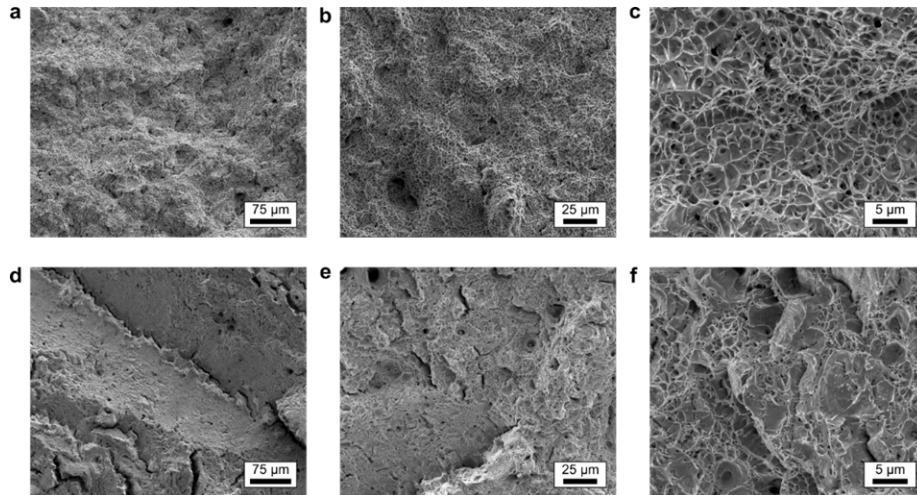


Fig. 8 | **Tensile fracture morphologies for overaged AM and wrought 17-4PH.** **a-c**, AM in the HIP+SA+552°C/4 h condition. **d-f**, Wrought in the SA+552°C/4 h condition.

surface (Fig. 8d,e,f) was ductile in nature and indistinguishable from the peak aged wrought fracture surface (Fig. 7u,v,w). The primary fractographic difference between overaged wrought and AM was the size distribution of dimples. In a similar manner to the peak aged dimpling, overaged AM has a uniform distribution of dimpling (Fig. 8c) whereas overaged wrought dimples varied greatly in size (Fig. 8e,f). As a final note on dimpling, there was no indication of AM fracture initiated or dominated by large-scale porosity.

2.4 Discussion

The preceding results show that a variety of heat treatments may be applied to AM 17-4PH in order to closely match strength and, in some cases, produce similar microstructures to wrought 17-4PH. In particular, all of the evaluated hardness-matched heat treatment protocols were able to produce AM strengths within 10% of wrought. With regard to microstructure, the closest match between AM and wrought was obtained with the two-stage HIP+SA and Hom+SA treatments. Both of these treatments produced equiaxed, martensitic AM grain structures of similar scale to wrought. However, the HIP treatment was unsuccessful in eliminating the sub-micrometer porosity that persisted as a constant differentiator between the AM and wrought microstructure. Additionally, the fracture morphologies exhibited by AM were varied and consistently incongruent with wrought fracture. Most importantly, the ductility for heat treated AM was consistently lower than wrought across all evaluated heat treatments and ductility metrics. These results lead to the following questions:

1. How do strength and ductility properties generated in the current study compare to literature values?

2. Can the current data be used to down-select and identify a desirable heat treatment protocol for AM 17-4PH with wrought-level strength?
3. Can ductility reductions observed for AM 17-4PH be linked to AM-specific microstructural features?

In order to address these questions, the strength and ductility data provided in the current study will be directly compared to the breadth of AM 17-4PH mechanical properties assessments already published in the literature. Then, the microstructural, mechanical, and fractographic properties in the current study will be holistically reviewed to establish pros and cons resulting from each AM heat treatment versus wrought. Finally, the potential microstructural origins for the ductility reduction in AM 17-4PH will be commented upon.

2.4.1 Reviewing AM 17-4PH Mechanical Performance

To establish the state of AM 17-4PH mechanical performance, data was gathered and catalogued across 44 studies constituting the majority of LPBF AM 17-4PH mechanical properties literature published to-date¹⁻⁴⁴. The build strategy, which includes build geometry, feedstock material, and build machine/parameters, varied widely across the literature. Broadly, the build machine, powder atomizing media (i.e., water, Ar gas, or N₂ gas), and build atmosphere were drivers for differences in material behavior, but the post-build heat treatment protocol was a key differentiator for AM 17-4PH mechanical properties. Each heat treatment protocol presented in the literature had nuances, but the various protocols could be distilled and grouped by high-temperature “pre-aging” treatment(s) and low-temperature “aging” treatments. With standard groupings established, the strength (σ_{YS}) and ductility (EL , RA) data in the current study was compared directly, by heat treatment, to the breadth of literature data (Fig. 9).

The data in Fig. 9 has utility both for understanding the effect of heat treatment on AM 17-4PH broadly and contextualizing the results of the current study. First, the as-built condition (i.e., no pre-aging or aging heat treatment) can exhibit excellent ductility up to 50% EL and nearly 70% RA , but σ_{YS} is limited to approximately 900 MPa. Heat treatment is required to further increase strength, but, depending on the build strategy, heat treatment may not be effective in exceeding the 900 MPa strength bound. With an appropriate build strategy, peak-performing (i.e., highest strength and ductility) AM 17-4PH is in the region of 1250-1450 MPa σ_{YS} and 16-18% EL and may be obtained by any of the listed pre-aging treatments followed by a peak aging treatment. Overaging results in a 1-2% increase in EL at the cost of a 50-150 MPa strength reduction. The top performing build and heat treatment strategies in the AM 17-4PH literature were by Shi³² with a HIP+Peak Age treatment and Molaei¹⁷ with a HIP+SA+Overage treatment. With this broad context established, the data in Fig. 9 shows that the mechanical properties of the current study are well-within the “peak-performing” bounds for AM 17-4PH. Therefore, causes for performance deficiencies

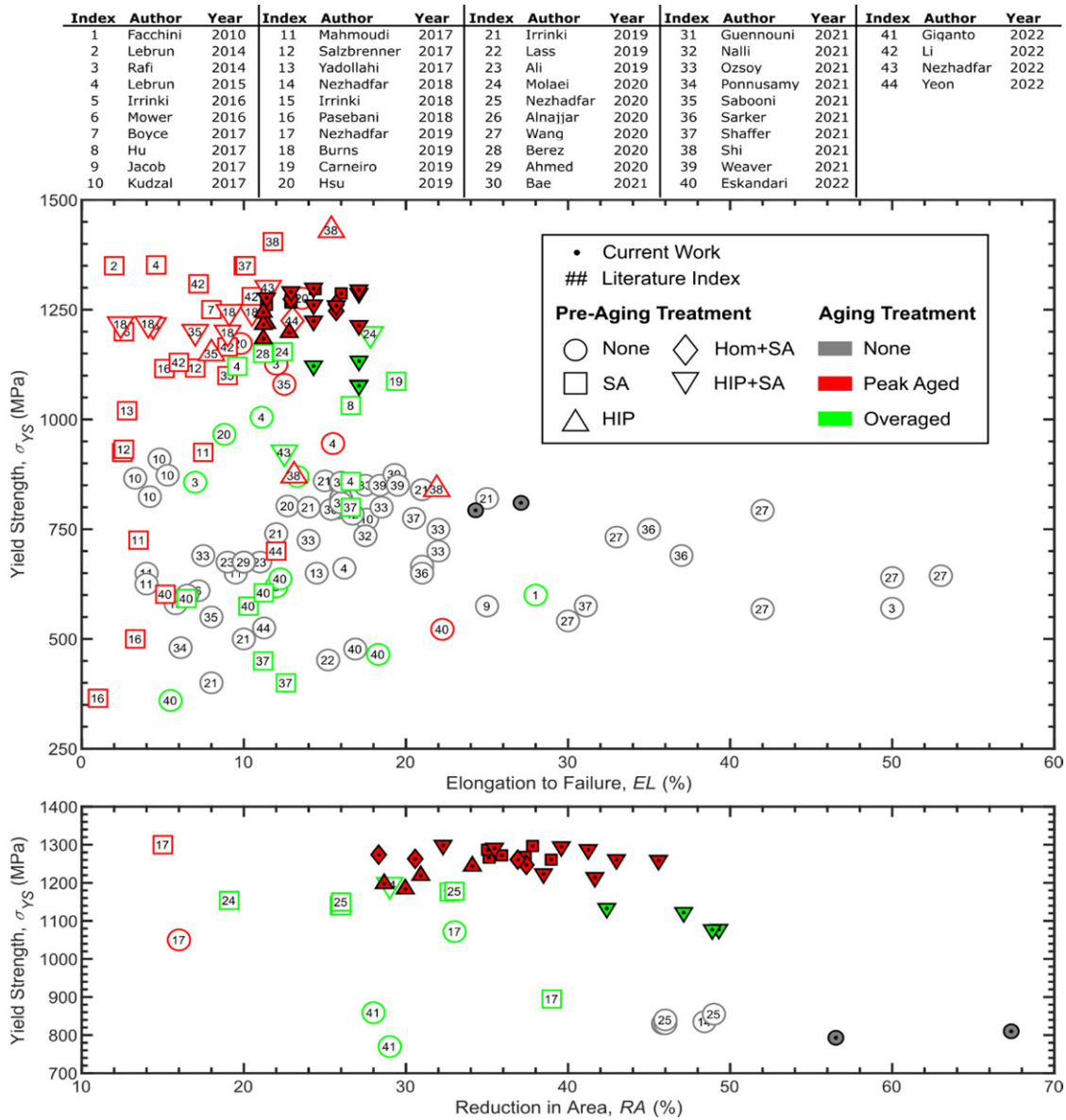


Fig. 9 | Summary of yield strength and ductility data available for LPBF AM 17-4PH. Pre-aging treatments are defined as follows: “None” indicates as-built material with or without a stress relief heat treatment at 650°C for 1 h. “SA” indicates a $\geq 1000^\circ\text{C}$ treatment. “HIP” indicates ≥ 100 MPa of gas pressure was applied during a $\geq 1000^\circ\text{C}$ heat treatment. “Hom+SA” indicates two stages of $\geq 1000^\circ\text{C}$ heat treatments without elevated pressure. Aging treatments followed pre-aging treatments and are defined as follows: “Peak Aged” indicates a $\leq 500^\circ\text{C}$ heat treatment, typically for 1 h. “Overaged” indicates a $> 500^\circ\text{C}$ heat treatment, typically for 4 h.

(i.e., reduced AM ductility versus wrought) in the current study are likely representative of the broader limitations in AM 17-4PH mechanical performance with current processing techniques.

2.4.2 Choosing an AM 17-4PH Heat Treatment

The present study demonstrates that a variety of heat treatments may be applied to AM 17-4PH in order to achieve similar levels of enhanced strength. The question then becomes, “Which of these heat treatments is most desirable?” Beyond strength, other factors of interest might include ductility, level of

anisotropy, desired microstructure, fracture mode, or the number of required heat treatment cycles (i.e., cost). Alternatively, the goal might be simply to mimic the wrought material in order to provide an AM material substitute. To guide the peak aged condition discussion, strength and ductility metrics were consolidated in Fig. 10 for the peak aged conditions of AM and wrought 17-4PH. First, the HIP+460°C/1 h condition has the poorest performance with its markedly lower strength and ductility than the other peak aged conditions. Further, the HIP+460°C/1 h condition exhibited significant amounts of intergranular fracture (Fig. 7g) which is indicative of a dominant, brittle failure mode. Similarly, the Hom+SA+460°C/1 h condition was dominated by quasi-cleavage (Fig. 7k), again indicative of brittle fracture and a marker for poor performance.

The remaining peak age conditions can be divided by higher strength (SA+460°C/1 h, HIP+SA+460°C/1 h) and lower strength with higher ductility (HIP+SA+500°C/1 h). If higher strength is desirable, then it becomes a question of cost versus acceptable microstructure. The SA+460°C/1 h heat treatment is the lowest cost by requiring only two treatment cycles, but yields a non-standard microstructure with clear remnants of the as-built solidification structure (Fig. 2a,b,d,e) and anisotropic fracture behavior

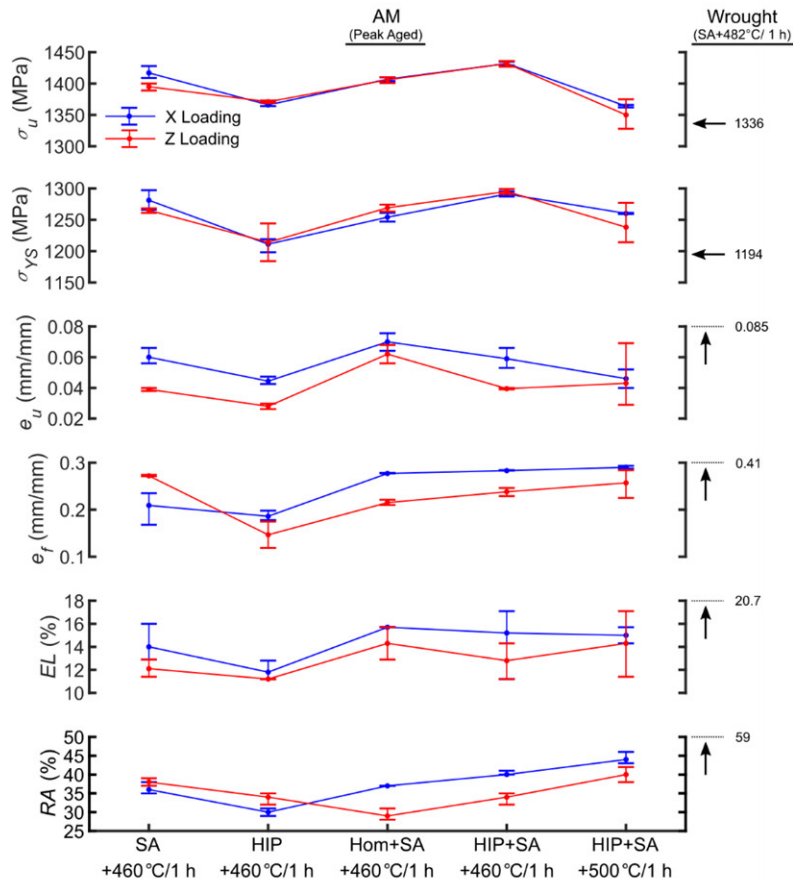


Fig. 10 | Comparison of strength and ductility metrics for peak aged 17-4PH.

(Fig. 7a,b). Interestingly, the SA+460°C/1 h condition has strikingly similar strength and ductility to the HIP+SA+460°C/1 h condition (Fig. 10) regardless of the microstructural and fracture behavior differences. If cost is less of a concern and mimicking wrought microstructure is desirable, then the HIP+SA treatment produced the closest AM microstructure (Fig. 2m,n,o) to the wrought microstructure (Fig. 2p,q,r). The HIP+SA treatment can be followed by the 460°C/1 h aging treatment for maximum strength, or the 500°C/1 h treatment may be applied for enhanced ductility and near identical strength to wrought (Fig. 10). However, the 500°C/1 h heat treatment differentiates itself from wrought and the 460°C/1 h treatment with poorer uniform elongation (Fig. 5f), modified WHR (Fig. 5f), anisotropic fracture behavior (Fig. 7q,r), and instances of brittle IG fracture (Fig. 7s). Though it has a lower RA , the higher strength 460°C/1 h heat treatment has comparable ductility to the 500°C/1 h treatment with respect to e_f and EL and a better matched WHR to wrought than the 500°C/1 h treatment.

With the various characteristics and deficiencies of the AM heat treatments compared, there are several stand-out heat treatments for AM 17-4PH. The SA+460°C/1 h treatment can be applied for high strength and good ductility at low cost, but with the risk of extraneous factors introduced by its unique microstructure. If a wrought substitution is desired, the HIP+SA+460°C/1 h heat treatment may be applied to AM 17-4PH for strength-matching within 10%, good WHR matching, isotropic fracture behavior, and a similar martensitic microstructure to wrought 17-4PH. Though not discussed at length, the HIP+SA+552°C/4 h heat treatment may be similarly utilized for good matching between overaged AM and wrought. However, these recommendations must be caveated with the fact that, regardless of heat treatment, comparable strength AM 17-4PH is consistently less ductile than wrought 17-4PH.

2.4.3 Ductility Reduction in AM 17-4PH

With wrought strength and microstructure matched, ductility reduction relative to wrought remains as a key barrier to maximizing the mechanical performance of AM 17-4PH. The fractographic examination in Fig. 7 shows the typical hallmarks of reduced ductility with instances of brittle IG and/or QC fracture across all peak aged AM conditions. These brittle features disappear and are replaced with ductile dimples in overaged AM (Fig. 8), but the AM ductility reduction relative to wrought persists (Fig. 6a) even in the absence of brittle fracture. The overaged AM fracture surfaces consisted exclusively of a nearly uniform distribution of fine dimples (Fig. 8b), so the microstructural driver(s) for this fracture feature should necessarily be controlling the ductility reduction. Review of the peak aged AM dimpling showed a clear variation in dimple size that qualitatively varied by high-temperature heat treatment (i.e., SA, HIP, etc.). Noting that sub-micrometer porosity also varied with high-temperature heat treatment (Fig. 3), these observations motivated a quantitative examination of the ductile dimple spacing and comparison to the pore spacing for each condition of AM 17-4PH.

Fig. 11 demonstrates a high correlation ($R^2 = 0.73$) between the median spacing of sub-micrometer scale pores and the median spacing of dimples on AM 17-4PH fracture surfaces. This correlation holds for the entire range of evaluated AM heat treatments indicating a potentially critical role of the small-scale porosity in the fracture process. Notably, the correlation may be increased to $R^2 = 0.85$ if the HIP+460°C/1 h condition is treated as an outlier and removed from the regression analysis. This outlier behavior may be rationalized by recognizing Cr_{23}C_6 carbide precipitation that was identified as a likely cause for reduced stress-corrosion cracking resistance in the HIP+460°C/1 h condition (discussed later in Chapter 3). The median dimple spacing is low relative to the trendline which would be expected if additional carbides were active in the fracture process (i.e., pores and carbides would add to increase dimple density). Returning to the primary point of pore driven ductile fracture, this proposed microstructure-fracture linkage is consistent with existing studies of ductile fracture in the presence of porosity⁶⁶. Voids and/or inclusions can serve as void nucleation sites that grow and coalesce to decorate the final fracture surface. Review of the dimple and pore spacing magnitudes shows that dimple spacing is generally lower than the pore spacing. If pores were the sole contributor to dimpling, then the magnitudes of the spacings should be equivalent (i.e., one pore per dimple). In a similar manner to the Cr_{23}C_6 carbide discussion, this spacing difference suggests a consistent presence of additional dimple nucleation sites. Additional secondary particles that might contribute to these differences are phases such as NbC ⁶⁷, Cr_7C_3 ⁶⁸, MnS ⁶⁹, and/or oxide inclusions^{12,32,70} previously demonstrated to be present in AM 17-4PH, but not characterized in this study.

It must be noted that that the pore-dimple correlation that does not address remaining, critical details of the AM fracture process including the prevalence of QC and IG-type fractures. Additional interrupted tension tests and additional microscopic analysis are required to draw a direct link between the ductile fracture process and this sub-micrometer porosity. However, assuming that the aforementioned dimple correlation is accurate, sub-micrometer scale porosity could represent the critical barrier to enhanced ductility in AM 17-4PH. This would be particularly true for the HIP+SA+552°C/1 h condition whose

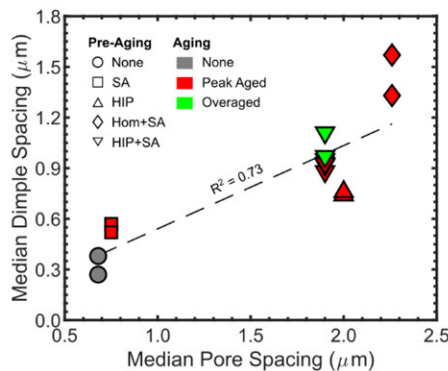


Fig. 11 | Relationship between pore spacing and fracture surface dimple spacing in AM 17-4PH.

fracture process is apparently dominated by these pores/dimples (Fig. 8b). Consequently, it is critical to understand the origin and prevalence of this microstructural feature in AM alloys in order to support and justify mitigation efforts. If mitigation is not feasible, then understanding the impacts of this sub-micrometer porosity on higher order properties (e.g., fatigue, stress corrosion cracking behavior, etc.) will be critical. Chapters 3 through 6 of this dissertation will address each of these topics in further detail.

2.5 Conclusions

Tension testing, microstructure examination, and fractographic analysis were used to evaluate and compare heat treated AM 17-4PH to its wrought counterpart. The results of this investigation were contextualized within the breadth of existing AM 17-4PH literature and used to identify the current limitations of AM 17-4PH mechanical performance. A microstructural feature was then linked to the AM fracture process and identified as a potential cause for current AM mechanical performance limitations. The following are key conclusions from this study:

- Two-stage high-temperature post-build heat treatments, each at $>1000^{\circ}\text{C}$, were most effective in producing a martensitic grain structure in AM 17-4PH similar to wrought 17-4PH.
- Nanometer-scale porosity with a median size of 60 nm was present in the “as-built” condition of AM 17-4PH. With the application of $>1000^{\circ}\text{C}$ heat treatments, this small-scale porosity expanded and coarsened to sub-micrometer scale porosity with median sizes ranging from 0.13-0.28 μm depending on the treatment. The hot isostatic press treatment was ineffective in eliminating this small-scale porosity.
- A broad range of high-temperature heat treatments were found to be effective in maximizing AM 17-4PH strength if followed by an appropriate aging treatment. Of the evaluated treatments, the HIP+SA+ $460^{\circ}\text{C}/1$ h treatment provided the best combination of wrought-like microstructure and mechanical properties, but the less-costly SA+ $460^{\circ}\text{C}/1$ h treatment was also able to provide excellent mechanical properties.
- Heat treated AM 17-4PH was consistently less ductile than wrought 17-4PH. This ductility deficit was associated with brittle intergranular and/or cleavage fracture features present in all conditions of peak aged AM 17-4PH. An overaging heat treatment yielded ductile-dimpling based fracture in AM 17-4PH, but overall ductility was still reduced relative to wrought.
- Ductile dimple spacing was quantified and found to be correlated ($R^2 = 0.73$) with variation in the sub-micrometer pore spacing across the range of examined AM 17-4PH conditions. This microstructural correlation is especially relevant for overaged AM 17-4PH whose fracture is controlled by these

dimples. This pore-fracture linkage could represent a critical barrier to enhanced ductility in AM 17-4PH, but additional studies are required to validate this claim.

2.6 Acknowledgements

This research was financially supported by the Office of Naval Research under Grant No. N00014-18-1-2427 with Dr. Airan Perez as the Scientific Officer. Zachary Harris performed the EBSD characterization, tension testing, and gathered the fractographic images. Crestienne DeChaine gathered the reduction in area data.

2.7 References

1. Facchini, L. *et al.* Metastable austenite in 17-4 precipitation-hardening stainless steel produced by selective laser melting. *Adv. Eng. Mater.* **12**, 184–188 (2010).
2. LeBrun, T., Tanigaki, K., Horikawa, K. & Kobayashi, H. Strain rate sensitivity and mechanical anisotropy of selective laser melted 17-4 PH stainless steel. *Mech. Eng. J.* **1**, SMM0049 (2014).
3. Mahmoudi, M. *et al.* Mechanical properties and microstructural characterization of selective laser melted 17-4 PH stainless steel. *Rapid Prototyp. J.* **23**, 280–294 (2017).
4. Salzbrenner, B. C. *et al.* High-throughput stochastic tensile performance of additively manufactured stainless steel. *J. Mater. Process. Technol.* **241**, 1–12 (2017).
5. Yadollahi, A., Shamsaei, N., Thompson, S. M., Elwany, A. & Bian, L. Effects of building orientation and heat treatment on fatigue behavior of selective laser melted 17-4 PH stainless steel. *Int. J. Fatigue* **94**, 218–235 (2017).
6. Nezhadfar, P. D., Masoomi, M., Thompson, S., Phan, N. & Shamsaei, N. Mechanical Properties of 17-4 PH Stainless Steel Additively Manufactured under Ar and N₂ Shielding Gas. in *Solid Freeform Fabrication 2018: Proceedings of the 29th Annual International Solid Freeform Fabrication Symposium – An Additive Manufacturing Conference* 1301–1310 (2018).
7. Irrinki, H. *et al.* Effects of particle characteristics on the microstructure and mechanical properties of 17-4 PH stainless steel fabricated by laser-powder bed fusion. *Powder Technol.* **331**, 192–203 (2018).
8. Pasebani, S., Ghayoor, M., Badwe, S., Irrinki, H. & Atre, S. V. Effects of atomizing media and post processing on mechanical properties of 17-4 PH stainless steel manufactured via selective laser melting. *Addit. Manuf.* **22**, 127–137 (2018).
9. Nezhadfar, P. D., Shrestha, R., Phan, N. & Shamsaei, N. Fatigue behavior of additively

- manufactured 17-4 PH stainless steel: Synergistic effects of surface roughness and heat treatment. *Int. J. Fatigue* **124**, 188–204 (2019).
10. Burns, D. E. *et al.* Investigating Additively Manufactured 17-4 PH for Structural Applications. *J. Mater. Eng. Perform.* **28**, 4943–4951 (2019).
 11. Carneiro, L., Jalalahmadi, B., Ashtekar, A. & Jiang, Y. Cyclic deformation and fatigue behavior of additively manufactured 17–4 PH stainless steel. *Int. J. Fatigue* **123**, 22–30 (2019).
 12. Hsu, T. H. *et al.* Microstructure and property of a selective laser melting process induced oxide dispersion strengthened 17-4 PH stainless steel. *J. Alloys Compd.* **803**, 30–41 (2019).
 13. Rafi, H. K., Pal, D., Patil, N., Starr, T. L. & Stucker, B. E. Microstructure and Mechanical Behavior of 17-4 Precipitation Hardenable Steel Processed by Selective Laser Melting. *J. Mater. Eng. Perform.* **23**, 4421–4428 (2014).
 14. Irrinki, H. *et al.* Microstructures, properties, and applications of laser sintered 17-4PH stainless steel. *J. Am. Ceram. Soc.* **102**, 5679–5690 (2019).
 15. Lass, E. A., Stoudt, M. R. & Williams, M. E. Additively Manufactured Nitrogen-Atomized 17-4 PH Stainless Steel with Mechanical Properties Comparable to Wrought. *Metall. Mater. Trans. A* **50**, 1619–1624 (2019).
 16. Ali, U. *et al.* Identification and characterization of spatter particles and their effect on surface roughness, density and mechanical response of 17-4 PH stainless steel laser powder-bed fusion parts. *Mater. Sci. Eng. A* **756**, 98–107 (2019).
 17. Molaei, R., Fatemi, A. & Phan, N. Multiaxial fatigue of LB-PBF additive manufactured 17–4 PH stainless steel including the effects of surface roughness and HIP treatment and comparisons with the wrought alloy. *Int. J. Fatigue* **137**, 105646 (2020).
 18. Nezhadfar, P. D. *et al.* Improved high cycle fatigue performance of additively manufactured 17-4 PH stainless steel via in-process refining micro-/defect-structure. *Addit. Manuf.* **36**, 101604 (2020).
 19. Alnajjar, M., Christien, F., Bosch, C. & Wolski, K. A comparative study of microstructure and hydrogen embrittlement of selective laser melted and wrought 17–4 PH stainless steel. *Mater. Sci. Eng. A* **785**, 139363 (2020).
 20. Wang, X., Liu, Y., Shi, T. & Wang, Y. Strain rate dependence of mechanical property in a selective laser melted 17–4 PH stainless steel with different states. *Mater. Sci. Eng. A* **792**, 139776 (2020).
 21. Berez, J. Qualification of Laser Powder Bed Fusion Processed 17-4PH Stainless Steel as a Function

- of Powder Condition. (Georgia Institute of Technology, 2020).
22. Ahmed, F. *et al.* Study of powder recycling and its effect on printed parts during laser powder-bed fusion of 17-4 PH stainless steel. *J. Mater. Process. Technol.* **278**, 116522 (2020).
 23. Bae, J., Kim, M. K., Oh, E., Yang, K. T. & Suhr, J. Experimental and numerical investigation of 17-4PH stainless steel fabricated by laser powder bed fusion and hot isostatic pressing. *Mater. Res. Express* **8**, (2021).
 24. LeBrun, T., Nakamoto, T., Horikawa, K. & Kobayashi, H. Effect of retained austenite on subsequent thermal processing and resultant mechanical properties of selective laser melted 17-4 PH stainless steel. *Mater. Des.* **81**, 44–53 (2015).
 25. Guennouni, N. *et al.* Comparative study of the microstructure between a laser beam melted 17-4PH stainless steel and its conventional counterpart. *Mater. Sci. Eng. A* **823**, 141718 (2021).
 26. Nalli, F., Cortese, L. & Concli, F. Ductile damage assessment of Ti6Al4V, 17-4PH and AlSi10Mg for additive manufacturing. *Eng. Fract. Mech.* **241**, 107395 (2021).
 27. Ozsoy, A., Yasa, E., Keles, M. & Tureyen, E. B. Pulsed-mode Selective Laser Melting of 17-4 PH stainless steel: Effect of laser parameters on density and mechanical properties. *J. Manuf. Process.* **68**, 910–922 (2021).
 28. Ponnusamy, P. *et al.* A study of tensile behavior of SLM processed 17-4 PH stainless steel. *Mater. Today Proc.* **45**, 4531–4534 (2021).
 29. Sabooni, S. *et al.* Laser powder bed fusion of 17-4 PH stainless steel: A comparative study on the effect of heat treatment on the microstructure evolution and mechanical properties. *Addit. Manuf.* **46**, 102176 (2021).
 30. Sarker, D. *et al.* Influence of Pore Formation and Its Role on the Tensile Properties of 17-4 PH Stainless Steel Fabricated by Laser Powder Bed Fusion. in *TMS 2021 150th Annual Meeting & Exhibition Supplemental Proceedings* 131–141 (2021).
 31. Shaffer, D. J., Wilson-Heid, A. E., Keist, J. S., Beese, A. M. & Palmer, T. A. Impact of retained austenite on the aging response of additively manufactured 17-4 PH grade stainless steel. *Mater. Sci. Eng. A* **817**, 141363 (2021).
 32. Shi, Q., Qin, F., Li, K., Liu, X. & Zhou, G. Effect of hot isostatic pressing on the microstructure and mechanical properties of 17-4PH stainless steel parts fabricated by selective laser melting. *Mater. Sci. Eng. A* **810**, 141035 (2021).

33. Weaver, J. S. *et al.* The effects of particle size distribution on the rheological properties of the powder and the mechanical properties of additively manufactured 17-4 PH stainless steel. *Addit. Manuf.* **39**, 101851 (2021).
34. Eskandari, H., Lashgari, H. R., Ye, L., Eizadjou, M. & Wang, H. Microstructural characterization and mechanical properties of additively manufactured 17-4PH stainless steel. *Mater. Today Commun.* **30**, (2022).
35. Irrinki, H. *et al.* Effects of Powder Attributes and Laser Powder Bed Fusion (L-PBF) Process Conditions on the Densification and Mechanical Properties of 17-4 PH Stainless Steel. *Jom* **68**, 860–868 (2016).
36. Giganto, S., Martínez-Pellitero, S., Barreiro, J. & Zapico, P. Influence of 17-4 PH stainless steel powder recycling on properties of SLM additive manufactured parts. *J. Mater. Res. Technol.* **16**, 1647–1658 (2022).
37. Li, K. *et al.* Homogenization timing effect on microstructure and precipitation strengthening of 17-4PH stainless steel fabricated by laser powder bed fusion. *Addit. Manuf.* **52**, 102672 (2022).
38. Nezhadfar, P. D., Gradl, P. R. & Shao, S. Microstructure and Deformation Behavior of Additively Manufactured 17 – 4 Stainless Steel : Laser Powder Bed Fusion vs . Laser Powder Directed Energy Deposition. *JOM* **74**, 1136–1148 (2022).
39. Yeon, S. *et al.* Normalizing Effect of Heat Treatment Processing on 17-4 PH Stainless Steel Manufactured by Powder Bed Fusion. *Metals (Basel)*. **12**, 704 (2022).
40. Mower, T. M. & Long, M. J. Mechanical behavior of additive manufactured, powder-bed laser-fused materials. *Mater. Sci. Eng. A* **651**, 198–213 (2016).
41. Boyce, B. L. *et al.* Extreme-Value Statistics Reveal Rare Failure-Critical Defects in Additive Manufacturing. *Adv. Eng. Mater.* **19**, (2017).
42. Hu, Z., Zhu, H., Zhang, H. & Zeng, X. Experimental investigation on selective laser melting of 17-4PH stainless steel. *Opt. Laser Technol.* **87**, 17–25 (2017).
43. Jacob, G., Brown, C., Donmez, A., Watson, S. & Slotwinski, J. Effects of powder recycling on stainless steel powder and built material properties in metal powder bed fusion processes. *NIST Adv. Manuf. Ser.* **100–6**, (2017).
44. Kudzal, A. *et al.* Effect of scan pattern on the microstructure and mechanical properties of Powder Bed Fusion additive manufactured 17-4 stainless steel. *Mater. Des.* **133**, 205–215 (2017).

45. EOS. EOS-17-003 Material Data Sheet EOS StainlessSteel EOS M290 IndustryLine. (2017). Available at: https://cdn.eos.info/5d5320af77f01059/dacbc1700a38/EOS-17-003_Datenblatt-Industry-Line_EN_A4_V2_Web.pdf. (Accessed: 2nd September 2019)
46. ASTM International & International Standards Organization. ISO/ASTM 52921:2013(E) Standard Terminology for Additive Manufacturing - Coordinate Systems and Test Methodologies. (2013).
47. ASTM International. ASTM F3301-18a Additive Manufacturing - Post Processing Methods - Standard Specification for Thermal Post-Processing Metal Parts Made Via Powder Bed Fusion. (2018).
48. ASTM International. ASTM A693-16 Standard Specification for Precipitation-Hardening Stainless and Heat-Resisting Steel Plate, Sheet, and Strip. (2016).
49. Bachmann, F., Hielscher, R. & Schaeben, H. Texture Analysis with MTEX - Free and Open Source Software Toolbox. *Solid State Phenom.* **160**, 63–68 (2010).
50. Nyssönen, T., Peura, P. & Kuokkala, V. T. Crystallography, Morphology, and Martensite Transformation of Prior Austenite in Intercritically Annealed High-Aluminum Steel. *Metall. Mater. Trans. A Phys. Metall. Mater. Sci.* **49**, 6426–6441 (2018).
51. Al-Maharma, A. Y., Patil, S. P. & Markert, B. Effects of porosity on the mechanical properties of additively manufactured components: a critical review. *Mater. Res. Express* **7**, (2020).
52. ASTM International. ASTM E384-17 Standard Test Method for Microindentation Hardness of Materials. (2017).
53. ASTM International. ASTM E140-12b Standard Hardness Conversion Tables for Metals Relationship Among Brinell Hardness, Vickers Hardness, Rockwell Hardness, Superficial Hardness, Knoop Hardness, Scleroscope Hardness, and Leeb Hardness. (2019).
54. ASTM International. ASTM E8/E8M-16a Standard Test Methods for Tension Testing of Metallic Materials. (2016). doi:https://doi.org/10.1520/E0008_E0008M-16A
55. Hertzberg, R. W., Vinci, R. P. & Hertzberg, J. L. *Deformation and Fracture Mechanics of Engineering Materials*. (John Wiley & Sons, Inc., 2013).
56. Betegón, C. & Hancock, J. W. Two-Parameter Characterization of Elastic-Plastic Crack-Tip Fields. *J. Appl. Mech.* **58**, 104 (1991).
57. Murr, L. E. *et al.* Microstructures and properties of 17-4 PH stainless steel fabricated by selective laser melting. *J. Mater. Res. Technol.* **1**, 167–177 (2012).

58. AlMangour, B. & Yang, J. M. Improving the surface quality and mechanical properties by shot-peening of 17-4 stainless steel fabricated by additive manufacturing. *Mater. Des.* **110**, 914–924 (2016).
59. Vunnam, S., Saboo, A., Sudbrack, C. & Starr, T. L. Effect of powder chemical composition on the as-built microstructure of 17-4 PH stainless steel processed by selective laser melting. *Addit. Manuf.* **30**, 100876 (2019).
60. Coseglio, M. S. D. R. Sulphide stress cracking of 17-4 PH for applications in oilfield components. *Mater. Sci. Technol.* **33**, 1863–1878 (2017).
61. German, R. M. Coarsening in Sintering: Grain Shape Distribution, Grain Size Distribution, and Grain Growth Kinetics in Solid-Pore Systems. *Crit. Rev. Solid State Mater. Sci.* **34**, 263–305 (2010).
62. Meredith, S. D., Zuback, J. S., Keist, J. S. & Palmer, T. A. Impact of composition on the heat treatment response of additively manufactured 17-4 PH grade stainless steel. *Mater. Sci. Eng. A* **738**, 44–56 (2018).
63. Krauss, G. Martensite in steel: strength and structure. *Mater. Sci. Eng. A* **273–275**, 40–57 (1999).
64. Moyer, J. M. & Ansell, G. S. The Volume Expansion Accompanying the Martensite Transformation in Iron-Carbon Alloys. *Metall. Trans. A* **6A**, 1785–1791 (1975).
65. Miettinen, J. Calculation of Solidification-Related Thermophysical Properties for Steels. *Metall. Mater. Trans. B* **28**, 281–297 (1997).
66. Pineau, A., Benzerga, A. A. & Pardoën, T. Failure of metals I: Brittle and ductile fracture. *Acta Mater.* **107**, 424–483 (2016).
67. Cheruvathur, S., Lass, E. A. & Campbell, C. E. Additive Manufacturing of 17-4 PH Stainless Steel: Post-processing Heat Treatment to Achieve Uniform Reproducible Microstructure. *JOM* **68**, 930–942 (2016).
68. Lashgari, H. R., Kong, C., Adabifiroozjaei, E. & Li, S. Microstructure, post thermal treatment response, and tribological properties of 3D printed 17-4 PH stainless steel. *Wear* **456–457**, (2020).
69. Alnajjar, M. *et al.* Influence of microstructure and manganese sulfides on corrosion resistance of selective laser melted 17-4 PH stainless steel in acidic chloride medium. *Corros. Sci.* **168**, 108585 (2020).
70. Sun, Y., Hebert, R. J. & Aindow, M. Non-metallic inclusions in 17-4PH stainless steel parts produced by selective laser melting. *Mater. Des.* **140**, 153–162 (2018).

Chapter 3 - Stress Corrosion Cracking Behavior of AM 17-4PH

The following chapter is adapted from a prior publication:

Shoemaker, T. K., Harris, Z. D. & Burns, J. T. Comparing Stress Corrosion Cracking Behavior of Additively Manufactured and Wrought 17-4PH Stainless Steel. *Corrosion* **78**, 528–546 (2022).

3.1 Introduction

The precipitation-hardened, martensitic stainless steel 17-4PH exhibits both high strength and good corrosion resistance^{1,2}. Due to these favorable properties, it is widely employed in aggressive operating environments across the marine, petrochemical, nuclear, and aerospace sectors. While 17-4PH has a long history in its conventional wrought form, a new form of 17-4PH is becoming popular through the use of additive manufacturing (AM) technologies. In particular, the laser powder bed fusion (LPBF) technique³ with powder meeting the 17-4PH composition is being used to generate “additive” 17-4PH. Unlike wrought 17-4PH, which exhibits a martensitic microstructure, the rapid solidification process associated with LPBF typically results in a reduced-strength ferritic microstructure in the as-built condition^{4,5}. However, the underlying composition of AM 17-4PH gives it the potential to reach the strength of its wrought counterpart through appropriate heat treatment. The strength of heat treated AM 17-4PH can meet or exceed the strength of wrought 17-4PH⁶⁻⁸.

Traditionally manufactured 17-4PH can be susceptible to environmental degradation; specifically, in-service failures have been reported for 17-4PH marine vessel propeller shafts⁹, fasteners on spacecraft^{10,11}, valves on petrochemical pipelines^{12,13}, various oilfield equipment^{1,14,15}, nuclear reactor components¹⁶, among others^{2,17}. In many of the above instances⁹⁻¹³, component failure was attributed to hydrogen-driven stress corrosion cracking (SCC) based on the observation of brittle fracture morphologies and the presence of a known hydrogen-rich environment. Laboratory testing has established that the susceptibility of wrought 17-4PH to SCC is strongly dependent on environmental conditions^{16,18}. For example, high resistance to SCC was observed at open circuit potentials in dilute chloride solutions^{16,19-23}, while increased SCC susceptibility was noted when 17-4PH was exposed to cathodic polarizations in similar environments^{16,20,21,24,25}. Additionally, a strong heat treatment dependence on the SCC behavior was observed in dilute chloride environments, with peak aged alloys often exhibiting increased susceptibility to SCC relative to solution treated or over aged conditions^{11,16,20,21,25-27}. Interestingly, significant heat-to-heat variability was also noted during salt spray-based SCC experiments, even in the over-aged condition²⁸.

The clear dependence of SCC behavior in wrought 17-4PH on heat treatment and the reported heat-to-heat variability strongly suggest an important role of the underlying microstructure in establishing the SCC susceptibility of 17-4PH. As such, it is likely that AM 17-4PH will exhibit different SCC behavior relative to a similar strength wrought 17-4PH alloy since important differences in microstructure are expected. For example, though properly heat-treated AM 17-4PH will have the traditional precipitation hardened martensitic structure, it is likely that the ferritic microstructure of the as-built condition will induce a different austenite morphology during the solution-annealing step as compared to wrought 17-4PH, thus impacting the morphological details of the martensitic structure. Additionally, AM 17-4PH may contain specific defects that will not be present in wrought materials, such as porosity, lack of fusion defects, and delamination between build layers²⁹. AM alloys have also been reported to contain unique secondary phases such as oxide inclusions³⁰⁻³³ and have larger prior austenite grain sizes³⁴. To date, studies of AM 17-4PH has focused on microstructure, strength, fatigue^{29,35-38} and general corrosion behavior³⁹⁻⁴¹. However, despite the importance of the SCC failure mode for 17-4PH components and the likelihood of differences in SCC behavior for AM and wrought 17-4PH, studies of SCC behavior are limited³⁴.

The objective of this chapter is to quantify and compare the SCC performance of AM and wrought 17-4PH at similar strength levels and identify the microstructural features responsible for any differences. First, the SCC behavior as a function of applied potential under full immersion in 0.6 M NaCl solution is measured for both AM and wrought 17-4PH under various heat treatment conditions using fracture mechanics-based testing. High-magnification microscopy and electron backscatter diffraction are then employed to identify key differences in microstructural parameters. The mechanistic influence of observed microstructural variations on the SCC behavior are interpreted in the context of an established decohesion-based model for hydrogen-driven SCC and the implications of the current findings are then discussed.

3.2 Methods

3.2.1 Materials

A subset of the wrought and AM 17-4PH material tempers in Chapter 2 was utilized for the current study. For the AM material, fracture test specimens were excised from the same stock material yielded by the build strategy described in Chapter 2 (Fig. 12). The two stock material orientations were used to produce single edge notch tension (SENT) fracture test specimens oriented in two Mode I cracking⁴² orientations designated X-Y and Z-Y. The first letter in these designations indicates the loading direction and the second letter indicates the crack growth direction (i.e., X-Y is loaded parallel to X and cracks parallel to Y). The heat treatment process for these specimens was in accordance with the protocols described in Chapter 2, but a subset of tempers was chosen for the current SCC evaluation. To represent the AM peak aged condition, AM HIP+460°C/1 h and HIP+SA+460°C/1 h conditions were evaluated and are hereafter

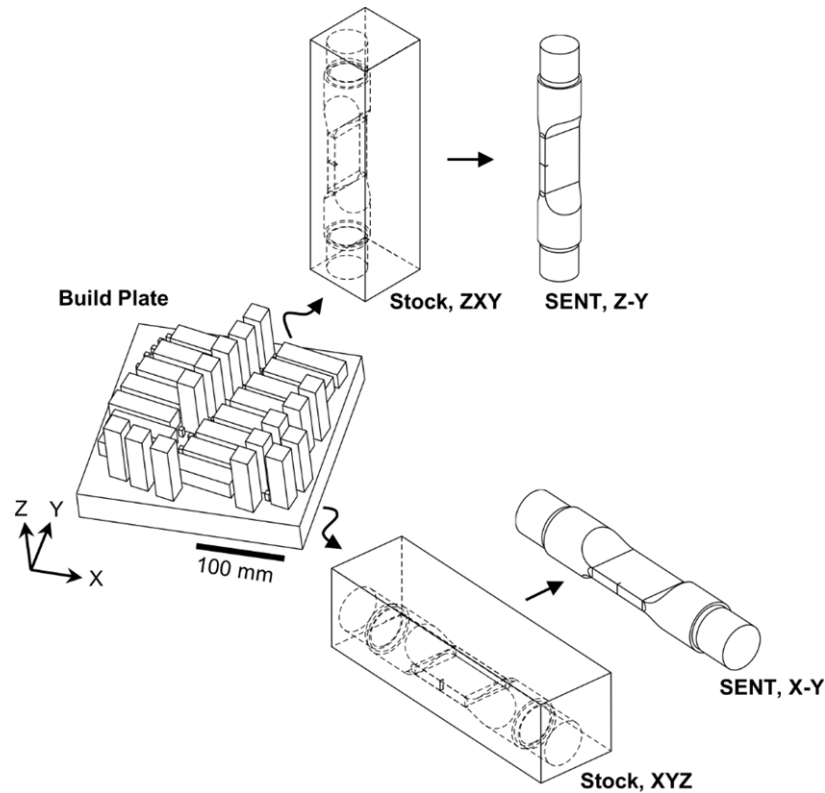


Fig. 12 | **AM build and fracture specimen geometries.** Single edge notch tension (SENT) fracture test specimens were machined from two orientations of stock material (ZXY, XYZ) cut from the displayed build plate.

referred to as “HIP+Peak Age” and “HIP+SA+Peak Age”, respectively. For the AM overage condition, the HIP+SA+552°C/4 h condition was evaluated and hereafter referred to as “HIP+SA+Overage”. For wrought 17-4PH, SENT specimens were machined in the L-T orientation. The wrought SA+482°C/1 h and SA+552°C/4 h conditions are hereafter referred to as “SA+Peak Age” and “SA+Overage”.

3.2.2 Stress Corrosion Cracking

Fracture mechanics-based testing to characterize the stress corrosion cracking behavior was performed using servo-hydraulic load frames. The crack length was actively monitored using the direct current potential drop (dcPD) method⁴³ and fed into a closed-loop control system to enable stress intensity (K) controlled loading. The SENT specimen geometry, with a 12.20 x 2.67 mm ($B/W = 4.6$) gage section, was utilized in a pinned-pinned configuration with a linear elastic K calculation⁴⁴. Plasticity effects on the mechanical driving force were evaluated⁴⁵ and determined to be negligible for all evaluated material conditions, justifying the use of K in the current study. Prior to SCC testing, samples were fatigue precracked 0.250 mm out of a 0.940 mm long EDM notch with a root radius of 0.038 mm. Precracks were grown in lab air under cyclic loading at a stress ratio (R) of 0.1 and constant maximum K of 7 MPa \sqrt{m} .

Environmental control was enabled by isolating the SENT gage section within an acrylic cell capable of flowing liquid solution for immersion testing or gas for atmospheric control. The SENT gage section was polished with 600 grit SiC paper, sonicated in acetone then methanol then deionized (DI) water, and double-coated with a butyl-rubber peel-off lacquer (MICCRO XP-2000) leaving a 5 mm window around the Mode I crack path exposed. For inert environment testing, dry nitrogen gas was flowed through the cell at a sufficient rate to maintain a relative humidity (RH) below 5%. During immersion testing, a platinum-coated Nb mesh counter electrode and saturated calomel reference electrode (SCE) were placed in the cell. A neutral, quiescently aerated 0.6M NaCl solution (pH = 6.2) was flowed from a 2 L reservoir using a peristaltic pump at 20 mL/min and electrochemical potential was applied and/or monitored using a potentiostat operated in floating ground mode. To stabilize the chemistry just prior to SCC testing, the sample was held at open circuit potential (OCP) for 8-24 h and monitored. The OCP (E_{OCP}) was found to stabilize at $-0.190 \pm 0.050 V_{SCE}$ for all examined forms and heat treatments of 17-4PH.

Stress corrosion cracking tests were performed either at a fixed $dK/dt = 2 \text{ MPa}\sqrt{\text{m/h}}$ (rising K) or a constant K (i.e., $dK/dt = 0 \text{ MPa}\sqrt{\text{m/h}}$). False crack growth rates caused by dcPD artifacts can occur in positive dK/dt SCC testing⁴⁶, and thus tests were performed in both an inert environment to establish false rates/test resolution limits and aggressive environments to capture SCC crack growth rates (da/dt). For the aggressive environment tests, the electrochemical potential (E_{app}) of interest was applied for 30-60 minutes at a K of $\sim 5 \text{ MPa}\sqrt{\text{m}}$ to establish the target crack-tip environment; testing commenced by increasing K at the aforementioned dK/dt . After rising to the maximum K of interest, the SENT was unloaded at 0.05-0.10 mm/min in displacement control, sonicating in DI water then methanol, heat tinted at 250°C for 1 h to indicate the ending crack length with a straw-brown oxide⁴⁷, and fatigued to fracture to avoid ductile fracture distortion at the crack tip. For final K and da/dt calculations, all fracture surfaces were measured to recalibrate the Johnson equation⁴⁸ crack length calculations with one or two known crack length/PD combinations⁴⁹. Fractographic features were examined using an SEM operated in secondary electron imaging mode.

Constant K SCC tests were performed at fixed K and several different E_{app} ; multiple conditions were explored on a single sample and fatigue was performed after each SCC increment to sharpen the crack and enable clear distinction on the fracture surface to confirm cracking. The starts of the tests were similar to the rising K tests with precracking, an OCP hold, and a slow rise in K at OCP. Once a maximum K of $30 \text{ MPa}\sqrt{\text{m}}$ was reached, the environment was held at an E_{app} of interest for a period 8-24 hours to capture SCC growth kinetics. At the conclusion of the hold period or after approximately 0.2 mm of crack extension, the environment was returned to OCP and the crack was extended 0.1-0.3 mm by fatiguing in constant amplitude load control at an initial maximum K of $20 \text{ MPa}\sqrt{\text{m}}$ with $R = 0.1$ or 0.5 . This process

was repeated a number of times per sample such that bands of fatigue and SCC crack growth were clearly distinguished on the fracture surface. Generally, the applied potential steps started at or near OCP and were driven incrementally more negative (cathodic). Anodic potentials (i.e., $E_{app} > E_{OCP}$) were not evaluated during these constant K SCC tests. To verify critical “takeoff” potentials where SCC susceptibility started, several tests had less cathodic steps repeated to verify shutoff in SCC crack growth. Post-test, the samples were unloaded, cleaned, heat tinted, and fatigued similarly to the rising K experiments. Instantaneous crack growth kinetics were captured by dcPD, but SEM fractography was performed to evaluate and measure the morphologies and actual lengths of the SCC regions. While there was good correspondence between the dcPD and fractography, the reported growth rates were determined by dividing the fractographically measured SCC crack extension by the elapsed time for dcPD-indicated crack extension. The one exception was the AM HIP+Peak Age alloy, whose fracture surface was sufficiently tortuous that distinguishing the fatigue and SCC regions was not possible, so the dcPD-indicated crack growth rates are reported.

3.3 Results

3.3.1 Mechanical Properties and Microstructure

A detailed evaluation of the microstructure and mechanical behavior of the AM and wrought 17-4PH was presented in Chapter 2, but the particular tempers covered in the current chapter are briefly reviewed for interpretation of the current results. First, note that the wrought and AM materials heat treated for study in this chapter all meet the respective ASTM A693⁵⁰ mechanical property requirements for H900 (Peak Age) and H1025 (Overage) tempers. In the peak age conditions, the AM material has higher strength than the wrought alloy, but the strength increase is traded for a reduction in ductility. The aging temperature to reach peak strength is similar in the AM material regardless of whether or not it is solution annealed, but aging with only a HIP treatment results in a significant loss of ductility. Overaging resulted in the nearest match between wrought and AM mechanical properties, but the ductility of the wrought material was still significantly higher than AM. The results in Chapter 2 showed that the AM material had minimal anisotropy in mechanical properties after heat treatment. Exceptions to this include generally lower ductility in the X direction and slight strength anisotropy in the overage condition. In all cases, 17-4PH undergoes minimal hardening as indicated by the high n in the Ramberg-Osgood fits.

Microstructure evaluation of the wrought and AM materials in the three peak age conditions of interest showed minimal microstructural anisotropy among the various material planes (i.e., XY, XZ, LS, ST). Therefore, only single planes for the AM HIP+Peak Age, AM HIP+SA+Peak Age, and wrought SA+Peak Age conditions are shown in the following microstructure review. The overaged microstructures are not shown since the aging process only impacted the Cu precipitates (not visible at this magnification), thus the grain/martensite structure is effectively identical to the corresponding peak age microstructure.

This strong similarity between the overage and peak age condition microstructures at the μm length scale is expected given the relatively stable microstructure of 17-4PH, except for minimal austenite reversion^{4,51} and precipitate coarsening⁵², at the employed aging heat treatment temperatures/times.

To highlight general microstructural differences, OIM maps captured through EBSD are shown in Fig. 13. In all conditions, the microstructure was primarily martensitic (colored regions) with negligible

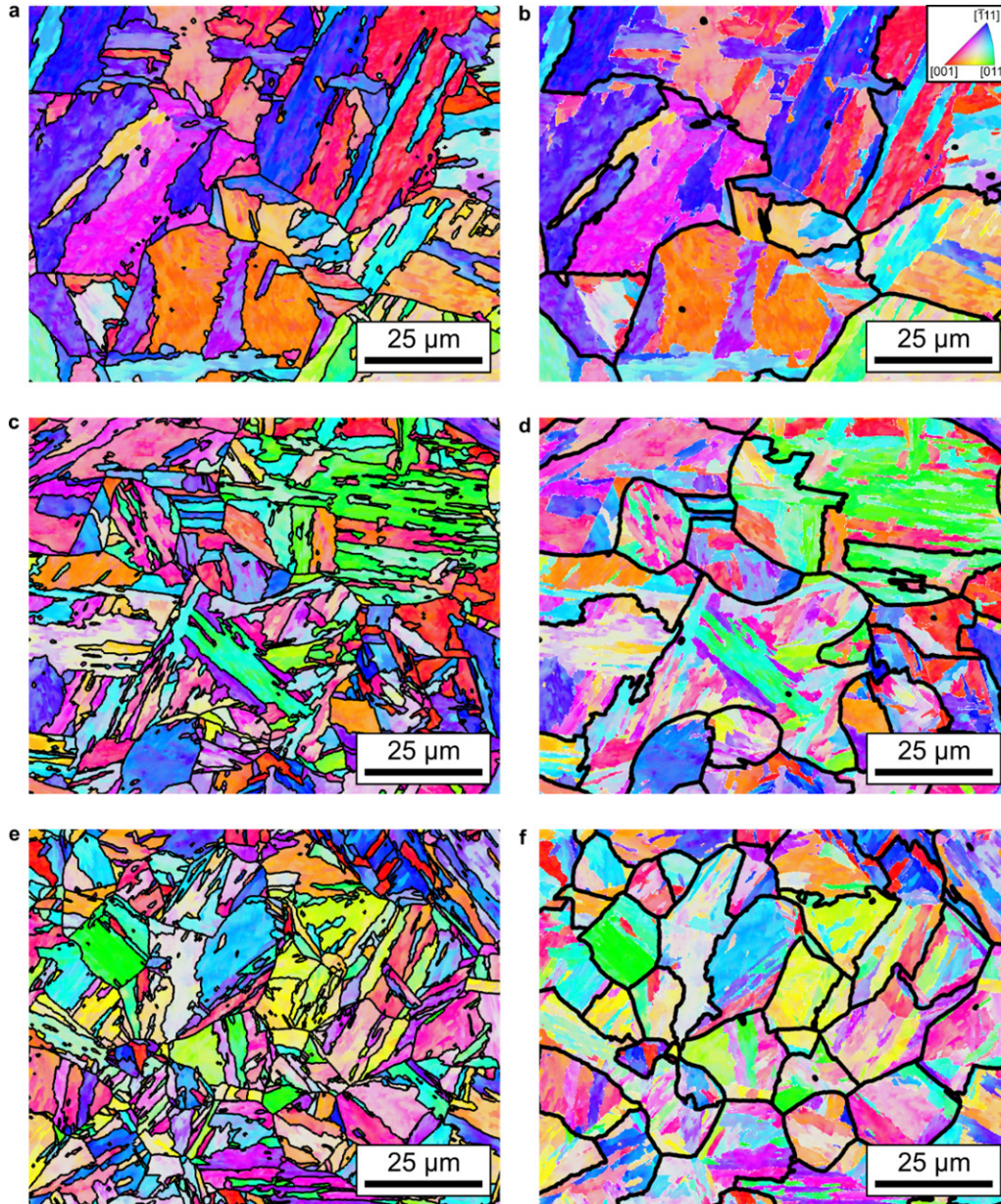


Fig. 13 | **AM and wrought 17-4PH grain structure.** **a-b**, AM in the HIP+Peak Age condition. **c-d**, AM in the HIP+SA+Peak Age condition. **e-f** Wrought in the SA+Peak Age condition. Colored regions indicate martensite grain orientations. Grain boundaries are identified with black outlines in (a,c,e). Prior austenite grain boundaries are highlighted with the bold, black outlines in (b,d,f).

austenite phase fractions. At the given length scale, discernable features include the martensite (M) block and prior austenite grain (PAG) structures. In the wrought SA+Peak Age condition, the M blocks and PAGs were finer than those observed for both the AM HIP+Peak Age and AM HIP+SA+Peak Age conditions. With just the HIP treatment, the AM material had the coarsest M block and PAG structure. Adding a SA treatment after the HIP had little effect on the PAG size, but the M block structure appeared to refine to nearly the size of the wrought material.

Finer features in the microstructure were revealed by SE imaging at 5000x magnification, shown in Fig. 14. The primary distinguishing feature between the wrought and AM materials at this length scale is the existence of porosity and secondary particles in the AM material versus the relatively clean microstructure in the wrought material. The AM HIP+Peak Age material has a combination of porosity and small ($< 0.25 \mu\text{m}$) secondary particles. Some of these particles seem to be aggregated along prior austenite grain boundaries (Fig. 14a). Porosity was evident in all evaluated treatments of AM 17-4PH, as indicated by the circular features with light halos in Fig. 14a,b. Typical pore sizes were on the order of 0.1-0.5 μm in diameter. In comparison, there are no indications of porosity in the wrought 17-4PH. The small ($< 0.5 \mu\text{m}$),

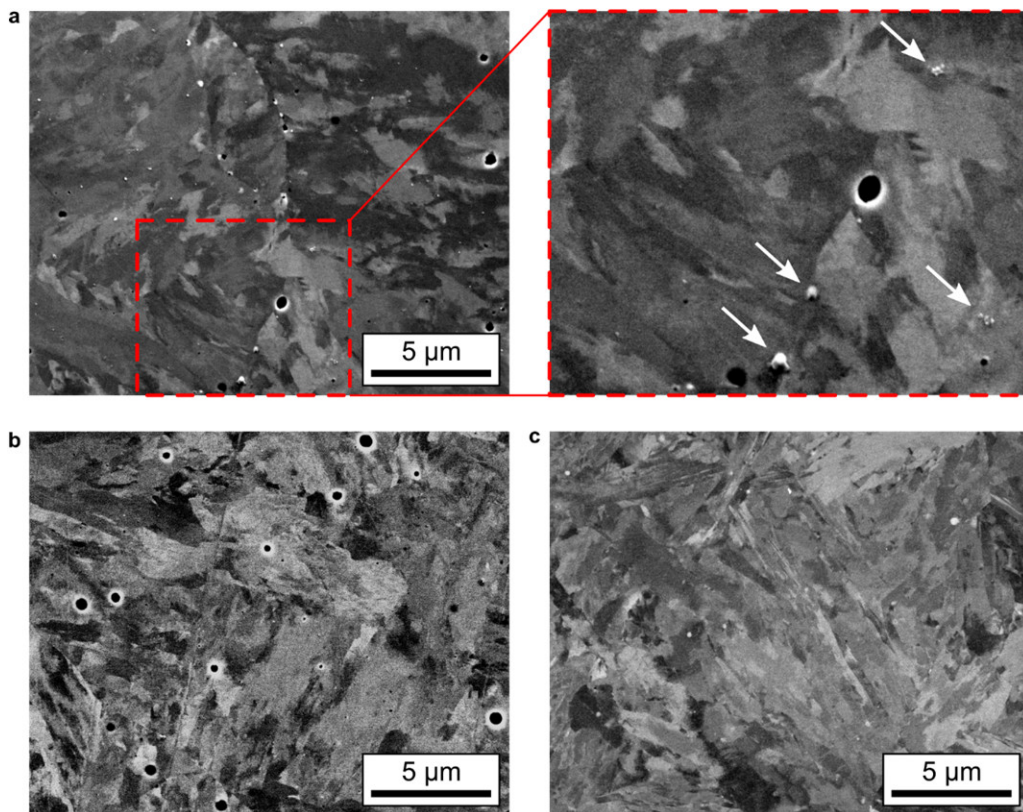


Fig. 14 | Pores and particles in AM 17-4PH. **a**, AM in the HIP+Peak Age condition. **b**, AM in the HIP+SA+Peak Age condition. **c**, Wrought in the SA+Peak Age condition. All images are secondary electron micrographs. White arrows indicate particles protruding out of plane.

bright, circular features in the wrought material are not pores but more likely Nb carbides known to be present in both wrought^{53,54} and AM⁵⁵ 17-4PH.

3.3.2 Stress Corrosion Cracking Behavior

3.3.2.1 Rising K Kinetics

The crack growth rate versus applied stress intensity relationships measured in dry N_2 (RH < 5%) for wrought and AM 17-4PH heat-treated to the peak aged and overaged conditions are shown in Fig. 15.

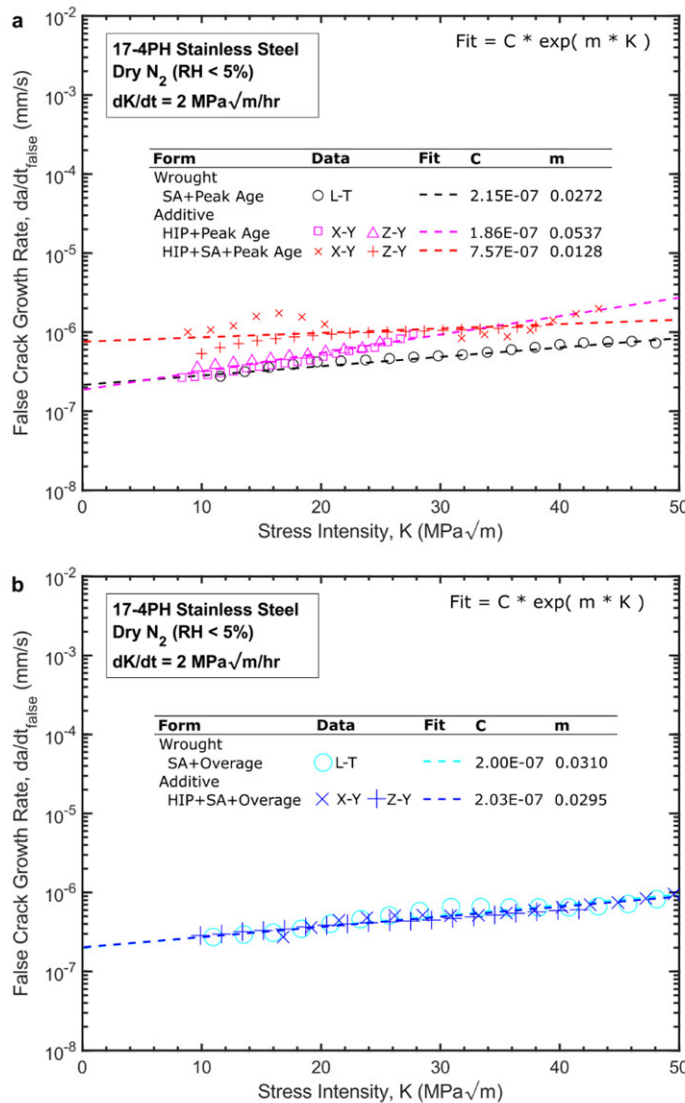


Fig. 15 | Inert environment false crack growth rates under rising K for AM and wrought 17-4PH. **a**, Peak aged 17-4PH. **b**, Overaged 17-4PH. Rising K false crack growth rates were gathered for various forms, heat treatments, and loading orientations of 17-4PH at $dK/dt = 2 \text{ MPa}\sqrt{\text{m/h}}$ in a dry N_2 (inert) environment. Growth rates shown are dcPD artifacts associated with crack tip plasticity and specimen compliance not crack extension. Exponential fit lines for these false growth rates establish resolution limits for aggressive environment tests.

All tested material conditions exhibit a nominally linear increase in $\log(da/dt)$ with increasing K instead of the characteristic rapid acceleration in da/dt typical of Stage I SCC crack growth⁵⁶. Such behavior has been observed during dry N_2 testing in numerous prior studies across a range of alloy systems^{46,57-66}, which have collectively demonstrated that these linear increases in $\log(da/dt)$ with K are not due to real crack extension. Instead, this apparent crack growth is due to geometric contractions of the test specimen⁶⁷ and localized, crack tip plasticity-induced changes in resistivity⁶⁵ that act together to increase the dcPD-measured voltage. Prior work⁴⁶ demonstrated that these ‘false’ crack growth rate versus stress intensity relationships can be fit to the following equation:

$$\left(\frac{da}{dt}\right)_{false} = C \cdot \exp(mK) \quad (3.1)$$

The fitted C and m coefficient for each condition are shown in Fig. 15. Note that X-Y and Z-Y oriented AM specimens for a given heat treatment condition exhibited similar ‘false’ da/dt versus K relationships and were therefore simultaneously fit to Eq. (3.1). Nominally identical ‘false’ da/dt responses were observed for wrought and AM 17-4PH heat-treated to the overaged condition, while more significant differences were noted amongst the tested peak aged conditions. Specifically, the wrought peak aged 17-4PH exhibited reduced ‘false’ da/dt for a given applied K relative to the peak aged AM 17-4PH. The most salient differences were observed between the two peak aged heat treatments in the AM material, with the ‘false’ da/dt in the HIP+Peak Age condition exhibiting a ~4-fold stronger dependence on K (quantified by the m coefficient) than the HIP+SA+Peak Age condition. The presence of heat treatment-dependent ‘false’ da/dt versus K behavior is consistent with prior results in other alloy systems. For example, a similar magnitude (~3-fold) difference in the m coefficient was noted between non-aged and overaged Monel K-500⁶³.

The finding that the observed linear $\log(da/dt)$ vs. K relationships are artifacts and not indicative of real crack growth is corroborated by fractography. Specifically, as shown in Fig. 16a, evidence of crack blunting (indicated by white arrows) was observed on the fracture surface of the HIP+Peak Age AM material. This observation, coupled with a lack of features suggestive of real SCC extension, confirm the absence of SCC during testing in dry N_2 (RH < 5%). Identical blunting features were noted on the fracture surfaces of all other tested material conditions. Interestingly, similar blunting features were also observed across all tested material conditions during slow-rising K experiments conducted in 0.6 M NaCl near OCP ($E_{app} = -0.190$ V_{SCE}), as shown in Fig. 16b (indicated by white arrows) for the AM HIP+SA+Peak Age material. Such features (along with similar measured kinetics as the dry N_2 results; not shown) demonstrate that 17-4PH under near-OCP conditions in 0.6 M NaCl does not experience SCC crack growth, consistent with expectations from prior literature for 17-4PH immersed in 0.6 M NaCl at ambient temperature^{22,68}.

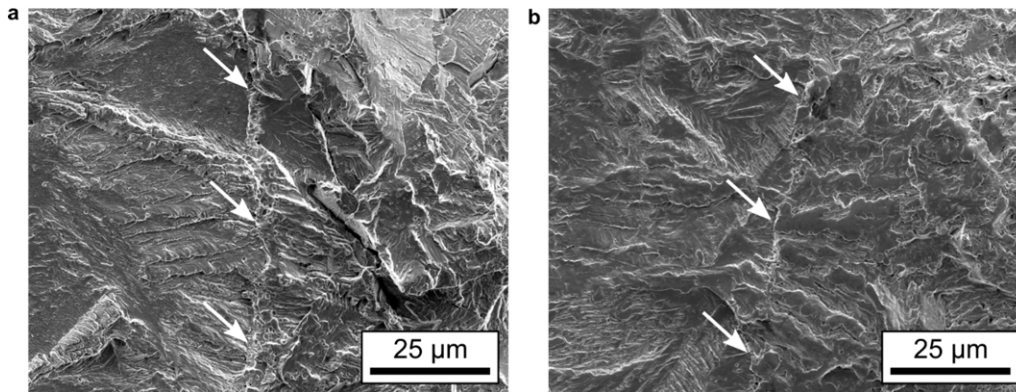


Fig. 16 | **Crack tip blunting resulting from rising K SCC tests with no crack extension.** **a**, HIP+Peak Age AM 17-4PH tested in dry N_2 . **b**, HIP+SA+Peak Age AM 17-4PH tested in 0.6M NaCl at $E_{app} = -0.190 V_{SCE}$. These are two examples of typical morphologies for 17-4PH fatigue precrack fronts (identified with white arrows) after rising to $K = 30 \text{ MPa}\sqrt{\text{m}}$ at $dK/dt = 2 \text{ MPa}\sqrt{\text{m}}/\text{h}$ with no SCC crack extension. Note that the crack extension direction is from left to right and the samples shown were fatigued for further testing after the aforementioned rising K tests.

A limited number of anodically polarized (i.e., $E_{app} > -0.190 V_{SCE}$) SCC tests were also performed in 0.6M NaCl. At an applied potential 50 mV anodic of OCP (i.e., $-0.140 V_{SCE}$), both wrought and AM were not susceptible to SCC as indicated by growth rates (not shown) at or below their respective test resolution limits established in dry N_2 . At more aggressively anodic potentials, both the wrought and AM materials underwent severe crevice corrosion under the lacquer surrounding the crack path. In multiple cases, this macroscopic dissolution led to failure of the dcPD wires and premature conclusions to the SCC tests. Fractographic inspection of samples showed no clear indication of SCC crack extension.

Cathodic SCC crack growth behavior as a function of stress intensity was captured at $E_{app} = -1.100 V_{SCE}$, shown in Fig. 17. Note that false growth rate fits established in Fig. 15 were subtracted from the raw data to yield the true crack growth rates following the approach described by Harris et al.⁴⁶ This correction also accounted for the effect of deviations from the prescribed $dK/dt = 2 \text{ MPa}\sqrt{\text{m}}/\text{h}$ loading protocol (discussed below) on the ‘false’ growth rates⁶⁶. In general, AM 17-4PH displays higher SCC crack growth rates than wrought 17-4PH across all heat treatments, loading orientations, and applied stress intensities. In the Stage II growth region (i.e., nominally K independent growth rate at higher K), the AM material generally cracked 4-5x faster than wrought. The only exception is a single test in the AM HIP+SA+Overage (Z-Y) condition where the threshold stress intensity (K_{TH}) was elevated slightly. Noting the generally increased variability in the stage I region (i.e., low K , transient growth), the increased threshold may reflect test-to-test and initial crack tip variability. Another trend is the isotropic behavior in the AM material. The stage II crack growth rates coalesced across the loading orientations (i.e., X-Y and Z-Y) for each of the AM heat treatments. All of the peak aged AM conditions exhibited similar Stage II growth rates, with

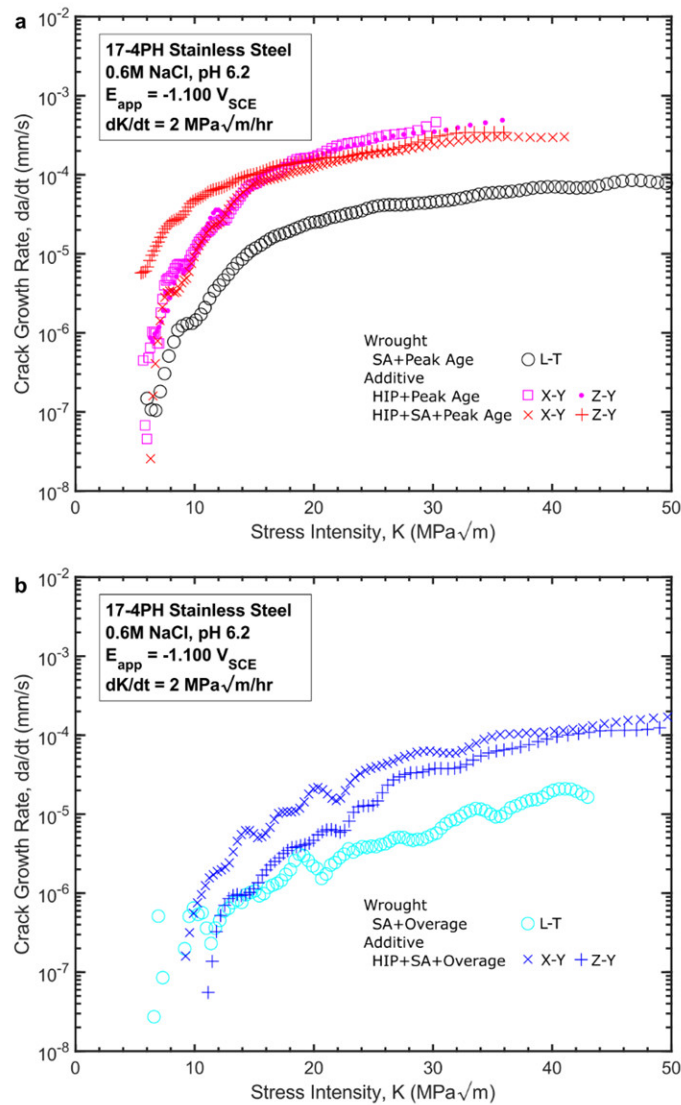


Fig. 17 | **Rising K SCC crack growth rates at a cathodic applied potential for AM and wrought 17-4PH.** a, Peak aged 17-4PH. b, Overaged 17-4PH. Rising K tests were performed in 0.6M NaCl with a cathodic applied potential ($E_{app} = -1.100 V_{SCE}$) for various forms, heat treatments, and loading orientations of 17-4PH at $dK/dt = 2 \text{ MPa}\sqrt{\text{m}}/\text{h}$.

growth rates only slightly elevated without a solution anneal. The peak aged threshold stress intensities were consistent across both the wrought and AM materials. However, these thresholds are near the max K ($7 \text{ MPa}\sqrt{\text{m}}$) applied to grow the precrack, thus may be influenced by the plastic zone from the precrack. A further minimized precrack plastic zone size (i.e., lower max K) might be required to decouple the apparent $K_{TH,SCC}$ from the precrack. In the overaged condition, growth rates were generally depressed relative to the peak age conditions as expected²⁰. There is indication that the overaged AM material may have a slightly higher threshold stress intensity than wrought condition, but the threshold is still low and overshadowed by the generally elevated growth rates in the AM material.

Several subtleties associated with the presented cathodic SCC data need to be highlighted. The fracture surfaces in all examined cases were rough and tortuous with increasing amounts of branching (as indicated by out of plane features) with higher applied K . The ending crack lengths were optically measured post-test and consistently found to be on the order of 1.5 times longer than dcPD-indicated final crack lengths. This underprediction by in-situ dcPD necessitated the previously described two-point, post-test corrections to the crack length and associated K , da/dt calculations. The fatigue precrack front, discernable by fatigue-SCC morphology change, and ending SCC crack length, marked by heat tinting, were used as reference points in this analysis. Functionally, this means that the reported $dK/dt = 2 \text{ MPa}\sqrt{\text{m/h}}$ is only strictly accurate for the low K results. Specifically, as the K increases, the dK/dt increased up to a maximum of $\sim 15 \text{ MPa}\sqrt{\text{m/h}}$. However, this variable dK/dt had little impact on growth rates as indicated by the less than 2-fold and 3-fold change in growth rate beyond $K = 30 \text{ MPa}\sqrt{\text{m/h}}$ for the peak aged and overaged materials, respectively.

3.3.2.2 Constant K Kinetics

The effects of various applied potentials were examined through a series of constant K SCC tests in 0.6M NaCl, see Fig. 18. Based on the rising K tests, a K of 30-40 $\text{MPa}\sqrt{\text{m}}$ was chosen to target the Stage II crack growth region. For this testing, an absence of measurable crack growth after an 8-24 hr test period for a given E_{app} was used to identify non-susceptible region, indicated by a crack growth rate of $1 \times 10^{-7} \text{ mm/s}$ and a downward arrow in Fig. 18. The crack growth kinetics observed during constant K testing can be dependent on load and polarization history (due to blunting, charging, or transient behavior), as such all reported data in Fig. 18 were measured in the ‘freshly fatigued’ condition (i.e., polarized within 30 min of fatigue).

The general applied potential dependence of the SCC susceptibility in Fig. 18 are consistent with prior reports on the SCC behavior of high strength steels^{59,60}. Specifically, high resistance to SCC is observed at mildly cathodic potentials that then transitions to significant SCC susceptibility as the applied potentials becomes more cathodic. Critically, the border between these non-susceptible and SCC-susceptible regions provides a ‘take-off’ potential that can be used as a proxy to rank the relative SCC susceptibility of each form/heat treatment of 17-4PH. Stark differences in this take-off potential metric were found for the wrought and AM materials in the peak aged conditions. As shown in Fig. 18, AM 17-4PH exhibited take-off potentials that were between 200-400 mV more positive than the wrought condition. The peak aged AM condition that did not undergo a solution annealing step was the most susceptible, with an estimated takeoff potential between -0.400 and -0.500 V_{SCE} . However, with a solution anneal, the peak aged AM takeoff potential shifted to a slightly more cathodic potential (-0.600 V_{SCE}), but still exhibits rapid growth rates ($\sim 1 \times 10^{-3} \text{ mm/s}$) in the -0.600 to -0.800 V_{SCE} range. Interestingly, the peak aged AM condition

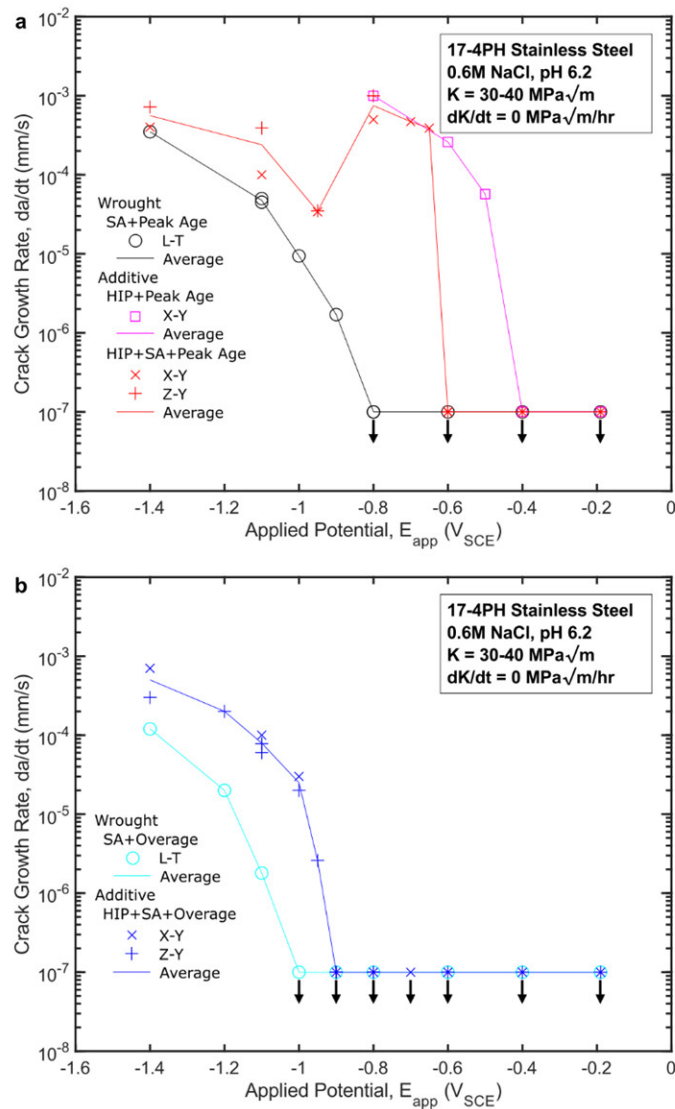


Fig. 18 | Constant K SCC crack growth rates as a function of applied potential for AM and wrought 17-4PH. **a**, Peak aged 17-4PH. **b**, Overaged 17-4PH. Constant K SCC crack growth rates were gathered as a function of applied potential in 0.6M NaCl for various forms, heat treatments, and loading orientations of 17-4PH. Where no crack extension was observed, a growth rate of $1 \times 10^{-7} \text{ mm/s}$ with a down arrow is shown.

has a distinct transition at cathodic potentials beyond $-0.800 \text{ V}_{\text{SCE}}$. The crack growth rate decreases by an order of magnitude and then follow the general trend for the peak aged wrought condition, though at an elevated rate. Multiple loading orientations were evaluated for the AM material and the SCC behavior was isotropic across all applied potentials and heat treatment conditions.

In the overaged condition, the AM 17-4PH exhibits a slightly less cathodic takeoff potential than wrought (i.e., indicating increased SCC susceptibility) and generally higher crack growth rates in the susceptible range, though the magnitude of the differences are less pronounced than was observed for the

peak aged condition. Comparison of the peak aged and overaged AM condition shows that overaging shifts the takeoff potential more negative, but similar rapid crack growth rates are observed at highly susceptible conditions (e.g., -1.200 to -1.400 V_{SCE}). Conversely for wrought 17-4PH, overaging has a dual benefit of improving the takeoff potential and depressing the crack growth rate for a given applied potential.

3.3.2.3 Fractography

Fractography showed that differing loading rates, orientations, and K values did not impact the fracture morphology, except for the observation of increased branching and tortuosity at high K . Differences in morphology were primarily observed as a function of form, heat treatment, and applied potential, which are detailed below and summarized in Table 3. Regarding the peak aged condition, representative fractographs are shown in Fig. 19. For peak aged wrought 17-4PH, crack growth was almost exclusively transgranular (TG). Though only shown at $E_{app} = -1.100 V_{SCE}$, Fig. 19a is representative of the fracture morphologies observed for peak age wrought 17-4PH across all susceptible E_{app} . Conversely, peak aged AM 17-4PH generally exhibited mixed IG+TG failure, with the fraction of IG depending on the applied potential and solution-annealing protocol. For example, between the take-off potential and -0.800 V_{SCE} , a significant fraction of IG was observed for both HIP+SA+Peak Age and HIP+Peak Age, with former exhibiting mostly IG fracture (Fig. 19d). However, as the applied potential became more cathodic, the extent of TG fracture increased for both conditions, with HIP+Peak Age (Fig. 19b) exhibiting mixed TG and IG fracture and HIP+SA+Peak Age (Fig. 19c) transition to largely TG fracture. Interestingly, the applied potential where the AM HIP+SA+Peak Age condition began to exhibit increasingly TG-dominant crack growth ($\approx -0.925 V_{SCE}$) closely corresponds to the unexpected reduction in growth rate shown in Fig. 18a.

In the overaged condition, the wrought and AM materials both exhibit primarily IG crack growth across all applied potentials, shown in Fig. 20. For wrought 17-4PH, IG was mixed with nearly evenly spaced small regions of TG fracture. The same was true for the AM material, but the TG regions were

Table 3 | SCC morphologies evaluated as a function of applied potential and 17-4PH form/heat treatment.

Form	E_{app} :	SCC Fracture Morphology			
		-0.600 V_{SCE}	-0.800 V_{SCE}	-1.100 V_{SCE}	-1.400 V_{SCE}
Wrought					
SA+Peak Age	-	-		TG	TG, Branching
SA+Overage	-	-		Mixed IG + TG	Mixed IG + TG, LT Plane Fissuring
Additive					
HIP+SA+Peak Age	-		IG	TG* + IG	Mixed TG + IG, Branching
HIP+Peak Age		TG* + IG	TG* + IG	TG* + IG	Not Evaluated
HIP+SA+Overage		-	IG* + TG	IG* + TG	IG* + TG, Branching

TG = Transgranular Fracture; IG = Intergranular Fracture; * = Dominant Morphology

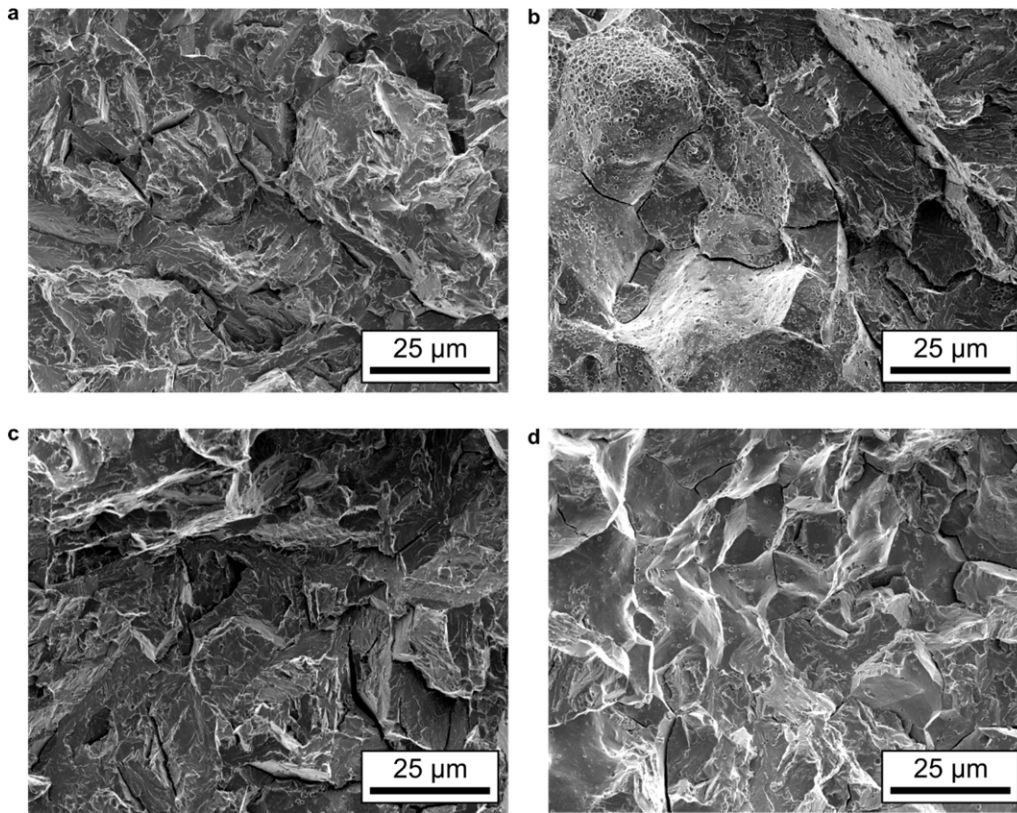


Fig. 19 | **Stress corrosion cracking morphologies for peak aged wrought and AM 17-4PH.** **a**, Wrought in the SA+Peak Age condition at $E_{app} = -1.100 V_{SCE}$. **b**, AM in the HIP+Peak Age condition at $E_{app} = -1.100 V_{SCE}$. **c-d**, AM in the HIP+SA+Peak Age condition at $E_{app} = -1.100 V_{SCE}$ (**c**) and $E_{app} = -0.800 V_{SCE}$ (**d**). All fractographs were gathered from cathodic polarization SCC tests in 0.6M NaCl.

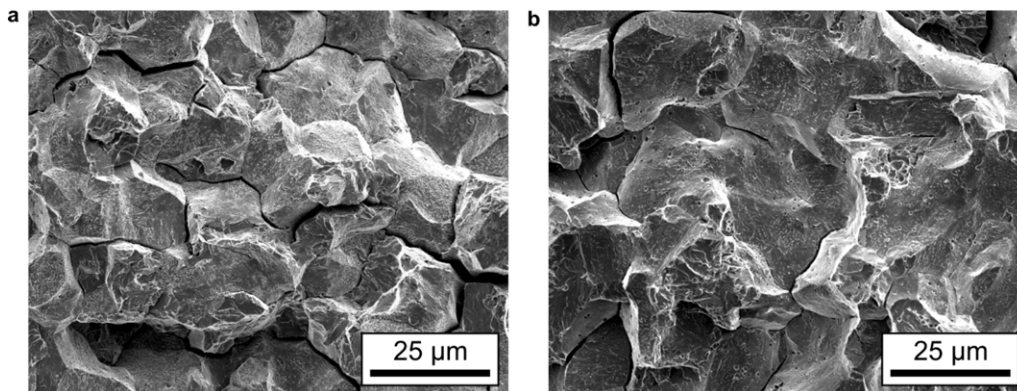


Fig. 20 | **Stress corrosion cracking morphologies for overaged wrought and AM 17-4PH.** **a**, wrought in the SA+Overage condition. **b**, AM in the HIP+SA+Overage condition. Fractographs were both from SCC tests in 0.6M NaCl under cathodic polarization at $E_{app} = -1.100 V_{SCE}$.

further spaced, resulting in IG being more dominant. Interestingly, the overaged wrought material exhibited a number of larger-scale out of plane fissures parallel to the LT plane at highly cathodic potentials; these features were not observed in the AM material. Given the plane and spacing, these fissures might have been following delta ferrite stringers formed during hot-rolling^{69,70}. While specific characterization aimed at identifying delta ferrite stringers was not performed for the current study, stringers were noted in the wrought plate during other characterization activities (and not in the AM material).

High magnification micrographs of the intergranular facets observed for the various tested conditions are shown in Fig. 21. As previously mentioned, the wrought SA+Peak Age condition was unique in that intergranular fracture was not broadly observed. Conversely, both AM HIP+SA+Peak Age and AM HIP+Peak Age exhibited significant IG fracture between the take-off potential and $-1.000 V_{SCE}$. With a HIP+SA treatment (Fig. 21a), the peak aged AM material had IG facets decorated with $0.1-0.5 \mu\text{m}$ pore-like features and sub-surface particles less than 100 nm in size. The remainder of the facet was relatively smooth. Without the SA treatment, the peak aged AM material had a combination of the pore-like features and particles protruding from the facets (Fig. 21b). The small, nm-scale particles appear to be increased in

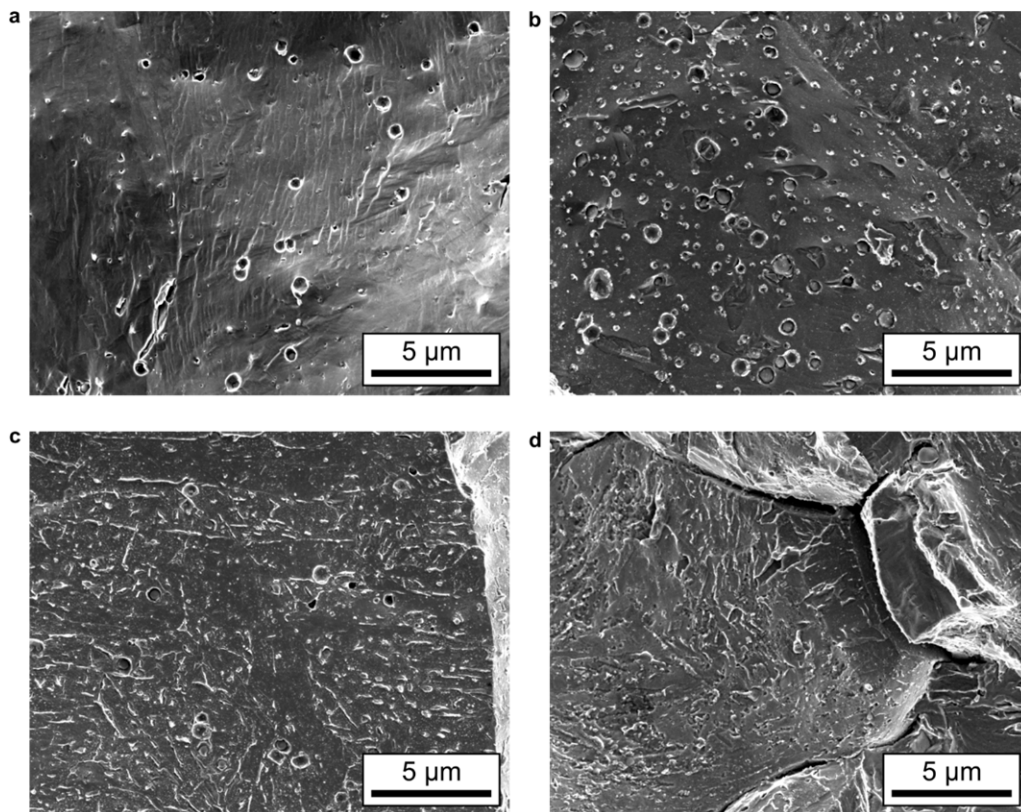


Fig. 21 | **Intergranular SCC fracture morphologies for wrought and AM 17-4PH.** **a**, AM in the HIP+SA+Peak Age condition. **b**, AM in the HIP+Peak Age condition. **c**, AM in the HIP+SA+Overage condition. **d**, Wrought in the SA+Overage condition. Fractographs were all gathered from cathodic polarization tests in 0.6M NaCl at $E_{app} = -1.100 V_{SCE}$.

size and number relative to the solutionized AM material. Additionally, protruding crater-like features that surround the particles and instances of broken particles may indicate that they may play a role in the fracture of the facet. In the overage conditions (Fig. 21c,d), fracture was dominated by IG for both the AM and wrought material. Unlike the peak aged materials, the facets are less smooth and are covered with features that suggest local plasticity. The porosity is still evident on the AM facets while the wrought facets exhibit no evidence of porosity.

3.4 Discussion

The preceding results demonstrate that AM 17-4PH exhibits increased SCC susceptibility relative to wrought 17-4PH at comparable yield strength levels across all evaluated heat treatments, environments, and loading schemes. Clear differences in both metallurgical features and fracture morphology were also noted across the tested conditions. Three questions arise from these results:

1. What is responsible for the observed increase in SCC susceptibility of AM 17-4PH?
2. What is responsible for the observed changes in fracture morphology as a function of applied potential?
3. What causes the more positive take-off applied potential for the HIP+Peak Age relative to the HIP+SA+Peak Age AM conditions?

In the following discussion, a decohesion-based failure framework for hydrogen-driven SCC is employed to link the observed susceptibility trends to changes in the governing microstructure features that are induced by the AM process. Based on this mechanistic framework, the contribution of the observed differences in prior austenite grain (PAG) size, hydrogen-metal interactions, compositional heterogeneities, second phase particles, and porosity to the SCC susceptibility of the wrought and AM materials are considered. The implications of these evaluations are then discussed in the context of possible process modifications that may improve the SCC resistance of AM 17-4PH.

3.4.1 Decoherence-based Mechanistic Framework for SCC

It is well-established that hydrogen embrittlement is responsible for SCC in high strength steels exposed to aqueous chloride environments under cathodic polarization^{59,60,71}. A litany of theories have been proposed to describe the microscale mechanism(s) responsible for such hydrogen-induced degradations in fracture resistance⁷²⁻⁷⁵. Recent literature strongly suggests that hydrogen-assisted fracture occurs *via* interface decohesion that is synergistically driven by the combined interactions of hydrogen-induced reductions in cohesive strength and hydrogen-modified deformation behavior^{72,73,76}. While it has known shortcomings that preclude quantitative prediction, the decohesion-based model for K_{TH} proposed by Gerberich⁷⁴ (and subsequently modified by others^{61,62}) phenomenologically captures the general

dependencies of SCC on hydrogen and microstructure-based parameters^{57,65,77}. As such, this framework can be leveraged to understand the mechanistic influence of possible AM-induced microstructural changes:

$$\text{Failure Criteria at } x_{crit} \sim K_{TH} = \frac{1}{\beta'} \exp \left[\frac{(\{k_{IG} + \sum_{i=0}^n \beta_i C_i\} - \alpha C_{H\sigma})^2}{\alpha'' \sigma_{ys}} \right] \quad (3.2)$$

Where k_{IG} is the Griffith toughness of the susceptible interface (e.g., martensite lath interfaces, grain boundaries, etc.) which can be modified (either negatively or positively) by the presence of trace impurities. The influence of these impurities is described by $\sum_{i=0}^n \beta_i C_i$, where C_i and β_i are the local concentration and potency of the effect of the i th impurity on the intrinsic Griffith toughness. α describes the degradative potency of hydrogen, while $C_{H\sigma}$ is the hydrostatic stress-enhanced hydrogen concentration that is pertinent to the fracture process zone. Lastly, σ_{ys} is the alloy yield strength and the α'' and β' parameters are coefficients determined from modeling of dislocation shielding on the crack tip elastic stress.

It is important to recognize that the variations in SCC susceptibility observed in Fig. 17 and Fig. 18 are represented by differences in crack growth kinetics while Eq. (3.2) describes the dependence of K_{TH} on hydrogen content and microstructure-based parameters. However, the authors propose that the Gerberich model for K_{TH} can be more generally interpreted, and thus extended, to serve as a description of the conditions required for hydrogen-assisted crack advance or a proxy for interface failure stress (*i.e.*, a failure criteria). This paradigm allows Eq. (3.2) to then serve as a platform to qualitatively assess the observed variation in SCC kinetics in the context of potential AM-induced microstructure modifications. The extension of this general framework to understand how AM-specific microstructure features may impact the susceptibility of SCC crack growth is justified by three considerations. First, recent work has extended the Ritchie-Knott-Rice (RKR) paradigm for crack advance⁷⁸ to hydrogen environment-assisted cracking (HEAC) conditions⁴⁶. The RKR model proposes that crack advance occurs when a local failure criteria (e.g., critical stress⁷⁸ or strain⁷⁹) is exceeded over a critical distance (x_{crit}) ahead of the crack tip. In a HEAC paradigm, this failure criterion is degraded by the local hydrogen content^{46,80}. The authors propose that the Gerberich relationship (Eq. (3.2)) describing the dependence of the continuum-scale threshold (e.g., K_{TH}) on microstructure-dependent parameters is analogous to, and thus can be extended to broadly capture, how the local failure criteria at x_{crit} is impacted by microstructure variations. Second, it is recognized that the salient role of H diffusivity for HEAC is not captured by the Gerberich framework. However, (1) this omission will be explicitly considered by discussion of the AM-specific H-material interactions that will impact $C_{H\sigma}$, and (2) prior work has demonstrated synergy between micro-mechanical models that describe the microstructure dependence of K_{TH} and crack growth kinetics^{59,61,81–83}. Finally, this framework will not be used for quantitative predictions; as such, the rigor of the functional form of Eq. (3.2) will not

compromise the use of this framework to postulate how microstructure variations may impact the failure criteria.

Once justified, evaluation of the parameters in Eq. (3.2) highlights several factors that may influence the relative SCC susceptibility of AM versus wrought 17-4PH. First, differences in yield strength could have an impact, with higher yield strength leading to a reduced failure criterion. Second, a difference in hydrogen-material interactions, such as the increase in the diffusible hydrogen concentration at a given applied electrochemical potential, could increase the hydrogen available to participate in the fracture process, leading to an increase in $C_{H\sigma}$ and a decrease in the failure criterion. Third, differences in the near-crack deformation behavior or slip morphology that impede dislocation emission could lower the failure criterion through modifications in the α'' and β' terms. Fourth, variations in the trace impurity content at the susceptible interface, as would be expected for both differences in aging condition and AM/wrought stock, could either degrade or increase k_{IG} via modification of the $\sum_{i=0}^n \beta_i C_i$ term in Eq. (3.2), leading to a concomitant decrease or increase the failure criterion. Finally, variations in the local stress state in the fracture process zone at the crack tip (particularly modifications in the hydrostatic stress distribution as may be induced by porosity, inclusions, etc.), could serve to locally affect $C_{H\sigma}$ and therefore modify the failure criterion. It should be noted that the AM and wrought materials tested in the current study were specifically heat-treated to minimize variations in the yield strength. For example, the AM HIP+SA+Peak Age material has a ~100 MPa increase in yield strength relative to the AM HIP+Peak Age material (which is nominally identical to the wrought SA+Peak Age material), but a -200 mV_{SCE} more negative take-off potential than the AM HIP+Peak Age alloy (Fig. 18a). As such, yield strength differences are unlikely to be the source of the observed variations in SCC susceptibility and the following discussion will focus on the other identified parameters.

In addition to understanding the contribution of microstructural features, Eq. (3.2) can be leveraged to mechanistically understand the observed changes in fracture morphology as a function of applied potential for a given alloy condition (Table 3). First, k_{IG} in Eq. (3.2) is not limited to describing the intrinsic Griffith toughness of a grain boundary; it can be used to describe the intrinsic toughness of any crack pathway⁸⁴. Second, it is unlikely that the $\alpha C_{H\sigma}$ term in Eq. (3.2) will be constant for all possible crack pathways under a constant environmental condition. For example, literature demonstrates that the driving force for hydrogen segregation to $\Sigma 3$ boundaries is low^{85,86}, which would act to strongly reduce the hydrogen present at this interface (and therefore reduce $C_{H\sigma}$). While the specific details of the hydrogen trap binding energies for the prior austenite grain boundaries and the martensite lath interfaces in the current materials are not known, literature suggests it is reasonable to expect variations in the extent of hydrogen trapping between these features⁸⁷. Similarly, due to the intrinsic differences between these interface features (e.g.,

prior austenite grain boundaries and martensite laths), it is also likely that the intrinsic toughness and degradative effects of hydrogen (i.e., α in Eq. (3.2)) will be distinct for each.

Functionally, this means that k_{IG} and $\alpha C_{H\sigma}$ will vary between possible fracture pathways, which would lead to different fracture paths becoming favorable at different applied potentials. This variation in fracture pathway was specifically noted for the AM HIP+SA+Peak Age condition (Table 3), where the fracture morphology was observed to transition from IG to TG-dominant fracture as the applied potential became increasingly negative. Considering Eq. (3.2), this could manifest if prior austenite grain boundaries in the AM HIP+SA+Peak Age material are described by a low k_{IG} and a modestly applied potential dependent $\alpha C_{H\sigma}$ term, but the TG fracture pathway is characterized by a high k_{IG} and stronger applied potential dependence of $\alpha C_{H\sigma}$. Such a scenario is illustrated schematically in Fig. 22 for two conditions of peak aged 17-PH.

For AM in the HIP+SA+Peak Age condition, the failure stress required for interface decohesion at low hydrogen concentrations (which trends to k_{IG}) must be higher for the martensite lath boundaries than the PAG boundaries given the observed IG fracture at more positive applied potentials. As the hydrogen content is increased, the interface failure stress is reduced for both boundaries, but at different rates (e.g., due to different α values), resulting in a cross-over. This postulated cross-over potential is likely associated with the unexpected decline in crack growth kinetics for the AM HIP+SA+Peak Age material at $-0.950 V_{SCE}$ (Fig. 18a). As shown in Table 3 and Fig. 19, the dominant fracture mode for the AM HIP+SA+Peak

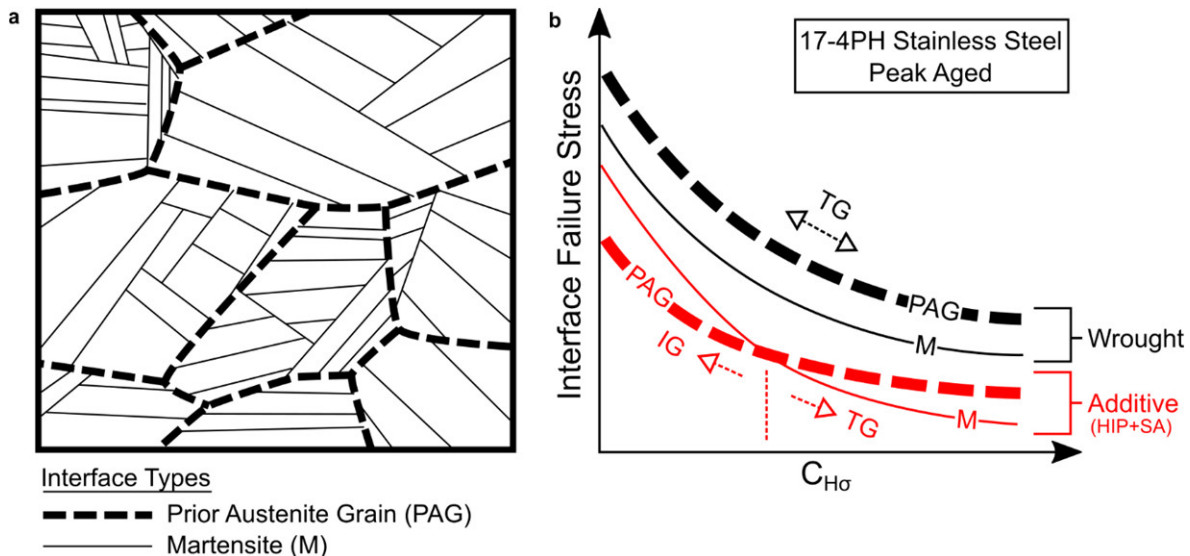


Fig. 22 | **Postulated variation of grain boundary interface failure stress with stress assisted hydrogen concentration for peak aged 17-4PH.** **a**, Schematic illustration of the primary grain boundary interfaces in 17-4PH. **b**, The postulated response of those interfaces' failure stresses to stress assisted hydrogen concentration ($C_{H\sigma}$) in peak aged 17-4PH. The intergranular (IG) and transgranular (TG) fractographic bases for these postulations are superimposed for reference.

Age material changes from IG to primarily TG between -0.800 and -1.100 V_{SCE}. It is therefore reasonable to suggest that there is an intermediate potential between these two bounding conditions where both IG and TG fracture pathways are (effectively) equally favorable. If multiple fracture pathways are equally favorable, this will likely lead to an increasingly tortuous, mixed fracture pathway that would reduce the local driving force for crack advance (i.e., due to crack branching and/or deflections) and decrease in the crack growth rate. Indeed, a mixture of the fracture morphologies shown in Fig. 19c,d was observed at -0.950 V_{SCE} (image not shown). However, once the applied potential became sufficiently negative that a single fracture pathway (a different fracture path in this case, Fig. 19c) was dominant, then the crack growth rate increased from the locally reduced value, as observed in Fig. 18a.

Conversely, wrought in the SA+Peak Age condition exhibited a consistent TG fracture pathway not subject to the aforementioned variations seen in AM 17-4PH (Table 3). Accordingly, the wrought growth rate steadily increased as the applied potential became increasingly negative (Fig. 18a). These observations might point to a higher PAG k_{IG} relative to martensite lath boundaries in wrought as compared to AM and/or an attenuated H degradation of wrought PAGs as described by α . Clearly, other factors are likely to contribute to these processes (e.g., differences in trace impurity contents, local deformation, etc.) and high-fidelity atomistic simulations are required to confirm the above postulations. However, this thought experiment highlights the utility of the current decohesion-based mechanistic framework (Eq. (3.2)) to postulate mechanistic underpinnings for observed behavior.

3.4.2 Microstructural Origins of Degraded SCC Performance

3.4.2.1 Grain Boundary Impurity Segregation

The current investigation shows that IG fracture in AM 17-4PH is associated with both enhanced SCC susceptibility and accelerated crack growth rates relative to the wrought material. In the peak age condition, this phenomenon is especially evident as wrought 17-4PH exhibits a transgranular fracture morphology (Table 3), whereas the AM material had increased SCC susceptibility that correlated with IG fracture (Table 3 and Fig. 18a). Comparison of the various fracture morphologies (Fig. 19, Fig. 20) and grain structures (Fig. 13) shows that the intergranular fracture is occurring along the prior austenite grain (PAG) boundaries. Generally, fracture along PAGs in steels during ambient temperature deformation can be promoted by (1) elemental segregation of deleterious impurities during thermal treatment, (2) nucleation of secondary phases on the grain boundary, and/or (3) aggressive environments⁸⁸. The latter was directly evaluated through varying E_{app} (Fig. 18), while the former two can be grouped under a phenomenon called temper embrittlement⁸⁹.

Under certain thermal processing schedules, many steels exhibit a transition from ductile microvoid coalescence or TG fracture to IG-dominated brittle fracture. For example, this ‘temper embrittlement’ has

been reported in wrought 17-4PH after prolonged exposure (on the order of months) to temperatures between 300°C and 450°C⁹⁰⁻⁹². It is notable that this embrittlement occurs in the absence of an aggressive environment (though hydrogen-rich environments can exacerbate the effect⁹³) and is largely attributed to the segregation of impurity elements to PAG boundaries, including: Si, Ge, Sn, N, P, As, Sb, Bi, S, Se, Te⁸⁸. Mechanistically, these segregated impurities act to degrade the grain boundary toughness (i.e., k_{IG} in Eq. (3.2) with the impact of the impurities captured by the $\sum_{i=0}^n \beta_i C_i$ term), leading to reduced fracture resistance. Critically, this embrittlement has also been observed under more conventional heat treatment schedules (e.g., the H1025 temper) for 17-4PH with phosphorus contents of ~0.03 wt. %⁹⁴.

Considering the current alloys, the AM material does have 6-fold more S and 65% more Si than the wrought material, though these levels are still well within the acceptable limits for 17-4PH per ASTM A693⁵⁰. However, given the differences in thermal processing between the AM and wrought alloys, it is possible that even larger differences in concentration are present at grain boundaries. For example, >1000-fold increases in the grain boundary S concentration over the bulk content were recently measured in Monel K-500 using Auger electron spectroscopy⁶³. This local agglomeration of impurities at the grain boundary can be exacerbated by three factors: (1) large grain size⁹⁵, (2) long-term exposures to intermediate temperatures⁹⁶, or (3) slow cooling rates after high temperature heat treatments⁹⁷. Regarding grain size effects, since larger grains result in a lower grain boundary area, such grains will likely have an increased grain boundary impurity content than small grains for a constant bulk impurity content. Conversely, increased time at intermediate temperatures and/or slow cooling rates allow for the diffusion of impurities towards grain boundaries, increasing the grain boundary impurity content.

Compared to the wrought alloy, the AM material in this study has several features that likely promote elemental segregation including a larger PAG size (Fig. 13) and the slow 310°C/h cooling rate from the HIP treatment. For example, the HIP+Peak Age condition, which had the worst SCC susceptibility, has both of these contributing factors. Conversely, the wrought peak aged material has the smallest PAG size (Fig. 13), did not undergo the HIP treatment, and has improved SCC resistance. The improved SCC resistance of the AM HIP+SA+Peak Age condition, that underwent a high temperature (1040°C) solution annealing treatment followed by air cooling, exhibited improved SCC resistance relative to the AM HIP+Peak Age alloy (Fig. 18a). This is also consistent with a likely role of temper embrittlement. Specifically, the SA treatment will act to both re-homogenize grain boundary impurities and refine the PAG size (as demonstrated in Fig. 13), while the air-cool would reduce the extent of re-segregation back to the grain boundaries during cooling (since it is significantly faster than the 310°C/h cooling rate employed in the HIP treatment). Similar trends in behavior are observed for the overaged alloys, with the AM HIP+SA+Overage condition exhibiting higher SCC susceptibility than the wrought SA+Overage condition

(Fig. 18b). Lastly, the increased observation of IG fracture in both the AM and wrought overaged material relative to the peak aged alloys is also consistent with temper embrittlement effects. Tempering to the overaged condition involves holding the specimen at 552°C for 4 h, while tempering to the peak aged condition requires 1 hour at 460/482°C. Such prolonged exposure would exacerbate impurity segregation in the overaged condition, increasing the likelihood of IG fracture pathways being favorable relative to TG pathways.

3.4.2.2 Porosity

Review of the microstructure (Fig. 14) and fractography (Fig. 21) shows that sub- μm pores are omnipresent across all evaluated AM conditions. It is likely that this porosity is due to insoluble Ar^{98} that was introduced both during powder atomization (as the atomizing gas) and during the build itself (as the inert build atmosphere). Porosity is a well-established challenge for AM alloys^{35,36,99–102} and is associated with a general reduction in toughness and ductility¹⁰³. However, it should be noted that the pore size range of interest in AM materials is typically 5-20 $\mu\text{m}^{33,35,36,104}$. The 0.1-0.5 μm pores observed in this study (Fig. 14a,b) are well below this typically evaluated range and, more critically, appear to be resistant to HIP treatments. As such, it is likely that such sub-micrometer pores will be present in AM 17-4PH components. However, understanding of how these 0.1-0.5 μm pores affect crack propagation behavior is highly limited, especially with regards to SCC.

It is logical to suggest a deleterious influence of this sub- μm porosity on the SCC resistance given the large number of pores present on the fracture surfaces of all tested AM conditions (both TG and IG; Fig. 21). Qualitative examination[†] of the voids observed on the fracture surface indicates little change in the void shape and size relative to the pores noted in the metallurgical cross-sections (Fig. 14). This qualitative similarity suggests minimal damage evolution occurred proximate to the voids during crack advance, consistent with the theoretical expectation that small voids will grow at slower rates relative to large voids¹⁰⁵. Critically, such minimal damage evolution suggests a brittle fracture process that, coupled with the discontinuous nature of subcritical SCC growth, provides a plausible mechanistic pathway by which these voids may contribute to the generally increased SCC susceptibility of AM 17-4PH (Fig. 18). Specifically, the interaction of these pores with hydrogen in the fracture process zone likely impacts how these voids contribute to SCC. Hydrogen is expected to agglomerate proximate to/within the pores in the fracture process zone due to both (1) the local enhancement in hydrostatic stress increasing local solubility¹⁰⁶ and (2) hydrogen trapping at the pores. At low concentrations, hydrogen has been shown to

[†] This qualitative examination is expanded and clarified via a statistically relevant, quantitative examination of pore-crack interactions in Chapters 4 & 5.

accelerate void growth and nucleation processes¹⁰⁷, but as the hydrogen concentration is increased to elevated levels (as would be expected proximate to the crack tip¹⁰⁶), a transition to brittle fracture modes occurs^{76,108}. As such, it is possible that this local elevation in hydrogen content could reduce the intrinsic fracture resistance that, coupled with the elevated local stresses proximate to the voids (since they are stress concentration sites), may result in easier crack initiation at pores.

The observed increases in crack growth rate under fixed K loading for all AM conditions relative to their wrought counterparts (Fig. 18) directionally supports this proposed role of porosity. This can be rationalized using the aforementioned Ritchie-Knott-Rice model for crack propagation⁷⁸, where the fracture resistance (which can be degraded by hydrogen)⁸⁰ must be exceeded over a critical distance in order for crack extension to take place. If the proposed hydrogen-induced crack initiation occurs at these voids, the high number density of such features (Fig. 14 and Fig. 21) indicates that it is plausible a void will reside between a given crack tip position and the critical distance associated with crack advance. These pre-initiated cracks could act to reduce the critical length (x_{crit}) that must be exceeded for crack propagation or vary the critical stress/strain needed for failure, leading to a general increase in both SCC susceptibility and the crack propagation rate, consistent with the up-shift in da/dt and more positive ‘take-off’ potentials noted in Fig. 18. This proposed contribution of porosity is also directionally consistent with previously invoked mechanisms for hydrogen-induced fracture in TWIP steels¹⁰⁹ and IN718¹¹⁰. Specifically, in these materials, it is postulated that voids nucleated at intersecting slip bands or deformation twin/grain boundary junctions serve as crack initiation sites that facilitate subsequent crack propagation. While direct evaluation of this proposed mechanism is outside the scope of the current study, future efforts will focus on confirming this mechanistic role of voids *via* high-fidelity microstructure characterization and targeted modeling approaches.

3.4.2.3 Secondary Phase Particles

In addition to porosity, examination of the fractographs (Fig. 21) and metallurgical cross-section micrographs (Fig. 14) also reveals the presence of sub- μm size secondary phase particles. Literature establishes that the most commonly observed particles that form in conventional 17-4PH are NbC and Cr_{23}C_6 ^{53,54,91,111}, while these phases along with Cr_7C_3 ¹¹², MnS ¹¹³, and oxide inclusions^{32,33,114} have been reported in AM 17-4PH. Of these, NbC, Cr_{23}C_6 , and oxide inclusions are the most likely secondary phase particles in the current study. Regarding NbC, Nb is a strong carbide former that is generally added to sequester C to reduce Cr_{23}C_6 nucleation^{55,115}. NbC particles are observed after all standard heat treatments for 17-4PH^{54,55,111}, consistent with its reported solvus of $>1250^\circ\text{C}$ ⁵⁵. However, it is generally considered to be non-detrimental from a mechanical property perspective due to its low volume fraction and large nearest neighbor distances.

Conversely, grain boundary precipitation of Cr_{23}C_6 is associated with increased corrosion susceptibility in stainless steels due to the local depletion of the Cr content¹¹⁶. Critically, while Nb is added to suppress Cr_{23}C_6 formation, the Nb content typical of 17-4PH (<0.3 wt.%) is not high enough to completely prevent nucleation of this deleterious phase during common heat treatments^{54,55}. One challenge associated with Cr_{23}C_6 is that volume fractions are generally low, making detection difficult *via* standard characterization techniques like x-ray diffraction⁵⁵. As such, it is most common for this phase to be reported after long-term (months) of long term exposures at 300-400°C (meant to replicate in-service conditions at nuclear powerplants)⁹¹, unless specific characterization approaches meant to highlight this secondary phase are performed (*e.g.*, double loop electrochemical potentiodynamic reactivation tests (DL-EPR))⁵⁴. For example, these DL-EPR experiments have demonstrated the presence of Cr_{23}C_6 after aging at or above 500°C in wrought 17-4PH⁵⁴. Phase diagrams for 17-4PH⁵⁵ predict that Cr_{23}C_6 will start precipitating at ~700°C for the Nb content in the current alloys; these results suggest that the pertinent temperature range for Cr_{23}C_6 formation in 17-4PH under typical heat treatments is 500-700°C.

Regarding the currently employed high temperature heat treatments, the HIP treatment was conducted at 1125°C, which is above the Cr_{23}C_6 solvus⁵⁵. However, given the slow cooling rates associated with the HIP treatment (310°C/h), an appreciable amount of time was spent in the noted temperature range where Cr_{23}C_6 precipitation is favorable. Conversely, the SA treatment (conducted at 1040°C) is also above the Cr_{23}C_6 solvus⁵⁵, but was followed by air cooling, which would drastically reduce the time spent in the temperature range where Cr_{23}C_6 precipitation is favorable. Considering these differences in the context of the SCC susceptibility noted for the peak aged AM materials, it is interesting to note that the HIP+SA+Peak Age exhibited increased SCC resistance relative to the HIP+Peak Age condition. This improvement, coupled with the notable reduction in secondary phase particles on the fracture surface for the HIP+SA+Peak Age relative to the HIP+Peak Age condition (Fig. 21), suggests that these Cr_{23}C_6 carbides may be contributing to the increased SCC susceptibility of the AM materials. Mechanistically, it seems reasonable that a process similar to that previously postulated for the voids observed in the AM material would be operative for the Cr_{23}C_6 particles. Specifically, the presence of hydrogen and the increased local stress proximate to these particles would act to make crack initiation more favorable, leading to enhanced SCC susceptibility. Such a scenario has been explicitly invoked in prior modeling of hydrogen-assisted cracking of carbide-containing steels¹¹⁷.

As previously discussed, the SA treatment should have attenuated elemental segregation and Cr carbides precipitated during the HIP, yet the SCC growth kinetics of the AM material in the HIP+SA+Peak Age condition still underperform wrought (Fig. 18a), suggesting a role of other factors. While porosity appears to be the most likely contributor, it is pertinent to note that several LPBF stainless steel studies

have shown that oxygen introduced through the build atmosphere or powder can result in finely dispersed Mn/Si/Nb/Cu rich oxides on the order of 0.05-0.10 μm in size³⁰⁻³³. These oxides can occur with as little as 260 wppm of dissolved O^{31} , and have been theorized to be electrochemically active during SCC, albeit under supercritical water conditions³⁰. The current lot of AM material has multiple of these hallmarks including a 600/480 wppm O concentration in the powder/build and second phase particles less than 0.25 μm in size (Fig. 14a) that are insoluble up to 1040°C (Fig. 21a). It is expected that these insoluble second phase particles are oxide inclusions that, in a similar manner to Cr_{23}C_6 carbides, enable easier crack extension along the grain boundary in AM 17-4PH. While literature indicates that the electrochemical activity of these oxides is likely minimal under the dilute neutral chloride solution conditions¹¹⁸, it is possible that the observed easier crack extension observed in the AM HIP+SA+Peak Age condition may be facilitated by an influence of these fine oxide particles on the local crack tip stress field. However, like the aforementioned discussion on sub- μm porosity, additional studies are needed to understand the mechanistic details regarding how the oxide inclusions and other secondary phase particles may affect the local crack tip fields.

3.4.2.4 Hydrogen-Metal Interactions

In addition to the above microstructural features, it is also likely that differences in hydrogen-metal interactions such as diffusivity, solubility, and trapping may exist between wrought and AM 17-4PH. While a detailed study of these parameters is ongoing for these alloys, it is still useful to comment on (1) what specific parameters would be mechanistically impactful and (2) how such impacts would arise. First, it is well established across multiple alloy systems that SCC susceptibility is directly tied to the hydrogen concentration available to participate in the fracture process (i.e., the diffusible hydrogen concentration)¹⁰⁶. As such, the observed differences in cracking kinetics could be related to differences in the diffusible hydrogen concentration (captured by $C_{H\sigma}$ in Eq. (3.2)) for a given electrochemical potential between the AM and wrought conditions. Fig. 14 demonstrates that subtle, but tangible differences in microstructure exist between AM and wrought 17-4PH. Such subtle microstructural variations can induce significant differences in the diffusible hydrogen concentration, as demonstrated in a prior study that assessed the hydrogen uptake behavior of five separate heats of a Ni alloy that were all heat-treated in accordance with the governing procurement specification¹¹⁹. Regarding AM materials, a recent study by Bertsch et al. has evaluated the hydrogen uptake behavior of austenitic stainless steels manufactured using LPBF, direct energy deposition (DED), and conventional processes¹²⁰. Critically, these authors report a systematic increase in hydrogen uptake for both AM (LPBF and DED) materials relative to the conventional alloy. If such an increase were to be observed for the 17-4PH, this would potentially explain the enhanced SCC susceptibility of all tested AM 17-4PH materials relative to their wrought counterparts. Moreover, Bertsch

et al. also reported tangible differences in hydrogen uptake between the two AM materials in their study, consistent with the variations observed for different processing approaches (albeit post-build) in Fig. 18. Studies are now underway to measure the diffusible hydrogen concentration as a function of applied potential in the current materials and will be reported in a forthcoming manuscript.

Second, it is also possible that differences in hydrogen diffusivity could contribute to the differences in crack growth rates shown in Fig. 18. The previously highlighted RKR failure criterion for crack advance is independent of the diffusivity, but the rate at which the criterion is met (i.e., the rate of crack advance) is explicitly linked to diffusivity. Given the accelerated crack growth kinetics for the AM material across all tested conditions, this would suggest that the AM material exhibits an increased hydrogen diffusivity relative to the wrought condition. Prior studies comparing conventional and AM austenitic stainless steels have reported both increased^{121,122} and reduced¹²³ hydrogen diffusivities in AM materials. Interestingly, these studies claimed an important role of the sub-grain boundaries introduced by the AM processing in either accelerating¹²² or slowing¹²³ hydrogen diffusion. While measurements of the hydrogen diffusivity in AM versus wrought 17-4PH are not available in the open literature, these studies in austenitic steels highlight the potential role of AM-induced microstructural features in modifying diffusion behavior. Considering the current study, hydrogen trapping at the widespread sub- μm porosity observed in the AM alloys (Fig. 14, Fig. 21) would be reasonably expected to impact the hydrogen diffusivity. However, such traps would be expected to slow hydrogen diffusion¹⁰⁶, which would result in reduced crack growth kinetics. This expectation is directionally opposed to the observed increase in crack growth rate for all tested AM 17-4PH materials (Fig. 18) as a function of applied potential, underscoring the need for direct measurements of the hydrogen diffusion and trapping behavior in these alloys.

3.4.2.5 Crack-tip Deformation Behavior

While the above ‘bulk’ characteristics will play an important role in establishing SCC susceptibility, SCC ultimately proceeds *via* highly localized interactions between hydrogen, deformation, and microstructural features within the fracture process zone proximate to the crack tip¹⁰⁶. As such, local characterization of the near-crack region is necessary to determine differences in near-crack deformation as a function of electrochemical potential (i.e., hydrogen content) and heat treatment condition. Critically, any observed variations in the local deformation behavior can then be leveraged to understand the microscale mechanisms governing SCC susceptibility. The influence of this local deformation is phenomenologically captured in Eq. (3.2) by the α'' and β' terms and mechanistically contributes to crack advance under the RKR paradigm *via* effects on the local mechanical driving force. Prior studies of the near-crack region suggest that hydrogen exposure results in a more localized deformation distribution proximate to the crack for a given driving force^{72,124,125}. However, considering the current alloys, how this

hydrogen-enabled localization is affected by the widespread sub- μm porosity, oxide inclusions, and carbides present in the AM 17-4PH is unclear. Moreover, prior reports have documented fundamental differences in the general deformation behavior between conventional and AM materials¹²⁶ as well as in hydrogen-charged versus hydrogen-free precipitation-hardened alloys¹⁰⁸. Whether or not such differences could manifest in the near-crack region for the AM and wrought 17-4 PH is also not known. It should be recognized that an evaluation of the local deformation will not be able to explicitly decouple all of these potential contributions given that they will be acting simultaneously and likely synergistically. However, local near-crack evaluations will provide insights on the extent to which these factors are potential contributors, which could then be leveraged to justify more targeted studies. Such studies of the near-crack deformation behavior for the current materials will be presented in the proceeding chapters of this dissertation.

3.4.3 Implications

The present study demonstrates a systematic increase in SCC susceptibility for AM 17-4PH relative to wrought 17-4PH with a similar yield strength. Leveraging established mechanistic frameworks, the increased susceptibility of the AM material was speculated to arise from five potential factors: (1) differences in grain boundary impurity content, (2) widespread porosity, (3) the presence and/or modification of secondary phase particles, (4) differences in hydrogen-metal interactions between the AM and wrought material, and (5) differences in crack-tip deformation behavior for AM and wrought materials. The latter two contributions will be addressed in future studies, but additional commentary can be provided on the other three possibilities. First, regarding the oxide inclusions, the elemental analysis indicates an order of magnitude increase in the O content of the AM material relative to the wrought condition, driven by the high O content of the powder. While the exact contribution of the observed oxide inclusions remains unclear, reducing the O content would minimize such inclusions. Second, grain boundary impurity segregation and Cr_{23}C_6 precipitation are likely related to the slow cooling profile associated with the HIP treatment. Given that this cooling rate was an unspecified standard practice for the HIP supplier, the above results and discussion indicate that it would be worthwhile to evaluate the effect of post-HIP cooling rate on SCC behavior in AM 17-4PH steel. In addition to enabling the development of a SCC-resistant HIP protocol, the results of such a study could be used to justify the addition of a specific HIP protocol for 17-4PH in ASTM F3301¹²⁷. Lastly, it is clear from microscopy of the metallurgical cross-sections (Fig. 14) and fracture surfaces (Fig. 21) that the sub- μm porosity was resistant to the HIP treatment. As such, it is expected that such small-scale porosity will be present in an AM final component. Given the challenges associated with detecting sub- μm pores using conventional techniques, additional efforts are needed to rigorously understand the influence of these small pores on the SCC susceptibility of 17-4PH. If the

proposed deleterious role of small pores on SCC resistance is confirmed, then changes in HIP protocol should be studied with a focus on consistently eliminating or minimizing this sub- μm sized porosity.

3.5 Conclusions

Fracture mechanics-based experiments were performed to reveal the relative susceptibilities of wrought and AM forms of 17-4PH to stress corrosion cracking in 0.6M NaCl as a function of applied electrochemical potential. Intrinsic features leading to differences between the two material forms were evaluated using a combination of compositional, fractographic, and microstructural analysis. The following are key conclusions from this comparative study.

- AM 17-4PH has similar SCC performance to wrought at open circuit and anodic potentials in 0.6M NaCl. Under rising stress intensity loading ($2 \text{ MPa}\sqrt{\text{m/h}}$), both AM and wrought underwent crack tip blunting with no apparent SCC crack extension at $E_{app} \sim E_{OCP}$. At anodic potentials ($E_{app} > E_{OCP}$), similar blunting was observed until excessively anodic potentials led to general dissolution in both AM and wrought.
- At cathodic applied potentials ($E_{app} < E_{OCP}$), AM 17-4PH consistently underperformed the wrought 17-4PH SCC performance. A combination of rising ($dK/dt = 2 \text{ MPa}\sqrt{\text{m/h}}$) and constant ($dK/dt = 0 \text{ MPa}\sqrt{\text{m/h}}$) stress intensity testing showed that AM 17-4PH cracked up to 5-fold faster with E_{app} susceptibility ranges 200-400 mV wider than wrought depending on heat treatment.
- Increased SCC susceptibility in AM 17-4PH was linked to fracture dominated by intergranular cracking morphologies. High magnification examination of the AM intergranular facets showed evidence of toughness-reducing secondary particles and pores not present in wrought 17-4PH. Based on analysis of 17-4PH phase diagrams, bulk composition analysis results, and the heat treatment protocols used in this study, the particles are likely a combination of Cr_{23}C_6 carbides and oxide inclusions.
- Potential factors responsible for the increased susceptibility of the AM 17-4PH were informed by a decohesion-based model for hydrogen-assisted cracking and include: (1) differences in grain boundary impurity content, (2) widespread porosity, (3) the presence and/or modification of secondary phase particles, (4) differences in hydrogen-metal interactions between the AM and wrought material, and (5) differences in crack-tip deformation behavior for AM and wrought materials.
- It is likely that the (1) significant O content (600 wppm) in the powder, (2) slow cooling (310°C/h) during the HIP process, and (3) argon gas used as a powder atomizing media and as a build atmosphere resulting in widespread sub- μm porosity all negatively affected the SCC resistance of AM 17-4PH.

Such initial insights can be leveraged to inform targeted processing modifications to potentially improve the SCC behavior of AM 17-4PH.

3.6 Acknowledgements

This research was financially supported by the Office of Naval Research under Grant No. N00014-18-1-2427 with Dr. Airan Perez as the Scientific Officer. Helpful discussions with Prof. John Scully and Ms. Lauren Singer at the University of Virginia are gratefully acknowledged. This chapter was adapted from a manuscript coauthored by Trevor Shoemaker, Zachary Harris, and James Burns. T.S. performed the SCC testing, fractography, and SEM microscopy. Z.H. performed the tension testing and EBSD microscopy. T.S. and Z.H. wrote the manuscript. J.B. supervised the study. All authors interpreted the results, reviewed, and revised the manuscript.

3.7 References

1. Coseglio, M. S. D. R. Sulphide stress cracking of 17-4 PH for applications in oilfield components. *Mater. Sci. Technol.* **33**, 1863–1878 (2017).
2. Tavares, S. S. M., Corte, J. S. & Pardal, J. M. Failure of 17-4PH stainless steel components in offshore platforms. in *Handbook of Materials Failure Analysis with Case Studies from the Oil and Gas Industry* (eds. Aliofkhaezrai, M. & Salam Hamdy Makhlof, A.) **74**, 353–370 (Elsevier, 2016).
3. Zhang, Y. *et al.* Additive Manufacturing of Metallic Materials: A Review. *J. Mater. Eng. Perform.* **27**, 1–13 (2018).
4. Meredith, S. D., Zuback, J. S., Keist, J. S. & Palmer, T. A. Impact of composition on the heat treatment response of additively manufactured 17–4 PH grade stainless steel. *Mater. Sci. Eng. A* **738**, 44–56 (2018).
5. Vunnam, S., Saboo, A., Sudbrack, C. & Starr, T. L. Effect of powder chemical composition on the as-built microstructure of 17-4 PH stainless steel processed by selective laser melting. *Addit. Manuf.* **30**, 100876 (2019).
6. LeBrun, T., Nakamoto, T., Horikawa, K. & Kobayashi, H. Effect of retained austenite on subsequent thermal processing and resultant mechanical properties of selective laser melted 17-4 PH stainless steel. *Mater. Des.* **81**, 44–53 (2015).
7. Boyce, B. L. *et al.* Extreme-Value Statistics Reveal Rare Failure-Critical Defects in Additive Manufacturing. *Adv. Eng. Mater.* **19**, (2017).
8. LeBrun, T., Tanigaki, K., Horikawa, K. & Kobayashi, H. Strain rate sensitivity and mechanical

- anisotropy of selective laser melted 17-4 PH stainless steel. *Mech. Eng. J.* **1**, SMM0049 (2014).
9. Arisoy, C. F., Başman, G. & Şeşen, M. K. Failure of a 17-4 PH stainless steel sailboat propeller shaft. *Eng. Fail. Anal.* **10**, 711–717 (2003).
 10. Raymond, L. & Kendall, E. G. Failure of 17-4 PH Stainless Steel Bolts on a Titan Space Launch Vehicle. in *ASM Failure Analysis Case Histories: Mechanical and Machine Components* (ASM International, 2019).
 11. Stanley, J. K. *Stress Corrosion Cracking and Hydrogen Embrittlement of High-Strength Fasteners*. (1973).
 12. Jiang, T., Zhong, J., Zhang, X., Wang, W. & Guan, K. Hydrogen embrittlement induced fracture of 17-4 PH stainless steel valve stem. *Eng. Fail. Anal.* **113**, 104576 (2020).
 13. Tavares, S. S. M., Pardal, J. M., Menezes, L., Menezes, C. A. B. & D'Ávila, C. Failure analysis of PSV springs of 17-4PH stainless steel. *Eng. Fail. Anal.* **16**, 1757–1764 (2009).
 14. Thompson, R. M., Kohut, G. B., Canfield, D. R. & Bass, W. R. Sulfide stress cracking failures of 12Cr and 17-4PH stainless steel wellhead equipment. *Corrosion* **47**, 216–220 (1991).
 15. Fantechi, F. & Innocenti, M. Chloride stress corrosion cracking of precipitation hardening S.S. impellers in centrifugal compressor. Laboratory investigations and corrective actions. *Eng. Fail. Anal.* **8**, 477–492 (2001).
 16. Truman, J. E. Stress-corrosion cracking of martensitic and ferritic stainless steels. *Int. Met. Rev.* **26**, 301–349 (1981).
 17. Liu, M. *et al.* Experimental investigation of failure behavior of the cracked 17-4PH steel blades in a top gas energy recovery turbine. *Eng. Fail. Anal.* **105**, 545–554 (2019).
 18. Salinas-Bravo, V. M. & Gonzalez-Rodriguez, J. G. Stress corrosion cracking susceptibility of 17-4PH turbine steel in aqueous environments. *Br. Corros. J.* **30**, 77–79 (1995).
 19. Carter, C. S., Farwick, D. G., Ross, A. M. & Uchida, J. M. Stress Corrosion Properties of High Strength Precipitation Hardening Stainless Steels. *Corrosion* **27**, 190–197 (1971).
 20. Prasad Rao, K. & Raja, K. S. Environmental cracking behaviour of the Precipitation hardened stainless steel, 17-4 PH, under applied potential. *Mater. Corros.* **46**, 370–375 (1995).
 21. Fujii, C. Stress-Corrosion Cracking Properties of 17-4 PH Steel. in *Stress Corrosion—New Approaches* 213–225 (ASTM International, 1976). doi:10.1520/STP28681S
 22. Ghosh, R. *et al.* Effect of Heat Treatment Anomaly on the Stress Corrosion Cracking Behavior of

- 17-4 PH Martensitic Stainless Steel. *Trans. Indian Inst. Met.* **72**, 1503–1506 (2019).
23. Gerhold, W. F. & Escalante, E. *NBSIR 74-560: Stress corrosion behavior of selected types of stainless steels and titanium alloys in a marine environment.* (1974).
 24. Shahinian, P. & Judy, R. Stress-Corrosion Crack Growth in Surface-Cracked Panels of High-Strength Steels. *Stress Corros. Approaches, ASTM STP 610* 128–142 (1976). doi:10.1520/stp28675s
 25. Judy, R. W., Fujii, C. T. & Goode, R. J. *NRL Report 7639 Properties of 17-4PH Steel.* (1973).
 26. Raja, K. S. & Prasad Rao, K. On the hardness criterion for stress corrosion cracking resistance of 17-4PH stainless steel. *J. Mater. Sci. Lett.* **12**, 963–966 (1993).
 27. Karaminezhaad, M., Sharafi, S. & Dalili, K. Effect of molybdenum on SCC of 17-4PH stainless steel under different aging conditions in chloride solutions. *J. Mater. Sci.* **41**, 3329–3333 (2006).
 28. Humphries, T. S. & Nelson, E. E. *NASA TM-78257 Stress Corrosion Cracking Evaluation of Martensitic Precipitation Hardening Stainless Steel.* (1980).
 29. Yadollahi, A. *et al.* Effects of crack orientation and heat treatment on fatigue-crack-growth behavior of AM 17-4 PH stainless steel. *Eng. Fract. Mech.* **226**, 106874 (2020).
 30. Lou, X., Andresen, P. L. & Rebak, R. B. Oxide inclusions in laser additive manufactured stainless steel and their effects on impact toughness and stress corrosion cracking behavior. *J. Nucl. Mater.* **499**, 182–190 (2018).
 31. Yan, F., Xiong, W., Faierson, E. & Olson, G. B. Characterization of nano-scale oxides in austenitic stainless steel processed by powder bed fusion. *Scr. Mater.* **155**, 104–108 (2018).
 32. Hsu, T. H. *et al.* Microstructure and property of a selective laser melting process induced oxide dispersion strengthened 17-4 PH stainless steel. *J. Alloys Compd.* **803**, 30–41 (2019).
 33. Shi, Q., Qin, F., Li, K., Liu, X. & Zhou, G. Effect of hot isostatic pressing on the microstructure and mechanical properties of 17-4PH stainless steel parts fabricated by selective laser melting. *Mater. Sci. Eng. A* **810**, 141035 (2021).
 34. Alnajjar, M., Christien, F., Bosch, C. & Wolski, K. A comparative study of microstructure and hydrogen embrittlement of selective laser melted and wrought 17–4 PH stainless steel. *Mater. Sci. Eng. A* **785**, 139363 (2020).
 35. Romano, S., Nezhadfar, P. D., Shamsaei, N., Seifi, M. & Beretta, S. High cycle fatigue behavior and life prediction for additively manufactured 17-4 PH stainless steel: Effect of sub-surface porosity and surface roughness. *Theor. Appl. Fract. Mech.* **106**, (2020).

36. Nezhadfar, P. D. *et al.* Improved high cycle fatigue performance of additively manufactured 17-4 PH stainless steel via in-process refining micro-/defect-structure. *Addit. Manuf.* **36**, 101604 (2020).
37. Mower, T. M. & Long, M. J. Mechanical behavior of additive manufactured, powder-bed laser-fused materials. *Mater. Sci. Eng. A* **651**, 198–213 (2016).
38. Akita, M., Uematsu, Y., Kakiuchi, T., Nakajima, M. & Kawaguchi, R. Defect-dominated fatigue behavior in type 630 stainless steel fabricated by selective laser melting. *Mater. Sci. Eng. A* **666**, 19–26 (2016).
39. Schaller, R. F., Taylor, J. M., Rodelas, J. & Schindelholz, E. J. Corrosion Properties of Powder Bed Fusion Additively Manufactured Stainless Steels. *Corrosion* **73**, 796–807 (2017).
40. Irrinki, H. *et al.* Effects of powder characteristics and processing conditions on the corrosion performance of 17-4 PH stainless steel fabricated by laser-powder bed fusion. *Prog. Addit. Manuf.* **3**, 39–49 (2018).
41. Stoudt, M. R., Ricker, R. E., Lass, E. A. & Levine, L. E. Influence of Postbuild Microstructure on the Electrochemical Behavior of Additively Manufactured 17-4 PH Stainless Steel. *Jom* **69**, 506–515 (2017).
42. ASTM International. ASTM E399-19 Standard Test Method for Linear-Elastic Plane-Strain Fracture Toughness K_{Ic} of Metallic Materials. (2019).
43. Donald, J. K. & Ruschau, J. Direct Current Potential Difference Fatigue Crack Measurement Techniques. *Fatigue Crack Meas. Tech. Appl.* 11–38 (1991).
44. Tada, H., Paris, P. C. & Irwin, G. R. *The Stress Analysis of Cracks Handbook, Third Edition.* (ASME, 2000). doi:10.1115/1.801535
45. Kumar, V., German, M. D. & Shih, C. F. EPRI NP-1931 Engineering approach for elastic-plastic fracture analysis. (1981).
46. Harris, Z. D., Dubas, E. M., Popemack, A. S., Somerday, B. P. & Burns, J. T. Elucidating the loading rate dependence of hydrogen environment-assisted cracking in a Ni-Cu superalloy. *Theor. Appl. Fract. Mech.* **111**, 102846 (2021).
47. McAdam, D. J. J. & Geil, G. W. Rate of Oxidation of Steels as Determined from Interference Colors of Oxide Films. *J. Res. Natl. Bur. Stand. (1934)*. **23**, 63–124 (1939).
48. Johnson, H. H. Calibrating the Electric Potential Method for Studying Slow Crack Growth. *Mater. Res. Stand.* **5**, 442–445 (1965).

49. Axelsson, N. & Baric, J. Improved data regression methods for crack growth characterization. (Chalmers University of Technology, 2016).
50. ASTM International. ASTM A693-16 Standard Specification for Precipitation-Hardening Stainless and Heat-Resisting Steel Plate, Sheet, and Strip. (2016).
51. Bhambroo, R., Roychowdhury, S., Kain, V. & Raja, V. S. Effect of reverted austenite on mechanical properties of precipitation hardenable 17-4 stainless steel. *Mater. Sci. Eng. A* **568**, 127–133 (2013).
52. Wang, Z., Li, H., Shen, Q., Liu, W. & Wang, Z. Nano-precipitates evolution and their effects on mechanical properties of 17-4 precipitation-hardening stainless steel. *Acta Mater.* **156**, 158–171 (2018).
53. Antony, K. C. Aging Reactions in Precipitation Hardenable Stainless Steel. *J. Met.* 922–927 (1963).
54. Tavares, S. S. M., da Silva, F. J., Scandian, C., da Silva, G. F. & de Abreu, H. F. G. Microstructure and intergranular corrosion resistance of UNS S17400 (17-4PH) stainless steel. *Corros. Sci.* **52**, 3835–3839 (2010).
55. Cheruvathur, S., Lass, E. A. & Campbell, C. E. Additive Manufacturing of 17-4 PH Stainless Steel: Post-processing Heat Treatment to Achieve Uniform Reproducible Microstructure. *JOM* **68**, 930–942 (2016).
56. Gangloff, R. P. Hydrogen Assisted Cracking of High Strength Alloys. in *Comprehensive Structural Integrity* (eds. Milne, I., Ritchie, R. O. & Karimhaloo, B.) (Elsevier Science, 2003).
57. Crane, C. B. & Gangloff, R. P. Stress corrosion cracking of Al-Mg alloy 5083 sensitized at low temperature. *Corrosion* **72**, 221–241 (2016).
58. Harris, Z. D. & Burns, J. T. The Effect of Loading Rate on the Environment-Assisted Cracking Behavior of AA7075-T651 in Aqueous NaCl Solution. *Corros. Mater. Degrad.* **2**, 360–375 (2021).
59. Lee, Y. & Gangloff, R. P. Measurement and modeling of hydrogen environment-assisted cracking of ultra-high-strength steel. *Metall. Mater. Trans. A Phys. Metall. Mater. Sci.* **38 A**, 2174–2190 (2007).
60. Pioszak, G. L. & Gangloff, R. P. Hydrogen Environment Assisted Cracking of Modern Ultra-High Strength Martensitic Steels. *Metall. Mater. Trans. A Phys. Metall. Mater. Sci.* **48**, 4025–4045 (2017).
61. Harris, Z. D. *et al.* The Effect of Microstructural Variation on the Hydrogen Environment-Assisted Cracking of Monel K-500. *Metall. Mater. Trans. A Phys. Metall. Mater. Sci.* **47**, 3488–3510 (2016).

62. Burns, J. T., Harris, Z. D., Dolph, J. D. & Gangloff, R. P. Measurement and Modeling of Hydrogen Environment Assisted Cracking in a Ni-Cu-Al-Ti Superalloy. *Metall. Mater. Trans. A* **47**, 990–997 (2016).
63. Harris, Z. D. & Burns, J. T. The effect of isothermal heat treatment on hydrogen environment-assisted cracking susceptibility in Monel K-500. *Mater. Sci. Eng. A* **764**, 138249 (2019).
64. Harris, Z. D., Guiseva, K., Scully, J. R. & Burns, J. T. On the hydrogen environment-assisted cracking resistance of a compositionally complex Co–Ni–Cr–Fe–Mo–Ti alloy. *Mater. Sci. Eng. A* **802**, 140601 (2020).
65. Gangloff, R. P., Ha, H. M., Burns, J. T. & Scully, J. R. Measurement and Modeling of Hydrogen Environment-Assisted Cracking in Monel K-500. *Metall. Mater. Trans. A* **45**, 3814–3834 (2014).
66. Steiner, P., Harris, Z., Vicente Moraes, C., Kelly, R. & Burns, J. Investigation of IG-SCC growth kinetics in Al-Mg alloys in thin film environments. *Corrosion* **77**, 838–852 (2021).
67. Tarnowski, K. M., Dean, D. W., Nikbin, K. M. & Davies, C. M. Predicting the influence of strain on crack length measurements performed using the potential drop method. *Eng. Fract. Mech.* **182**, 635–657 (2017).
68. Rhodes, P. R. Environment-Assisted Cracking of Corrosion-Resistant Alloys in Oil and Gas Production Environments : A Review. *Corrosion* **57**, 923–966 (2001).
69. Srinath, J. *et al.* Metallurgical Analysis of a Failed 17-4 PH Stainless Steel Pyro Bolt Used in Launch Vehicle Separation Systems. *Mater. Perform. Charact.* **4**, MPC20140063 (2015).
70. Humphries, T. S. & Nelson, E. E. *NASA-TM-X-53910 Stress Corrosion Cracking Evaluation of Several Precipitation Hardening Stainless Steels.* (1969).
71. Kehler, B. A. & Scully, J. R. Predicting the effect of applied potential on crack tip hydrogen concentration in low-alloy martensitic steels (Reprinted from Proceedings of the CORROSION/2007 research topical symposium ‘Advances in Environmentally Assisted Cracking’, 2007). *Corrosion* **64**, 465–477 (2008).
72. Robertson, I. M. *et al.* Hydrogen Embrittlement Understood. *Metall. Mater. Trans. B* **46B**, 1085–1103 (2015).
73. Djukic, M. B., Bakic, G. M., Sijacki Zeravic, V., Sedmak, A. & Rajicic, B. The synergistic action and interplay of hydrogen embrittlement mechanisms in steels and iron: Localized plasticity and decohesion. *Eng. Fract. Mech.* **216**, 106528 (2019).

74. Gerberich, W. W. Modelling hydrogen induced damage mechanisms in metals. in *Gaseous Hydrogen Embrittlement of Materials in Energy Technologies* (eds. Gangloff, R. P. & Somerday, B. P.) 209–246 (Woodhead Publishing, 2012).
75. Tehrani, A. & Curtin, W. A. The role of atomistic simulations in probing hydrogen effects on plasticity and embrittlement in metals. *Eng. Fract. Mech.* **216**, 106502 (2019).
76. Harris, Z. D. *et al.* Elucidating the contribution of mobile hydrogen-deformation interactions to hydrogen-induced intergranular cracking in polycrystalline nickel. *Acta Mater.* **158**, 180–192 (2018).
77. Martinez-Paneda, E., Niordson, C. F. & Gangloff, R. P. Strain gradient plasticity-based modeling of hydrogen environment assisted cracking. *Acta Mater.* **117**, 321–332 (2016).
78. Ritchie, R. O., Knott, J. F. & Rice, J. R. On the Relationship Between Critical Tensile Stress and Fracture Toughness in Mild Steel. *J. Mech. Phys. Solids* **21**, 395–410 (1973).
79. Ritchie, R. O. & Thompson, A. W. On Macroscopic and Microscopic Analyses for Crack Initiation and Crack Growth Toughness in Ductile Alloys. *Metall. Trans. A* **16**, 233–248 (1985).
80. Dadfarnia, M. *et al.* On modeling hydrogen-induced crack propagation under sustained load. *Jom* **66**, 1390–1398 (2014).
81. McMahon, M. E., Steiner, P. J., Lass, A. B. & Burns, J. T. The effect of loading orientation on the stress corrosion cracking of Al-Mg alloys. *Corrosion* **73**, 713–723 (2017).
82. McMahon, M. E., Steiner, P. J., Lass, A. B. & Burns, J. T. The effect of temper and composition on the stress corrosion cracking of Al-Mg alloys. *Corrosion* **73**, 347–361 (2017).
83. Pioszak, G. L. & Gangloff, R. P. Hydrogen Environment Assisted Cracking of a Modern Ultra-High Strength Martensitic Stainless Steel. *Corrosion* **73**, 1132–1156 (2017).
84. Gerberich, W. W., Oriani, R. A., Lii, M.-J., Chen, X. & Foecke, T. The necessity of both plasticity and brittleness in the fracture thresholds of iron. *Philos. Mag. A* **63**, 363–376 (1991).
85. O'Brien, C. J. & Foiles, S. M. Hydrogen segregation to inclined twin grain boundaries in nickel. *Philos. Mag.* **96**, 2808–2828 (2016).
86. Tehrani, A. & Curtin, W. A. Atomistic study of hydrogen embrittlement of grain boundaries in nickel: I. Fracture. *J. Mech. Phys. Solids* **101**, 150–165 (2017).
87. Shi, R. *et al.* Quantitative investigation on deep hydrogen trapping in tempered martensitic steel. *J. Alloys Compd.* **854**, 157218 (2021).

88. Briant, C. L. & Banerji, S. K. Intergranular failure in steel: the role of grain-boundary composition. *Int. Met. Rev.* **23**, 164–199 (1978).
89. Yoshino, K. & McMahon, C. J. The cooperative relation between temper embrittlement and hydrogen embrittlement in a high strength steel. *Metall. Trans.* **5**, 363–370 (1974).
90. Jun, W. *et al.* The effect of long-term isothermal aging on dynamic fracture toughness of type 17-4 PH SS at 350°C. *Mater. Trans.* **46**, 846–851 (2005).
91. Wang, J. *et al.* The microstructure evolution of type 17-4PH stainless steel during long-term aging at 350 °C. *Nucl. Eng. Des.* **236**, 2531–2536 (2006).
92. Yrieix, B. & Guttman, M. Aging between 300 and 450°C of wrought martensitic 13–17 wt-%Cr stainless steels. *Mater. Sci. Technol.* **9**, 125–137 (1993).
93. McMahon, C. J. Hydrogen-induced intergranular fracture of steels. *Eng. Fract. Mech.* **68**, 773–788 (2001).
94. Misra, R. D. K., Prasad, C. ., Balasubramaniam, T. V. & Rao, P. R. Effect of phosphorus segregation on impact toughness variation of 17-4 precipitation hardened stainless steel. *Scr. Metall.* **20**, 713–716 (1986).
95. Garrison, W. M. & Moody, N. R. Hydrogen embrittlement of high strength steels. in *Gaseous hydrogen embrittlement of materials in energy technologies Volume 1* (eds. Gangloff, R. P. & Somerday, B. P.) 421–492 (Woodhead Publishing, 2012).
96. Mulford, R. A. Grain boundary segregation in Ni and binary Ni alloys doped with sulfur. *Metall. Trans. A* **14**, 865–870 (1983).
97. Karlsson, L. & Norden, H. Non-Equilibrium Grain Boundary Segregation of Boron in Austenitic Stainless Steel. *Acta Metall.* **36**, 35–48 (1988).
98. Lass, E. A., Zhang, F. A. N. & Campbell, C. E. Nitrogen Effects in Additively Manufactured Martensitic Stainless Steels : Conventional Thermal Processing and Comparison with Wrought. *Metall. Mater. Trans. A* **51**, 2318–2332 (2020).
99. Weaver, J. S. *et al.* The effects of particle size distribution on the rheological properties of the powder and the mechanical properties of additively manufactured 17-4 PH stainless steel. *Addit. Manuf.* **39**, 101851 (2021).
100. Concli, F. *et al.* Bending Fatigue Behavior of 17-4 PH Gears Produced by Additive Manufacturing. *Appl. Sci.* **11**, 3019 (2021).

101. Zai, L. *et al.* Laser powder bed fusion of precipitation-hardened martensitic stainless steels: A review. *Metals (Basel)*. **10**, 1–25 (2020).
102. Dobson, S., Vunnam, S., Frankel, D., Sudbrack, C. & Starr, T. Powder variation and mechanical properties for SLM 17-4 PH stainless steel. *Solid Free. Fabr. 2019 Proc. 30th Annu. Int. Solid Free. Fabr. Symp. - An Addit. Manuf. Conf. SFF 2019* 478–493 (2019).
103. Stephens, R. ., Horn, J. J., Poland, D. D. & Safer, E. A. INFLUENCE OF DENSITY AND POROSITY SIZE AND SHAPE ON FATIGUE AND FRACTURE TOUGHNESS OF HIGH STRENGTH FL4405 P/M STEEL. in *Effects of Product Quality and Design Criteria on Structural Integrity, ASTM STP 1337* 72–101 (American Society for Testing and Materials, 1998).
104. Sola, A. & Nouri, A. Microstructural porosity in additive manufacturing: The formation and detection of pores in metal parts fabricated by powder bed fusion. *J. Adv. Manuf. Process.* **1**, 1–21 (2019).
105. Needleman, A., Tveergard, V. & Hutchinson, J. W. Void Growth in Plastic Solids. in *Topics in Fracture and Fatigue* (ed. Argon, A. S.) 145–178 (Springer-Verlag, 1992).
106. Gangloff, R. P. H-Enhanced Deformation and Fracture in the Crack Tip Process Zone. in *Material Performance in Hydrogen Environments: Proceedings of the 2016 International Hydrogen Conference* (eds. Somerday, B. P. & Sofronis, P.) 1–35 (ASME Press, 2016).
107. Liang, Y., Ahn, D. C., Sofronis, P., Dodds, R. H. & Bammann, D. Effect of hydrogen trapping on void growth and coalescence in metals and alloys. *Mech. Mater.* **40**, 115–132 (2008).
108. Harris, Z. D., Bhattacharyya, J. J., Ronevich, J. A., Agnew, S. R. & Burns, J. T. The combined effects of hydrogen and aging condition on the deformation and fracture behavior of a precipitation-hardened nickel-base superalloy. *Acta Mater.* **186**, 616–630 (2020).
109. Koyama, M. *et al.* Hydrogen embrittlement associated with strain localization in a precipitation-hardened Fe-Mn-Al-C light weight austenitic steel. *Int. J. Hydrogen Energy* **39**, 4634–4646 (2014).
110. Zhang, Z., Obasis, G., Morana, R. & Preuss, M. Hydrogen assisted crack initiation and propagation in a nickel-based superalloy. *Acta Mater.* **113**, 272–283 (2016).
111. Murayama, M., Katayama, Y. & Hono, K. Microstructural evolution in a 17-4 PH stainless steel after aging at 400 °C. *Metall. Mater. Trans. A* **30**, 345–353 (1999).
112. Lashgari, H. R., Kong, C., Adabifiroozjaei, E. & Li, S. Microstructure, post thermal treatment response, and tribological properties of 3D printed 17-4 PH stainless steel. *Wear* **456–457**, (2020).

113. Alnajjar, M. *et al.* Influence of microstructure and manganese sulfides on corrosion resistance of selective laser melted 17-4 PH stainless steel in acidic chloride medium. *Corros. Sci.* **168**, 108585 (2020).
114. Sun, Y., Hebert, R. J. & Aindow, M. Non-metallic inclusions in 17-4PH stainless steel parts produced by selective laser melting. *Mater. Des.* **140**, 153–162 (2018).
115. Murthy, A., Lekakh, S., Richards, V. & Van Aken, D. Microstructure and Properties of Nb, V and N Modified Cb7Cu-1 (17-4 PH) Steel. *Int. J. Met.* **4**, 59–69 (2010).
116. Lima, A. S., Nascimento, A. M., Abreu, H. F. G. & De Lima-Neto, P. Sensitization evaluation of the austenitic stainless steel AISI 304L, 316L, 321 and 347. *J. Mater. Sci.* **40**, 139–144 (2005).
117. Novak, P., Yuan, R., Somerday, B. P., Sofronis, P. & Ritchie, R. O. A statistical, physical-based, micro-mechanical model of hydrogen-induced intergranular fracture in steel. *J. Mech. Phys. Solids* **58**, 206–226 (2010).
118. Schindelholz, E. J., Melia, M. A. & Rodelas, J. M. Corrosion of Additively Manufactured Stainless Steels—Process, Structure, Performance: A Review. *Corrosion* **77**, 484–503 (2021).
119. Troconis, B. C. R., Harris, Z. D., Ha, H., Burns, J. T. & Scully, J. R. The effect of heat-to-heat variations in metallurgy and hydrogen-metal interactions on the hydrogen embrittlement of Monel K-500. *Mater. Sci. Eng. A* **703**, 533–550 (2017).
120. Bertsch, K. M., Nagao, A., Rankouhi, B., Kuehl, B. & Thoma, D. J. Hydrogen embrittlement of additively manufactured austenitic stainless steel 316 L. *Corros. Sci.* **192**, 109790 (2021).
121. Hu, X., Lach, T. G. & Terrani, K. A. Deuterium permeation and retention in 316L Stainless Steel Manufactured by Laser Powder Bed Fusion. *J. Nucl. Mater.* **548**, 152871 (2021).
122. Lin, J. *et al.* Hydrogen permeation behavior and hydrogen-induced defects in 316L stainless steels manufactured by additive manufacturing. *Mater. Chem. Phys.* **250**, 123038 (2020).
123. Park, J.-M. *et al.* Hydrogen uptake and its influence in selective laser melted austenitic stainless steel: A nanoindentation study. *Scr. Mater.* **194**, 113718 (2021).
124. Harris, Z. D., Thompson, A. W. & Burns, J. T. Multiscale Assessment of Deformation Induced by Hydrogen Environment-Assisted Cracking in a Peak-Aged Ni-Cu Superalloy. *Jom* **72**, 1993–2002 (2020).
125. Birenis, D. *et al.* Interpretation of hydrogen-assisted fatigue crack propagation in BCC iron based on dislocation structure evolution around the crack wake. *Acta Mater.* **156**, 245–253 (2018).

126. Shamsujjoha, M., Agnew, S. R., Fitz-gerald, J. M., Moore, W. R. & Newman, T. A. High Strength and Ductility of Additively Manufactured 316L Stainless Steel Explained. *Metall. Mater. Trans. A* **49**, 3011–3027 (2018).
127. ASTM International. ASTM F3301-18a Additive Manufacturing - Post Processing Methods - Standard Specification for Thermal Post-Processing Metal Parts Made Via Powder Bed Fusion. (2018).

Chapter 4 - Degradation of Additively Manufactured Metal by Sub-Micrometer Porosity

The following chapter is adapted from a manuscript written to be a short article. Primary figures are included within the main text and supplemental figures are grouped at the end of the chapter.

The previous chapter demonstrated that AM 17-4PH is more susceptible to EAC (i.e., elevated SCC growth rates in wider bands of cathodic applied potentials) than its wrought counterpart. Therefore, it is critical to understand how AM-specific microstructural features are impacting EAC susceptibility and leading to this degradation. In the current chapter, sub-micrometer porosity introduced during AM processing is directly linked to increases in the EAC susceptibility of the ‘matched-strength’ AM alloy versus its wrought equivalent. These results reveal that this porosity locally concentrates plastic damage near the crack path, increases the number of favorable fracture pathways, and degrades EAC resistance. This work demonstrates that the size scale of porosity that can deleteriously impact fracture properties is significantly smaller than is currently appreciated or even recognized by AM stakeholders. Moreover, this small-scale porosity is resistant to traditional densification approaches, and thus it will be present in AM components placed into service using current AM approaches. This chapter underscores the need for continued refinement of AM processing to attenuate these deleterious features.

4.1 Introduction

Metal additive manufacturing (AM) involves the layer-by-layer build-up of material to produce complex components^{1,2}. This process has distinct cost³ and logistical⁴ advantages over conventional manufacturing techniques that require a multitude of processing steps to shape wrought metals. However, the AM process creates novel microstructures that are unlike traditional metals due to: (1) inheritance of properties from the AM feedstock material, (2) the physics of melting/re-melting to “build-up” a component, and (3) the wide range of potential processing parameters for the build. These AM-specific microstructures have hindered widespread adoption of this processing approach due to insufficient first-order mechanical properties when compared to wrought incumbents⁵. However, recent advancements in AM technology and material post-processing have resulted in reliable production of AM alloys with strengths on-par with their wrought counterparts⁶. While strength is an essential design parameter, suitable first-order mechanical properties are insufficient to satisfy the range of requirements for incorporating AM metals into structural engineering applications.

For structural components requiring long service-lives, component failure is often governed by higher-order properties; such properties will therefore determine whether a material is acceptable for deployment⁷. For example, environment-assisted cracking (EAC) is a pertinent failure mode in many applications. Yet, studies on EAC behavior of AM alloys remain highly limited⁸ making EAC a critical barrier to the widespread adoption of AM metals for structural applications. Moreover, EAC has a well-established sensitivity to subtle microstructural changes in wrought alloys⁹⁻¹¹. Given the microstructural complexities of AM metals, this absence of EAC data is concerning and strongly motivates investigation into the effect of AM-specific microstructural features on EAC behavior. For example, while porosity is intermittently observed in wrought materials, it is widely observed in AM materials. These pores can arise from the feedstock atomization process, gaseous build atmosphere, metallurgical interactions, and/or process parameter choices. Since these root causes are inherent to the AM process, porosity is a microstructural feature intrinsic to all metallic AM alloys¹².

Depending on their origins, pores in AM metals exhibit a range of sizes and morphologies^{13,14}. Careful processing can reduce the number of large pores¹³, but small-size (less than a few μm) porosity remain common in many AM materials¹⁵⁻¹⁹. These small-size pores are below the detection limits of conventional non-destructive inspection techniques^{16,17} and resistant to densification methods (e.g., hot isostatic pressing; HIP)^{15,20}. Consequently, these pores are difficult to characterize and will be present in AM components. Additionally, given the focus on first-order mechanical properties and processing/microstructural relationships, these small-scale pores are commonly ignored or dismissed in the literature^{13,21}. Such pores may not significantly influence other mechanical properties^{18,22,23}, but the incremental nature of EAC growth and the widespread presence of these fine-scale defects may negatively affect EAC susceptibility of AM materials. However, the potential impact of this small-scale porosity on the EAC behavior of AM materials has yet to be tangibly considered. The proceeding study reports, for the first time, that AM-induced sub-micrometer porosity plays a causal role in increasing the EAC susceptibility of a high-performance AM steel.

4.2 Methods

4.2.1 Materials

Wrought and AM 17-4PH material was processed for study in this chapter as described in Chapters 2 and 3. For the AM material, microstructure and test specimens were evaluated in the HIP+SA+Overage condition. Tension and fracture test specimens were evaluated in the X and X-Y orientations, respectively. Similarly, the SA+Overage wrought material tension and fracture specimens were evaluated in the L and L-T orientation, respectively. Microstructural evaluations were performed using the same processes documented in Chapter 2. FIB trench-milling to verify porosity was performed by first depositing a layer

of Pt to minimize near-surface damage²⁴, then stepped-trench milling with an I-beam accelerating voltage of 30 keV and current of 9.0 nA, and finish milling at 30 keV and 90 pA.

4.2.2 Environment-Assisted Cracking

Fracture mechanics-based testing to characterize environmentally assisted cracking behavior was performed in a similar manner to Chapter 3. The EAC fracture mechanics experiments were performed such that the specimen was maintained at a nominally constant K of 30 MPa $\sqrt{\text{m}}$ as the crack extended; some deviation from this value occurred due to the tortuous nature of the crack path which introduced error in the dcPD system. These errors were accounted for post-experiment using the physical measurements of the crack length. After a minimum of 300 μm of crack extension, each sample was unloaded, cleaned, and either fractured for typical fractographic examination using an SEM or left with cracking intact for crack path analysis. Samples intended for path analysis were ground from the side to expose the centerline crack path for consistency and to assess the region of maximum constraint (i.e., most near to plane strain conditions). After grinding, the crack path was polished in the manner previously described for microstructural evaluation.

4.2.3 Crack Wake Analysis

Microstructure proximate to the crack path (i.e., the crack wake) was imaged and processed using the previously described SEM and EBSD procedures. To ensure proper comparison of wrought and AM fracture morphologies, test stress intensities were mapped onto the crack path to match the mechanical driving force represented by image areas. Porosity adjacent to the crack path was quantified using image analysis techniques and MATLAB algorithms on backscatter electron images. Images were normalized to remove the background microstructure (i.e., converted to black/white based off of a brightness threshold), the crack path was manually painted/identified, and pores were located/sized using a circle finding algorithm. Pore to crack path and pore nearest neighbor distances were calculated with the previously identified spatial locations of the pores and the crack path.

4.3 Results and Discussion

To isolate the role of porosity, AM 17-4PH stainless steel was built using the laser powder bed fusion process (Fig. 23a) and heat-treated post-build to produce a similar base microstructure to a conventional pore-free wrought alloy equivalent (Fig. 23b, Supplemental Fig. 1). The heat-treatment included HIP to maximize density (99.2% of wrought), a solution anneal, and age-hardening; this resulted in an AM alloy with comparable yield strength (1078 MPa) to the wrought material (1059 MPa), see Supplemental Fig. 2. Stress intensity (K)-controlled fracture mechanics (FM)-based measurements of the EAC susceptibility were then performed by immersing FM specimens in 0.6 M NaCl solution while

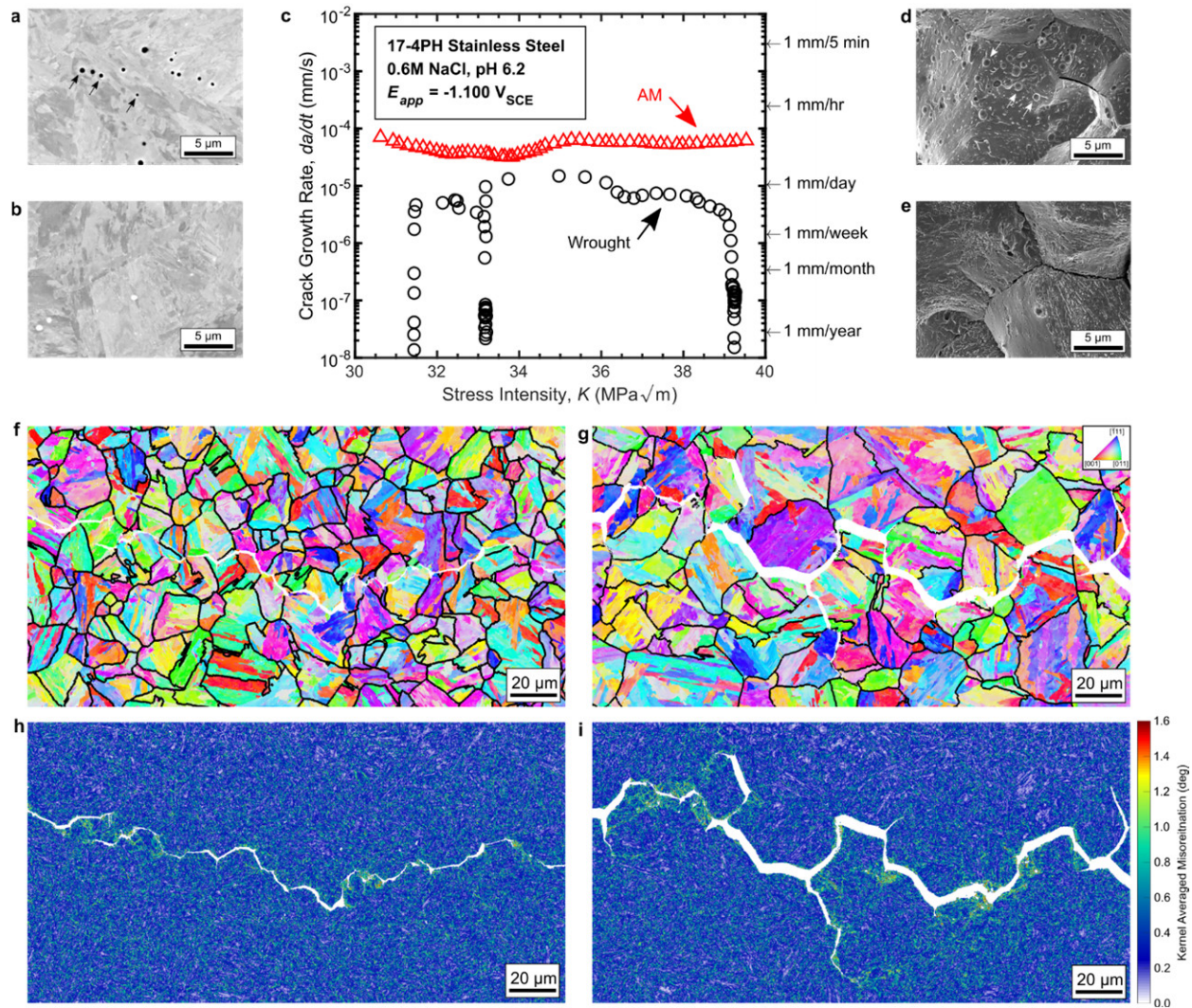


Fig. 23 | **Environment assisted cracking in equivalent wrought and AM alloys.** **a-b**, Microstructure for AM (**a**) and wrought (**b**) 17-4PH stainless steel with arrows highlighting porosity in AM. **c**, Environment assisted crack growth kinetics. **d-e**, Fracture surfaces for AM (**d**) and wrought (**e**) corresponding to the conditions in (**c**) with white arrows highlighting porosity. **f-i**, Crack wake grain structure (**f, g**) and deformation (**h, i**) maps for wrought (**f, h**) and AM (**g, i**). White regions indicate the crack paths with primary growth occurring from left to right. Black outlines and colored regions indicate prior austenite grain boundaries and martensite orientations, respectively, in the grain structure maps.

subjected to cathodic polarization. This resulted in a hydrogen (H)-generating environment and crack growth that was actively monitored (Fig. 23c, Supplemental Fig. 3).

Despite similar microstructure and mechanical properties, Fig. 23c demonstrates that the EAC growth rates for AM 17-4PH are consistently faster (~7-fold higher on average) than those measured for the wrought material. Additionally, the wrought alloy exhibited periods of decelerated growth, indicated by the intermittent drops in growth rate in Fig. 23c. Such decreases were not observed in the AM material and highlight a further discrepancy between the two materials. While differences in EAC kinetics were

observed, the AM (Fig. 23d) and wrought (Fig. 23e) material both exhibit rock candy-like fracture morphologies consistent with cracking along prior austenite grain boundaries (PAGBs)²⁵. Close examination of the AM fracture surface revealed numerous small (<1 μm), dimple-like features (white arrows, Fig. 23d) on the intergranular facets. These features are identified as pores based on their comparable size to the porosity observed in the AM bulk microstructure (Fig. 23a), their absence from the fracture surface of the wrought material (Fig. 23e), and the results of a cross-sectional FIB analysis (Supplemental Fig. 4).

To elucidate the microstructural factors responsible for the difference in AM and wrought EAC behavior, the grain structure and plastic deformation proximate to the crack path in each material were interrogated *via* electron backscatter diffraction (EBSD). Consistent with the intergranular fracture morphologies in Fig. 23d-e, the inverse pole figure (IPF) maps for the wrought (Fig. 23f) and AM material (Fig. 23g) indicate crack propagation primarily occurred along PAGBs. These maps also indicate an increase in the extent of crack branching in the AM material (Fig. 23g). Kernel average misorientation (KAM) maps for the wrought (Fig. 23h) and AM (Fig. 23i) specimens revealed discrete areas of increased KAM (which correlates with extent of plastic deformation) proximate to the crack path for both conditions. These discrete areas were consistently broader, exhibited moderately higher KAM values, and extended larger distances from the crack path in the AM material. Such data are consistent with the observed increase in EAC susceptibility for the AM material, but identifying the causal factors driving this enhanced cracking requires higher fidelity characterization.

High-magnification backscatter electron imaging (BEI) provided more direct insights into the microstructural basis for the increased EAC susceptibility of the AM material. Several distinct interactions between the crack and proximate porosity were revealed. For example, Fig. 24a shows evidence of the significant expansion of pores located adjacent to the crack path, with some pores exhibiting 2 to 3-fold increases in diameter over the bulk porosity. Moreover, as shown in Fig. 24b, the primary crack path appears to preferentially extend from pore-to-pore (intersections noted by the black arrows). The ability of these sub-micrometer pores to serve as crack initiation sites is clearly shown in Fig. 24c, while the multiple instances of cracks branching towards and through these pores (Fig. 24d-e) suggests that the small-scale porosity contributes to the increased crack branching observed in the AM material. Finally, the active crack tip (Fig. 24f) exhibited multiple of the above interactions, including pore intersection (upper branch) and preferential extension towards a pore (lower branch).

The microscopy-based evaluations in Fig. 24 provide direct evidence of interactions between an EAC-driven crack and the sub-micrometer porosity, but do not indicate how this small-scale porosity enhances EAC susceptibility. To understand the interactions between the growing crack and porosity, two

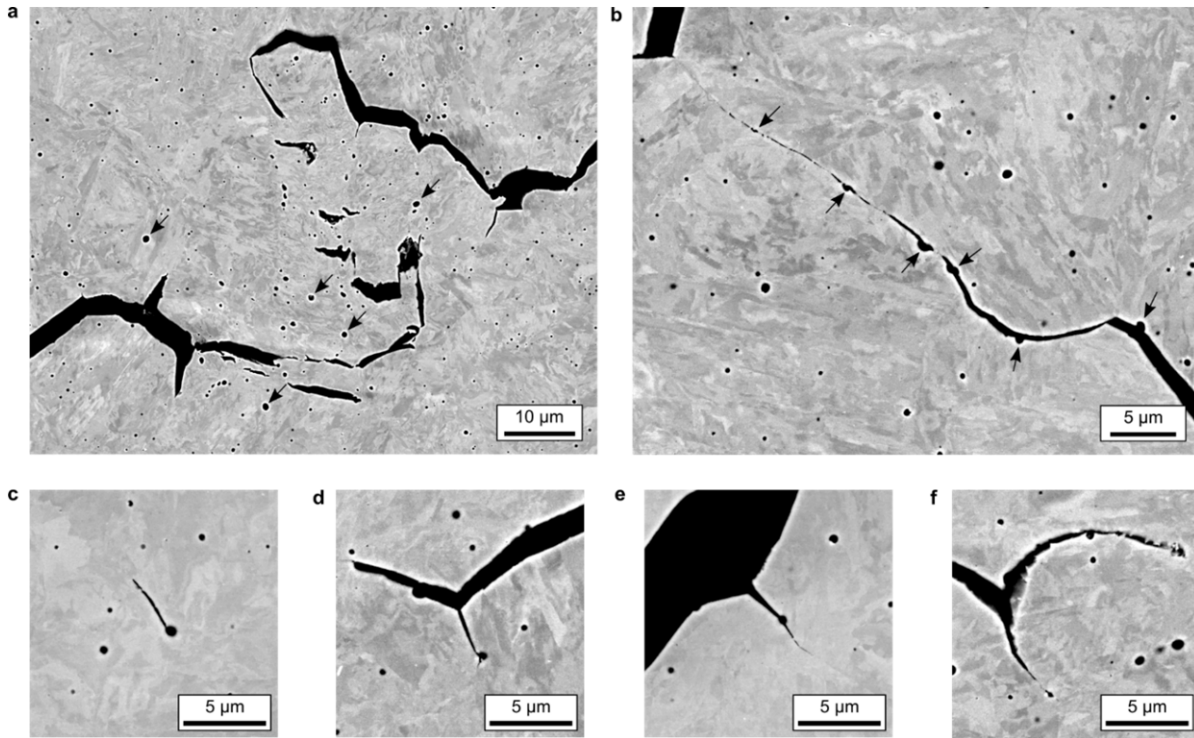


Fig. 24 | **Environment assisted crack path-pore morphological interactions in AM.** **a**, Crack wake with large pores adjacent to the crack path highlighted. **b**, Crack path with split pores along the path highlighted. **c**, Secondary crack extending from a pore. **d**, Crack branch extending from the primary crack path to a pore. **e**, Crack branch extending through a pore. **f**, The primary, active crack tip halted at the end of a test.

additional evaluations were performed. First, wide-area, high-resolution scanning electron microscopy and image analysis was executed to quantify the size and spatial distribution of $\sim 15,000$ pores proximate to the crack path. Fig. 25a shows a subsection of the analysis region and clearly demonstrates that a gradient in pore size exists as a function of distance from the crack path. Specifically, the number of ‘large’ pores appears to increase as the crack path is approached. This qualitative assessment is confirmed when the pore size versus distance from the crack path is quantitatively analyzed. Specifically, while the box-whisker plots in Fig. 25b show that the interquartile ranges and median pore size ($0.28 \mu\text{m}$) remains relatively constant with distance from the crack path, the fraction of large pores ($>0.6 \mu\text{m}$) increases within $20 \mu\text{m}$ of the crack path (Fig. 25c). Notably, not all of the pores within this $20 \mu\text{m}$ bound are enlarged; rather, select pores are expanding in an apparently stochastic manner (Fig. 25a). There are two possible explanations for this behavior. First, a fraction of the identified “pores” may be oxide-inclusions^{26,27} of a similar size and morphology to the pores (Supplemental Fig. 4); such inclusions would be more resistant to expansion relative to pores. Second, it is expected that sub-micrometer pore growth near a crack will be a complex function of several variables (grain orientation, crack tortuosity, proximity to other microstructural features, etc.). As such, it is not surprising that the present mesoscale analysis indicates seemingly stochastic growth of only a sub-set of the pores. Regardless, the current data confirm that a statistically significant number of

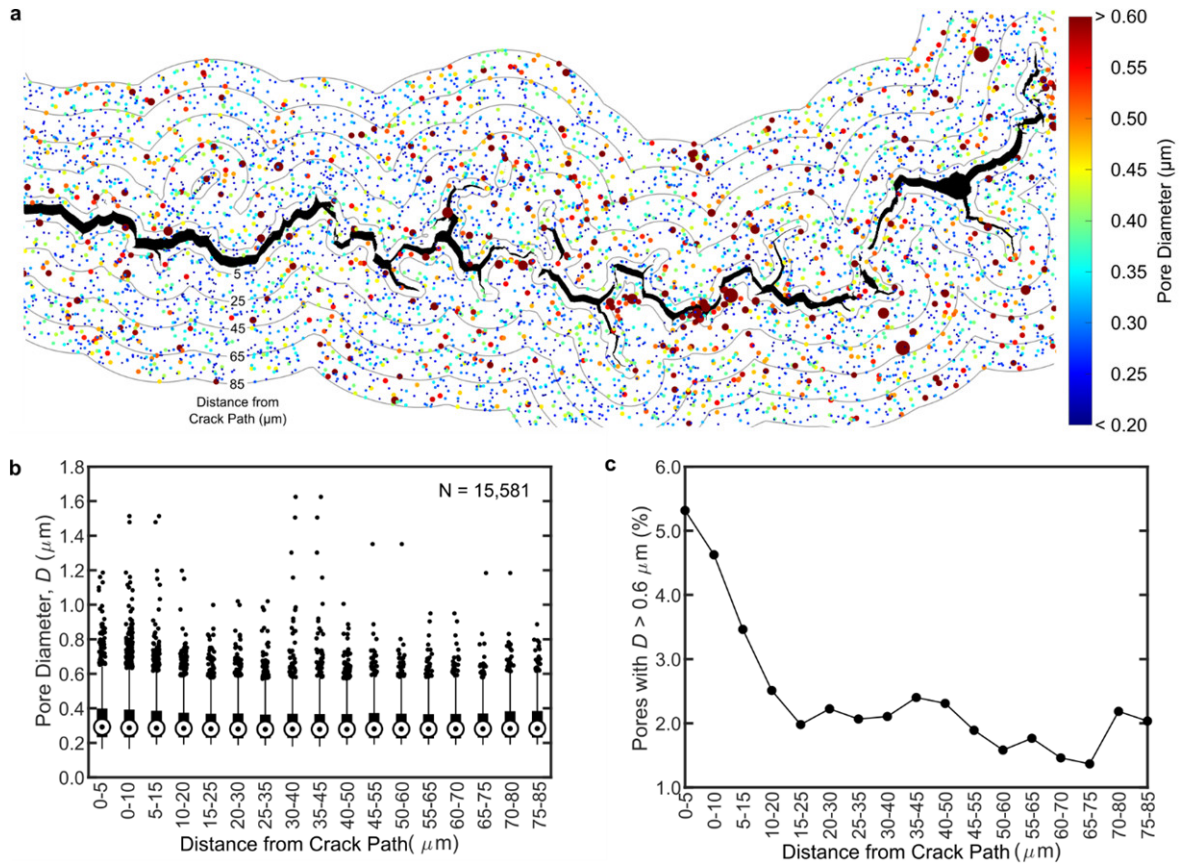


Fig. 25 | **AM pore morphology proximate to an environment assisted crack path.** **a**, Map of pores (colored by diameter) adjacent to the crack path (black). Note that the pores are replaced by circles and magnified 7x in size for clarity. **b**, Box and whisker plot distributions of pore diameters as a function of distance from the crack path. **c**, Percentage of large outlier pores as a function of distance from the crack path.

sub-micrometer circular-features, likely pores, are undergoing plastic expansion, localizing damage, and potentially reducing EAC-resistance.

Second, complementary EBSD and BEI were performed proximate to the crack path to characterize the interplay of local pore/crack path morphology (Fig. 26a), grain structure (Fig. 26b), and deformation morphology (Fig. 26c). Consistent with Fig. 24d-e, a small crack branch appears to be propagating towards the pore cluster outlined in Area (i). Similarly, as expected from Fig. 25, Areas (ii)-(v) exhibit evidence of increased plastic deformation (*via* higher KAM) local to the pores, with Area (v) showing a clear example of an expanded pore proximate to the crack path. However, the most salient result is that Area (ii) contains a highly localized ‘spur’ of elevated plastic deformation that originates from the crack path and appears to be emanating towards the porosity in this region. The location of this ‘spur’ is particularly notable given that it does not occur along the preferred EAC fracture path (i.e., PAGBs), but extends across the grain interior.

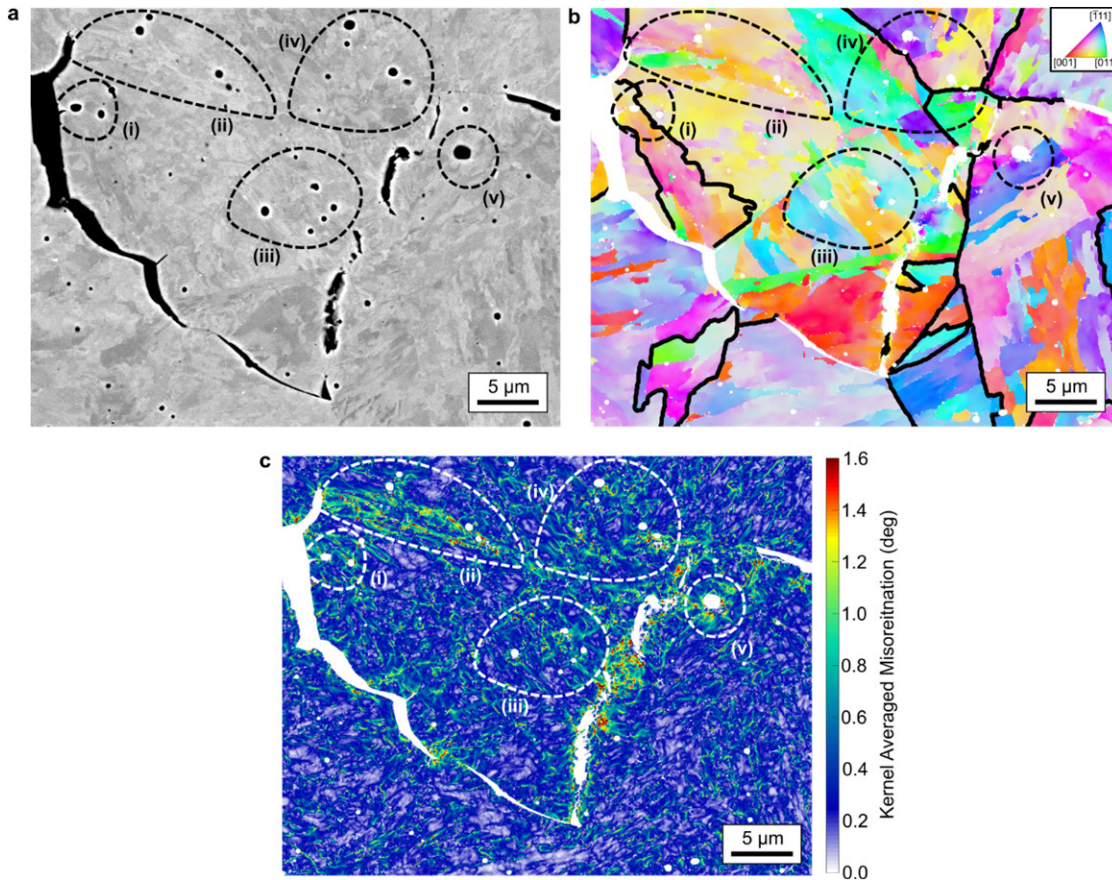


Fig. 26 | **AM pore-deformation interaction in environment assisted cracking.** **a.** Pore morphology relative to the crack path (black). **b.** Pore morphology relative to the crack path (white), local martensite grain structure (colored), and prior austenite grain boundaries (black). **c.** Pore morphology relative to the local deformation structures (colored) and crack path (white). Equivalent areas of interest (i-v) are bounded with dashed lines in **a-c**.

The present data demonstrate that sub-micrometer porosity contributes to the increased frequency of crack branching and elevated plastic deformation observed proximate to the EAC path in AM 17-4PH. Since AM 17-4PH exhibited faster EAC growth rates than wrought 17-4PH, it follows that the sub-micrometer porosity is a causal factor for degraded EAC resistance. This negative influence on the EAC resistance can be understood by considering how porosity may affect H-driven EAC. Most generally, H-driven EAC proceeds *via* the following interconnected mechanisms²⁸: (1) H uptake from the environment at the crack tip, (2) stress-assisted H diffusion into the region ahead of the crack tip and subsequent accumulation at microstructural features, and (3) incremental crack advance when the local mechanical driving force exceeds the H-degraded fracture resistance of a susceptible interface. Note that crack advance does not occur in AM 17-4PH under the present loading conditions in the absence of an H-producing environment (Supplemental Fig. 5). Therefore, traditional fracture toughness evaluations would not reveal the synergistic, deleterious interaction of sub-micrometer pores and H-driven EAC that occurs in aggressive environments.

Given this mechanistic basis, the present results suggest that sub-micrometer porosity degrades the AM alloy by exacerbating step (3) of the EAC process. With a median pore spacing of 2.4 μm (Supplemental Fig. 6), it is effectively a statistical certainty that pores will be present on or proximate to the EAC-susceptible interface. Critically, when located *on* the susceptible interface, a pore will simultaneously act to both increase the local mechanical driving force (i.e., as a stress concentrator²⁹) and lower the interface fracture resistance (i.e., as an interfacial defect³⁰). For pores *proximate to* a susceptible interface, the increased hydrostatic stresses near the pores will attract H, resulting in further degradations in the interface fracture resistance. This proposed interplay of pore-degraded interface fracture resistance and pore-amplified local stress/H content would reduce the amount of ‘bulk’ H required for crack advance, reduce the H diffusion time per crack growth increment, and result in accelerated EAC growth rates (as observed in Fig. 23c for the AM material). Such a dual negative role is strongly supported by the presented evidence. Specifically, the increased crack branching (Fig. 23) and evidence of branches being associated with pores (Fig. 24d-e) in the AM material demonstrates that the number of susceptible fracture pathways was increased by the sub-micrometer porosity. Additionally, the increased KAM levels proximate to pores (Fig. 26c) confirms that such small-scale pores do serve as stress concentration sites.

These data present challenges for a number of stakeholders involved in implementing AM processes. Of these, the most salient impact is on those industries actively striving to implement AM alloys for safety-critical applications where EAC is a potential failure mode. Increased attention needs to be paid to the small-scale porosity involved in the degradation of the EAC resistance of AM materials. The AM material used in this study would be considered an exemplar build, with strength/microstructure comparable to wrought material, few pores larger than a few μm , and >99% density. Yet, despite these ideal first-order properties, the EAC susceptibility of this material was significantly increased. Critically, the sub-micrometer pores (Supplemental Fig. 5) that govern this behavior are resistant to densification treatments (i.e., HIP) and well below the detection limit of non-destructive techniques^{31,32} used for component qualification^{33,34}. Consequently, these pores will likely be present in AM components built using current best practices. This reality underscores the importance of identifying the origins of such small-scale porosity during AM builds so that prevention/mitigation strategies can be developed and integrated into AM processes for components operated in aggressive environments.

4.4 Conclusion

In summary, this study shows that sub-micrometer porosity degrades the EAC resistance of a high-performance AM alloy. Evidence of enhanced deformation proximate to these pores has been identified and causally linked to a proliferation of EAC. These results are of immediate relevance to those interested in deploying AM alloys in aggressive environments. This work demonstrates that the size/scale of porosity

that degrades EAC performance is significantly smaller than currently recognized or appreciated by the AM community. Given the desire to implement AM materials into service, this realization has substantial implications for future inspection and qualification of AM components. Alternatively, advancements in AM processing techniques are required to either remove or modify these pores to attenuate their deleterious effects. In either case, continued study of the novel microstructure-performance interactions introduced by AM is critical if this promising technology is to be employed safely in society.

4.5 Acknowledgements

This research was financially supported by the Office of Naval Research under Grant No. N00014-18-1-2427 with Dr. Airan Perez as the Scientific Officer. Helpful discussions with Profs. John Scully, Ji Ma, and Tao Sun at the University of Virginia are gratefully acknowledged. This chapter was adapted from a manuscript coauthored by Trevor Shoemaker, Zachary Harris, Adam Thompson, and James Burns. T.S. performed the crack growth rate testing/analysis, fractographic imaging, crack wake imaging, and pore analysis. Z.H. performed the tension testing, gathered the EBSD data, and performed the grain structure and KAM analyses. A.T. performed the FIB trench-milling. T.S. and Z.H. wrote the manuscript. J.B. supervised the study. All authors interpreted the results, reviewed, and revised the manuscript.

4.6 References

1. Frazier, W. E. Metal additive manufacturing: A review. *J. Mater. Eng. Perform.* **23**, 1917–1928 (2014).
2. Vafadar, A., Guzzomi, F., Rassau, A. & Hayward, K. Advances in metal additive manufacturing: A review of common processes, industrial applications, and current challenges. *Appl. Sci.* **11**, 1–33 (2021).
3. Singamneni, S. *et al.* Additive Manufacturing for the Aircraft Industry: A Review. *J. Aeronaut. Aerosp. Eng.* **08**, 1–13 (2019).
4. Sanchez, S. M., Luhrs, C., McDonald, M. L. & Lynch, G. *Acquisition of Additive Manufacturing Capabilities for Expeditionary Operations.* (2021).
5. Lewandowski, J. J. & Seifi, M. Metal Additive Manufacturing: A Review of Mechanical Properties. *Annu. Rev. Mater. Res.* **46**, 151–186 (2016).
6. Haghdad, N., Laleh, M., Moyle, M. & Primig, S. Additive manufacturing of steels: a review of achievements and challenges. *J. Mater. Sci.* **56**, 64–107 (2021).
7. Raja, V. S. & Shoji, T. *Stress Corrosion Cracking Theory and Practice.* (Woodhead Publishing, 2011).

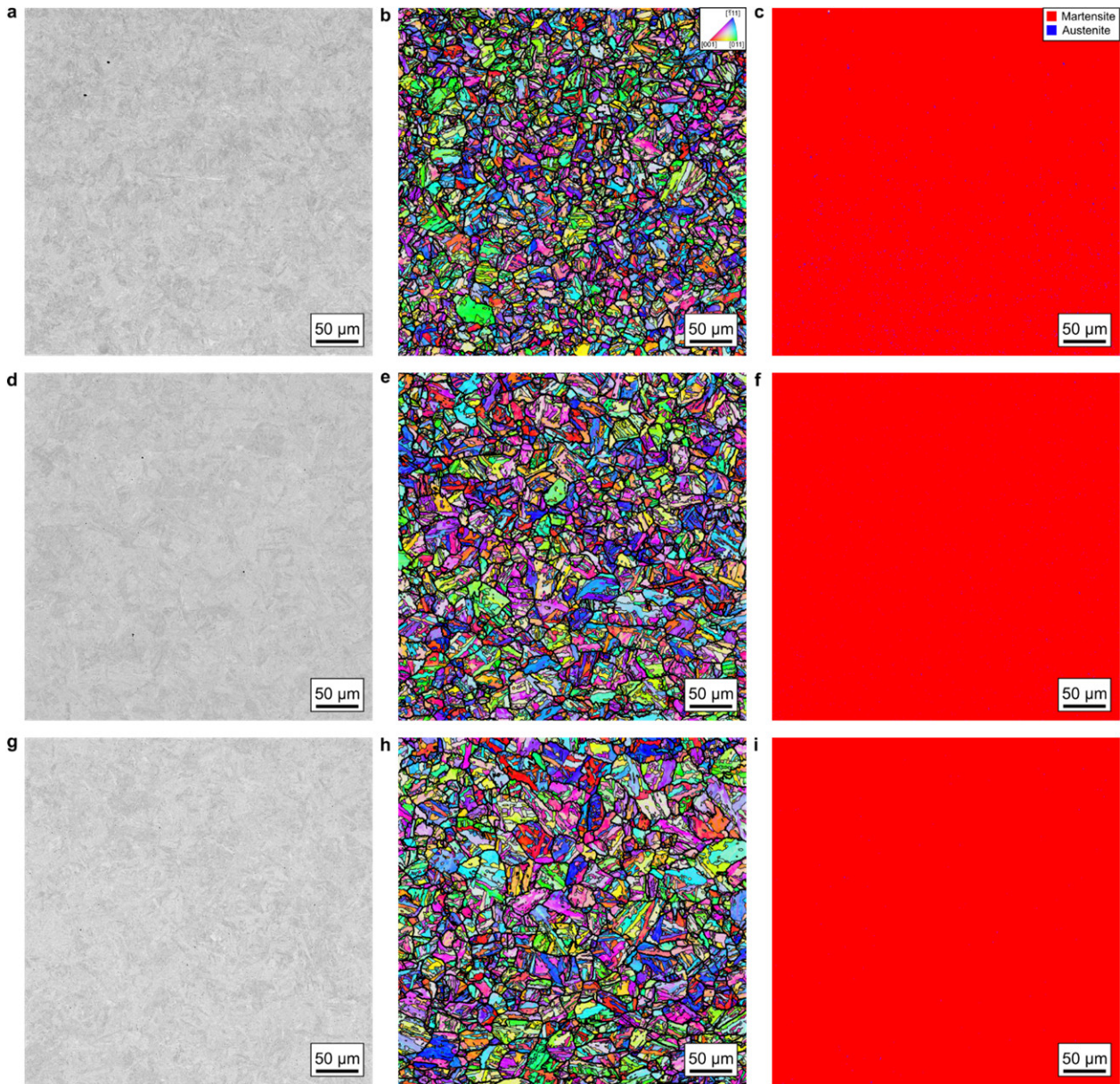
8. Schindelholz, E. J., Melia, M. A. & Rodelas, J. M. Corrosion of Additively Manufactured Stainless Steels—Process, Structure, Performance: A Review. *Corrosion* **77**, 484–503 (2021).
9. Bruemmer, S. M. & Was, G. S. Microstructural and microchemical mechanisms controlling intergranular stress corrosion cracking in light-water-reactor systems. *J. Nucl. Mater.* **216**, 348–363 (1994).
10. Snape, E. Roles of Composition and Microstructure in Sulfide Cracking of Steel. *Corrosion* **24**, 261–282 (1968).
11. Thompson, A. W. & Bernstein, I. M. The Role of Metallurgical Variables in Hydrogen-Assisted Environmental Fracture. in *Advances in Corrosion Science and Technology Volume 7* (eds. Fontana, M. G. & Staehle, R. W.) 53–175 (Plenum Press, 1980).
12. Sola, A. & Nouri, A. Microstructural porosity in additive manufacturing: The formation and detection of pores in metal parts fabricated by powder bed fusion. *J. Adv. Manuf. Process.* **1**, 1–21 (2019).
13. du Plessis, A., Yadroitsava, I. & Yadroitsev, I. Effects of defects on mechanical properties in metal additive manufacturing: A review focusing on X-ray tomography insights. *Mater. Des.* **187**, 108385 (2020).
14. Yadollahi, A. & Shamsaei, N. Additive manufacturing of fatigue resistant materials: Challenges and opportunities. *Int. J. Fatigue* **98**, 14–31 (2017).
15. Lavery, N. P. *et al.* Effects of hot isostatic pressing on the elastic modulus and tensile properties of 316L parts made by powder bed laser fusion. *Mater. Sci. Eng. A* **693**, 186–213 (2017).
16. Xue, J., Feng, Z., Tang, J., Tang, C. & Zhao, Z. Selective laser melting additive manufacturing of tungsten with niobium alloying: Microstructure and suppression mechanism of microcracks. *J. Alloys Compd.* **874**, 159879 (2021).
17. Yamamoto, T., Hara, M. & Hatano, Y. Effects of fabrication conditions on the microstructure, pore characteristics and gas retention of pure tungsten prepared by laser powder bed fusion. *Int. J. Refract. Met. Hard Mater.* **95**, 105410 (2021).
18. Prithivirajan, V. & Sangid, M. D. The role of defects and critical pore size analysis in the fatigue response of additively manufactured IN718 via crystal plasticity. *Mater. Des.* **150**, 139–153 (2018).
19. Liu, J. *et al.* Effect of scanning speed on the microstructure and mechanical behavior of 316L stainless steel fabricated by selective laser melting. *Mater. Des.* **186**, 108355 (2020).

20. Poulin, J.-R., Kreitchberg, A. & Brailovski, V. Effect of hot isostatic pressing of laser powder bed fused Inconel 625 with purposely induced defects on the residual porosity and fatigue crack propagation behavior. *Addit. Manuf.* **47**, 102324 (2021).
21. Gong, H. *et al.* Influence of defects on mechanical properties of Ti–6Al–4V components produced by selective laser melting and electron beam melting. *Mater. Des.* **86**, 545–554 (2015).
22. Biswal, R. *et al.* Criticality of porosity defects on the fatigue performance of wire + arc additive manufactured titanium alloy. *Int. J. Fatigue* **122**, 208–217 (2019).
23. Poulin, J.-R., Kreitchberg, A., Terriault, P. & Brailovski, V. Long fatigue crack propagation behavior of laser powder bed-fused inconel 625 with intentionally-seeded porosity. *Int. J. Fatigue* **127**, 144–156 (2019).
24. Thompson, A. W., Harris, Z. D. & Burns, J. T. Examination of focused ion beam-induced damage during platinum deposition in the near-surface region of an aerospace aluminum alloy. *Micron* **118**, 43–49 (2019).
25. Prasad Rao, K. & Raja, K. S. Environmental cracking behaviour of the Precipitation hardened stainless steel, 17-4 PH, under applied potential. *Mater. Corros.* **46**, 370–375 (1995).
26. Hsu, T. H. *et al.* Microstructure and property of a selective laser melting process induced oxide dispersion strengthened 17-4 PH stainless steel. *J. Alloys Compd.* **803**, 30–41 (2019).
27. Li, K. *et al.* Homogenization timing effect on microstructure and precipitation strengthening of 17–4PH stainless steel fabricated by laser powder bed fusion. *Addit. Manuf.* **52**, 102672 (2022).
28. Gangloff, R. P. Hydrogen Assisted Cracking of High Strength Alloys. in *Comprehensive Structural Integrity* (eds. Milne, I., Ritchie, R. O. & Karimhaloo, B.) (Elsevier Science, 2003).
29. Williams, M. L. & Schapery, R. A. Spherical flaw instability in hydrostatic tension. *Int. J. Fract. Mech.* **1**, 64–72 (1965).
30. Moody, N. R., Garrison, W. M., Smugeresky, J. E. & Costa, J. E. The Role of Inclusion and Pore Content on the Fracture Toughness of Powder-Processed Blended Elemental Titanium Alloys. *Metall. Trans. A* **24A**, 161–174 (1993).
31. Jolley, B. R., Uchic, M. D., Sparkman, D., Chapman, M. & Schwalbach, E. J. Application of Serial Sectioning to Evaluate the Performance of x-ray Computed Tomography for Quantitative Porosity Measurements in Additively Manufactured Metals. *Jom* (2021). doi:10.1007/s11837-021-04863-z
32. Schoepner, G. & Babish, C. A. *EN-SB-08-012, Revision D, In-Service Inspection Crack Size*

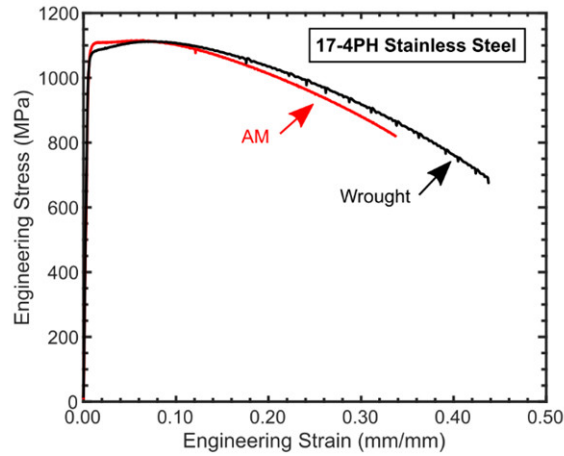
Assumptions for Metallic Structures. (2018).

33. Babish, C. A. *EZ-SB-19-01 Durability and Damage Tolerance Certification for Additive Manufacturing of Aircraft Structural Metallic Parts.* (2019).
34. Kundu, S. *et al.* Review of requirements for the durability and damage tolerance certification of additively manufactured aircraft structural parts and AM repairs. *Materials (Basel)*. **13**, (2020).

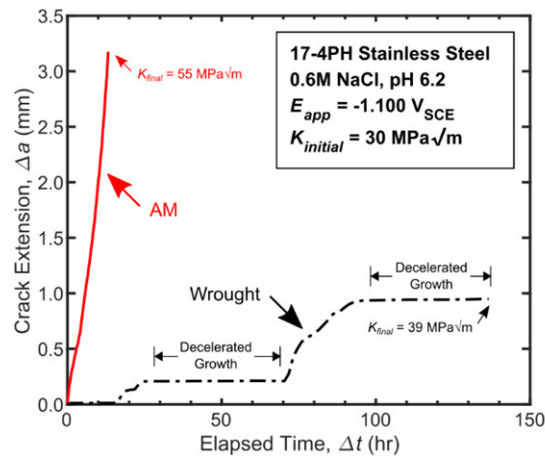
4.7 Supplemental Figures



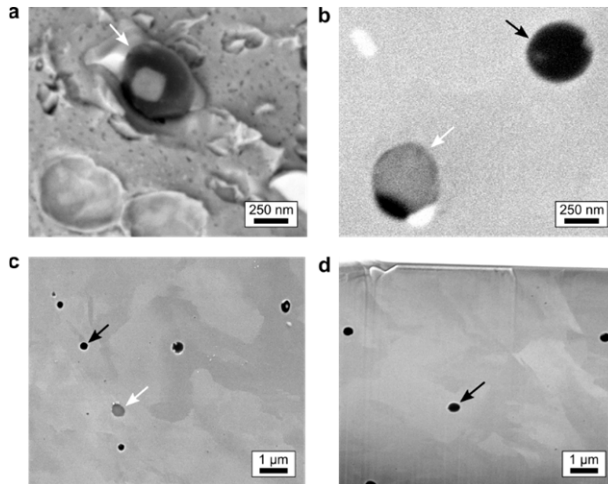
Supplemental Fig. 1 | **Microstructure comparison for 17-4PH stainless steels.** **a-c**, Wrought microstructure. **d-f**, AM microstructure in the XY plane. **g-i**, AM microstructure in the XZ plane. Black regions in **a**, **d**, **g** indicate relative amounts of large-scale porosity. Bold and fine black lines indicate PAGBs and martensite block boundaries, respectively, in **b**, **e**, **h**. Phase distributions are shown in **c**, **f**, **i**.



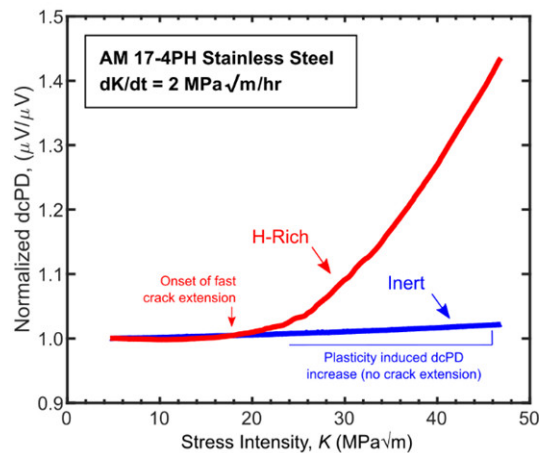
Supplemental Fig. 2 | **Tensile properties for 17-4PH stainless steels.** Representative engineering stress-strain curves for the AM and wrought material used in this study.



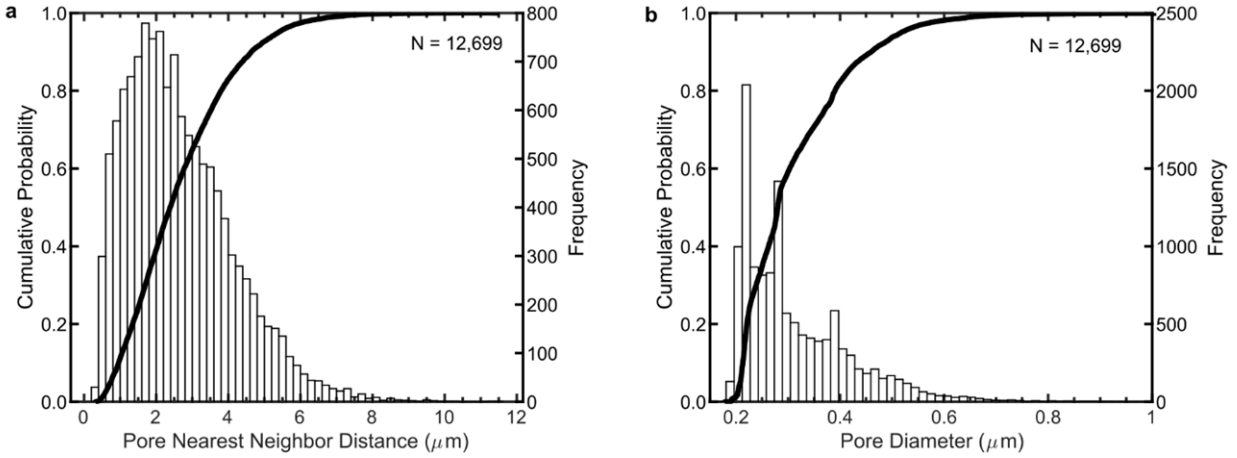
Supplemental Fig. 3 | **Environment assisted crack growth curves.** Crack extension versus time data corresponding to the growth rate data in the main text. Note that the main text growth rates were trimmed to reflect regions of growth with equivalent K since the AM test ended at a higher K_{final} .



Supplemental Fig. 4 | **Identification of both pores and oxides in AM 17-4PH.** **a**, Backscatter electron (BSE) image of an AM 17-4PH fracture surface. **b**, BSE image of a mechanically polished surface. **c**, Secondary electron (SE) image of a mechanically polished surface. **d**, SE image of a deformation-free trench created using a FIB. With the fracture surface in (**a**), dimples could be the remnants of a pore, or the dimples could be sites where oxide-inclusions (white arrows) have fallen away. BSE (atomic number) and SE (topographic) contrast differences in (**b,c**) show both oxide-inclusions and pores (black arrows) are present in the microstructure and could contribute to dimpling. SE contrast in the FIB trench (**d**) further verifies that hollow pores are present and not an artifact caused by oxide-inclusion pull-out during mechanical polishing of (**b,c**).



Supplemental Fig. 5 | **Environment effect on AM 17-4PH cracking.** Relative susceptibility of AM 17-4PH to cracking in a H-Rich environment (0.6M NaCl, pH 6.2, $E_{app} = -1.100 V_{SCE}$) versus an inert environment (Dry N_2 , RH $\sim 0\%$). Data is presented as recommended by ASTM E1820-18a for evaluation of fracture toughness.



Supplemental Fig. 6 | **Nominal pore statistics in the AM material.** **a**, Distances from each pore to its nearest neighbor pore. **b**, Pore diameters. Bold black lines are cumulative probability distributions and bars are occurrence frequencies of each measure. Data was extracted from pores at distances greater than 35 μm from the crack path to reflect the “nominal” pore unaffected by EAC.

Chapter 5 - Stress Corrosion Crack Wake Deformation in Peak Aged AM 17-4PH

5.1 Introduction

The previous two chapters studied general AM 17-4PH SCC behavior (Chapter 3) and linked deficits in AM SCC performance to sub-micrometer scale porosity (Chapter 4). Chapter 4 focused only on the overaged condition of AM 17-4PH and its interactions with porosity. However, significant SCC performance deficits (i.e., faster growth rates, increased susceptibility ranges) were also identified in the peak aged condition of AM 17-4PH in Chapter 3. The purpose of the current chapter is to extend the methods in Chapter 4 to the peak aged condition of 17-4PH and elaborate upon the operative fracture mechanisms. First, stress corrosion crack growth rates will be evaluated and compared for wrought and AM 17-4PH at two, key electrochemical potentials ($E_{app} = -0.8, -1.1 \text{ V}_{SCE}$) in 0.6M NaCl. Then, the crack path, crack wake morphology, and crack wake deformation structure will be evaluated. These results will be synthesized via the framework established in Chapter 3 to identify causal factor(s) leading to SCC performance deficits in peak aged AM 17-4PH.

5.2 Materials and Methods

The current chapter re-utilizes the experimental and analysis methods from Chapter 4 for study of peak aged 17-4PH. Stress corrosion cracking behavior is evaluated for the HIP+SA+460°C/1 h and SA+482°C/1 h (peak aged) conditions of AM and wrought 17-4PH, respectively. Refer to Chapters 2 and 3 for material processing and heat treatment details. To briefly review the Chapter 4 methods, stress corrosion cracks are grown in 0.6M NaCl (pH 6.2) with an applied electrochemical potential (E_{app}) and an initial $K \sim 30 \text{ MPa}\sqrt{\text{m}}$. After a minimum of 300 μm of crack extension the test is halted, the sample is ground from the side, and the crack path is polished for microstructural examination. The crack wake (i.e., microstructure proximate to the crack path) is imaged using a combination of EBSD and SEM imaging. EBSD data yields maps of grain orientations, boundaries, and kernel averaged misorientations (KAM) in the crack wake. Pore sizes, locations, and distances from the crack path are quantified using image analysis techniques on backscatter electron images.

5.3 Results

Stress corrosion cracking behavior was evaluated for peak aged wrought and AM 17-4PH in 0.6M NaCl at $E_{app} = -0.8$ and $-1.1 V_{SCE}$. First, Fig. 27 compares crack growth rate (da/dt) versus stress intensity (K) data for the various environmental and material conditions. In all cases, stress corrosion crack growth occurred within minutes of applying the respective potential (i.e., $E_{app} = -0.8$ or $-1.1 V_{SCE}$) at $K \sim 30 \text{ MPa}\sqrt{\text{m}}$ and continued at a constant rate until testing was halted. At $-1.1 V_{SCE}$, wrought had a $5 \times 10^{-5} \text{ mm/s}$ crack growth rate whereas AM had a $2 \times 10^{-4} \text{ mm/s}$ growth rate – a 4-fold faster rate than wrought. This increased SCC susceptibility in AM is compounded at $-0.8 V_{SCE}$ where AM grew at $1 \times 10^{-3} \text{ mm/s}$ – 20 times faster than wrought at $-1.1 V_{SCE}$. Furthermore, wrought is not susceptible to SCC at $-0.8 V_{SCE}$ as established in Chapter 3. Notably, the various crack growth experiments in Fig. 27 were performed independently of the study in Chapter 3, but the measured crack growth rates are consistent with those reported in Chapter 3 demonstrating the repeatability of EAC behavior. After crack growth kinetics were gathered, the samples in Fig. 27 were ground and polished for inspection of the stress corrosion crack paths and crack wake microstructure.

The images in Fig. 28 show the relative levels of stress corrosion crack path branching for peak aged AM and wrought 17-4PH. Consistent with prior work¹⁻³, wrought 17-4PH underwent a degree of stress corrosion crack path branching as indicated by the multiple primary crack paths and small secondary branches in Fig. 28a. Comparatively, AM 17-4PH at a matched potential underwent significantly more crack path branching (Fig. 28b) than wrought (Fig. 28a). In AM, there were multiple primary crack paths

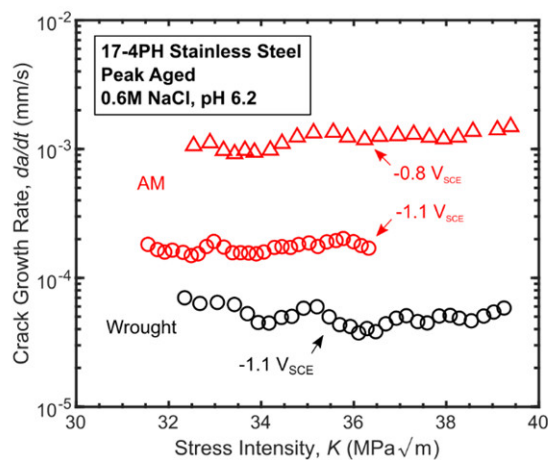


Fig. 27 | **Stress corrosion crack growth rates for peak aged AM and wrought 17-4PH.** Crack growth rate as a function of stress intensity (K) is plotted for AM and wrought 17-4PH at $E_{app} = -0.8, -1.1 V_{SCE}$ in 0.6M NaCl (pH 6.2). The applied stress intensity was initially held constant ($dK/dt = 0 \text{ MPa}\sqrt{\text{m}}/\text{h}$) at $K \sim 30 \text{ MPa}\sqrt{\text{m}}$; variation in K occurred as the crack extended. Note that peak aged wrought 17-4PH is not SCC susceptible at $E_{app} = -0.8 V_{SCE}$.

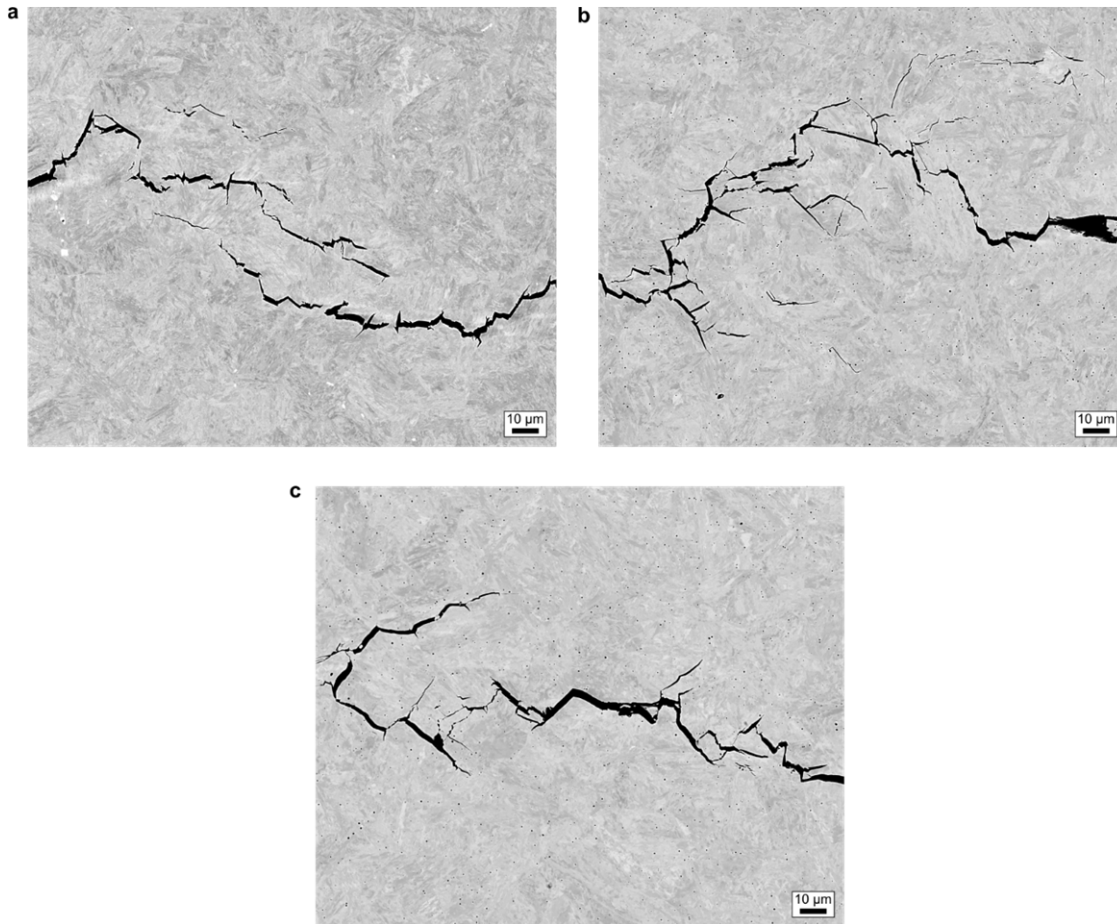


Fig. 28 | **Stress corrosion crack path branching in peak aged AM and wrought 17-4PH. a**, Wrought, $E_{app} = -1.1 V_{SCE}$. **b**, AM, $E_{app} = -1.1 V_{SCE}$. **c**, AM, $E_{app} = -0.8 V_{SCE}$. Stress corrosion crack wakes are shown for peak aged AM and wrought 17-4PH at $K = 32 \text{ MPa}\sqrt{\text{m}}$ in 0.6M NaCl (pH 6.2) at various applied potentials.

with both secondary and tertiary branches. Additionally, there were multiple instances of small, disconnected cracks indicating a level of secondary crack nucleation not seen in wrought 17-4PH. The aforementioned cases constitute a direct comparison between AM and wrought at $E_{app} = -1.1 V_{SCE}$, but peak growth rates occurred in AM 17-4PH at $-0.8 V_{SCE}$ (Fig. 27). At peak susceptibility, AM 17-4PH continued to have a higher degree of crack path branching than wrought 17-4PH with significant levels of secondary branching ($-0.8 V_{SCE}$, Fig. 28c). However, the large number of tertiary branches noted in AM at $-1.1 V_{SCE}$ were not present at $-0.8 V_{SCE}$.

To understand the microstructural interfaces responsible for these crack path differences in peak aged AM and wrought 17-4PH, EBSD was used to characterize the microstructure proximate to the crack paths (i.e., the crack wake, Fig. 29). Both AM and wrought 17-4PH are fully martensitic, so martensite boundaries are highlighted with fine, black outlines and prior austenite grain (PAG) boundaries are reconstructed with the bold, black outlines in Fig. 29b,d,f. The microstructure proximate to the crack path

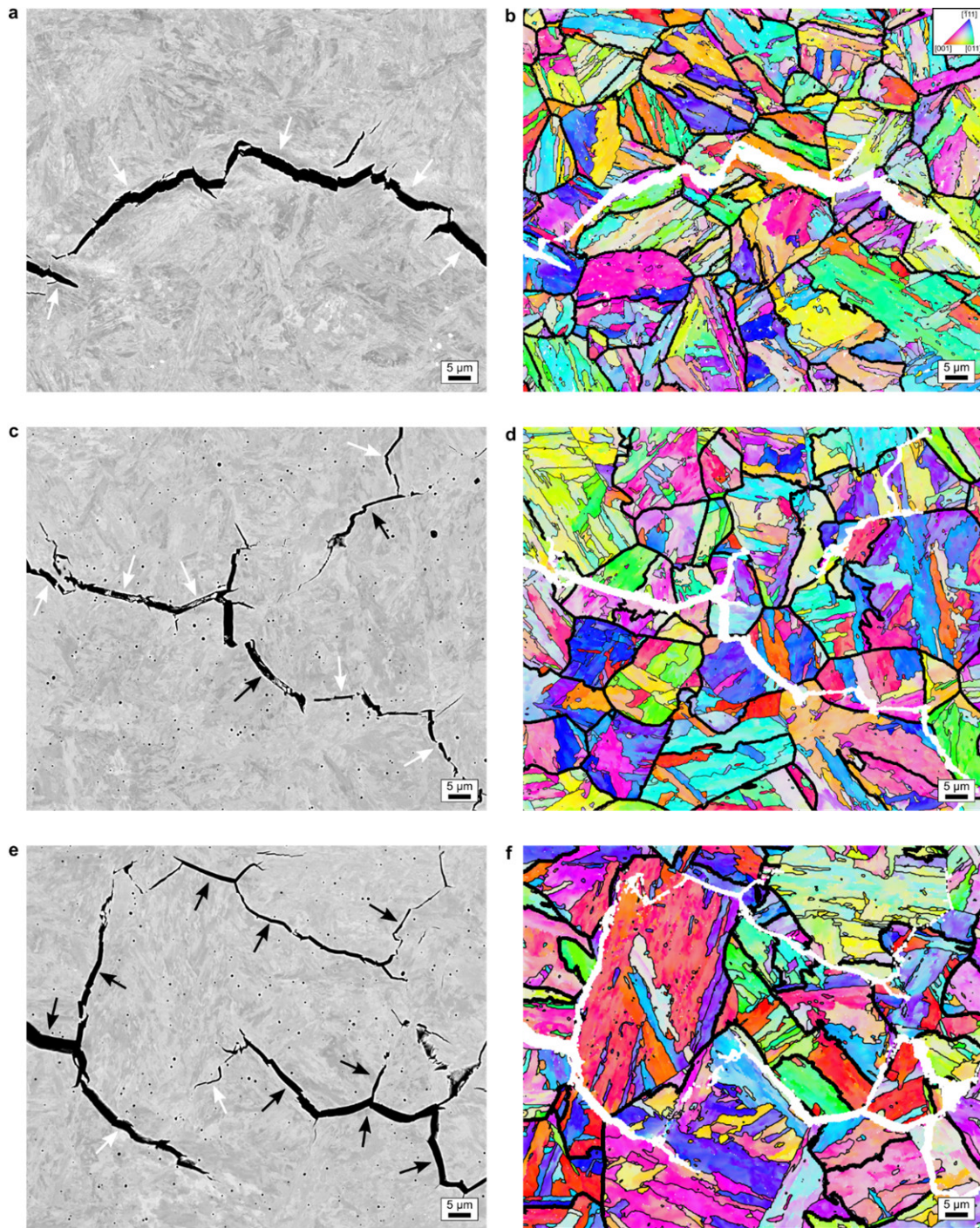


Fig. 29 | **Identification of stress corrosion cracking failure interfaces for peak aged AM and wrought 17-4PH.** **a-b**, Wrought, $E_{app} = -1.1 V_{SCE}$. **c-d**, AM, $E_{app} = -1.1 V_{SCE}$. **d-e**, AM, $E_{app} = -0.8 V_{SCE}$. The stress corrosion crack path is compared for peak aged AM and wrought 17-4PH in 0.6M NaCl (pH 6.2) at various applied potentials. The crack path is shown via backscatter electron images (**a,c,e**) and OIM maps identifying the proximate grain structure (**b,d,e**). OIM coloration indicates grain orientation with fine and bold black outlines identifying martensite and prior austenite grain boundaries, respectively. White and black arrows on the backscatter images indicate transgranular and intergranular fracture, respectively.

(white) was then used to identify the microstructural interfaces susceptible to SCC. For peak aged wrought 17-4PH at $-1.1 V_{SCE}$ (Fig. 29a,b), the crack path primarily traverses through and along the martensite features with no clear interaction with the PAG boundaries. Select instances of this type of growth are highlighted with white arrows on the companion backscatter electron image in Fig. 29a to indicate transgranular (TG) fracture. For AM 17-4PH at $-1.1 V_{SCE}$ (Fig. 29c,d), similar cases of TG are present and indicated in Fig. 29c. However, unlike wrought there are several clear instances of fracture along PAG boundaries which are indicated with black arrows in Fig. 29c. These PAG boundary crack paths indicate a level of intergranular (IG) fracture in AM that is not present in wrought 17-4PH. Continuing to AM at $-0.8 V_{SCE}$ (Fig. 29e,f), the crack path transitions to a primarily IG fracture mode with limited instances of TG (Fig. 29e). Note that these various observations align well with the fractographic analysis in Chapter 3, but the current results are more rigorous with their direct identification of the fracture interfaces through EBSD.

Complementary KAM analyses of AM and wrought 17-4PH stress corrosion crack wakes were performed to quantify the relative levels of deformation involved in the respective fracture processes, see Fig. 30. Representative KAM maps of AM and wrought crack wakes at $-1.1 V_{SCE}$ are first compared in Fig. 30a,b. In both materials, there are significant levels of intermittent deformation (i.e., green/blue regions) throughout the microstructure. These deformed regions are on the same scale as the martensite grain morphology and likely a remnant of the martensite transformation process⁴. More importantly, this background deformation is not exceeded to a significant degree for either wrought (Fig. 30a) or AM (Fig. 30b) in the presence of SCC at $-1.1 V_{SCE}$. Where present, instances of deformation above the background level were highly localized to the region adjacent to the crack path. For AM 17-4PH at $-0.8 V_{SCE}$, the background deformation continued to dominate the KAM map, but was accompanied by a number of discrete regions of enhanced deformation (Fig. 30c) not present in the $-1.1 V_{SCE}$ KAM maps. Several of these discrete regions were enumerated, magnified, and compared to the underlying microstructure via backscatter electron (BSE) imaging (Fig. 30c1,c2,c3,c4). In Fig. 30c1, enhanced deformation is present in the area between two crack path branches with the highest degree of deformation occurring at a circular feature at the edge of a branch (black arrow). Fig. 30c2 shows enhanced deformation approximately aligned with a region of circular microstructural features that are likely pores. The two other magnified regions (Fig. 30c3,c4) show a similar alignment of enhanced deformation and pore-like features. Notably, these discrete regions of enhanced deformation were not universal as demonstrated by the (★) region in Fig. 30c; much of the deformation at $-0.8 V_{SCE}$ remained highly localized to the area adjacent to the crack path in a similar manner to $-1.1 V_{SCE}$.

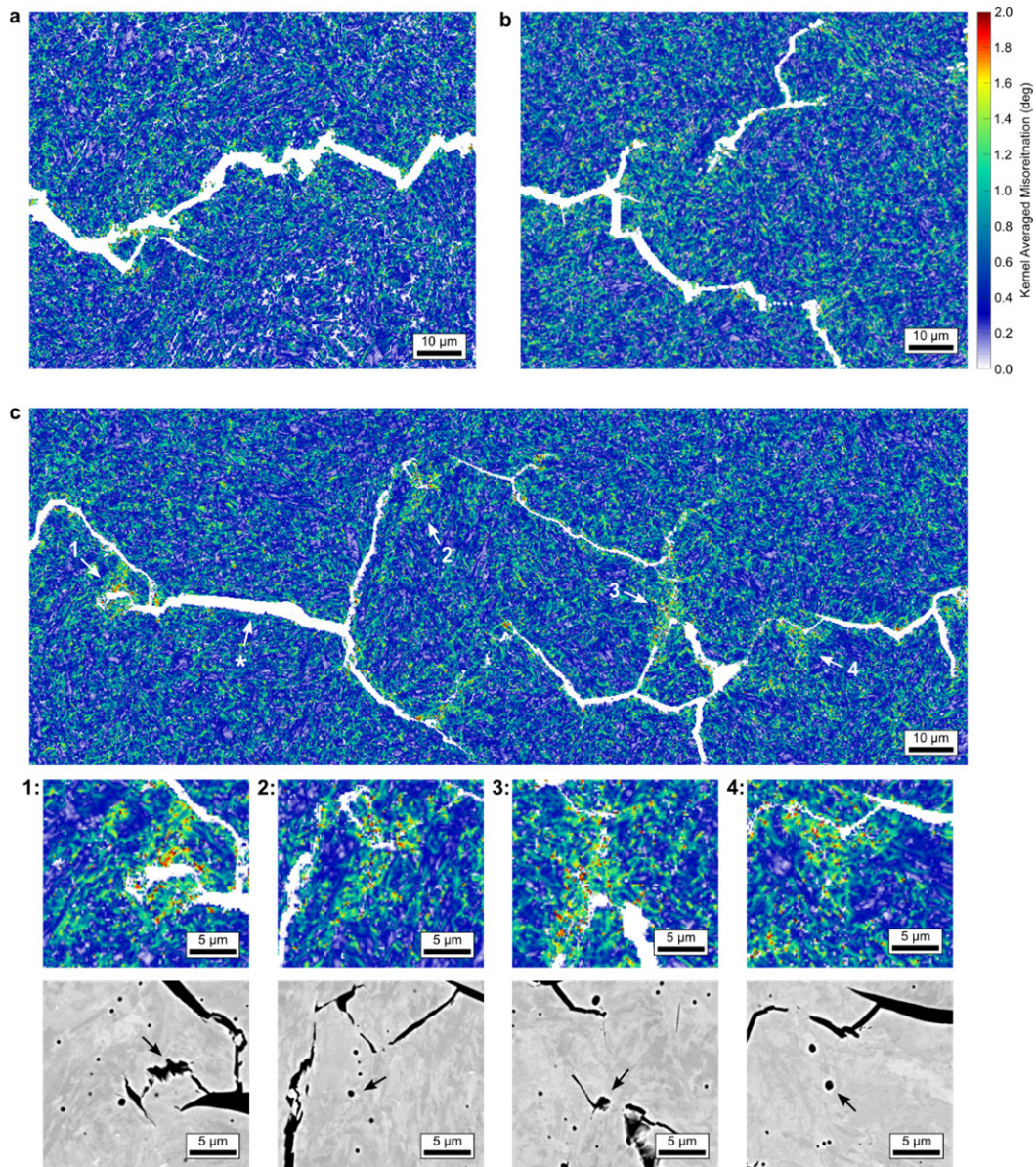


Fig. 30 | Stress corrosion crack wake deformation in peak aged AM and wrought 17-4PH. **a**, Wrought, $E_{app} = -1.1 V_{SCE}$. **b**, AM, $E_{app} = -1.1 V_{SCE}$. **c**, AM, $E_{app} = -0.8 V_{SCE}$. Deformation is quantified and compared via KAM in stress corrosion crack wakes for peak aged AM and wrought 17-4PH in 0.6M NaCl (pH 6.2) at various applied potentials (**a,b,c**). Areas of interest are identified with white arrows in (**c**). For the numbered areas of interest, magnified KAM maps are shown with equivalent backscatter electron images. Black arrows in the backscatter images indicate regions of high deformation.

The KAM in Fig. 30 indicated possible deformation-based interaction between porosity and the crack path for AM 17-4PH at $-0.8 V_{SCE}$. In order to investigate this interaction further, wide-area, high magnification images of the AM 17-4PH crack wakes at $-0.8 V_{SCE}$ and $-1.1 V_{SCE}$ are compared in Fig. 31. The white arrows in Fig. 31 indicate a significant level of interaction between the crack path and pore-like features at both applied potentials. At both potentials, the pores are seen intersecting with the crack path,

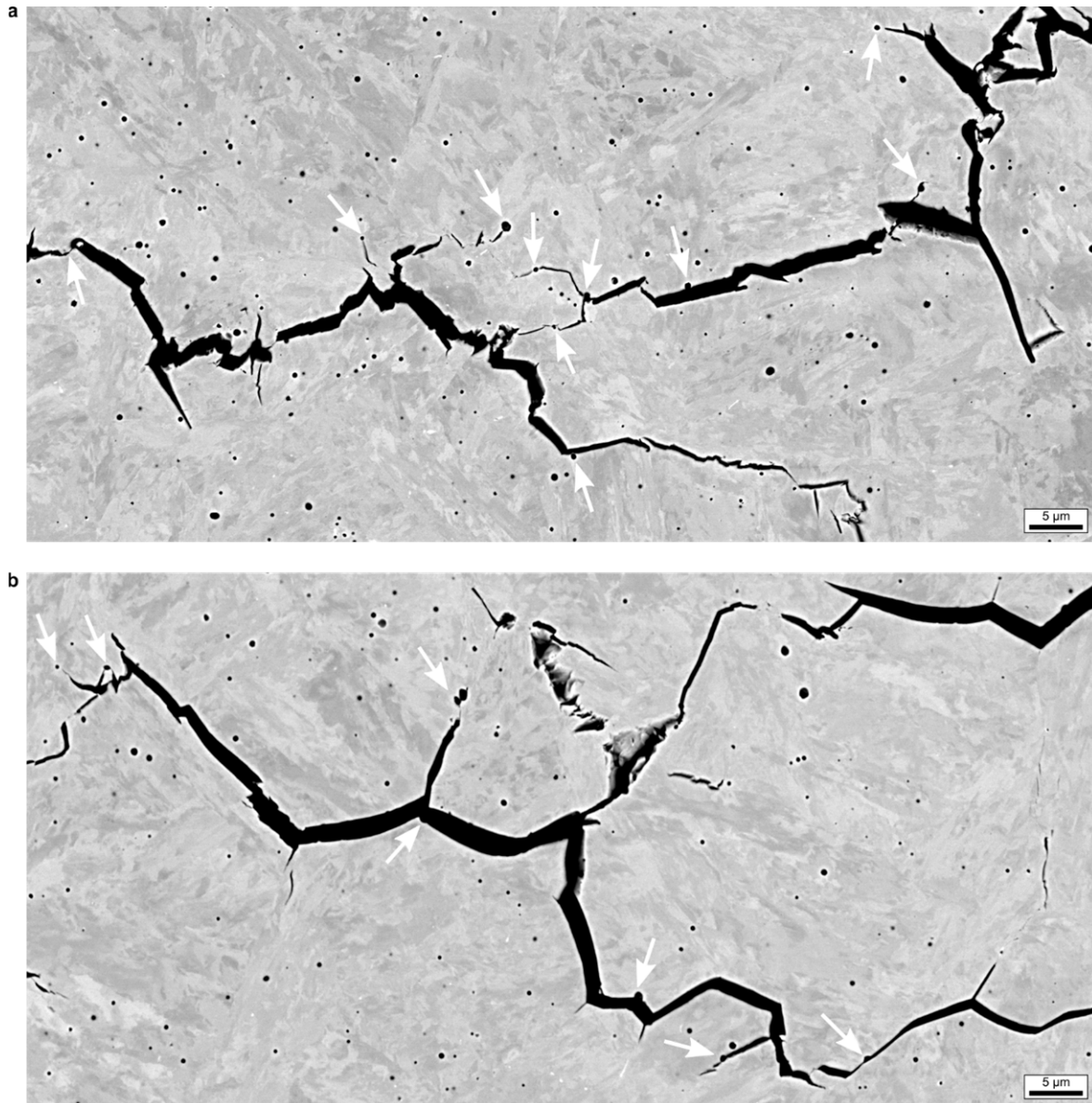


Fig. 31 | Pore-stress corrosion crack path interaction in peak aged AM 17-4PH. **a**, $E_{app} = -1.1 V_{SCE}$. **b**, $E_{app} = -0.8 V_{SCE}$. The stress corrosion crack path is shown for peak aged AM 17-4PH in 0.6M NaCl (pH 6.2) at $E_{app} = -1.1, -0.8 V_{SCE}$. Intersections of the crack path with porosity are highlighted with white arrows.

some crack path branches extend toward pores, and there are some cases of secondary cracking extending from (i.e., nucleating from) pores. These various types of pore-crack interactions are largely similar at $-0.8 V_{SCE}$ and $-1.1 V_{SCE}$; this indicates that the role of porosity in the respective fracture processes is not potential dependent. This conflicts somewhat with the results in Fig. 30 which indicated a deformation-based interaction with pores specifically at $-0.8 V_{SCE}$, but perhaps the differences at $-0.8 V_{SCE}$ are too subtle to be apparent with the morphological examination in Fig. 31.

5.4 Discussion

The preceding results demonstrate several key differences in the stress corrosion cracking behavior of peak aged AM and wrought 17-4PH. Using wrought 17-4PH as the baseline, AM 17-4PH has (1) higher SCC growth rates, (2) increased levels of crack branching, (3) unique susceptibility to SCC at $-0.8 V_{SCE}$, (4) a transition from transgranular to intergranular fracture at $-0.8 V_{SCE}$, and (5) interactions between porosity and the stress corrosion crack path. These differences between AM and wrought are most pronounced at $-0.8 V_{SCE}$ which leads to a key question, “Why does AM 17-4PH undergo unique intergranular SCC susceptibility with the fastest crack growth rates at $-0.8 V_{SCE}$?” This is a difficult question that does not have a clear answer with the current results. However, the preceding chapters have provided a framework to begin understanding this issue. The proceeding discussion will leverage the H-driven decohesion model described in Chapter 3. The goal of this discussion will be to evaluate factors contributing to increased SCC susceptibility in peak aged AM 17-4PH.

5.4.1 H-Assisted Decoherence Framework Review

First, the reader is directed to Chapter 3 for an exhaustive description of the current discussion’s theoretical foundation. To briefly review, hydrogen embrittlement is the governing mechanism for the cathodic polarization induced SCC studied in the current chapter. The microstructural considerations for this fracture mechanism may be interpreted through a H-assisted decohesion/deformation framework presented as Eq. 3.2 in Chapter 3. Critically, the factors in Eq. 3.2 may be used as a guide to mechanistically link observed fracture behaviors to microstructural features and dependencies. These factors include the material yield strength (σ_{ys}), toughness of a microstructural interface (k_{IG}), toughness modifications via elemental segregation ($\sum_{i=0}^n \beta_i C_i$), stress-enhanced hydrogen concentration ($C_{H\sigma}$), degradative potency of hydrogen (α), and H-affected deformation factors (α'' , β') in the fracture process zone. A rigorous set of magnitudes with a combined functional description for these factors (i.e., as a failure criteria) is beyond the scope of this work. Instead, the goals are to (1) qualitatively link 17-4PH fracture behaviors to these factors and (2) identify SCC critical microstructural features with a firm mechanistic basis. For example, strength-matching the AM and wrought 17-4PH microstructure eliminated the σ_{ys} factor as a likely contributor to the significant degradation in AM 17-4PH SCC performance, so remaining microstructural and mechanistic factors may be systematically considered in order to understand the AM performance deficit.

5.4.2 Pore-Crack Interactions

Based on the current results, porosity is a clear microstructural factor that is contributing to differences in AM and wrought 17-4PH SCC performance. The sheer number of interactions between the crack path and porosity in Fig. 31 shows the salient role of porosity at both $-0.8 V_{SCE}$ and $-1.1 V_{SCE}$ in peak aged AM 17-4PH. These morphological crack-pore interactions are mostly consistent with those identified

in overaged AM 17-4PH at $-1.1 V_{SCE}$ in Chapter 4. Additionally, in the overaged material, increased KAM was observed proximate to the porosity which verified the presence of local stress enhancement sufficient to induce plastic deformation (i.e., α'' , β' impacts). However, evidence of pore-based stress enhancement is not so direct in the current case of peak aged AM 17-4PH. At $-1.1 V_{SCE}$, KAM mapping in Fig. 30b shows no evidence of deformation localized to porosity that would corroborate stress enhancement. At $-0.8 V_{SCE}$, there is some evidence of plasticity co-located with porosity (Fig. 30c2,c4), but several features of the crack wake dilute this observation. First, it must be noted that some of those discrete KAM regions at $-0.8 V_{SCE}$ are located at crack path branches/intersections/kinks (Fig. 30c1,c3). Plasticity in kinked regions could be separately explained by the larger driving force needed to extend a non-Mode I crack⁵ (i.e., a crack that is not orthogonal to the load application direction). This kinked crack effect is a continuum-mechanical mechanism independent of the microstructure-based decohesion framework. Second, the lack of deformation in much of the crack wake at $-0.8 V_{SCE}$ (Fig. 30c*, for example) suggests a significant role of brittle fracture. The conflict between clear morphological pore-interactions at $-1.1 V_{SCE}$ and $-0.8 V_{SCE}$ (Fig. 31) and the KAM observations (Fig. 30) highlights a need for further examination. In order to elucidate the pore-crack interaction in peak aged AM 17-4PH, the pore size proximate to the crack path was quantified using the methodology developed in Chapter 4.

The evaluation in Fig. 32 quantifies the percentage of large pores (i.e., with diameters $>0.6 \mu\text{m}$) adjacent to the stress corrosion crack path in peak aged AM 17-4PH. This metric indicates the propensity for pore expansion (deformation) during the SCC fracture process. Note that the peak aged distributions are also compared to the overaged results from Chapter 4 since all testing and material processing details

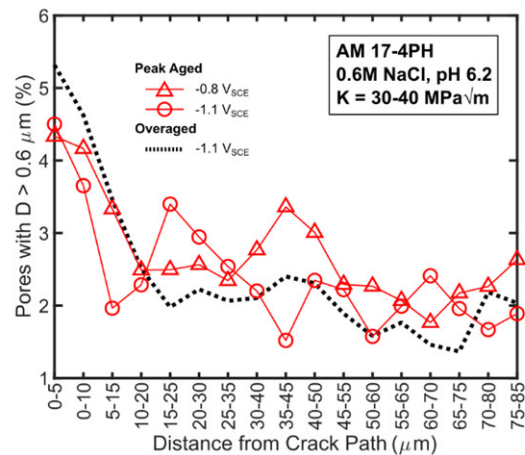


Fig. 32 | Comparison of pore expansion proximate to stress corrosion cracking in peak aged and overaged AM 17-4PH. The percentage of large, outlier pores (diameter, D , $>0.6 \mu\text{m}$) is shown as a function of distance from the stress corrosion crack path for two heat treatments (peak age, overage) of AM 17-4PH. All tests were performed in 0.6M NaCl (pH 6.2) at $K = 30\text{-}40 \text{ MPa}\sqrt{\text{m}}$ with $E_{app} = -0.8 V_{SCE}$ or $-1.1 V_{SCE}$.

(except for aging heat treatment) were the same. First, the number of large pores at large distances from the crack path is constant at ~2% for all conditions. This indicates that similar background distributions of pore sizes are present for each condition. The critical comparisons are at distances $< 5 \mu\text{m}$ and $< 25 \mu\text{m}$ from the crack path. At $< 5 \mu\text{m}$, the peak aged condition at $-0.8 V_{\text{SCE}}$ and $-1.1 V_{\text{SCE}}$ both exceed the background level with ~4.25% of pores exceeding a $0.6 \mu\text{m}$ diameter. Comparatively, ~5.25% of pore diameters exceed $0.6 \mu\text{m}$ in the overaged condition. Additionally, the distance over which pores exceed the ~2% background is extended about $5 \mu\text{m}$ farther in the overaged condition than in the peak aged condition. These pore distributions indicate that (1) the peak aged condition at $-0.8 V_{\text{SCE}}$ and $-1.1 V_{\text{SCE}}$ have equal levels of pore expansion and (2) more pores experience expansion in the overaged than the peak aged condition.

Notably, quantifying the mean and median sizes of the $>0.6 \mu\text{m}$ pore groups as a function of distance from the crack path (in any condition) does not produce any statistically relevant results; hence, the use of a count-based metric in Fig. 32. If the median or mean size of the $>0.6 \mu\text{m}$ pore groups is directly plotted versus distance from the crack path, then the trend is flat with no upswing at low crack path distances like shown in Fig. 32. This trend of count-based rather than size-based dependence is likely a result of load redistribution and a small, critical strain that limits pore expansion. For the overaged condition, select pores expand in the presence of the crack tip stress field, reach a critical strain, then shed load to the surrounding microstructure via plastic deformation (Chapter 4) which halts expansion. For the peak aged condition, the same mechanism is likely present, but the lower capacity for plastic deformation in the peak aged condition limits measurable KAM (Fig. 30b,c*) and the number of pores that will expand (Fig. 32). This small, critical strain results in pore expansion to sizes large enough to be measurable versus the median pore size of the total distribution, but the critical strain is too small for expanded pores to significantly exceed the total pore distribution's mean/median outlier size. This small size-change in addition to the small number of pores that expand (2.25-3.25% depending on aging condition) makes separation of the expanded pores from outliers difficult, except via a count-based metric.

Returning to the decohesion framework discussion, the differences in peak aged and overaged AM 17-4PH pore expansion and KAM behaviors suggest subtle, mechanistically different roles for porosity in the two tempers' SCC fracture processes. In the peak aged condition, pores proximate to the crack undergo a lesser degree of expansion than in the overaged condition (Fig. 32). Additionally, the reduced KAM in the peak aged condition (Fig. 30b,c*) indicates that the expansion more commonly terminates with brittle fracture. This behavior suggests that the pores can affect $C_{H\sigma}$ as an elastic stress concentration in the following manner: (1) a pore locally magnifies the stress, (2) enhanced stress promotes higher local hydrogen concentrations via lattice dilation, (3) increased hydrogen content reduces the cohesive strength of local interface(s), and (4) decohesion occurs with little plastic accommodation (i.e., brittle fracture). This

elastic stress concentration behavior is most pronounced in the peak aged condition at $-1.1 V_{SCE}$ with minimal KAM (Fig. 30b). However, at $-0.8 V_{SCE}$ there are cases of increased KAM proximate to pores (Fig. 30c2,c4).

The difference in KAM for the peak aged condition at $-1.1 V_{SCE}$ and $-0.8 V_{SCE}$ (Fig. 30b,c) might be understood by postulating reasons behind the crack path differences observed in Fig. 29c,e. There could be two cases of pore-enhanced SCC. In case (i), a pore could promote brittle fracture at the nearest/intersecting interface as an elastic stress concentration in the previously described manner. In this case, transgranular fracture would be expected since martensite interfaces are most prevalent. Further, significant crack path branching might be expected due to the number of martensite interfaces that are proximate to each pore. Brittle (Fig. 30b), transgranular (Fig. 29c) fracture and maximal branching (Fig. 28b) are all consistent with case (i) and the $-1.1 V_{SCE}$ behavior. In case (ii), a pore could shed load via plastic accommodation (i.e., resulting in enhanced local KAM) after reaching a critical strain. This load shedding could promote fracture at the nearby interface that is most susceptible to SCC (i.e., highest α , and lowest $\sum_{i=0}^n \beta_i C_i, k_{IG}$) rather than the interface closest to the pore itself. If the PAG boundaries in AM 17-4PH were most susceptible to SCC, then case (ii) is consistent with the shift to intergranular fracture (Fig. 29e) and pore-enhanced KAM (Fig. 30c2,c4) at $-0.8 V_{SCE}$. Case (ii) is also consistent with the overaged condition where porosity plastically deforms at a length-scale that is readily apparent via KAM mapping and intergranular fracture is dominant (Chapter 4). From the perspective of the decohesion framework, the case (ii) pores might be considered to modify the (α'', β') parameters due to the plastic accommodation. Unfortunately, these mechanistic insights do not provide clear answers to the initial question on the unique SCC susceptibility of AM 17-4PH at $-0.8 V_{SCE}$. Higher levels of plastic accommodation at pores should (1) dissipate strain energy and (2) reduce the magnitude of the crack tip stress singularity via load redistribution; each of these factors typically increase resistance to local failure/decohesion of an SCC susceptible interface. These effects are consistent with the generally lower crack growth rate in the overaged condition, but inconsistent with the maximal growth rate at $-0.8 V_{SCE}$ in the peak aged condition. This suggests that other factor(s), beyond pore-plasticity effects, are contributing to enhanced SCC susceptibility in peak aged AM 17-4PH.

5.4.3 Intergranular Fracture along PAG Boundaries

The defining characteristic for peak aged AM 17-4PH SCC behavior at $-0.8 V_{SCE}$ is the intergranular fracture mode (Fig. 29e,f). From a decohesion framework perspective, this fracture mode is informed by k_{IG} , $\sum_{i=0}^n \beta_i C_i$, and α which describe the SCC susceptibility of an interface. Intergranular fracture is notably absent from peak aged wrought 17-4PH (Fig. 29a,b), so preferential intergranular fracture indicates lower PAG boundary resistance to SCC in AM 17-4PH. This increased SCC susceptibility

may be intrinsic to the PAG interface (k_{IG}), induced by elemental segregation ($\sum_{i=0}^n \beta_i C_i$), and/or H could have a higher degradative potency (α) due to the character of the interface. Unfortunately, direct examination of these factors requires nanoscale or targeted investigations that are beyond the scope of the current work.

A second consideration is the large increase in crack growth rate magnitude with AM 17-4PH intergranular fracture. Chapter 3 postulated that peak aged AM 17-4PH cracks slower at $-1.1 V_{SCE}$ than $-0.8 V_{SCE}$ due to mixed mode fracture (i.e., TG+IG at $-1.1 V_{SCE}$), increased crack path tortuosity, and, consequentially, geometric dilution of the mechanical driving force⁶. The results in Fig. 28 corroborate this postulation with the apparent increase in branching at $-1.1 V_{SCE}$, but it remains unclear why peak aged AM 17-4PH $-0.8 V_{SCE}$ crack growth is 20-fold faster than peak aged wrought 17-4PH at $-1.1 V_{SCE}$. The current decohesion framework can describe the location and susceptibility of an interface to H, but H diffusivity is required to determine the rate at which H-assisted decohesion (i.e., crack growth) can occur. In order to answer this crack growth rate question, H diffusivity measurements are required, which are again beyond the scope of the current work.

5.5 Conclusions

In summary, stress corrosion cracking behavior was compared for peak aged AM and wrought 17-4PH in 0.6M NaCl at cathodic applied potentials. Fracture mechanics based crack growth kinetics were gathered and compared for the two forms of 17-4PH. Underlying fracture mechanisms were investigated through examination of the crack path and interpreted through a hydrogen-assisted decohesion framework. The following are key conclusions from this study:

- At an equivalent applied potential ($-1.1 V_{SCE}$), AM 17-4PH cracks 4-fold faster than wrought 17-4PH. This growth rate difference is accompanied by significantly enhanced crack path branching and interaction with sub-micrometer scale porosity in AM 17-4PH.
- Examination of the crack wake morphology and deformation structure showed that sub-micrometer scale pores interact with and likely enhance SCC fracture in peak aged AM 17-4PH.
- Quantification of the stress corrosion crack wake deformation and porosity deformation showed subtle differences in the pore-crack interactions dependent on applied potential. It was postulated that pores act primarily as elastic stress concentrators promoting enhanced crack branching and brittle, transgranular fracture at highly cathodic applied potentials ($-1.1 V_{SCE}$) while load shedding via pore-plasticity promotes intergranular fracture along susceptible PAG boundaries at intermediate potentials ($-0.8 V_{SCE}$).

- The fastest crack growth rates in AM 17-4PH are characterized by intergranular fracture along PAG boundaries at $-0.8 V_{SCE}$. The underlying phenomena driving this behavior could not be determined using the methods in this work. Future work might be able to provide insights into this performance deficit with nanoscale characterization of the PAG boundaries and quantification of H diffusivity in AM 17-4PH.

5.6 Acknowledgements

This research was financially supported by the Office of Naval Research under Grant No. N00014-18-1-2427 with Dr. Airan Perez as the Scientific Officer. Zachary Harris gathered the EBSD data and produced the grain structure and KAM maps.

5.7 References

1. Bloom, F. K. Stress Corrosion Cracking Of Hardenable Stainless Steels. *CORROSION* **11**, 39–49 (1955).
2. Raja, K. S. & Rao, K. P. Effect of Applied Potentials on Environmental Cracking Behavior of 17-4PH Stainless Steel Weldments. *Corros. Sci.* **51**, 498–506 (1995).
3. Jiang, T., Zhong, J., Zhang, X., Wang, W. & Guan, K. Hydrogen embrittlement induced fracture of 17-4 PH stainless steel valve stem. *Eng. Fail. Anal.* **113**, 104576 (2020).
4. Shamsujjoha, M. Evolution of microstructures, dislocation density and arrangement during deformation of low carbon lath martensitic steels. *Mater. Sci. Eng. A* **776**, 139039 (2020).
5. Spagnoli, A., Carpinteri, A. & Vantadori, S. On a kinked crack model to describe the influence of material microstructure on fatigue crack growth. *Frat. ed Integrita Strutt.* **25**, 94–101 (2013).
6. Meggiolaro, M. A. Stress intensity factor equations for branched crack growth. *Eng. Fract. Mech.* **72**, 2647–2671 (2005).

Chapter 6 - Corrosion Fatigue Behavior of AM 17-4PH

6.1 Introduction

The previous three chapters explored the EAC behavior of AM 17-4PH via stress corrosion cracking evaluations at constant or rising monotonic loads. Stress corrosion cracking constitutes one of the two major types of EAC, the other being corrosion fatigue. The cyclic loads involved in corrosion fatigue induce crack extension by a combination of slip accumulation and environmental influences that are mechanistically distinct and/or combinatory with SCC. Therefore, a study of environment assisted sub-critical cracking is not complete without evaluating both corrosion fatigue and SCC behaviors. Furthermore, fatigue cracking is one of the most common causes for real structural failures in engineering applications¹, so understanding the influence(s) of environment on this damage process is critical. To-date, fatigue crack growth evaluations for AM 17-4PH have been limited to lab-air environments, so it is necessary to establish baseline corrosion fatigue behavior in common, fatigue-accelerating environments.

Two common environments that can accelerate fatigue crack growth are humid air and seawater. Though seemingly innocuous, the water content in humidified air has a demonstrable effect on fatigue crack growth due to dissociation of H from the water vapor and subsequent H-embrittlement at the fatigue crack tip². This effect can lead to fatigue crack growth rate differences that are dependent on the environment's relative humidity (RH). Critically, downstream fatigue life predictions can be non-conservative if based on growth rates gathered in dry (RH <5%) or uncontrolled atmospheric conditions. Seawater is a second major environment of concern, particularly for stainless steels which are commonly deployed in marine applications. The chloride in seawater can breakdown the protective chromium oxide layer in stainless steels^{3,4} and the aqueous environment can support a range of crack tip processes including local acidification and hydrogen embrittlement⁵. Both of these processes in seawater environments can accelerate fatigue crack growth with similar downstream concerns to those mentioned for humidity. Together, these two environments represent a key cross-section for understanding the basic corrosion fatigue response for AM 17-4PH.

The objective of this chapter is to use fracture mechanics based fatigue crack growth rate testing and fractographic analysis to compare the corrosion fatigue performance of AM and wrought 17-4PH in humid air and 0.6M NaCl as a seawater substitute^{6,7}. Growth rates will be gathered and compared for strength-matched wrought and AM 17-4PH in the peak aged and overaged conditions to establish their

relative susceptibilities to corrosion fatigue. For AM 17-4PH, two loading orientations will be tested to identify any anisotropic fatigue behaviors. Post-mortem fractographic analysis will then be used to identify microstructural interactions and susceptibilities to corrosion fatigue. The mechanistic underpinnings for the observed fatigue behaviors will be interpreted using established trends for corrosion fatigue crack growth and through comparison with previous studies on environment assisted cracking of AM 17-4PH.

6.2 Methods

6.2.1 Materials

Wrought and AM 17-4PH was processed for study in this chapter as described in Chapters 2 and 3. The AM material was heat treated using the HIP+SA+460°C/1 h and HIP+SA+552°C/4 h protocols (refer to Chapter 2) that are hereafter called “peak aged” and “overaged” AM 17-4PH, respectively. Similarly, the wrought material was heat treated using the SA+482°C/1 h and SA+552°C/4 h heat treatments that will be called “peak aged” and “overaged” wrought 17-4PH. Fracture specimens for the AM material were tested in the X-Y and Z-Y orientations while all wrought material was tested in the L-T orientation (refer to Chapter 3).

6.2.2 Corrosion Fatigue Evaluation

Fracture mechanics based corrosion fatigue crack growth rate testing was performed using a servo-hydraulic load frame to apply sinusoidal load waveforms. The SENT fracture specimen geometry was used in conjunction with a dcPD system to capture in-situ crack lengths and enable stress intensity (K) controlled loading (additional details in Chapter 3). To control the crack tip environment, an acrylic cell was affixed to the SENT specimen to apply either a gaseous or a liquid environment during fatigue loading. A gaseous, humid air environment (RH > 90%) was obtained by bubbling N₂ gas through deionized water then through the sealed cell. Liquid environment testing was performed in neutral, quiescently aerated 0.6M NaCl (pH = 6.2) flowed through the cell at 20 mL/min. Prior to testing in liquid, the specimen was cleaned and held at the freely corroding open circuit potential (OCP) for 24 h to allow the chemistry to stabilize. After the hold, testing either proceeded freely corroding at OCP or an electrochemical potential (E_{app}) was applied using the procedure described in Chapter 3.

Various fatigue loading protocols were used to capture the corrosion fatigue crack growth rate (da/dN) as a function of stress intensity range (ΔK) or environmental cracking factors. Each test was preceded by pre-cracking 0.25 mm in lab air at a K_{max} of 7 MPa \sqrt{m} with a stress ratio (R) of 0.1 to establish a sharp, initial crack. All primary fatigue testing was then performed at $R = 0.5$ with a loading frequency (f) of 10 Hz. To capture da/dN vs. ΔK , fatigue testing consisted of a three-part protocol consisting of (1) a ΔK shed, (2) constant ΔK , then (3) rising ΔK . The ΔK shed was performed K -controlled starting at $K_{max} > 7$ MPa \sqrt{m} and then a steady ΔK reduction (i.e., shed) until $da/dN \leq 1 \times 10^{-7}$ mm/cycle to establish a threshold

stress intensity range (ΔK_{th}). The normalized stress intensity gradient (C)⁸ during the shed was fixed at -0.75 mm^{-1} . Part two of the protocol was a constant $\Delta K \sim \Delta K_{th}$ for 0.050-0.150 mm of crack extension. If da/dN remained constant (i.e., minimal hysteresis from the shed), then the protocol continued to the next stage. Part three consisted of a constant load waveform producing a rising ΔK as the crack grew. The fatigue test was ended during part three either with fast fracture or just prior to reaching the elastic, yield, or fracture mechanics limit load⁹. Note that the $C = -0.75 \text{ mm}^{-1}$ used for the shed is much more aggressive than the $C = -0.08 \text{ mm}^{-1}$ recommended by ASTM E647⁸; the aggressive C was justified by excellent agreement in the growth rates at overlapping ΔK during the shed and rise. In addition to the three-part protocol, several tests were performed with a fixed ΔK protocol while varying E_{app} or f . For each fixed ΔK test, growth rates were gathered over a minimum of 100 μm of crack extension to establish a mean growth rate and sufficient area for fracture morphology evaluation. To distinguish between growth regions at constant ΔK , regions of growth at $R = 0.1$ were introduced between the primary $R = 0.5$ regions to produce marker bands that aided in fractographic analysis.

After each fatigue test, the fracture surface was imaged and measured using optical and scanning electron microscopy (SEM). The majority of specimens were broken apart to produce a ductile fracture indicating the final crack length, but some specimen fracture surfaces were heat tinted ($250^\circ\text{C}/1 \text{ h}$) ahead of the break for further verification of the final crack length. Measurement of the final crack lengths generally agreed well with the dcPD calculated crack lengths, but recalibrating the dcPD calculation¹⁰ post-test with a fractographically measured feature (e.g., the precrack length) improved agreement to $\pm 0.05 \text{ mm}$. This recalibration procedure was successful for all but the highly negative applied potential ($E_{app} \leq -0.8 \text{ V}_{\text{SCE}}$) tests where two-point corrections¹¹ were needed for accurate growth rate calculations. Fracture morphology evaluations were performed using a FEI Quanta 650 SEM in secondary electron imaging mode. The aforementioned dcPD crack length calculations and fracture surface comparisons enabled accurate correlation of ΔK , f , and E_{app} with each fracture morphology image.

6.3 Results

6.3.1 Fatigue Crack Growth in Humid Air

Fatigue crack growth rates (da/dN) as a function of stress intensity range (ΔK) in humidified air were gathered and compared for AM and wrought 17-4PH at a stress ratio (R) of 0.5 (Fig. 33). In Fig. 33a, the stage I, II, and III regions fatigue crack growth are compared for peak aged wrought loaded in the L-T orientation and AM in the X-Y and Z-Y orientations. Starting at the low ΔK (stage I) region, growth rates are nominally similar between peak aged AM and wrought. If the threshold stress intensity factor⁸ (ΔK_{th}) is defined to be at a growth rate of $1 \times 10^{-7} \text{ mm/cycle}$, then $\Delta K_{th} = 3\text{-}4 \text{ MPa}\sqrt{\text{m}}$ for both material forms indicating similar threshold behavior. As ΔK and da/dN increased in stage I, the growth rates further

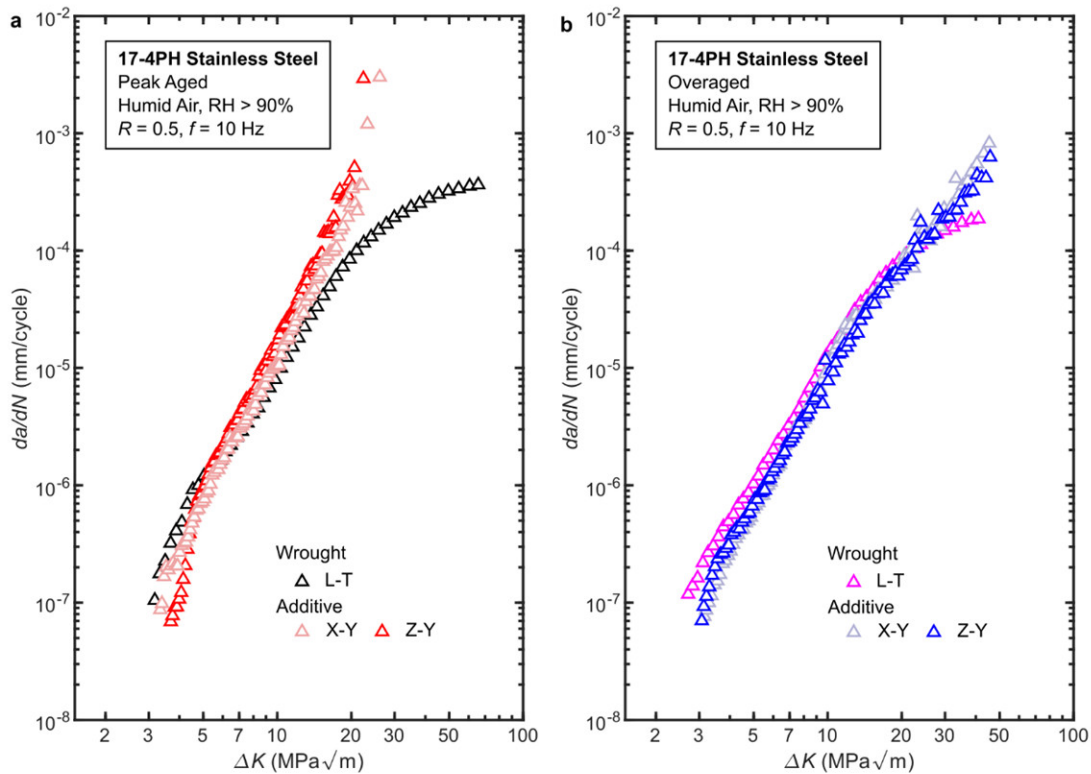


Fig. 33 | **Humid air fatigue crack growth rates for AM and wrought 17-4PH.** **a,** Peak aged 17-4PH. **b,** Overaged 17-4PH. Fatigue crack growth rates (da/dN) in humidified air ($RH > 90\%$) are shown as a function of stress intensity range (ΔK) for multiple loading orientations, forms, and heat treatments of 17-4PH. All data was gathered at a loading frequency (f) of 10 Hz and stress ratio (R) of 0.5.

coalesced and transitioned into stage II growth. Generally, the stage I and II humid air 17-4PH da/dN versus ΔK behavior was linear on the presented log-log scale. To quantify this behavior, Paris law¹² fits were performed on the humid air fatigue crack growth data, refer to Table 4. Across all conditions, the Paris law fits to stage I and II growth were excellent with $R^2 > 0.98$. Comparison of the fits verifies that there is minimal loading orientation dependence in the additive growth rates. However, comparison of the peak aged additive and wrought fits shows a slight difference in n which indicates a different slope for the stage I/II da/dN versus ΔK behavior. For the peak aged additive material, the growth followed the Paris-like behavior up to fast fracture at $\Delta K \sim 26 \text{ MPa}\sqrt{\text{m}}$, but the Paris law fits broke down for the wrought material as the fatigue crack growth transitioned to stage III. The wrought growth rate deviated below the Paris line starting at $\Delta K \sim 20 \text{ MPa}\sqrt{\text{m}}$ by leveling off at a maximum $da/dN \sim 3 \times 10^{-4} \text{ mm/cycle}$. The peak aged wrought test did not fast fracture and was halted manually to remain below the fracture mechanics limit load⁹. These differences in high ΔK behaviors indicate that the AM form has a lower cyclic toughness, and likely a lower fracture toughness, than its wrought equivalent.

Table 4 | **Paris law fits for AM and wrought 17-4PH fatigue crack growth in humid air.** A Paris law of the form $da/dN = C(\Delta K)^n$ was fitted to humid air fatigue crack growth rate data ($R = 0.5, f = 10$ Hz) for various forms, loading orientations, and heat treatments of 17-4PH. The units for C are $(\text{mm/cycle})/(\text{MPa}\sqrt{\text{m}})^n$. The displayed coefficient of determination (R^2) values are valid in the additive conditions for $3 \text{ MPa}\sqrt{\text{m}} \leq \Delta K < 50 \text{ MPa}\sqrt{\text{m}}$ and wrought for $3 \text{ MPa}\sqrt{\text{m}} \leq \Delta K < 20 \text{ MPa}\sqrt{\text{m}}$.

Form/Heat Treat	Orientation	C	n	R^2
Additive				
Peak Aged	X-Y	7.55×10^{-10}	4.24	0.992
	Z-Y	3.68×10^{-10}	4.67	0.982
Overaged	X-Y	2.90×10^{-9}	3.39	0.987
	Z-Y	4.30×10^{-9}	3.21	0.989
Wrought				
Peak Aged	L-T	3.89×10^{-9}	3.38	0.992
Overaged	L-T	4.51×10^{-9}	3.40	0.998

In the overaged condition, humid air fatigue crack growth rate was again largely similar between AM and wrought 17-4PH (Fig. 33b). No significant form or loading orientation dependence was observed at threshold with $\Delta K_{th} = 2.5\text{-}3.0 \text{ MPa}\sqrt{\text{m}}$. Review of the Paris law fits (Table 4) shows better correspondence of overaged wrought and AM 17-4PH stage I/II fatigue crack growth than in the peak aged condition. Notably, stage III growth for overaged AM 17-4PH did not conclude with fast fracture. Instead, the growth rate followed Paris-like behavior up to $\Delta K = 50 \text{ MPa}\sqrt{\text{m}}$ where the test was halted to remain below the fracture mechanics limit load. The overaged wrought material had largely similar stage III growth behavior to the peak aged wrought material with deviation from the Paris fit and a leveling off of the growth rate at high ΔK .

Consistent with the growth rate behaviors, the humid air fatigue crack growth morphologies were similar for AM and wrought 17-4PH except at high ΔK . In all conditions, stage I crack growth was transgranular with some faceted fracture features appearing in stage II growth (images not shown). Primary differences between the AM and wrought humid air fatigue fracture morphologies occurred in the high ΔK , stage III region, refer to Fig. 34. Reviewing these fracture morphologies shows that wrought in both the peak aged and overaged condition exhibited similar rough, transgranular (TG) fracture morphologies with large amounts of plasticity and tearing at $\Delta K \geq 25 \text{ MPa}\sqrt{\text{m}}$ (Fig. 34a,b). Conversely, AM 17-4PH in the peak aged condition exhibited a quasi-cleavage dominated fracture surface (Fig. 34c) consistent with the brittle, fast fracture at high ΔK (Fig. 33a). In the overaged condition, the AM 17-4PH fracture surface was covered with dimples (Fig. 34d) consistent with a ductile fracture mode at $\Delta K \geq 25 \text{ MPa}\sqrt{\text{m}}$. The overaged AM material did not undergo a brittle fast fracture (Fig. 33b), so this ductile fracture mode is consistent with the crack growth rate that steadily increased at high ΔK .

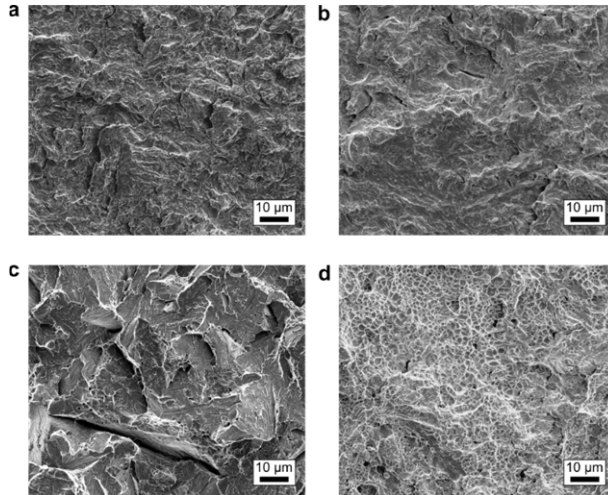


Fig. 34 | **High ΔK fatigue fracture morphology for AM and wrought 17-4PH.** **a-b,** Wrought in the peak aged (**a**) and overaged (**b**) condition. **c-d,** AM in the peak aged (**c**) and overaged (**d**) condition. Fatigue fracture surfaces shown resulted from humid air conditions at $\Delta K \geq 25 \text{ MPa}\sqrt{\text{m}}$, $R = 0.5$ for the various forms and heat treatments of 17-4PH.

6.3.2 Fatigue Crack Growth in 0.6M NaCl

To investigate the effect of a semi-aggressive environment, fatigue crack growth behavior was compared for AM and wrought 17-4PH in 0.6M NaCl under freely corroding conditions (open circuit potential, OCP). The OCP was monitored throughout testing and stayed relatively constant for all studied 17-4PH conditions at $E_{OCP} = -0.190 \pm 0.050 \text{ V}_{SCE}$. Fatigue crack growth rates are first compared for peak aged wrought and AM 17-4PH in Fig. 35a. In a similar manner to the humid air evaluation, growth rates were gathered ranging through the stage I, II, and III growth regions. In the higher ΔK stage II and III regions, the growth rates are strikingly similar between humid air (Fig. 33a) and 0.6M NaCl at OCP (Fig. 35a). However, there is a knee in the 0.6M NaCl growth rate curves occurring at $\Delta K \leq 9 \text{ MPa}\sqrt{\text{m}}$ where growth is accelerated relative to the consistent Paris-like behavior in humid air. This results in $\Delta K_{th} \sim 2 \text{ MPa}\sqrt{\text{m}}$ in 0.6M NaCl versus 3-4 $\text{MPa}\sqrt{\text{m}}$ in humid air. Notably, this acceleration is constant for both the wrought and additive forms with no loading orientation dependence. To further evaluate the accelerated growth behavior, fractographs are shown for wrought (Fig. 35b,d,f) and additive (Fig. 35c,e,g) at $\Delta K = 3 \text{ MPa}\sqrt{\text{m}}$ (Fig. 35b,c), $\Delta K = 5 \text{ MPa}\sqrt{\text{m}}$ (Fig. 35d,e), and $\Delta K = 7 \text{ MPa}\sqrt{\text{m}}$ (Fig. 35f,g). At $\Delta K < 3 \text{ MPa}\sqrt{\text{m}}$, there is an order of magnitude acceleration in growth rate between humid air (Fig. 33a) and 0.6M NaCl at OCP (Fig. 35a), but the transgranular morphology noted for humid air conditions persists in 0.6M NaCl (Fig. 35b,c). This transgranular morphology is maintained through $\Delta K = 5 \text{ MPa}\sqrt{\text{m}}$ (Fig. 35d,e) until $\Delta K = 7 \text{ MPa}\sqrt{\text{m}}$ (Fig. 35f,g) where faceted fracture starts to appear. These images also demonstrate that the fracture morphology for peak aged AM and wrought 17-4PH is similar, like the growth rate, in this environmentally accelerated growth region.

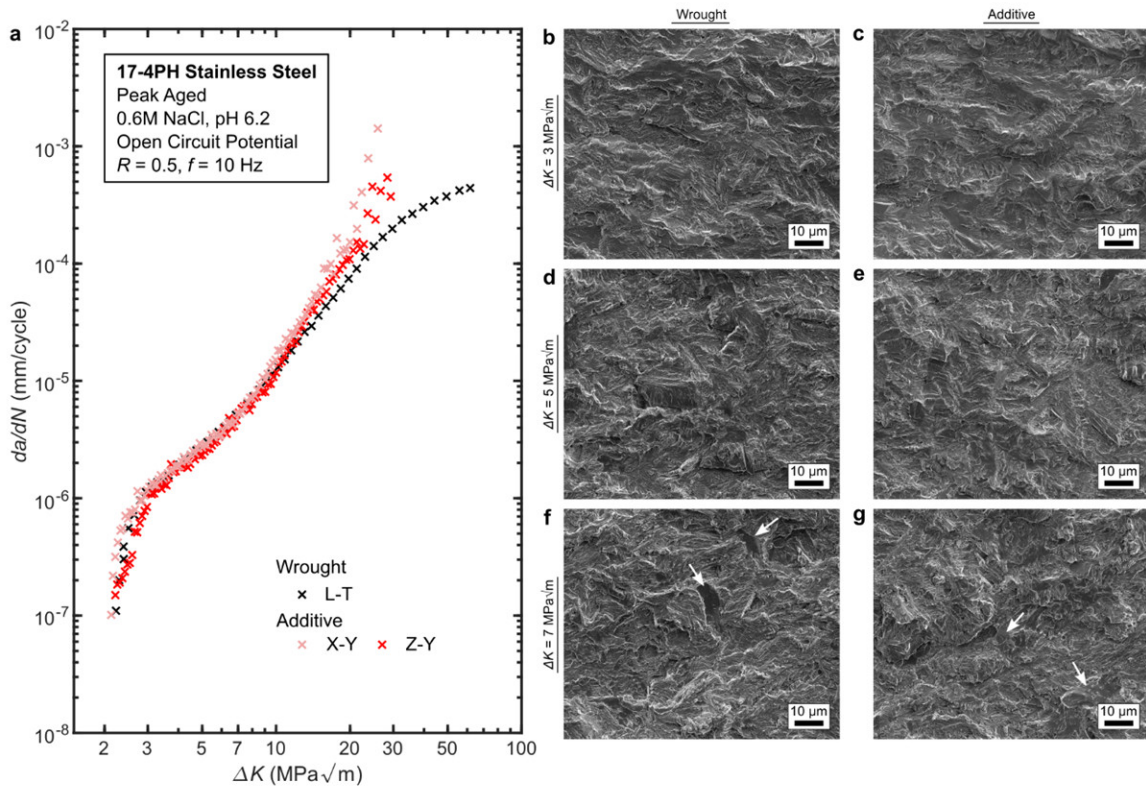


Fig. 35 | Open circuit potential 0.6M NaCl corrosion fatigue crack growth behavior for peak aged AM and wrought 17-4PH. **a**, Corrosion fatigue crack growth rate as a function of stress intensity range. **b-c**, $\Delta K = 3 \text{ MPa}\sqrt{\text{m}}$ fractography. **d-e**, $\Delta K = 5 \text{ MPa}\sqrt{\text{m}}$ fractography. **f-g**, $\Delta K = 7 \text{ MPa}\sqrt{\text{m}}$ fractography. Fractographs shown are representative of peak aged wrought (**b,d,f**) and additive (**c,e,g**) 17-4PH corrosion fatigue crack growth in neutral 0.6M NaCl (pH 6.2) under free corroding conditions (open circuit potential) at $R = 0.5$ and $f = 10 \text{ Hz}$. White arrows indicate the onset of faceted fatigue fracture.

Fatigue crack growth behavior for overaged wrought and AM 17-4PH in 0.6M NaCl at OCP is shown in Fig. 36. These data show that the overaged crack growth rates (Fig. 36a) do not undergo same the level of acceleration in 0.6M NaCl (i.e., relative to humid air in Fig. 33b) that was observed for the peak aged material (Fig. 33a, Fig. 35a). There is a growth rate acceleration at $\Delta K < 9 \text{ MPa}\sqrt{\text{m}}$ in 0.6 NaCl, but, for example, there is about half an order of magnitude of acceleration at $\Delta K = 3 \text{ MPa}\sqrt{\text{m}}$ in the overaged condition versus the full order of magnitude increase noted for the peak aged material. Similarly, the threshold stress intensity range was minimally impacted in the overaged condition shifting from 2.5-3.0 $\text{MPa}\sqrt{\text{m}}$ in humid air versus 2.0-2.5 $\text{MPa}\sqrt{\text{m}}$ in 0.6M NaCl at OCP. Both additive and wrought underwent similar levels of environmental acceleration which is again corroborated by similar fractographic behavior (Fig. 36b-g). The most notable fractographic feature in the overaged condition is the appearance of faceted fracture at lower ΔK (Fig. 36d,e) than in the peak aged condition (Fig. 35f,g), but this faceted type fracture appears at the same ΔK for both additive and wrought.

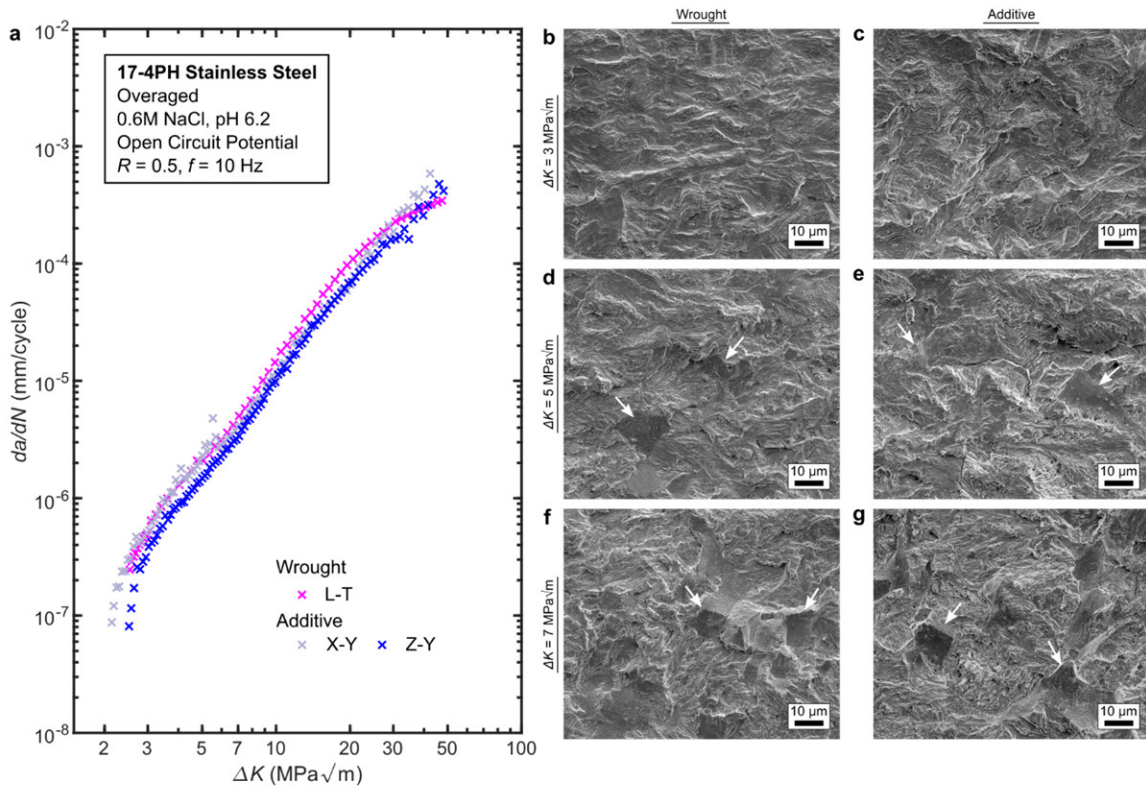


Fig. 36 | **Open circuit potential 0.6M NaCl corrosion fatigue crack growth behavior for overaged AM and wrought 17-4PH.** **a**, Corrosion fatigue crack growth rate as a function of stress intensity range. **b-c**, $\Delta K = 3$ MPa \sqrt{m} fractography. **d-e**, $\Delta K = 5$ MPa \sqrt{m} fractography. **f-g**, $\Delta K = 7$ MPa \sqrt{m} fractography. Fractographs shown are representative of overaged wrought (**b,d,f**) and additive (**c,e,g**) 17-4PH corrosion fatigue crack growth in neutral 0.6M NaCl (pH 6.2) under free corroding conditions (open circuit potential) at $R = 0.5$ and $f = 10$ Hz. White arrows indicate the onset of faceted fatigue fracture.

The previous data demonstrate that, for a given temper, wrought and AM 17-4PH experience similar levels of environmentally accelerated fatigue cracking in 0.6M NaCl at OCP. For both tempers, growth rates accelerated above the milder humid air baseline at $\Delta K < 9$ MPa \sqrt{m} in OCP 0.6M NaCl, but at $\Delta K > 9$ MPa \sqrt{m} the 0.6M NaCl and humid air growth rates coalesced. This establishes two regimes: (1) a region of mechanically dominated growth (i.e., $\Delta K > 9$ MPa \sqrt{m}) and (2) an environmentally enhanced growth region (i.e., $\Delta K < 9$ MPa \sqrt{m}). To further compare the effect of environment on AM and wrought 17-4PH fatigue crack growth, peak aged AM and wrought 17-4PH fatigue crack behavior was evaluated within the environmentally enhanced region ($\Delta K = 5$ MPa \sqrt{m}) for a range of applied potentials (E_{app}) in 0.6M NaCl, refer to Fig. 37. Note that a potential range of $-0.19 V_{SCE} < E_{app} < 1.2 V_{SCE}$ was chosen to explore the effect of cathodic applied potentials (i.e., $E_{app} < E_{OCP}$). The fatigue crack growth rates obtained in Fig. 37a indicate a trough-like behavior for both AM and wrought 17-4PH as follows: (1) at one edge of the trough the growth rates peak at $E_{app} \sim OCP$, (2) at the trough-bottom growth rates decrease at intermediate E_{app} , and (3) at the other edge of the trough the growth rates peak again at highly negative

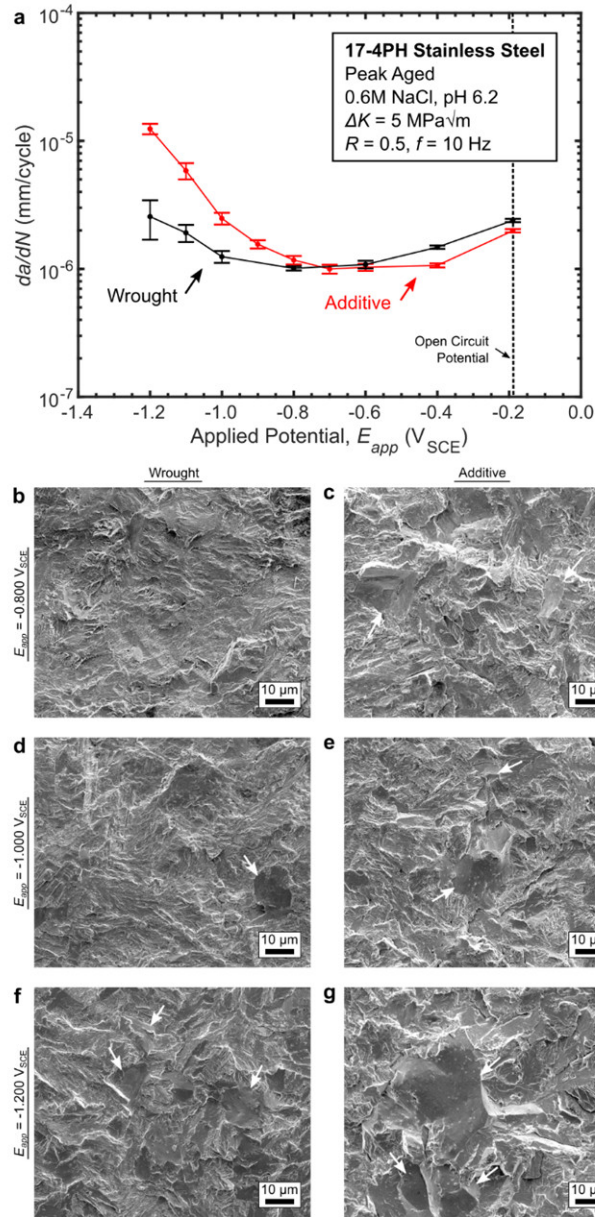


Fig. 37 | Variation of corrosion fatigue crack growth behavior with applied potential for peak aged AM and wrought 17-4PH. a, Fatigue crack growth rate variation with applied potential. b-c, $E_{app} = -0.8 \text{ V}_{SCE}$ fractography. d-e, $E_{app} = -1.0 \text{ V}_{SCE}$ fractography. f-g, $E_{app} = -1.2 \text{ V}_{SCE}$ fractography. Fractographs shown are representative of peak aged wrought (b,d,f) and additive (c,e,g) 17-4PH corrosion fatigue crack growth in neutral 0.6M NaCl (pH 6.2) at various applied potentials with fixed $\Delta K = 5 \text{ MPa}\sqrt{\text{m}}$, $R = 0.5$, and $f = 10 \text{ Hz}$. White arrows indicate the onset of faceted fatigue fracture.

(cathodic) E_{app} . Comparison of the peak at $E_{app} \sim E_{OCP}$ ($2 \times 10^{-6} \text{ mm/cycle}$, Fig. 37a) shows good agreement with the previously gathered data under freely corroding conditions ($\sim 2.3 \times 10^{-6} \text{ mm/cycle}$, Fig. 35a); this highlights the ability of the potentiostat to replicate a known environment. For the trough-bottom, both AM and wrought reach a growth rate minimum of $\sim 1 \times 10^{-6} \text{ mm/cycle}$ ($E_{app} = -0.7 \text{ V}_{SCE}$, Fig. 37a) which is approximately equal to their respective growth rates in humid air with a matched mechanical driving force

(i.e., $da/dN = 1 \times 10^{-6}$ mm/cycle at $\Delta K = 5$ MPa \sqrt{m} in Fig. 33a). This indicates that the applied potentials within this trough are driving crack growth to a mechanically rather than environmentally dominated mode. Critically, the width and bounds of this trough-bottom indicate the relative environmental susceptibility of AM and wrought. The E_{app} range for the AM trough ($-0.8 V_{SCE} < E_{app} < -0.4 V_{SCE}$) is 100 mV less-wide than the wrought trough ($-1.0 V_{SCE} < E_{app} < -0.5 V_{SCE}$) indicating a higher range of AM environmental susceptibility. Additionally, the cathodic takeoff potential for AM ($E_{app} = -0.8 V_{SCE}$) is 200 mV higher than wrought ($E_{app} = -1.0 V_{SCE}$) indicating a higher susceptibility to cathodic potentials for AM.

In order to understand this enhanced AM 17-4PH fatigue crack growth in 0.6M NaCl at cathodic applied potentials, a series of fractographs are shown starting at the $-0.8 V_{SCE}$ “takeoff” potential, see Fig. 37b-g. Beginning with the wrought behavior, Fig. 37b shows transgranular fracture at $E_{app} = -0.8 V_{SCE}$ that is representative of $-0.8 V_{SCE} < E_{app} < -0.19 V_{SCE}$ and consistent with the previously discussed OCP fracture behavior (Fig. 35d). The onset of enhanced crack growth rates occurred in wrought at $E_{app} = -1.0 V_{SCE}$, and the fractograph in Fig. 37d shows that this is correlated with the onset of faceted fracture. This faceted fracture correlation is further corroborated by Fig. 37f at $E_{app} = -1.2 V_{SCE}$ where the number and size of these facets is magnified. Consistent with the wrought behavior, the AM material was transgranular at OCP and intermediate applied potentials (i.e., $E_{app} > -0.8 V_{SCE}$, images not shown) until the onset of enhanced growth at $E_{app} = -0.8 V_{SCE}$. For the additive material, the onset of increased growth rate is correlated with faceted fractures starting at $-0.8 V_{SCE}$ (Fig. 37c) that steadily increase in size and number at $-1.0 V_{SCE}$ (Fig. 37e) and reach a maximum at $E_{app} = -1.2 V_{SCE}$ (Fig. 37g). Notably, these fracture features have been described simply “facets” because it was unclear whether cleavage was occurring in a transgranular fashion or if the facets were intergranular in nature. With the rounded morphology revealed by some of the larger facets in Fig. 37d, it is likely that some, if not all, of these facets are intergranular fractures occurring along prior-austenite grain boundaries (refer to Chapter 3).

6.4 Discussion

The preceding fatigue crack growth evaluations provide three, key takeaways for understanding the relative corrosion fatigue performance of AM and wrought 17-4PH. First, stage I and II fatigue crack growth behavior in humid air and 0.6M NaCl at OCP is similar for AM and wrought in both the peak aged and overaged conditions. Both material forms followed Paris-like behavior in humid air and underwent a similar growth rate acceleration at $\Delta K < 9$ MPa \sqrt{m} in 0.6M NaCl at OCP. Second, constant ΔK testing in the environmentally dominated region of fatigue (i.e., $\Delta K < 9$ MPa \sqrt{m}) showed that AM 17-4PH has a higher susceptibility to cathodic applied potentials in 0.6M NaCl. This manifested as a less-wide “trough” of reduced E_{app} susceptibility and a less cathodic takeoff potential in AM 17-4PH. Third, the enhanced fatigue crack growth rate under increasingly cathodic applied potential was fractographically correlated to the onset

of faceted (likely intergranular) fatigue fracture in both AM and wrought 17-4PH. These observations lead to the following questions:

1. Why do wrought and AM 17-4PH perform equally well in humid air and 0.6M NaCl at OCP, but AM underperforms relative to wrought at cathodic applied potentials in 0.6M NaCl?
2. What are the microstructural underpinnings of corrosion fatigue crack growth performance differences for AM and wrought 17-4PH in 0.6M NaCl at cathodic applied potentials?

The following discussion will first contextualize the gathered data within established trends and mechanisms for corrosion accelerated fatigue crack growth. This context will be used to identify the likely mechanisms for environmentally accelerated fatigue observed in the current work. With this mechanistic basis, possible microstructural origins for enhanced corrosion fatigue susceptibility in AM 17-4PH will be commented upon within the context of current and previous environment assisted cracking work on the alloy.

6.4.1 17-4PH Corrosion Fatigue Mechanisms

The shape of the fatigue crack growth rate curve (i.e., da/dN vs ΔK) may be used to categorize corrosion fatigue behavior into one of three types¹³. These types of corrosion fatigue crack growth are established by comparing growth rate curve(s) in an aggressive environment to an inert environment curve. The first type, Type A, consists of a generally higher da/dN at low ΔK (or K_{max}) in the aggressive environment that eventually coalesces with the inert environment curve at high ΔK . This signifies a “true” corrosion fatigue behavior where the environment is accelerating the fatigue process until mechanical fatigue overwhelms the effect of environment at high ΔK . Types B and C involve a superposition of corrosion fatigue and a second environmentally assisted crack process, stress corrosion cracking (SCC). For Type B, the aggressive environment growth rate equals the inert environment growth rate until K_{max} exceeds the threshold for stress corrosion cracking (K_{TH}); this results in a sharp increase in the aggressive environment’s da/dN at $K_{max} \geq K_{TH}$. Unlike Type B, Type C involves a superposition of both true corrosion fatigue and SCC. The general acceleration of Type A growth is superimposed onto Type B growth to produce a Type C da/dN vs ΔK curve. These “type” distinctions are useful because they may be used to identify the underlying environmentally assisted cracking mechanism(s) (i.e., mechanical fatigue, true corrosion fatigue, and/or stress corrosion cracking) responsible for accelerated da/dN in a given aggressive environment.

In the current work, these types may be used to identify the underlying mechanism for 17-4PH environmentally accelerated fatigue crack growth in 0.6M NaCl at OCP. As previously mentioned, a region of environmental acceleration is present for $\Delta K < 9 \text{ MPa}\sqrt{\text{m}}$ in 0.6M NaCl at OCP for both wrought and

AM 17-4PH when compared to humid air behavior. If humid air is considered to be the “inert” environment for the purposes of this analysis, then the general da/dN acceleration $\Delta K < 9 \text{ MPa}\sqrt{\text{m}}$ and absence of a sharp increase in da/dN at intermediate ΔK (i.e., no K_{TH} -type behavior) indicates that true corrosion fatigue behavior is occurring in 0.6M NaCl at OCP. Previous wrought 17-4PH corrosion fatigue work¹⁴ has discussed the likely mechanism for this form of corrosion fatigue as proceeding by (1) passive film rupture at the crack tip, (2) metal ion hydrolysis resulting in crack tip acidification, (3) anodic dissolution at the crack tip, and (4) dissolution-associated H-production that enables H-enhanced fatigue crack growth. This dissolution-based mechanism is consistent with fractographic similarities mentioned for humid air and 0.6M NaCl at OCP at low ΔK . Dissolution simply accelerated the transgranular crack extension rather than forcing localized fracture like cleavage or intergranular fracture that might be indicative of a secondary fracture mechanism. These observations are important because they establish that the AM process did not introduce microstructural defects or characteristics that modify a dissolution accelerated fatigue process. Further, this behavior is consistent with the work in Chapter 3 that showed similar (lack of) SCC susceptibility for wrought and AM 17-4PH in 0.6M NaCl at OCP.

The aforementioned type categorizations may be extended to understand the crack growth mechanisms active in Fig. 37. As previously mentioned, the $E_{app} = -0.19 \text{ V}_{\text{SCE}}$ results in Fig. 37a accurately simulated the OCP environment in NaCl (Fig. 35a), so the E_{app} versus da/dN curves may be used in combination with the da/dN vs ΔK curves for humid air (Fig. 33a) and 0.6M NaCl at OCP (Fig. 35a) to estimate a “type” behavior at each E_{app} . With $E_{app} = -0.19 \text{ V}_{\text{SCE}}$ established to be Type A behavior by comparison with Fig. 35a, the two remaining areas of interest in Fig. 37a are (1) the bottom of the growth rate trough at $-0.8 \text{ V}_{\text{SCE}} < E_{app} < -0.4 \text{ V}_{\text{SCE}}$ and (2) the growth rate increase at $E_{app} < -0.8 \text{ V}_{\text{SCE}}$. The growth rate correspondence at the bottom of the trough in Fig. 37 with the humid air growth rate (previously discussed in the Results section) might indicate a Type B behavior.

The trend towards humid air growth rates at intermediate E_{app} may be understood by recognizing the change in crack tip environment that occurs with increasingly cathodic E_{app} . At cathodic applied potentials, the acidic crack tip environment at OCP transitions to an alkaline environment¹⁵. Such an environment suppresses the aforementioned crack tip dissolution at OCP, which suppresses H-production, and reduces the environmental acceleration of fatigue crack growth. Cathodic H will be generated at intermediate E_{app} , but comparison of Fig. 33a and Fig. 37a shows H-production is insufficient to exceed humid air growth rates. However, this beneficial growth rate suppression at cathodic E_{app} is confounded by three factors. First, the high loading frequency in Fig. 37 ($f = 10 \text{ Hz}$) may be masking a time-based superposition of SCC based crack growth (i.e., da/dt from Type B behavior). The mechanical contribution from a crack growth rate captured on a cyclic basis (da/dN) at a high loading frequency can overwhelm the

contribution from a fixed da/dt . Second, the low K_{max} evaluated in Fig. 37 (i.e., $K_{max} = 10 \text{ MPa}\sqrt{\text{m}}$ at $\Delta K = 5 \text{ MPa}\sqrt{\text{m}}$, $R = 0.5$) could be below K_{TH} . At a slightly higher K_{max} , SCC effects could initiate resulting in drastically different growth rates. Third, cathodic E_{app} promotes a hydrogen (H) producing environment that could exacerbate H-embrittlement based crack growth acceleration. Of these three factors, the data in Fig. 37 shows evidence of factor three starting at $E_{app} = -0.8 \text{ V}_{\text{SCE}}$ or $-1.1 \text{ V}_{\text{SCE}}$ for AM and wrought 17-4PH, respectively, with growth acceleration and a transition to faceted/intergranular fracture. Less cathodic potentials could also be H embrittlement critical at lower loading frequencies (factor one) and higher mechanical driving forces (factor two).

To firmly establish the relevance of the takeoff potential at $-0.8 \text{ V}_{\text{SCE}}$ in Fig. 37, Fig. 38 shows the effect of both loading frequency and mechanical driving force variation for AM and wrought 17-4PH in 0.6M NaCl at $E_{app} = -0.8 \text{ V}_{\text{SCE}}$. For both material forms, there was negligible growth rate variation with reduction in loading frequency (Fig. 38a). With increasing ΔK , the growth rate increased for both AM and wrought (Fig. 38b), but these growth rate differences are indistinguishable from the humid air response (Fig. 33a). Review of the fracture morphologies yielded by the tests in Fig. 38 (images not shown) also indicated no significant differences from previously discussed fracture behaviors. Since neither f nor ΔK variation at $-0.8 \text{ V}_{\text{SCE}}$ resulted in significant growth rate differences from humid air behavior, these data verify that $-0.8 \text{ V}_{\text{SCE}}$ is a critical takeoff potential for AM 17-4PH H-assisted corrosion fatigue behavior. This result is interesting for two reasons. First, AM 17-4PH processed under the conditions in Fig. 38 has previously been shown to be to be SCC critical at $K > 30 \text{ MPa}\sqrt{\text{m}}$ $-0.8 \text{ V}_{\text{SCE}}$ in 0.6M NaCl (Chapter 3), yet increasing K_{max} to SCC critical levels showed no Type B corrosion fatigue behavior in Fig. 38b (i.e., no sharp increase in da/dN that would indicate K_{TH} exceedance). This indicates that Type A behavior with H-

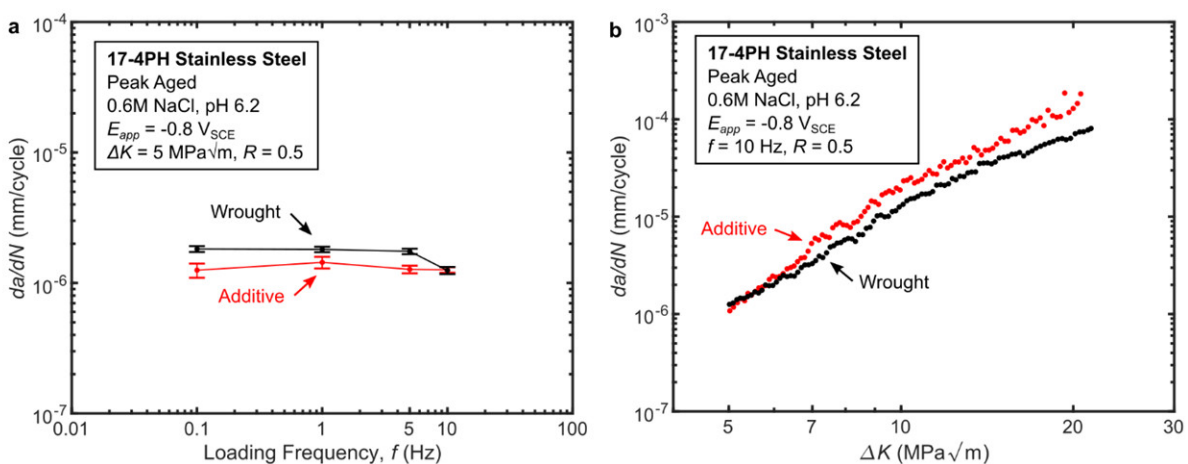


Fig. 38 | Effect of f and ΔK variation on da/dN near the “takeoff potential” for peak aged AM and wrought 17-4PH. a, Effect of loading frequency variation. b, Effect of stress intensity range variation. All corrosion fatigue crack growth rates shown were gathered in neutral 0.6M NaCl (pH 6.2) with fixed $E_{app} = -0.8 \text{ V}_{\text{SCE}}$ and $R = 0.5$.

assisted true corrosion fatigue is the likely mechanism for accelerated fatigue crack growth in 0.6M NaCl at $-0.8 V_{SCE}$, $R = 0.5$ for AM 17-4PH, rather than a superposition of SCC and mechanical fatigue. Second, as f trends to zero the applied load approaches monotonic conditions that should promote SCC. With no change in fatigue behavior observed in Fig. 38a at low f , either K_{TH} was not exceeded or the load perturbations at 0.1 Hz were sufficient to force cyclic-damage based crack growth while suppressing SCC based growth in AM 17-4PH at a known, SCC critical E_{app} .

6.4.2 H-Assisted Fatigue & Microstructure Linkages

The primary differences in AM and wrought 17-4PH corrosion fatigue behavior were observed at highly cathodic applied potentials ($E_{app} \geq 0.8 V_{SCE}$, Fig. 37), so this is the key regime for understanding AM 17-4PH corrosion fatigue performance. The previous discussion established that H-assisted true corrosion fatigue is the likely mechanism for enhanced growth rates at $-0.8 V_{SCE}$. Prior work (Chapter 3,4,5) has established the framework and microstructural origins for AM 17-4PH environmental crack behavior in the context of H-driven SCC. The current, corrosion fatigue context is not completely congruent with that previous SCC work because of the influences of cyclic loading, but there are some relevant corollaries. Specifically, the link between faceted/intergranular fracture and enhanced growth rate at $E_{app} \geq 0.8 V_{SCE}$ in the current work is consistent with previously observed intergranular SCC fracture morphologies and enhanced SCC susceptibility for peak aged AM 17-4PH at $E_{app} \geq 0.8 V_{SCE}$. This comparison shows that the critical environmental conditions and failure interface are similar for both H-assisted SCC and corrosion fatigue crack growth in AM 17-4PH. These similarities dually emphasize the importance and susceptibility of AM 17-4PH intergranular interfaces in H-assisted cracking.

In order to further evaluate the intergranular interfaces in the context of corrosion fatigue, high magnification images of the facets for peak aged wrought and AM 17-4PH are shown in Fig. 39. Notably, the presence of these facets in peak aged wrought 17-4PH (Fig. 39a) differentiates the H-assisted corrosion fatigue crack growth from SCC where the fracture morphology was completely transgranular under the same environmental conditions (Chapter 3). Additionally, the striated morphology on the AM facet in Fig. 39b ($E_{app} = -1.2 V_{SCE}$) supports a fatigue-specific failure mechanism at cathodic potentials beyond $-0.8 V_{SCE}$. But critically, dimples and secondary particles are present on the AM facet whereas the wrought facet is relatively smooth. Ignoring the additional fatigue striations, the particle and dimple decorated corrosion fatigue intergranular facet morphology matches the intergranular SCC morphology in peak aged AM 17-4PH (Chapter 3). Mechanistically, these AM-specific secondary features have been attributed to stress concentration and/or plasticity enhanced H-accumulation in the context of SCC (Chapter 4,5), but the fracture morphology similarities suggest that these processes could also be active in H-assisted corrosion fatigue. This re-emphasizes the degradative effects and importance of the particles, which are likely oxide

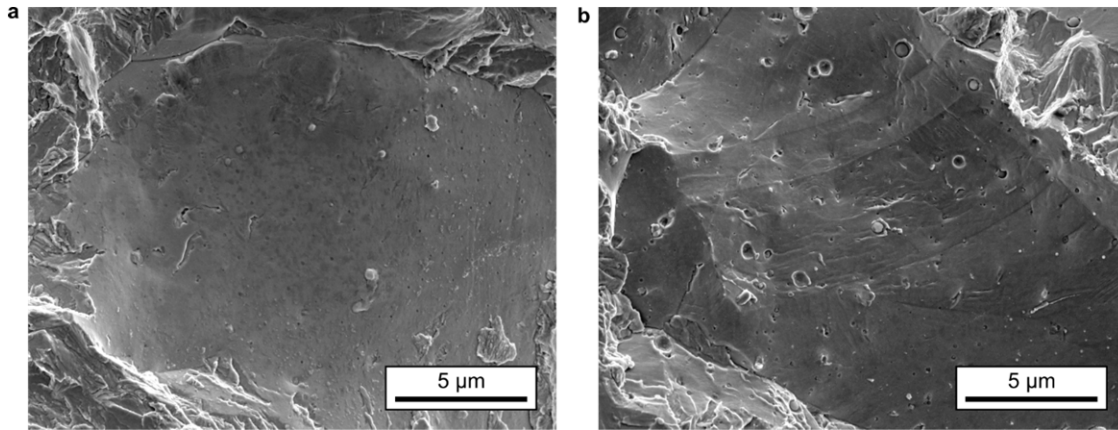


Fig. 39 | **Faceted corrosion fatigue fracture morphology for peak aged AM and wrought 17-4PH in cathodic conditions.** **a**, Wrought. **b**, Additive. Both fractographs were gathered from corrosion fatigue tests in neutral 0.6M NaCl (pH 6.2) with fixed $E_{app} = -1.2 V_{SCE}$, $\Delta K = 5 MPa\sqrt{m}$, and $R = 0.5$.

inclusions resulting from oxygen in the AM powder, and the dimples, which are likely the remnants of Ar gas porosity resulting from the Ar atomized powder and Ar build atmosphere, in H-assisted cracking of AM 17-4PH.

6.4.3 Practical Implications

This work has several implications for the corrosion fatigue performance of AM 17-4PH. First, fatigue crack growth behavior of wrought and AM 17-4PH is largely similar in a mild environment as exemplified by the humid air results. This is particularly true for overaged AM 17-4PH which has higher cyclic toughness than peak aged AM 17-4PH. In a corrosive 0.6M NaCl environment, wrought and AM 17-4PH perform equally well under freely corroding conditions (open circuit potential) and at intermediate cathodic potentials, but AM 17-4PH underperforms versus wrought 17-4PH at highly cathodic potentials. Specifically, peak aged AM 17-4PH has faster crack growth rates at less-cathodic applied potentials ($E_{app} < -0.8 V_{SCE}$) than peak aged wrought 17-4PH. Furthermore, monotonic loading in this highly cathodic regime will promote SCC in AM 17-4PH based on previous work. Both of these environmentally enhanced cracking behaviors in AM 17-4PH have been linked to sub-micrometer scale porosity and oxide inclusions uniquely present in the AM 17-4PH microstructure. These microstructure-performance linkages provide either (1) clear limitations for AM 17-4PH usage or (2) the opportunity to enhance the alloy's performance. For the former, AM 17-4PH processed as described in this work can be expected to have similar fatigue crack growth performance to wrought 17-4PH except at highly cathodic applied potentials. For the latter, future AM processing strategies should attempt to target and remove sub-micrometer scale porosity and oxide inclusions in AM 17-4PH. If successful, removal of those deleterious features might amend the aforementioned performance limitation and yield wrought-level corrosion fatigue crack growth performance.

6.5 Conclusions

Fracture mechanics based corrosion fatigue crack growth rate testing and fractographic analysis was used to compare the environmental cracking performance of AM and wrought 17-4PH. Strength-matched peak aged and overaged tempers of the two materials were compared primarily at $R = 0.5$ and $f = 10$ Hz in humid air and 0.6M NaCl environments. In 0.6M NaCl, various electrochemical potentials were applied to evaluate corrosion fatigue responses in a wide range of environments. The following are key conclusions from this study:

- With the processing schedule in this study, corrosion fatigue crack growth rates in AM 17-4PH were not found to be orientation dependent.
- In humid air, AM and wrought 17-4PH exhibit similar Paris-like behavior and growth rates up to $\Delta K = 20 \text{ MPa}\sqrt{\text{m}}$. At $\Delta K > 20 \text{ MPa}\sqrt{\text{m}}$, AM 17-4PH cracks faster than wrought 17-4PH. These faster AM growth rates were associated with cleavage and dimpled fracture morphologies in the peak aged and overaged conditions, respectively.
- In 0.6M NaCl at open circuit potential, AM and wrought 17-4PH undergo similar dissolution-based fatigue crack growth rate acceleration at $\Delta K \leq 9 \text{ MPa}\sqrt{\text{m}}$.
- For peak aged 17-4PH in 0.6M NaCl at cathodic applied potentials, dissolution-based fatigue crack growth acceleration is inhibited at intermediate applied potentials ($-0.8 \text{ V}_{\text{SCE}} < E_{\text{app}} < -0.5 \text{ V}_{\text{SCE}}$), but crack growth re-accelerates with cathodic H-assisted corrosion fatigue at $E_{\text{app}} \leq -0.8 \text{ V}_{\text{SCE}}$ for AM 17-4PH and $E_{\text{app}} \leq -1.0 \text{ V}_{\text{SCE}}$ for wrought 17-4PH.
- Cathodic H-assisted corrosion fatigue crack growth is typified by the onset of faceted/intergranular fracture morphologies for both wrought and AM 17-4PH, but these fracture features are uniquely decorated by porosity and oxide inclusions in AM 17-4PH.
- Increased cathodic H-assisted corrosion fatigue susceptibility and growth rate in AM 17-4PH is attributed to pore/inclusion interactions through comparison with previous stress corrosion cracking evaluations of the alloy.

6.6 Acknowledgements

This research was financially supported by the Office of Naval Research under Grant No. N00014-18-1-2427 with Dr. Airan Perez as the Scientific Officer.

6.7 References

1. Findlay, S. J. & Harrison, N. D. Why aircraft fail. *Mater. Today* **5**, 18–25 (2002).

2. Petit, J., Hénaff, G. & Sarrazin-Baudoux, C. Environmentally Assisted Fatigue in the Gaseous Atmosphere. in *Comprehensive Structural Integrity* **6**, 211–280 (Elsevier, 2003).
3. Soltis, J. Passivity breakdown, pit initiation and propagation of pits in metallic materials - Review. *Corros. Sci.* **90**, 5–22 (2015).
4. Donahue, J. R. & Burns, J. T. Effect of chloride concentration on the corrosion-fatigue crack behavior of an age-hardenable martensitic stainless steel. *Int. J. Fatigue* **91**, 79–99 (2016).
5. Turnbull, A. Environment-assisted Fatigue in Liquid Environments. in *Comprehensive Structural Integrity, Volume 6* (eds. Milne, I., Ritchie, R. O. & Karihaloo, B.) 163–210 (Elsevier, 2003).
6. Bogar, F. D. & Crooker, T. W. The Influence of Bulk-Solution-Chemistry Conditions on Marine Corrosion Fatigue Crack Growth Rate. *J. Test. Eval.* **7**, 155–159 (1979).
7. Ijsseling, F. P. General guidelines for corrosion testing of materials for marine applications. *Br. Corros. J.* **24**, 53–78 (1989).
8. ASTM International. ASTM E647-15e1 Standard Test Method for Measurement of Fatigue Crack Growth Rates. (2015). doi:10.1520/E0647-15E01
9. Anderson, T. L. *Fracture Mechanics: Fundamentals and Applications*. (CRC Press, 2005). doi:10.1201/9781420058215
10. Johnson, H. H. Calibrating the Electric Potential Method for Studying Slow Crack Growth. *Mater. Res. Stand.* **5**, 442–445 (1965).
11. Axelsson, N. & Baric, J. Improved data regression methods for crack growth characterization. (Chalmers University of Technology, 2016).
12. Chowdhury, P. & Sehitoglu, H. Mechanisms of fatigue crack growth - A critical digest of theoretical developments. *Fatigue Fract. Eng. Mater. Struct.* **39**, 652–674 (2016).
13. McEvily, A. J. & Wei, R. P. *AFOSR-TR-72-0408 Fracture Mechanics and Corrosion Fatigue*. (1972).
14. Lin, C.-K. & Lin, C.-P. Corrosion Fatigue Behavior of 17-4PH Stainless Steel in Different Tempers. in *Fatigue and Fracture Mechanics: 33rd Volume, ASTM STP 1417* (eds. Reuter, W. G. & Piascik, R. S.) 598–613 (ASTM International, 2002).
15. Yong, L., Zhiyong, L., Endian, F., Zhongyu, C. & Jinbin, Z. The effect of crack tip environment on crack growth behaviour of a low alloy steel at cathodic potentials in artificial seawater. *J. Mater. Sci. Technol.* **54**, 119–131 (2020).

Chapter 7 - Fatigue Crack Path Deflection and Residual Stresses in 17-4PH Stainless Steel Rod

7.1 Introduction

As discussed in Chapters 1 and 6, fatigue is a prominent failure mode for metallic structures used in engineering applications¹. Specifically, cyclic loading of a sufficient magnitude will induce a fatigue damage accumulation process resulting in crack nucleation, growth, and eventual fracture. This has motivated the development of several paradigms²⁻⁴ for predicting and/or managing the subcritical cracking associated with fatigue. Of these, the damage-tolerance paradigm⁵ is widely utilized in the aerospace industry where safety-of-flight structures are commonly subject to fatigue-critical conditions. This damage-tolerance paradigm relies on an assumed initial flaw that grows based on known material-loading interactions resulting in a predictable component life (i.e., number of load cycles to failure). Fundamentally, this approach to structural life management depends on translating the empirically measured fatigue crack growth rates from an exemplar material coupon to a more complex structure composed of the same material via the idea of fracture mechanics similitude⁶.

The reliance of the damage tolerance paradigm on empirically-measured fatigue crack growth rates underscores the importance of understanding the various factors that can affect a measured growth rate. For engineering purposes, fatigue crack growth rates are typically presented as a function of a stress intensity range (ΔK) with a given stress ratio (R) for a given material⁷. Based on the fracture mechanics similitude principle alone, these two factors should be sufficient to specify a material's fatigue crack growth rate, so processes and guidelines for reliably obtaining these datasets are provided in standards like ASTM E647⁸. However, simply determining a growth rate for a given ΔK , R , and material combination does not capture many nuances that can drastically modify an observed fatigue crack growth rate. As a few examples, the fatigue crack growth rate is subject to modification through differences in short versus long crack behavior⁹, microstructure influences on a crack tip stress field¹⁰, growth retardation due to variations in load waveform¹¹, residual stress effects^{12,13}, crack path modifications to the stress intensity¹⁴, environmental impacts on crack growth¹⁵, crack closure¹⁶, etc. These various modifiers can act alone or together to produce order of magnitude changes in a measured fatigue crack growth rate for a given material/stress intensity

range/stress ratio combination. Critically, these crack growth rate modifications can strongly impact downstream component life prediction and safe management of engineering structures.

The typical goal in measuring a fatigue crack growth rate is to gather the intrinsic fatigue crack growth response of a material. As such, the aforementioned confounding variables that can influence the growth rate are typically accounted for and/or controlled during growth rate testing. However, this elimination/control strategy can become difficult with the large number of possible modifiers to the fatigue process. The current chapter highlights a case where standard, fracture mechanics based fatigue crack growth rate measurement techniques produced anomalous growth rate and crack path behaviors that seemed to defy fracture mechanics similitude. Specifically, similitude was compromised during testing of a round rod material form of 17-4PH stainless steel but was not compromised for an equivalent-strength plate form of the same alloy. Given that variations in fatigue behavior between material forms are typically considered to be minimal with similar strength, microstructures, etc., the objective of this chapter is to quantify these anomalous fatigue behaviors and systematically investigate their microstructural and mechanistic origins. The effectiveness of fatigue process modifier elimination/control strategies like constraint modification, closure control, environment control, and microstructure modification are applied and evaluated via constant ΔK test strategies. The chapter concludes with residual stress characterization in the 17-4PH rod and an assessment of residual stress's role in these seemingly anomalous fatigue crack growth behaviors.

7.2 Methods

7.2.1 Materials

Two material forms of 17-4PH stainless steel were obtained from commercial suppliers and evaluated during this study. The first form was electric furnace (EF) melted, argon oxygen decarburized (AOD), hot-rolled, and centerless ground 15.9 mm diameter round rod (hereafter referred to as “rod”). The second form was EF melted, AOD refined, and hot-rolled 15.9 mm thick plate (hereafter referred to as “plate”). Both forms were solution annealed by their respective manufacturers, constituting the “As Received” (AR) condition. The manufacturer for the rod indicated a 1040°C/1 h/air cool solution anneal while the plate manufacturer indicated a 1040°C solution anneal for an unspecified time with an unspecified cooling rate. Elemental compositions for both forms of 17-4PH were measured by a commercial lab via glow discharge mass spectroscopy and inductively coupled plasma optical emission spectroscopy, refer to Table 5. A variety of heat treatments were performed on the materials after receipt, refer to Table 6. The H900 and H1025 heat treatment conditions represent common engineering tempers for peak strength or increased toughness, respectively. The SA condition represents the effects of a second solution anneal. Tensile testing was performed in accordance with ASTM E8¹⁷ at a constant displacement rate of 8×10^{-4} mm/s with an 8 mm gage length clip-on extensometer to measure modulus of elasticity (E), yield strength

Table 5 | Elemental compositions of the 17-4PH plate and rod used in this study in weight %.

Form	C	Mn	P	S	Si	Cr	Ni	Cu	Nb	Fe
Plate	0.041	0.51	0.018	0.001	0.32	15.20	4.85	3.22	0.26	bal.
Rod	0.034	0.41	0.017	0.001	0.66	14.80	4.70	3.11	0.26	bal.

Table 6 | Heat treatment codes/designations and associated processing parameters used in this study.

Heat Treat Code	Processing Details
AR - As Received	Solution annealed by the manufacturer.
H900 - Peak Aged	AR; Machine specimen; 482°C/1 h in lab air, air cool.
H1025 - Overaged	AR; Machine specimen; 552°C/4 h in lab air, air cool.
SA - Solution Annealed	AR; 1040°C/0.5 h in lab air, air cool; Machine specimen.

(σ_{YS}), ultimate strength (σ_u), and engineering strain at failure (e_f). Rockwell hardness (HRC) was determined via Vickers hardness measurements that were converted to HRC in accordance with ASTM E384/E140^{18,19}.

Microstructure was evaluated using the electron backscatter diffraction (EBSD) technique and electrolytic etching. Samples were prepared by mounting in cold-curing epoxy resin, incrementally grinding using 320/600/800/1200 grit paper, polishing incrementally using 3/1/0.5/0.25/0.1 μm polycrystalline diamond slurries, and finish polishing using 0.05 μm alumina or colloidal silica. Multiple material planes (i.e., relative to the hot-rolling direction) were examined for each form of material where L, T, S, R, C refer to the in-plane long (rolling), long-transverse, short-transverse, radial, and circumferential directions, respectively. Orientation imaging microscopy (OIM) via EBSD was performed using a FEI Helios G4 UC FIB/SEM equipped with an Oxford Instruments Symmetry EBSD detector. Inverse pole figure (IPF) maps were constructed from the OIM data using the MTEX software package²⁰, and prior austenite grain boundaries were reconstructed using methods provided by Nyysönen et al²¹. Select samples were electrolytically etched in 5 M NaOH with a direct current power supply and stainless steel wire counter electrode to reveal delta ferrite distributions via optical microscopy.

7.2.2 Fatigue Crack Growth Rate Measurement

Fracture mechanics based fatigue crack growth rate testing was performed using a servo-hydraulic load frame applying sinusoidal waveforms. Crack length (a) was continuously monitored using the direct current potential difference (dcPD) method²². A closed-loop feedback system monitoring the crack lengths and loads enabled stress intensity (K) controlled loading. The single edge notch tension (SENT) specimen geometry was utilized with a 2.67 mm thickness (B) and 12.20 mm width (W) gage section ($B/W = 4.6$). A single test specimen was side-grooved using 0.05 mm groove radii and a reduced thickness of 2.10 mm (B_W), all other SENTs were flat-sided. Each SENT had an electrical discharge machined (EDM) pre-notch with a 0.940 mm length and 0.038 mm root radius. The plate and rod SENTs were oriented in the L-T and

L-R Mode I loading-crack growth directions²³, respectively. Primary fixturing consisted of a pinned-pinned loading configuration with linear elastic K calculations²⁴ for the flat-sided SENTs. For the side-grooved SENT, the same K -solution was utilized, but with $B = \sqrt{B \cdot B_W}$ as recommended by Freed et. al²⁵. A single test was performed in a “fixed-fixed” configuration by rotating the SENT 90° in the grips to preclude crack mouth yawning allowed by the pins. This fixed-fixed test used a K -solution provided by Zhu²⁶ for clamped SENT specimens. Environmental control was obtained by affixing an acrylic cell and flowing N₂ gas either dry (RH ~ 0%) or humidified by bubbling through deionized water (RH > 90%). Otherwise, testing was performed in lab air with RH ~ 50%.

Fatigue test protocols consisted of either a stress intensity range (ΔK) shed/rise or a constant ΔK test. In both cases, testing was preceded by pre-cracking 0.250 mm out of the pre-notch at a constant $\Delta K = 6.3 \text{ MPa}\sqrt{\text{m}}$ and $R = 0.1$. For the shed/rise tests, the shed was performed at a normalized K-gradient (C) of either -0.08 mm^{-1} as recommended by ASTM E647⁸ or a more aggressive $C = -0.75 \text{ mm}^{-1}$. After the shed, the rising ΔK portions of the tests were performed with either $C = 0.5 \text{ mm}^{-1}$ or a constant amplitude load until a specified maximum ΔK or fast-fracture. Constant ΔK tests were performed at $\Delta K = 9 \text{ MPa}\sqrt{\text{m}}$ starting at the end of the precrack and typically ending at a normalized crack length (a/W) of 0.8. All testing was performed at a loading frequency of 10 Hz and fixed stress ratio (R). Post-test, fracture surfaces were examined using a combination of optical microscopy and white light interferometry. Each fracture surface was measured using optical microscopy to verify dcPD calculated crack lengths²⁷. The in-situ and post-test measured crack lengths were within typically 0.1 mm of each other. Fracture surface texture was captured using white light interferometry with a Zygo NewView 7300. Topographic data was gathered using a 2.5x objective with a 10.3 mm working distance and a low-resolution Frequency Domain Analysis (FDA). Extended scans were used to traverse the high peaks and low valleys while automatic stitching routines were used to cover the length and width of the fracture surface. Post processing was performed using MountainsMap® version 7.4 to remove data outliers, level the topography data based on the plane of the pre-notch, calculate/plot surface roughness (Rq)²⁸, and plot/extract topographic data.

7.2.3 Residual Stress Measurement

Residual stresses (σ_{RS}) and associated residual stress intensity factors (K_{RS}) were measured on a plane parallel to the Mode I crack plane in selected samples using the incremental slitting method. The slitting method determines an average through thickness residual stress acting normal to a specified plane as a function of position across the plane (i.e., a line profile of residual stress acting to open or close the slit). In general, the slitting method first involves cutting incrementally from the front face of the sample toward the back face on the plane of measurement. With each cut, a strain gage attached on the sample back face is used to measure strain as a function of incremental cut depth. This strain versus cut depth data

enables calculation of residual stress versus position from the front face^{29,30} as well as the residual stress intensity factor³¹. The slitting method in this work followed established experimental and data reduction practices³⁰ that have proven useful in prior work to account for residual stress effects on fatigue crack growth rate behavior^{12,32}. In this particular case, slitting measurements were performed on square shaped samples of dimensions $W \times W \times B$ cut adjacent to the crack path of selected SENT samples after fatigue crack growth rate testing as illustrated in Fig. 40. A slitting plane parallel to the nominal crack path for each sample was cut by wire EDM in 41 equal increments to a total depth of $0.95W$. The incremental strain measurements were then used to calculate σ_{RS} and K_{RS} as a function of a/W .

7.2.4 Fatigue Crack Growth Rate Simulation

The NASGRO equation was used to simulate the effect of residual stress on fatigue crack growth rate via superposition of a measured residual stress intensity (K_{RS}) on a nominal, applied stress intensity waveform (K_{app}). These calculations were performed using the methods described in the NASGRO software manual³³ and are briefly reviewed below. First, the nominal stress ratio ($R = K_{app,min}/K_{app,max}$)

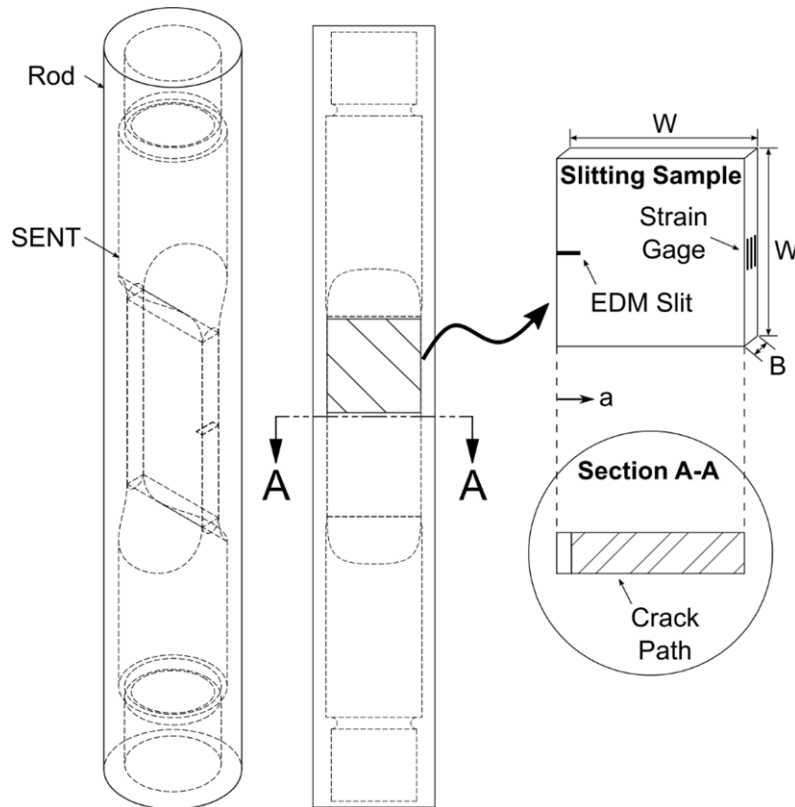


Fig. 40 | **Schematic of samples used for residual stress measurement via the slitting method.** SENT samples were machined from 17-4PH rod and fatigue tested along the nominal crack path identified in Section A-A. After fatigue testing, a portion of the SENT adjacent to the crack path was excised for use as a slitting sample, instrumented with a strain gage, and incrementally slit via EDM. Strains measured during the slitting process were used to calculate residual stress as a function of crack length (a) normalized by the SENT width (W) (i.e., a/W).

was transformed into a total stress ratio (R_{tot}) by superimposing the applied and residual stress intensity factors:

$$R_{tot} = \frac{K_{app,min} - K_{RS}}{K_{app,max} - K_{RS}} \quad (7.1)$$

Plasticity induced closure effects were then estimated using the Newman model³⁴. This yields a closure function (f) of the form below that depends on the effective stress ratio where K_{op} and K_{max} are the opening and maximum stress intensities for a load waveform, respectively.

$$f[R_{tot}] = \frac{K_{op}}{K_{max}} \quad (7.2)$$

The closure corrected threshold stress intensity range (ΔK_{th}) was then calculated as:

$$\Delta K_{th} = \frac{\Delta K_1 \left(\frac{1 - R_{tot}}{1 - f[R_{tot}]} \right)^{1 + R_{tot} C_{th}^p}}{(1 - A_0)^{(1 - R_{tot}) C_{th}^p}}, R_{tot} \geq 0 \quad (7.3)$$

$$\Delta K_{th} = \frac{\Delta K_1 \left(\frac{1 - R_{tot}}{1 - f[R_{tot}]} \right)^{1 + R_{tot} C_{th}^m}}{(1 - A_0)^{C_{th}^p - R_{tot} C_{th}^m}}, R_{tot} < 0$$

Then, the thickness corrected fracture toughness was estimated as:

$$K_c = K_{1c} \left(1 + B_k e^{-\left(A_k \frac{t}{t_0} \right)^2} \right) \quad (7.4)$$

Where t is the specimen thickness ($t = B$) and,

$$t_0 = 2.5 \left(\frac{K_{1c}}{\sigma_{ys}} \right)^2 \quad (7.5)$$

Finally, a simulated fatigue crack growth rate was calculated using the NASGRO equation³⁵:

$$\frac{da}{dN} = C \left[\frac{1 - f[R_{tot}]}{1 - R_{tot}} \Delta K \right]^n \frac{\left(1 - \frac{\Delta K_{th}}{\Delta K} \right)^p}{\left(1 - \frac{K_{max}}{K_c} \right)^q} \quad (7.6)$$

Note that the necessary empirical material parameters for this approach (e.g., p , m , C_{th} , etc.) were based on the built-in parameters provided by the NASGRO 9.1 software package for 17-4PH (H900, plate, L-T, material code: G2CB11AB1) and are, therefore, unlisted.

7.3 Results & Discussion

7.3.1 Microstructure & Mechanical Properties

Microstructural analysis and mechanical evaluation showed minor differences between the rod and plate material forms of 17-4PH in this study. As shown in Fig. 41, both materials have martensitic grain structures with similar martensite block sizes (Fig. 41a,d). Reconstruction of the prior austenite grain (PAG) boundaries shows equiaxed grains in both cases with a slightly coarser grain structure in the rod (Fig. 41b,e). Small quantities of delta ferrite aligned with the rolling direction, typical of 17-4PH³⁶, are present in both materials with the most severe cases shown in Fig. 41c,f. Phase analysis showed a negligible amount of retained austenite appearing as small ($\sim 3 \mu\text{m}$), widely spaced islands in both materials (images not shown). Broader area analyses confirmed these basic observations across multiple material planes (i.e., LT, LR, ST, etc.). Compositionally, both materials meet their respective ASTM A564/A693^{37,38} requirements, though the rod has double the Si content of the plate (Table 5). Similarly, mechanical evaluation of selected tempers of the materials showed that both meet ASTM A564/A693^{37,38} requirements with the rod generally having higher strength/hardness and lower ductility than the plate (Table 7).

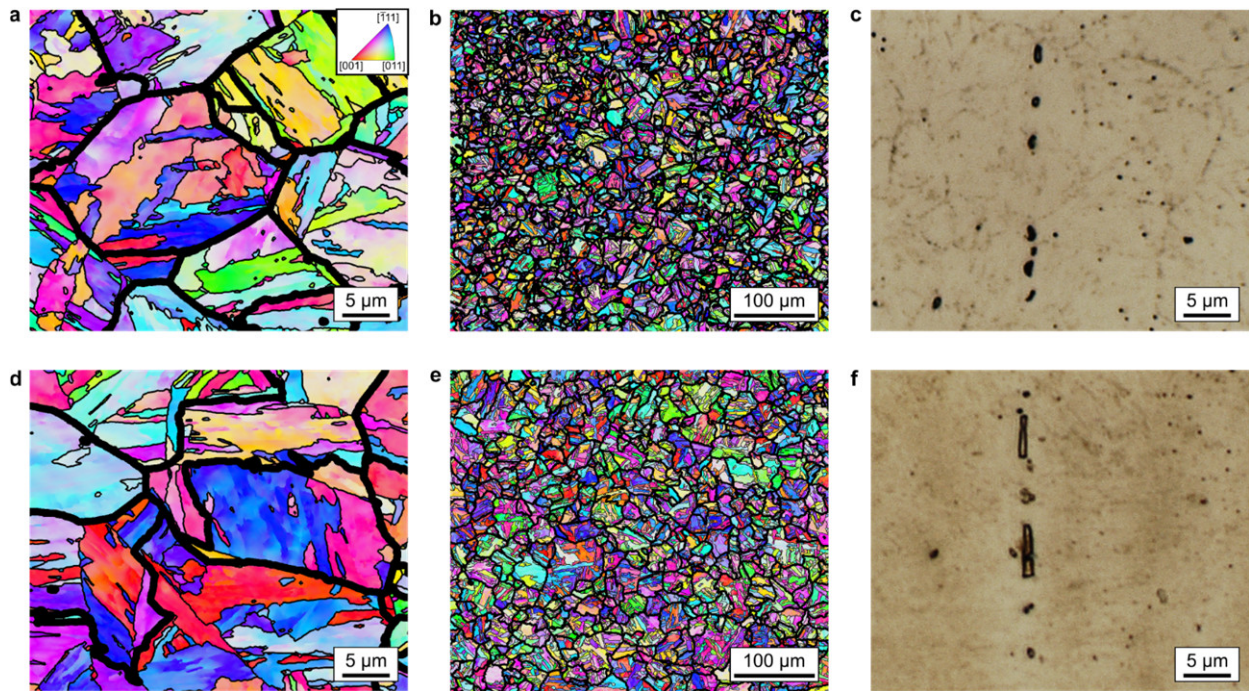


Fig. 41 | **Comparison of 17-4PH rod and plate microstructures.** a-c, 17-4PH plate microstructure. d-f, 17-4PH rod microstructure. Representative microstructure images are shown for 17-4PH plate (a, b, c) and rod (d, e, f). Grain orientation imaging maps are shown in (a, b, d, e) with bold and fine black outlines highlighting the PAG and martensite block boundaries, respectively. The most severe cases of delta ferrite stringers observed in each material form are shown in (c, f) with the L direction aligned vertically.

Table 7 | **Mechanical properties for selected tempers of the 17-4PH plate and rod used in this study.**

Form	Heat Treat	HRC	σ_{YS} (MPa)	σ_u (MPa)	E (GPa)	e_f (%)
Plate	H900	44	1194	1336	204	41
	H1025	37	1059	1110	207	44
Rod	H900	46	1410	1412	202	37
	H1025	38	1094	1099	199	42

7.3.2 Comparing 17-4PH Rod and Plate Fatigue Responses

Fatigue crack growth rates (da/dN) in humidified air as a function of stress intensity range (ΔK) were compared for 17-4PH rod and plate in the H900 condition at $R = 0.5$ and $R = 0.7$ (Fig. 42). At $R = 0.5$, growth rates were obtained at a variety of normalized K-gradients (C). In particular, the ASTM E647 recommended $C = -0.08 \text{ mm}^{-1}$ was used during the ΔK shed for the rod while the plate was tested at a much more aggressive $C = -0.75 \text{ mm}^{-1}$. In the case of the plate, there was good correspondence in da/dN between the shed and the subsequent ΔK rise. Conversely, there was an anomalous, order of magnitude mismatch in growth rate between the ΔK shed and rise for the rod with a maximum growth rate mismatch occurring at $\Delta K = 9 \text{ MPa}\sqrt{\text{m}}$. This mismatch yielded an apparent threshold stress intensity range (ΔK_{th}) of $7 \text{ MPa}\sqrt{\text{m}}$ for the rod while $\Delta K_{th} = 3 \text{ MPa}\sqrt{\text{m}}$ for the plate, assuming ΔK_{th} occurs at $1 \times 10^{-7} \text{ mm/cycle}$. In the stage II growth region, the plate displays a typical, Paris-law behavior while the rod has a nonlinear transition to stage III growth behavior. In stage III, the plate cracked without fracture until the test was halted at $\Delta K = 50 \text{ MPa}\sqrt{\text{m}}$ while the rod fast fractured at $\Delta K = 40 \text{ MPa}\sqrt{\text{m}}$. A more direct comparison of crack growth rates between the plate and rod was performed at $R = 0.7$ (Fig. 42b) with matched C . The aforementioned observations at $R = 0.5$ are largely similar at $R = 0.7$. Notably, the shed/rise growth rate mismatch for the rod recurred at $R = 0.7$ – though with a reduced magnitude.

Given (1) significant differences in ΔK_{th} for the rod and plate and (2) the apparent breakdown of linear elastic fracture mechanics (LEFM) similitude between the ΔK shed and rise for the rod, understanding the “mismatch” behavior in the rod is of interest. To begin investigating this mismatch phenomenon, constant $\Delta K = 9 \text{ MPa}\sqrt{\text{m}}$ fatigue crack growth rates as a function of normalized crack length (a/W) were gathered for the two material forms (Fig. 43a). If fracture mechanics similitude holds then a constant ΔK test should produce a constant crack growth rate for a given ΔK and R . For the plate, the crack growth rate held nominally constant at $6 \times 10^{-6} \text{ mm/cycle}$ across all tested a/W – consistent with Fig. 42a. The rod, however, exhibited a crack growth rate that varied from $5 \times 10^{-7} \text{ mm/cycle}$ up to $8 \times 10^{-6} \text{ mm/cycle}$ with two local growth rate minima occurring at $a/W = 0.39$ and 0.77 . Note that $a/W = 0.5$ for the rod corresponds to the centerline of the parent rod stock material while all a/W for the plate are confined to the center plane of the parent plate stock material. To complement the growth rate data, white light interferometry was used to produce 3-D topographic maps of these tests’ fracture surfaces (Fig. 43b). Examination of these topographic

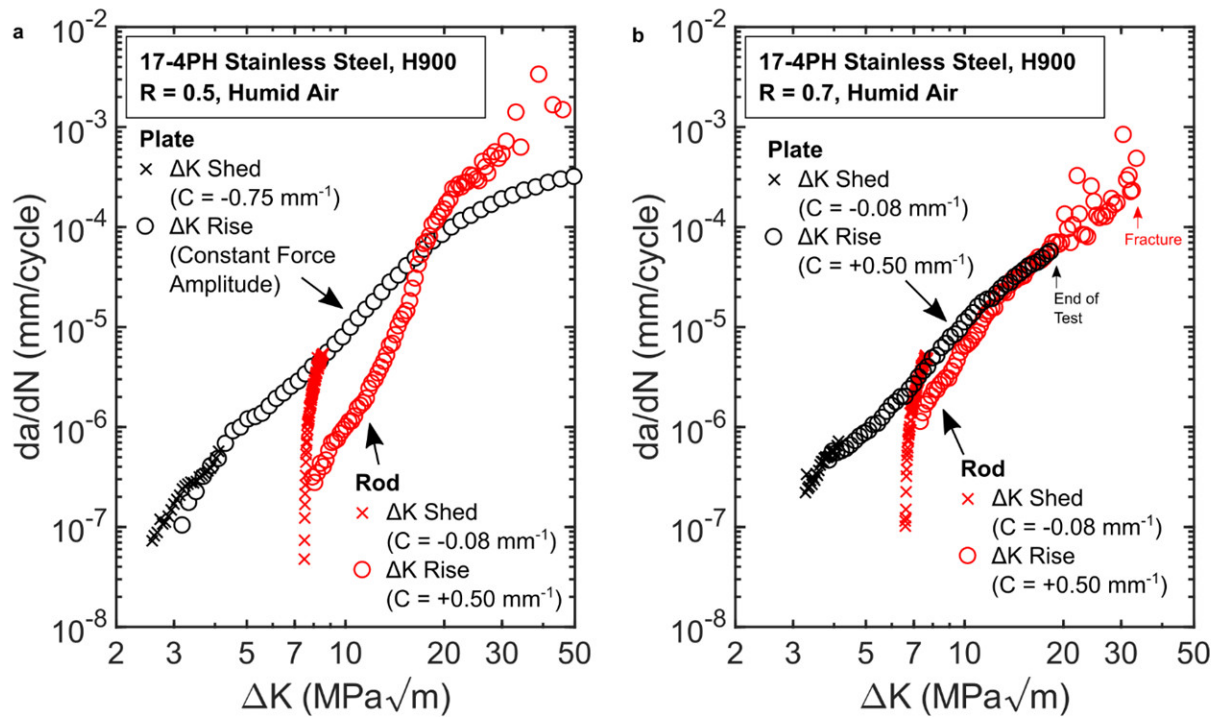


Fig. 42 | Comparison of fatigue crack growth rates for 17-4PH rod and plate in humid air. **a**, $R = 0.5$. **b**, $R = 0.7$. Fatigue crack growth rate (da/dN) versus stress intensity range (ΔK) in humid air ($>90\%$ RH) for 17-4PH plate and rod are compared at $R = 0.5$ (**a**) and $R = 0.7$ (**b**). Growth rates gathered under shedding or rising ΔK are identified along with the normalized K -gradients (C) used to control load application.

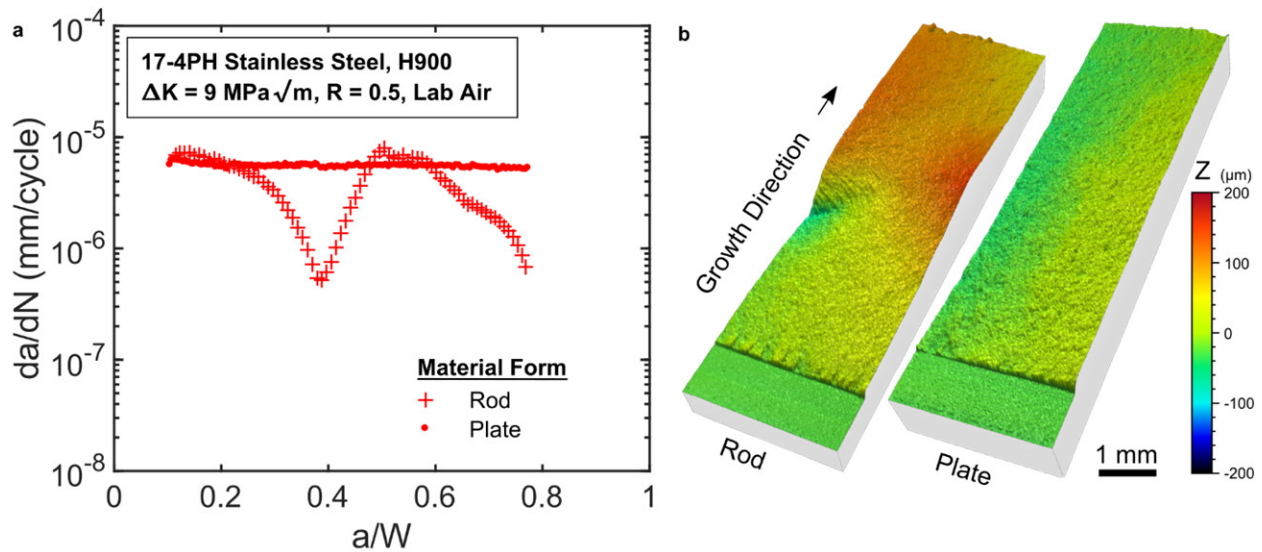


Fig. 43 | Comparison of 17-4PH rod and plate fatigue behavior at constant ΔK . **a**, Fatigue crack growth rate versus normalized crack length (a/W). **b**, Fatigue fracture topographies. Growth rates were captured in lab air as a function of a/W at a constant $\Delta K = 9 \text{ MPa}\sqrt{\text{m}}$, $R = 0.5$ for 17-4PH rod and plate in the H900 condition (**a**). Topographic height (Z) maps of the fracture surfaces from (**a**) are shown in (**b**). The primary growth region in (**b**) is preceded by EDM notch (0.94 mm) and precrack (0.25 mm) regions. Note also that the 1 mm scalebar in (**b**) only applies to planar dimensions; Z height is exaggerated for clarity.

maps shows that the plate fracture path is relatively flat with Z height variation less than 100 μm . Conversely, the fracture surface of the rod is wavy with a maximum peak to valley distance exceeding 200 μm with a local depression at intermediate a/W where the anomalous growth occurs.

These data show substantial fatigue crack growth behavior differences between the rod and plate material forms of 17-4PH in the H900 condition. These differences include higher cyclic toughness and lower ΔK_{th} in plate when compared to rod, but the most significant differences lie in the peculiar fatigue crack growth rate behavior of the rod. Unlike the plate, the rod has varying fatigue crack growth rates at a constant ΔK , order of magnitude differences in growth rate between a ΔK shed and rise, and a non-flat fatigue crack path. While cyclic toughness, roughly correlated with fracture toughness, and threshold stress intensity ranges are well known to vary between different alloy systems^{39,40}, the growth rate and fatigue crack path characteristics observed in the rod are surprising. These fatigue and fractographic observations in the rod lead to two key questions:

1. What microstructural feature(s) in the 17-4PH rod are leading to the variable growth rate and non-flat crack path?

2. What mechanics-based or fatigue crack growth mechanisms might be promoting these growth rate and crack path behaviors?

Given the nominal similarity of the microstructures of the plate and rod, as described in the previous section, the microstructural origin(s) for the observed fatigue behaviors are clearly subtle. There are a number of known fatigue mechanisms that could result in the growth rate and/or non-flat crack path. With regard to the crack path, mechanisms fatigue crack path deflection can be induced by material influences, mechanical influences, and/or environmental influences. Specifically, material crystallographic grain texture⁴¹ and secondary phase fracture⁴² have both been demonstrated to influence a crack path. Mechanically, a form of out of plane cracking called “shear lipping”⁴³ has been linked to a lack of crack tip constraint at free surfaces⁴⁴, T -stresses have been linked to out of plane cracking⁴⁵, and secondary stress fields (e.g., residual stress) can drive cracks out of plane⁴⁶. Environmental interactions with the fatigue process have also been demonstrated to influence the crack path^{47,48}. With regard to the unsteady growth rate, it is notable that the rod growth rate is generally lower rather than higher than the plate fatigue crack growth rate (Fig. 43a). The crack path itself could be a cause for growth rate reduction. It has been demonstrated that deviation from a flat, Mode I crack path will result in a reduction of mechanical driving force, and therefore growth rate, at the crack tip⁴⁹. Another common means for growth rate deceleration is crack closure, though closure is a broad phenomenon with several possible sub-mechanisms⁵⁰. In order to determine the true origin(s) of the observed crack path and growth rate behaviors, a variety of additional testing and characterization protocols were employed to interrogate each of these potential mechanisms.

7.3.3 Interrogating the 17-4PH Rod Fatigue Crack Growth Response

7.3.3.1 Effect of Closure

A mechanism that might explain the observed reduction in the 17-4PH rod crack growth rate is closure. Closure is a reduction in mechanical driving force at the crack tip due to a crack “closing” and thus reducing the effective crack length and associated stress intensity⁵⁰. Typically, closure is attributed to plasticity, fracture surface roughness, oxides, and/or residual stress⁵⁸ that might cause the two faces of a fracture surface to impinge¹⁶. One way to reduce or eliminate the effect of closure is by increasing the stress ratio of a cyclic load waveform to promote a larger opening at the crack tip and in the crack wake. This simple test for closure effects was performed as shown in Fig. 44. The magnitudes of the growth rate drops at $a/W = 0.39$ and beyond $a/W = 0.50$ clearly reduced with the increase in stress ratio, but remnants of the underlying phenomenon are still clearly present. The results of this test indicate that closure might be playing some role in the growth rate reduction process, especially with the non-flat crack path that may lead to impingement at elevated a/W (Fig. 43b). However, the persistent form of the growth rate behavior suggests that closure is not the root cause.

7.3.3.2 Effect of Side-Grooving

One possible mechanistic origin for both the non-flat crack path and the variable growth rate in the 17-4PH rod is a lack of crack tip constraint. Crack tip constraint may be defined as the degree of crack tip

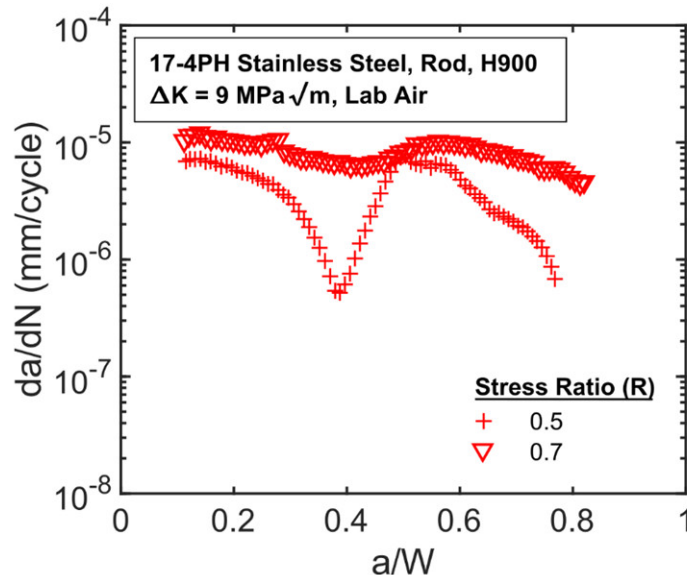


Fig. 44 | Effect of stress ratio modification on fatigue crack growth in 17-4PH rod. Fatigue crack growth rates are compared at two stress ratios ($R = 0.5, 0.7$) for 17-4PH rod in the H900 condition. Growth rates were captured in lab air as a function of a/W at a constant $\Delta K = 9 \text{ MPa}\sqrt{\text{m}}$.

stress triaxiality⁶ and can be estimated in terms of a T -stress for linear elastic conditions⁵¹. An increase in crack tip constraint can promote a stable (planar) crack path⁵². Conversely, a lack of constraint can result in an unstable non-Mode I crack path phenomenon called “shear lips”. One of the necessary conditions for shear lip formation is a state of plane stress that may be found at the free surface adjacent to a fatigue crack wake, but shear lips may be suppressed through the introduction of a scratch/notch adjacent to the wake to promote constraint and preclude plane stress conditions⁴³. Alternatively, a specimen may be “side-grooved”^{25,53} to achieve increased crack tip constraint and, therefore, reduce crack path deflection. A secondary effect of a flat crack path (i.e., minimal crack-tip deflection) is a stable mechanical driving force for crack extension⁵⁴. Assuming linear elastic continuum conditions, crack deflection for a Mode I crack will result in a reduction in stress intensity and reduce the crack growth rate; the extent of these reductions depends on various factors.

Referring back to Fig. 43, several of the aforementioned hallmarks of low crack tip constraint are present in the 17-4PH rod, so a replicate test was performed with side-grooves to evaluate the effect of increased constraint. The crack growth kinetics in Fig. 45 demonstrate that side grooving had negligible effect on the variable growth rate phenomenon in the rod. Similarly, white light interferometry showed a non-flat crack path with local depressions at intermediate a/W (not shown). These results demonstrate that the current case of crack path deflection is not best described as a “shear lip” phenomenon, which should be sensitive to additional constraint. This is not particularly surprising as the condition of plane stress (i.e.,

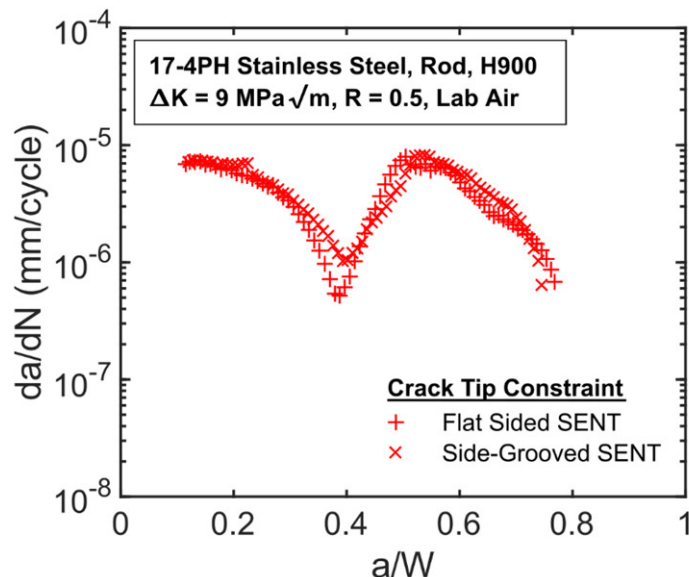


Fig. 45 | **Effect of crack tip constraint modification on fatigue crack growth in 17-4PH rod.** Different levels crack tip constraint were tested by fatigue cracking flat sided and side-grooved SENTs made from 17-4PH rod in the H900 condition. Growth rates were captured in lab air as a function of a/W at a constant $\Delta K = 9 \text{ MPa}\sqrt{\text{m}}$, $R = 0.5$.

low constraint) is only one of three conditions described as necessary for shear lip formation⁴³. The two other conditions necessary for shear lip formation include (1) available material slip systems on the shear lip plane and (2) fast enough growth rate to permit shear lip initiation within one load cycle. Condition (1) is likely met, but condition (2) is likely violated given the low, decelerating growth rate occurring over hundreds of microns of crack extension and associated with the observed crack path deflection.

7.3.3.3 Effect of Bulk T-Stress Modification

Regardless of the ineffectiveness of side-grooving to constrain the crack path, perhaps constraint is still the root cause of the crack path instability in the 17-4PH rod. As previously mentioned, the T -stress may be used to quantify the constraint of a crack tip stress field and is a function of the crack geometry, specimen geometry, and loading configuration⁵⁵. One way to quantify the relative constraint of a growing crack is by plotting the biaxiality ratio (β) which is the ratio of the stress intensity (K) and the T -stress with a crack length factor to normalize units. Generally, a compressive β is associated with increased constraint and crack path stability whereas a tensile β will drive out of plane growth⁵². The differences in constraint for two loading configurations (pinned-pinned and fixed-fixed) of the SENT sample geometry are shown in Fig. 46a. The displayed β distributions both assume a normalized distance between the load application points (H/W) of 5, but for pinned-pinned⁵² and fixed-fixed^{26,56} boundary conditions. Unlike side-grooving which primarily modifies the state of plane stress at the free surface adjacent to a crack front, the T -stress modifications in moving to a different loading configuration should affect the entire crack front. It is also notable that the pinned-pinned SENT configuration (used thus far) steadily transitions from a compressive to a tensile β with the crossover point occurring at $a/W \sim 0.6$. Conversely, a fixed-fixed SENT maintains a relatively steady, compressive β up to a/W of 0.6.

These differences in constraint between pinned-pinned and fixed-fixed SENT loading configurations motivated an investigation into the effect of bulk constraint on fatigue crack deflection in 17-4PH rod. The fatigue test results in Fig. 46b shows that the bounce in growth rate at $a/W = 0.39$ persisted with the change from a pinned-pinned to a fixed-fixed SENT configuration, though there is a generally upward trend in growth rate with increasing a/W . Note that this upward trend is likely due to imperfect scaling of the K solution used to control load application in the fixed-fixed configuration rather than T -stress impacts. It has previously been documented that subtle load train compliance differences can modify the fixed-fixed effective stress intensity, and the K -solution can require tuning for ideal results⁵⁷. Regardless of this issue, the additional constraint involved with fixed-fixed load application did not sufficiently modify the crack tip stress state to produce a constant crack growth rate.

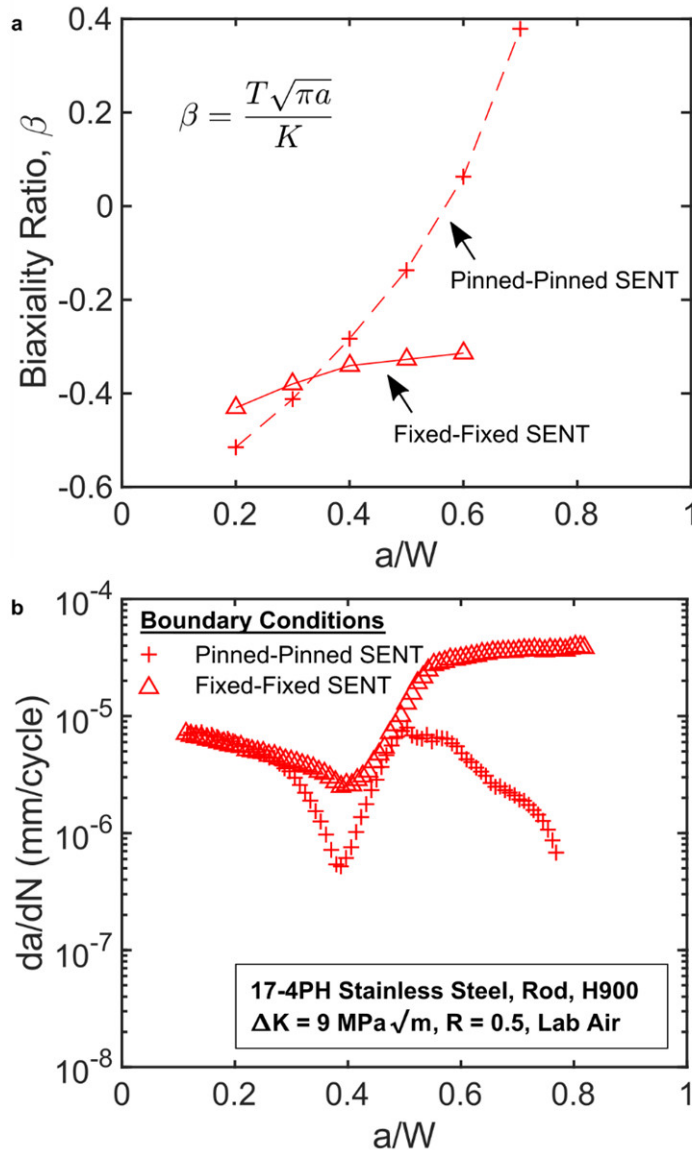


Fig. 46 | Comparison of T-stress variation and its effects on fatigue crack growth in 17-4PH rod. **a**, T -stress distributions via the biaxiality ratio (β) as a function of a/W in pinned-pinned and fixed-fixed SENT loading configurations. **b**, Fatigue crack growth rates versus a/W in pinned-pinned and fixed-fixed SENTs. Published T -stress distributions are compared for two SENT loading configurations (**a**). The effects of these T -stress distribution differences on fatigue crack growth rates were then tested on 17-4PH rod in the H900 condition at a constant $\Delta K = 9 \text{ MPa}\sqrt{\text{m}}$, $R = 0.5$ in lab air (**b**).

7.3.3.4 Effect of Environment

Environmental interactions with the fracture process also have the potential to affect a crack path. A couple examples of this behavior include fracture along a secondary phase in stainless steel⁴⁷ or hydrogen embrittlement interactions inducing preferential interfacial fracture in an aluminum alloy⁴⁸. Each of these cases had a much more extreme environment (i.e., high temperature water for the steel) or a much more

susceptible alloy (i.e., aluminum) than the current case of stainless steel in humid air (Fig. 42). However, an inert environment (e.g., dry N₂ gas) test was performed to rigorously eliminate environmental influences as a potential cause for the fatigue crack growth anomalies. This test was performed on material in the H1025 temper condition, rather than the H900 temper evaluated thus far, to simultaneously investigate the effect of heat treatment.

The results in Fig. 47 give the first hints at the root cause of the anomalous crack growth behavior in the 17-4PH rod. First, the inert environment seemed to have little effect on the growth rate reduction at $a/W = 0.39$. There was an overall reduction in the inert environment growth rate compared to a test in lab air, but this is expected since humidity in the air is known to cause a general acceleration of fatigue crack growth⁵⁹. More importantly, the growth rate depression in Fig. 47 seems to be reduced in comparison to the previous tests in Fig. 45 and Fig. 46b. The primary difference between these tests is an increase in the tempering time and temperature for H1025. This indicates that microstructural evolution or thermal stress relief during heat treatment is impacting the phenomena underlying the unique fatigue behavior in the rod.

7.3.3.5 Effect of Heat Treatment

Given the clear impact of heat treatment on the unsteady crack growth rate in the 17-4PH rod, it is worth discussing the microstructural features in the alloy that might be affected by heat treatment. 17-4PH nominally consists of a martensitic matrix with small volume fractions of retained austenite, delta ferrite, micron-scale Nb carbides, and nano-scale Cu precipitates⁶⁰. The Nb carbides are intended to sequester C

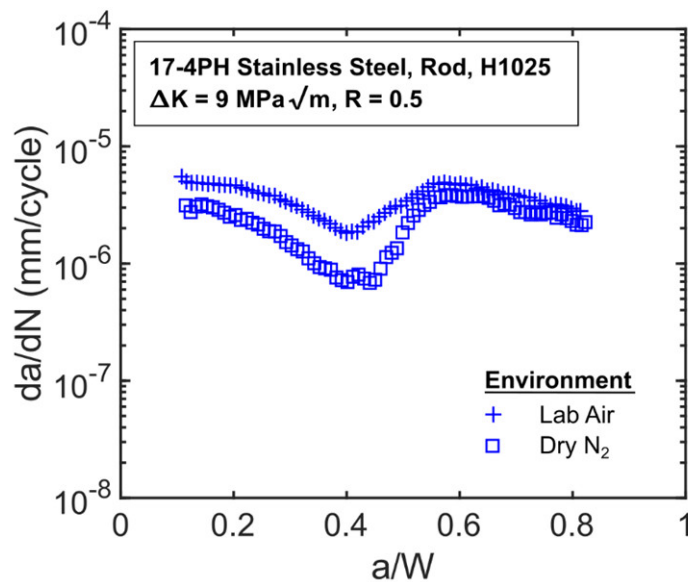


Fig. 47 | Effect of environment modification on fatigue crack growth in 17-4PH rod. Fatigue crack growth rates are compared in an inert (Dry N₂, RH ~ 0%) and benign (Lab Air, RH ~ 50%) environment for 17-4PH rod in the H1025 condition. Growth rates were captured as a function of a/W at a constant $\Delta K = 9 \text{ MPa}\sqrt{\text{m}}$, $R = 0.5$.

during hot working⁶¹ and are stable up to $\sim 1300^{\circ}\text{C}$ ⁶². Additionally, hot working may result in delta ferrite stringers⁶³ that tend to be stable up to $\sim 1040^{\circ}\text{C}$ ^{36,64}. The martensitic matrix is stable up to $\sim 700^{\circ}\text{C}$ ⁶², and the commonly employed solution annealing treatments at 1040°C will produce an austenitic structure, dissolve the Cu precipitates, and then transform back to martensite upon cooling to room temperature. After a solution annealing treatment, Cu that was dissolved into the martensite matrix during the solution anneal is precipitated via aging heat treatments up to 620°C that produce varying precipitate morphologies associated with various strength levels³⁸.

Noting the stability of these various phases, only the nano-scale Cu precipitate is expected to be evolving between the H900 and H1025 heat treatments (Table 6). Given that fatigue behavior is relatively insensitive to strength level in steels⁶⁵ and that Cu precipitation should be relatively homogenous³⁶, the Cu precipitates are an unlikely cause for the observed fatigue crack growth behavior in the 17-4PH rod. Still, there is a clear effect of heat treatment, so treatments that would modify other phases were tested. Namely, the AR condition was tested to represent a Cu precipitate free alloy, and a SA treatment was tested to re-crystallize the martensite structure. The results from these treatments were consolidated with previous experiments to show the effect of heat treatment on the 17-4PH rod fatigue crack growth phenomena (Fig. 48).

Interestingly, the AR and SA conditions, both solution annealed with Cu precipitates dissolved, exhibit vastly different fatigue crack growth behaviors. In the AR condition, the most severe case of crack

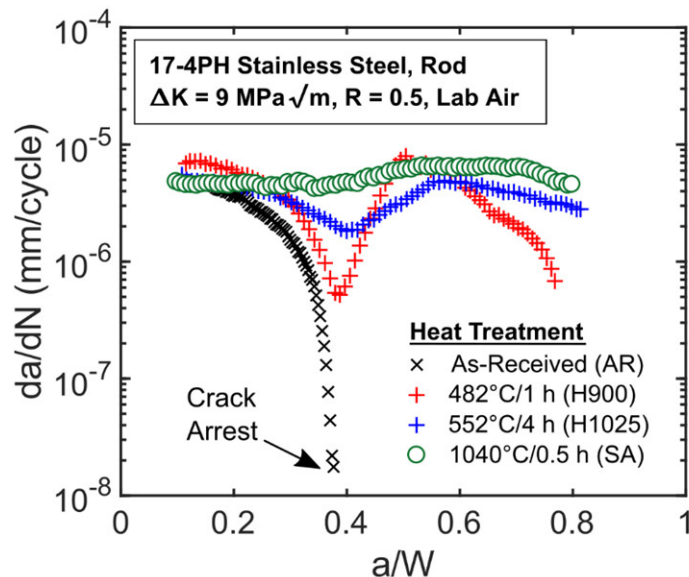


Fig. 48 | Effect of heat treatment on fatigue crack growth in 17-4PH rod. Fatigue crack growth rates are compared for 17-4PH rod in the as-received (AR) condition and heat treated to the H900, H1025, and SA conditions. Growth rates were captured as a function of a/W at a constant $\Delta K = 9 \text{ MPa}\sqrt{\text{m}}$, $R = 0.5$.

growth rate reduction was encountered with crack arrest occurring at $a/W = 0.39$. Conversely, the SA condition exhibited a nominally constant crack growth rate across the entire range of tested a/W . These results indicate that Cu precipitate evolution cannot be linked to the decelerating growth rate at $a/W = 0.39$ since they were not present. However, these results do reveal a different trend; the reduction in growth rate is attenuated by increasing exposure to elevated temperatures. One characteristic that is known to reduce/relax with high temperature exposure is residual stress⁶⁶. Residual stress may also influence the fatigue crack growth rate through modification of the local stress state at the crack tip and is, therefore, a potential cause for the fatigue behavior in the 17-4PH rod.

7.3.4 Residual Stress in 17-4PH Rod

To test the hypothesis that residual stress (RS) might be the root cause of the anomalous growth rate behavior in the 17-4PH rod, the various samples used to produce the growth rates in Fig. 48 were evaluated for RS via the slitting method (Fig. 49). With a peak tensile/compressive RS of +410/-160 MPa, the AR condition stainless steel rod clearly has significant levels of RS. Consistent with the results in Fig. 48, the RS subsides with increasing exposure to heat with peak tensile/compressive RS minimized at +130/-90 MPa in the AR condition. The residual stress intensities (K_{RS}) from slitting may then be plotted as a function of a/W (Fig. 49b). Comparison of the K_{RS} results with the growth rate results shows some clear correlations with the equivalent fatigue crack growth rate tests (Fig. 48). The peak compressive K_{RS} coincides at approximately the same a/W as the minimum growth rate zone for each heat treatment; even the slight shift of that minimum to higher a/W with elevated temperature heat treatment is reflected in the RS distribution. However, these correlations break down beyond a/W of 0.5. At high a/W , the K_{RS} is primarily tensile (Fig. 49b), which might be expected to increase growth rates, but the measured growth rates drop (Fig. 48). This is a likely effect of crack face contact (closure) as noted earlier.

To quantify the effect of residual stress on the 17-4PH fatigue crack growth rate, the NASGRO equation was utilized to simulate the previously evaluated effects of heat treatment and stress ratio, see Fig. 50. As might be expected given the K_{RS} values, there is good correlation in the simulated crack growth rates with the K_{RS} trends in Fig. 49b below $a/W = 0.5$. This indicates that the initial crack growth rate phenomenon is substantially driven by the residual stresses within the 17-4PH rod. However, the accuracy of the simulation breaks down in two ways: (1) the crack growth rate drop magnitudes are underpredicted by the simulation and (2) the crack growth rate reductions beyond $a/W = 0.5$ are not captured. The NASGRO simulation was not expected to perfectly replicate the empirically gathered growth rates, but these gross differences in crack growth rate trends suggest the presence of additional, operative mechanisms. The most obvious difference between the simulation (which assumes a flat, Mode I crack path) and testing is the potential for closure and/or crack deflection effects.

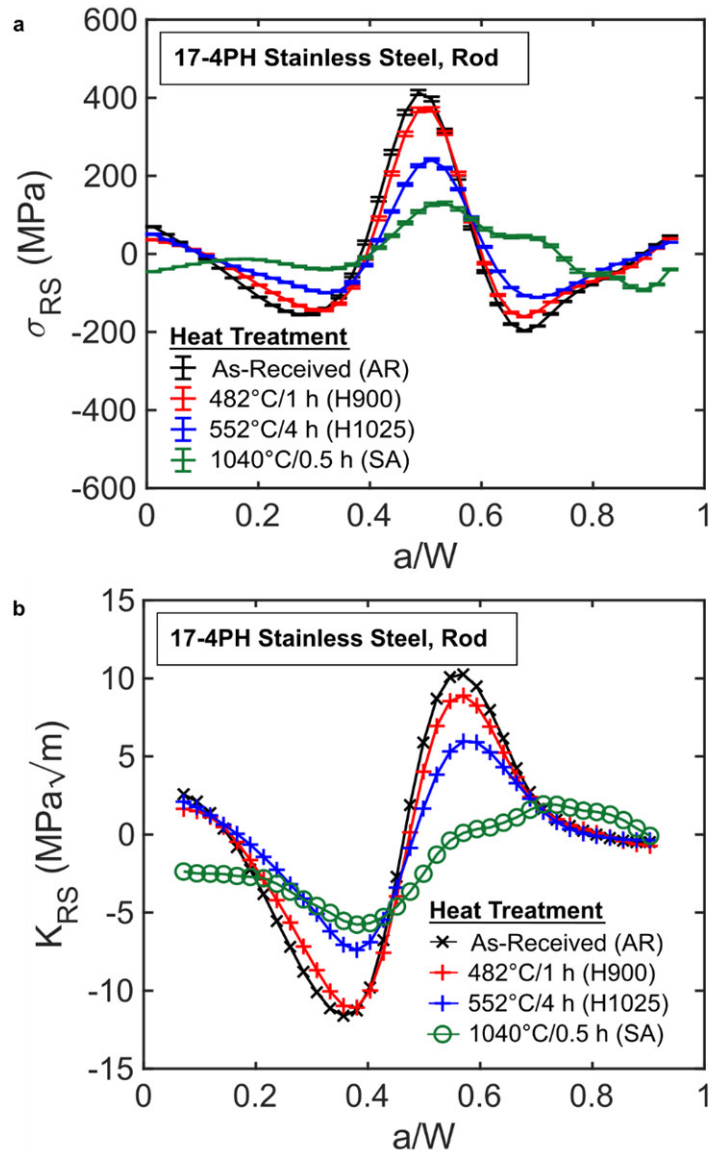


Fig. 49 | **Residual stress and stress intensity in various conditions of 17-4PH rod.** **a**, Residual stresses (σ_{RS}). **b**, Residual stress intensity factors (K_{RS}). Residual stresses and stress intensity factors are shown as a function of a/W for 17-4PH rod in various heat treatment conditions. All residual stresses shown were gathered via the slitting method.

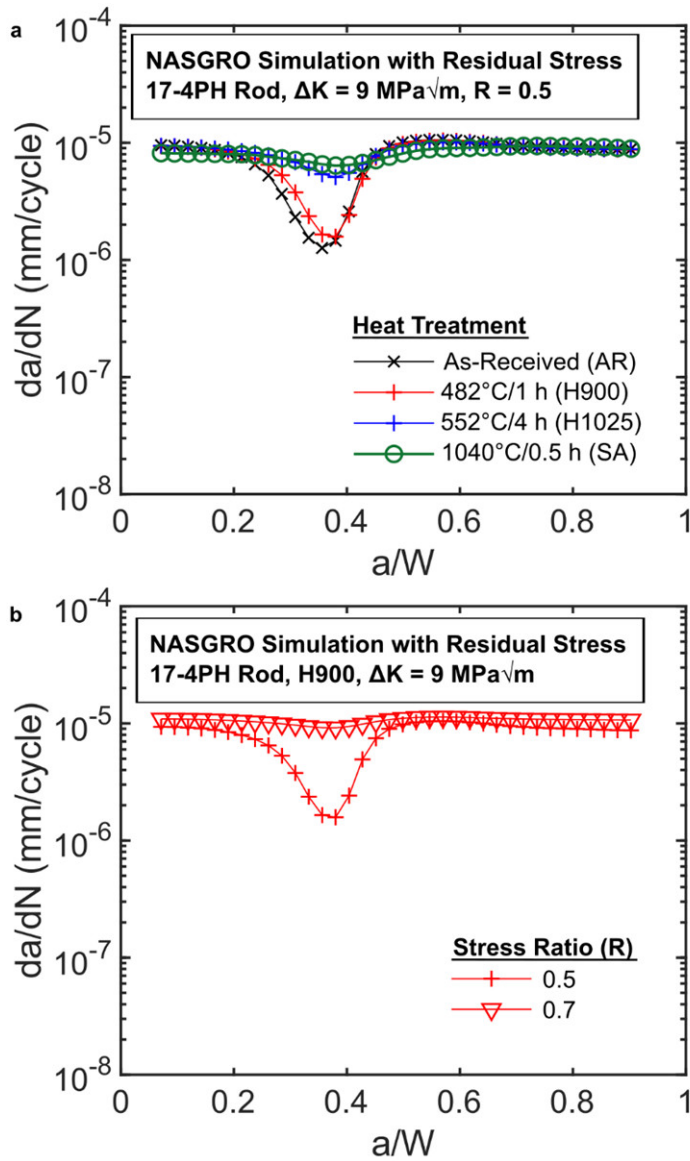


Fig. 50 | Simulated effects of measured residual stresses on fatigue crack growth in 17-4PH rod. **a**, Simulated heat treatment effect. **b**, Simulated stress ratio effect. Fatigue crack growth rates are simulated using the NASGRO equation with the inclusion of measured residual stress profiles. The simulations attempt to replicate experimental fatigue growth gathered for the 17-4PH rod under various heat treatments (**a**) and applied stress ratios (**b**) at a nominal, constant $\Delta K = 9 \text{ MPa}\sqrt{\text{m}}$.

As previously mentioned, closure decelerates fatigue crack propagation by reducing the mechanical driving force via crack wake impingement. Topographic mapping (Fig. 51) of the various fracture surfaces in Fig. 48 demonstrates that the non-flat crack path highlighted in Fig. 43 is modified by heat treatment. Specifically, the magnitude of the waviness in the crack path is reduced with increased heat treatment time and temperature (Fig. 51a). This waviness may be quantified by fitting a line profile across the fracture surface thickness at various a/W and calculating the angle of the crack path with respect to the Mode I fracture plane (Fig. 51b). Additionally, those same line profiles may be used to quantify the roughness (Rq) of the crack path as a function of a/W . Reviewing the trends across these datasets shows a general reduction

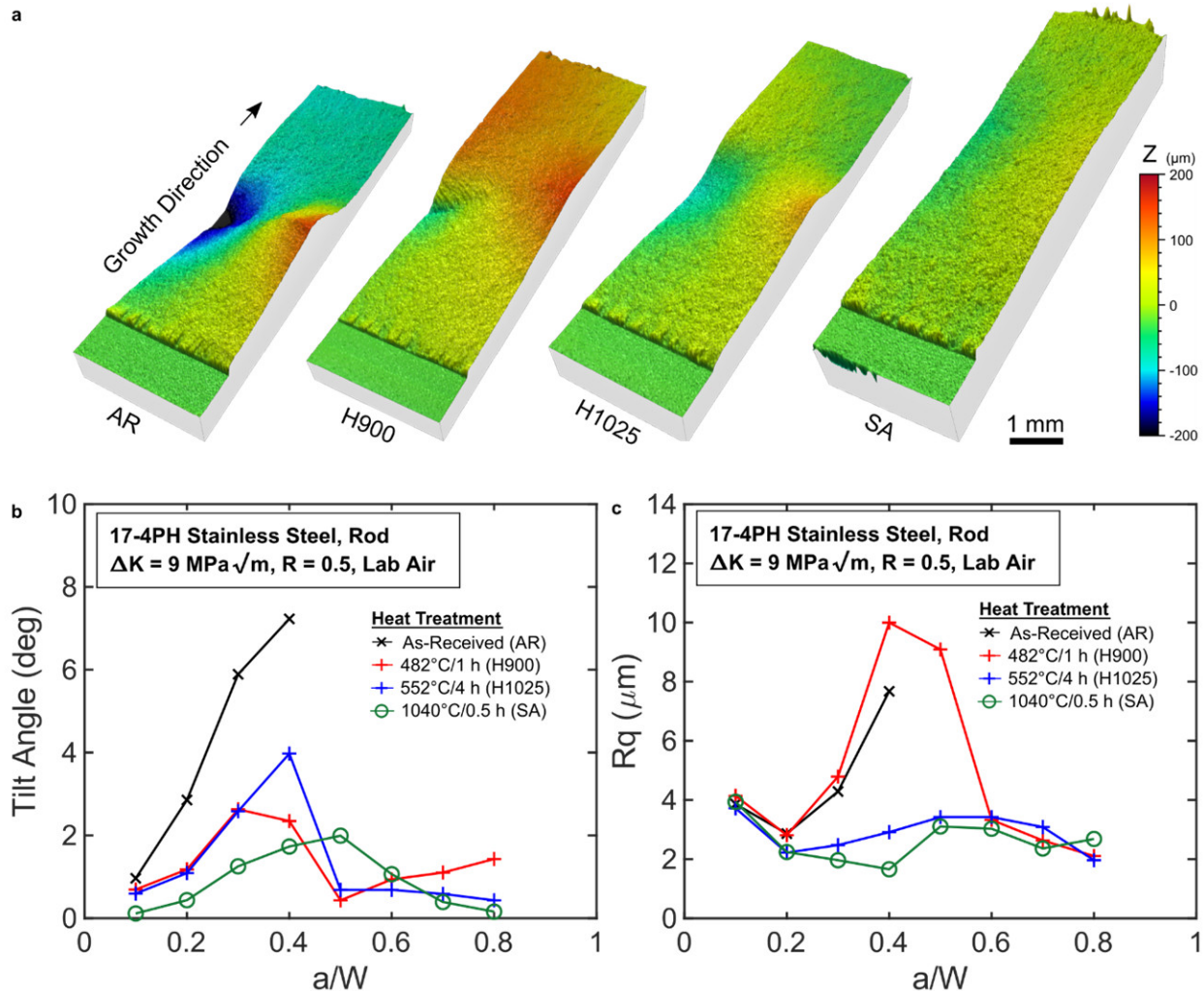


Fig. 51 | Variation in fracture surface topography induced by heat treatment of 17-4PH rod. **a**, Fracture surface topographic height (Z) maps. **b**, Fracture surface tilt angle variations. **c**, Fracture surface roughness (Rq) variations. Fatigue fracture surfaces for various conditions of 17-4PH rod (i.e., AR, H900, H1025, SA) were topographically mapped as a function of a/W (**a**). Line profiles traversing across the fracture surface thickness (i.e., B) at various a/W were used to calculate tilt angle (**b**) and roughness variations (**c**). All fatigue cracks shown were grown at a constant $\Delta K = 9 \text{ MPa}\sqrt{\text{m}}$, $R = 0.5$ in lab air. Note that the 1 mm scalebar in (**a**) only applies to planar dimensions; Z height is exaggerated for clarity.

in both tilt and surface roughness of the fracture surface with increasing heat treatment time and temperature. These downward trends are consistent with the crack growth rates in Fig. 48 and suggest that the crack wake closure could be occurring both microscopically and macroscopically via crack wake roughness and impingement, respectively. More precisely, the increase in roughness could lead to closure through closure at the crack tip, and the wake tilt could lead to closure through impingement behind the crack tip. Additionally, the tilt of the crack wake could lead to a direct reduction of the crack tip mechanical driving force through deflection as mentioned in Section 7.3.2.

To summarize, residual stress has been identified in 17-4PH rod and linked to various, anomalous fatigue behaviors in the material. The salient impacts of this residual stress include: (1) direct reduction of fatigue crack growth rate through superposition of a residual stress intensity (Fig. 50), (2) an increase in crack wake roughness with increasing residual stress intensity magnitude (Fig. 49a, Fig. 51c), (3) increasing crack path deflection with increasing residual stress intensity magnitude (Fig. 49a, Fig. 51b), and (4) closure induced fatigue crack growth rate reduction due to the aforementioned crack path modifications (Fig. 50, Fig. 51). Additional analysis is required to mechanistically link the residual stress to the crack path modifications, but the aforementioned observations strongly support a causal relationship between residual stress and the crack path modifications. It is also notable that the residual stress magnitude was reduced through common, low temperature aging heat treatments (i.e., H900, H1025), but this attenuation was not sufficient to completely remove the aforementioned fatigue impacts. The residual stress effects persisted until a high temperature solution annealing treatment was applied - though remnants of a residual stress field were still apparent (Fig. 49a). Finally, the impacts of these residual stresses on fatigue crack growth rates could be approximated to a first order through established, empirical algorithms (i.e., the NASGRO equation), but secondary closure effects due to crack wake roughness and topography led to significant error in the predictions.

7.3.5 Implications of this Work

There are several practical implications that result from this work. To review, various extrinsic factors that are known to have impacts on fatigue crack growth behavior were systematically evaluated including: material form, stress intensity gradients, crack tip constraint, stress ratio, test environment, and material heat treatment. These known factors were used to isolate and identify the root cause of an anomalous fatigue behavior that manifested as a variable crack growth rate and non-flat crack path at constant ΔK . The root cause of the behavior was residual stress. The severity of these residual stress impacts decreased for high R conditions and after heat treatment at high temperatures, but the effect of residual stress persisted through stress intensity gradient modifications, crack tip constraint modifications, stress ratio modifications, and test environment modifications. Additionally, the residual stress produced second

order impacts on the fatigue crack growth rate through roughness/topography induced closure that further confounded the issue. All of these fatigue crack growth impacts occurred without any clear indication of a difference from a microstructure or mechanical property perspective (refer to Section 7.3.1). These various observations highlight (1) residual stress is a subtle coupon-scale feature, and (2) that residual stress can dominate the fatigue crack growth behavior of a material even when confronted with various extrinsic modification strategies. This behavior also has practical relevance given that the 17-4PH rod was received in the solution annealed condition, but still exhibited the substantial residual stress profile that persisted through tempering. It is important to recognize the persistent nature of the residual stress in this material form for both engineering applications and laboratory testing. The presence of residual stress must be considered and/or accounted for in order to ensure that the engineering structural integrity analysis and laboratory data fidelity are not compromised.

7.4 Conclusions

Fracture mechanics based fatigue crack growth rate testing was used to compare the fatigue behavior of two forms of 17-4PH stainless steel. Characterization of the “rod” and “plate” material forms revealed several anomalous fatigue behaviors in the rod form that manifested as a variable crack growth rate and a non-flat crack path at constant ΔK . To interrogate this behavior, a number of extrinsic modifiers were applied to the fatigue process and characterized with the following conclusions:

- Residual stress present in 17-4PH rod was correlated with fatigue crack growth rate modifications, crack path deflections from a nominal Mode I crack path, and roughness/topography induced fatigue crack closure.
- Residual stresses in the 17-4PH rod were maximum in the “as-received” conditions (i.e., from the manufacturer) and attenuated with increasing heat treatment time and temperature. After a solution annealing treatment (1040°C/0.5 h), the residual stress field was largely removed, but remnants of residual stress were still apparent.
- Impacts on the fatigue crack growth rate from the residual stress field could be simulated via the NASGRO equation, but errors in the simulation were attributed to roughness and topography induced closure effects at long crack lengths (i.e., high a/W).
- Increased crack tip constraint via fracture specimen side-grooving and bulk T-stress modifications (i.e., modified SENT loading configurations) were insufficient to alleviate fatigue crack path deflection attributed to residual stresses.

- High heat treatment time/temperature (1040°C/0.5 h) was the most effective way to alleviate the residual stress induced fatigue behavior modifications.

7.5 Acknowledgements

This research was financially supported by the Office of Naval Research under Grant No. N00014-18-1-2427 with Dr. Airan Perez as the Scientific Officer and by NASA Space Technology Research Fellowship Grant Number 80NSSC19K1132. This chapter was adapted from a manuscript coauthored by Trevor Shoemaker, Zachary Harris, Christine Smudde, Michael Hill, and James Burns. T.S. performed the fatigue testing, fractography, and growth rate simulations. Z.H. performed the tension testing and gathered/analyzed the EBSD data. C.S. and M.H. performed the residual stress/stress intensity measurement and calculation. T.S. wrote the manuscript and J.B. supervised the study. All authors interpreted the results, reviewed, and revised the manuscript.

7.6 References

1. Stephens, R. ., Fatemi, A., Stephens, R. R. & Fuchs, H. O. *Metal Fatigue in Engineering*. (John Wiley & Sons, 2001).
2. Maddox, S. J. Fatigue design rules for welded structures. *Prog. Struct. Eng. Mater.* **2**, 102–109 (2000).
3. Macdonald, K. A. & Maddox, S. J. New guidance for fatigue design of pipeline girth welds. *Eng. Fail. Anal.* **10**, 177–197 (2003).
4. Tavares, S. M. O. & de Castro, P. M. S. T. An overview of fatigue in aircraft structures. *Fatigue Fract. Eng. Mater. Struct.* **40**, 1510–1529 (2017).
5. Jones, R. Fatigue crack growth and damage tolerance. *Fatigue Fract. Eng. Mater. Struct.* **37**, 463–483 (2014).
6. Anderson, T. L. *Fracture Mechanics: Fundamentals and Applications*. (CRC Press, 2005). doi:10.1201/9781420058215
7. Gallagher, J. *MCIC-HB-01R Damage Tolerant Design Handbook. A Compilation of Fracture and Crack-Growth Data for High-Strength Alloys*. (1983).
8. ASTM International. ASTM E647-15e1 Standard Test Method for Measurement of Fatigue Crack Growth Rates. (2015). doi:10.1520/E0647-15E01
9. Sadananda, K., Nani Babu, M. & Vasudevan, A. K. A review of fatigue crack growth resistance in the short crack growth regime. *Mater. Sci. Eng. A* **754**, 674–701 (2019).

10. Jones, R., Singh Raman, R. K. & McMillan, A. J. Crack growth: Does microstructure play a role? *Eng. Fract. Mech.* **187**, 190–210 (2018).
11. Skorupa, M. Load Interaction Effects During Fatigue Crack Growth Under Variable Amplitude Loading — a Literature Review . Part I : Empirical Trends. *Fatigue Fract. Eng. Mater. Struct.* **21**, 987–1006 (1998).
12. Ronevich, J. A., Elia, C. R. D. & Hill, M. R. Fatigue crack growth rates of X100 steel welds in high pressure gas considering residual stress effects. *Eng. Fract. Mech.* **194**, 42–51 (2018).
13. Ronevich, J. A. *et al.* Fatigue crack growth rates in high pressure hydrogen gas for multiple X100 pipeline welds accounting for crack location and residual stress. *Eng. Fract. Mech.* **228**, 106846 (2020).
14. Pook, L. P. A 50-year retrospective review of three-dimensional effects at cracks and sharp notches. *Fatigue Fract. Eng. Mater. Struct.* **36**, 699–723 (2013).
15. Vasudevan, A. K. & Sadananda, K. Classification of environmentally assisted fatigue crack growth behavior. *Int. J. Fatigue* **31**, 1696–1708 (2009).
16. Pippan, R. & Hohenwarter, A. Fatigue crack closure: a review of the physical phenomena. *Fatigue Fract. Eng. Mater. Struct.* **40**, 471–495 (2017).
17. ASTM International. ASTM E8/E8M-16a Standard Test Methods for Tension Testing of Metallic Materials. (2016). doi:https://doi.org/10.1520/E0008_E0008M-16A
18. ASTM International. ASTM E384-17 Standard Test Method for Microindentation Hardness of Materials. (2017).
19. ASTM International. ASTM E140-12b Standard Hardness Conversion Tables for Metals Relationship Among Brinell Hardness, Vickers Hardness, Rockwell Hardness, Superficial Hardness, Knoop Hardness, Scleroscope Hardness, and Leeb Hardness. (2019).
20. Bachmann, F., Hielscher, R. & Schaeben, H. Texture Analysis with MTEX - Free and Open Source Software Toolbox. *Solid State Phenom.* **160**, 63–68 (2010).
21. Nyssönen, T., Peura, P. & Kuokkala, V. T. Crystallography, Morphology, and Martensite Transformation of Prior Austenite in Intercritically Annealed High-Aluminum Steel. *Metall. Mater. Trans. A Phys. Metall. Mater. Sci.* **49**, 6426–6441 (2018).
22. Donald, J. K. & Ruschau, J. Direct Current Potential Difference Fatigue Crack Measurement Techniques. *Fatigue Crack Meas. Tech. Appl.* 11–38 (1991).

23. ASTM International. ASTM E399-19 Standard Test Method for Linear-Elastic Plane-Strain Fracture Toughness K_{Ic} of Metallic Materials. (2019).
24. Tada, H., Paris, P. C. & Irwin, G. R. *The Stress Analysis of Cracks Handbook, Third Edition*. (ASME, 2000). doi:10.1115/1.801535
25. Freed, C. N. & Krafft, J. M. Effect of Side Grooving on Measurements of Plane-Strain Fracture Toughness. *J. Mater.* **1**, 770–790 (1966).
26. Zhu, X. K. Full-range stress intensity factor solutions for clamped SENT specimens. *Int. J. Press. Vessel. Pip.* **149**, 1–13 (2017).
27. Johnson, H. H. Calibrating the Electric Potential Method for Studying Slow Crack Growth. *Mater. Res. Stand.* **5**, 442–445 (1965).
28. ASME. ASME B46.1-2009: Surface Texture (Surface Roughness, Waviness, and Lay). (2009).
29. Prime, M. B. Residual stress measurement by successive extension of a slot: the crack compliance method. *Appl. Mech. Rev.* **52**, 75–96 (1999).
30. Hill, M. R. The Slitting Method. in *Practical Residual Stress Measurement Methods* (ed. Schajer, G. S.) (John Wiley & Sons, 2013).
31. Schindler, H., Cheng, W. & Finnie, I. Experimental Determination of Stress Intensity Factors Due to Residual Stresses. *Exp. Mech.* **37**, 272–277 (1997).
32. Smudde, C. M., Elia, C. R. D., San, C. W., Hill, M. R. & Gibeling, J. C. The influence of residual stress on fatigue crack growth rates of additively manufactured Type 304L stainless steel. *Int. J. Fatigue* **162**, 106954 (2022).
33. Beek, J. M. *NASGRO Reference Manual, Version 9.1*. (NASA Johnson Space Center, 2019).
34. Newman, J. C. A crack opening stress equation for fatigue crack growth. *Int. J. Fract.* **24**, 131–135 (1984).
35. Forman, R. G. & Mettue, S. R. (*NASA-TM-102165*) *Behavior of Surface and Corner Cracks Subjected to Tensile and Bending Loads in Ti-6Al-4V Alloy*. (1990).
36. Viswanathan, U. K., Banerjee, S. & Krishnan, R. Effects of aging on the microstructure of 17-4 PH stainless steel. *Mater. Sci. Eng. A* **104**, 181–189 (1988).
37. ASTM International. ASTM A564/A564M-19a Standard Specification for Hot-Rolled and Cold-Finished Age-Hardening Stainless Steel Bars and Shapes. (2019).

38. ASTM International. ASTM A693-16 Standard Specification for Precipitation-Hardening Stainless and Heat-Resisting Steel Plate, Sheet, and Strip. (2016).
39. Beevers, C. J. Fatigue crack growth characteristics at low stress intensities of metals and alloys. *Met. Sci.* **11**, 362–367 (1977).
40. Tomita, Y. Development of fracture toughness of ultrahigh strength, medium carbon, low alloy steels for aerospace applications. *Int. Mater. Rev.* **45**, 27–37 (2000).
41. Hockauf, K., Hockauf, M., Wagner, M. F. X., Lampke, T. & Halle, T. Fatigue crack propagation in an ECAP-processed aluminium alloy - Influence of shear plane orientation. *Materwiss. Werksttech.* **43**, 609–616 (2012).
42. Srinath, J. *et al.* Metallurgical Analysis of a Failed 17-4 PH Stainless Steel Pyro Bolt Used in Launch Vehicle Separation Systems. *Mater. Perform. Charact.* **4**, MPC20140063 (2015).
43. Zuidema, J., Veer, F. & Van Kranenburg, C. Shear lips on fatigue fracture surfaces of aluminum alloys. *Fatigue Fract. Eng. Mater. Struct.* **28**, 159–167 (2005).
44. Kadhim, M. H., Latif, N. A., Harimon, M. A., Shamran, A. A. & Abbas, D. R. Effects of side-groove and loading rate on the fracture properties of aluminium alloy AL-6061. *Materwiss. Werksttech.* **51**, 758–765 (2020).
45. Shlyannikov, V. N. T -stress for crack paths in test specimens subject to mixed mode loading. *Eng. Fract. Mech.* **108**, 3–18 (2013).
46. Ma, Y. E., Liu, B. Q. & Zhao, Z. Q. Crack paths in a friction stir-welded pad-up for fuselage applications. *J. Aircr.* **50**, 879–885 (2013).
47. Wang, J. *et al.* Effect of δ -ferrite on the stress corrosion cracking behavior of 321 stainless steel. *Corros. Sci.* **158**, 108079 (2019).
48. Burns, J. T. *et al.* Effect of water vapor pressure on fatigue crack growth in Al-Zn-Cu-Mg over wide-range stress intensity factor loading. *Eng. Fract. Mech.* **137**, 34–55 (2015).
49. Meggiolaro, M. A. Stress intensity factor equations for branched crack growth. *Eng. Fract. Mech.* **72**, 2647–2671 (2005).
50. Ritchie, R. O. Mechanism of Fatigue-Crack Propagation in Ductile and Brittle Materials. *Int. J. Fract.* **100**, 55–83 (1998).
51. Gupta, M., Alderliesten, R. C. & Benedictus, R. A review of T-stress and its effects in fracture mechanics. *Eng. Fract. Mech.* **134**, 218–241 (2015).

52. Leever, P. S. & Radon, J. C. Inherent stress biaxiality in various fracture specimen geometries. *Int. J. Fract.* **19**, 311–325 (1982).
53. Johnson, F. A. & Radon, J. C. Mechanical and Metallurgical Aspects of Fracture Behavior of an Al-Alloy. *Int. J. Fract. Mech.* **8**, 21–36 (1972).
54. Suresh, S. *Fatigue of Materials*. (Cambridge University Press, 1998).
55. Zhu, X. K. & Joyce, J. A. Review of fracture toughness (G, K, J, CTOD, CTOA) testing and standardization. *Eng. Fract. Mech.* **85**, 1–46 (2012).
56. Liu, Z., Yu, D., Tang, J., Chen, X. & Wang, X. Stress intensity factor and T-stress solutions for three-dimensional clamped single edge notched tension (SENT) specimens. *Int. J. Press. Vessel. Pip.* **168**, 11–23 (2018).
57. Saxena, A., Bassi, F., Nibur, K. & Newman, J. C. On single-edge-crack tension specimens for tension-compression fatigue crack growth testing. *Eng. Fract. Mech.* **176**, 343–350 (2017).
58. Hill, M. R. & Kim, J. Fatigue Crack Closure in Residual Stress Bearing Materials. *J. ASTM Int.* **9**, (2011).
59. Petit, J., Hénaff, G. & Sarrazin-Baudoux, C. Environmentally Assisted Fatigue in the Gaseous Atmosphere. in *Comprehensive Structural Integrity* **6**, 211–280 (Elsevier, 2003).
60. Antony, K. C. Aging Reactions in Precipitation Hardenable Stainless Steel. *J. Met.* 922–927 (1963).
61. Herrera Lara, V., Guerra Fuentes, L., Covarrubias Alvarado, O., Salinas Rodriguez, A. & Garcia Sanchez, E. Hot Ductility of the 17-4 PH Stainless Steels. *J. Mater. Eng. Perform.* **25**, 1041–1046 (2016).
62. Lass, E. A., Zhang, F. A. N. & Campbell, C. E. Nitrogen Effects in Additively Manufactured Martensitic Stainless Steels : Conventional Thermal Processing and Comparison with Wrought. *Metall. Mater. Trans. A* **51**, 2318–2332 (2020).
63. Ludwigson, D. C. & Hall, A. M. *DMIC Report 111 The Physical Metallurgy of Precipitation-Hardenable Stainless Steels*. (1959).
64. Pollard, B. Selection of Wrought Precipitation-Hardening Stainless Steels. *ASM Handb. Welding, Brazing, Solder.* **6**, 482–494 (1993).
65. Barsom, J. M. Fatigue-Crack Propagation in Steels of Various Yield Strengths. *J. Eng. Ind.* **93**, 1190–1196 (1971).
66. Wang, Z., Chen, Y. & Jiang, C. Thermal relaxation behavior of residual stress in laser hardened 17-

4PH steel after shot peening treatment. *Appl. Surf. Sci.* **257**, 9830–9835 (2011).

Chapter 8 - Conclusions & Recommendations for Future Work

Microstructure, mechanical properties, environmentally assisted cracking behavior, and fatigue crack growth behavior have been explored and compared for wrought and AM 17-4PH stainless steel. First, best available practices were used to build high performance AM 17-4PH via the laser powder bed fusion process. Post-build heat treatment protocols were then evaluated and successfully employed to strength-match the AM and wrought 17-4PH steels. Microstructural defects from the AM build process that persisted through heat treatment were characterized. AM 17-4PH was then evaluated via mechanical, stress corrosion cracking, and corrosion fatigue testing and compared to strength-matched wrought 17-4PH. These various performance evaluations revealed key microstructure-fracture process interactions that resulted in generally degraded AM 17-4PH performance relative to its wrought incumbent. This chapter provides key conclusions and recommendations that may be used to inform usage limitations and/or guide future research for AM 17-4PH.

8.1 Key Conclusions

The preceding chapters provided narrow conclusions based upon their respective studies. The following are the key conclusions that resulted from a holistic analysis of the dissertation results and discussions. Key trends and metrics are identified that would not be apparent without exhaustive review of the dissertation. References to specific chapter(s) for each conclusion are provided for further reading as desired. Also, the conclusions are divided by their relation to processing, performance, and microstructure-performance relationships for 17-4PH. Processing conclusions focus on the effect of heat treatment on AM 17-4PH microstructure and performance. Performance conclusions focus on the relative performance of the strength-matched wrought and AM 17-4PH. The microstructure-performance conclusions identify linkages between the performance of AM 17-4PH and specific microstructural features.

8.1.1 Processing 17-4PH

- Building AM 17-4PH in an EOS M290 machine with Ar-atomized powder, EOS recommended build parameters, and an Ar atmosphere produced an anisotropic, ferritic microstructure with nanometer scale porosity (~60 nm). This “as-built” AM 17-4PH had a yield strength of ~800 MPa and tensile elongation of 24-27% depending on loading orientation (Ch.1).

- The as-built AM 17-4PH could be heat treated using a combination of homogenization (Hom), solution annealing (SA), and/or hot isostatic press (HIP) treatments followed an aging treatment (peak age or overage) to strength-match wrought 17-4PH. All tested combinations of pre-aging treatments were successful in matching wrought strength (>1000 MPa) if followed by an appropriate aging treatment (Ch.1).
- The aforementioned build and heat treatment protocols produced AM 17-4PH with mechanical properties that outperform the majority of AM 17-4PH literature (Ch.1).
- Two key microstructural effects of the pre-aging treatments were to (1) transform the ferritic microstructure to a martensitic microstructure and (2) modify the size/distribution of the as-built porosity. All evaluated pre-aging treatments were successful in producing martensitic microstructures, but two-stage HIP+SA and Hom+SA treatments were most effective in producing a wrought-like microstructure. A secondary effect of these high-temperature pre-aging treatments was to coarsen and/or expand sub-micrometer scale porosity. Depending on the heat treatment, this porosity expanded to 0.13-0.28 μm (Ch.1).
- The HIP treatment was ineffective in eliminating small-scale porosity. Overall density increased, but sub-micrometer scale porosity persisted and coarsened during the HIP (i.e., 60 nm in the as-built condition to 0.20 μm after HIP) (Ch.2).
- The sub-micrometer porosity in AM 17-4PH was accompanied by inclusions, likely oxides, of approximately the same size (Ch.4). The pores and oxides in AM 17-4PH were attributed to Ar introduced during the AM process (i.e., during powder atomization and/or via the build atmosphere) and 600 wppm of oxygen originally present in the powder, respectively (Ch.2,3).
- The slow cooling rate of the HIP (310°C/h) was linked to the presence of Cr₂₃C₆ carbides (Ch.3), poor SCC performance (Ch.3), and poor ductility (Ch.2). Performance could be improved if the HIP was followed by a solution anneal heat treatment with a faster cooling rate (1040°C/0.5 h/air cool).
- For wrought 17-4PH, aging treatments (482°C/1 h or 552°C/4 h) only slightly attenuate residual stress. A solution anneal treatment (1040°C/0.5 h) reduced residual stress to near-negligible levels (Ch.7).

8.1.2 Performance of Wrought and Strength-Matched AM 17-4PH

- AM 17-4PH is significantly less ductile than wrought 17-4PH. For the peak aged condition, elongation is reduced from 21% in wrought to 11-16% in AM. In the overaged condition, elongation is reduced from 21% in wrought to 15-17% in AM (Ch.1).

- AM 17-4PH is generally less ductile when loaded parallel to the build (Z) direction (Ch.1), but no anisotropic trends were observed in AM 17-4PH fatigue, corrosion fatigue, or stress corrosion cracking behavior (Ch.3,6).
- In humid air corrosion fatigue, AM and wrought 17-4PH have similar crack growth behavior at low to moderate mechanical driving forces. Both exhibit Paris-like behavior in the stage I and stage II fatigue crack growth regimes. At high mechanical driving forces, AM 17-4PH cracks faster than wrought 17-4PH (Ch.6).
- At open circuit potential in 0.6M NaCl, wrought and AM 17-4PH have similar stress corrosion and corrosion fatigue crack growth behaviors. With regard to SCC, neither wrought nor AM 17-4PH were found to be susceptible (Ch.3). With regard to corrosion fatigue, both wrought and AM 17-4PH underwent similar crack growth acceleration (Ch.6).
- At cathodic applied potentials in 0.6M NaCl, AM 17-4PH is significantly more susceptible to both corrosion fatigue and stress corrosion cracking than wrought 17-4PH. For stress corrosion cracking, AM 17-4PH had 200-400 mV wider cathodic E_{app} susceptibility ranges and up to 5-fold faster crack growth rates than wrought 17-4PH (Ch.3). For corrosion fatigue, AM 17-4PH had a 200 mV wider range of cathodic E_{app} susceptibility with generally faster crack growth rates than wrought (Ch.6).

8.1.3 Microstructure-Performance Relationships for 17-4PH

- Sub-micrometer scale pores actively participate in the fracture process for AM 17-4PH. This linkage was clearly demonstrated for stress corrosion cracking at cathodic applied potentials in 0.6M NaCl via crack path examination (Ch.4,5). Examination of intergranular facets provided evidence that these pores also participate in accelerating corrosion fatigue crack growth in 0.6M NaCl at cathodic applied potentials (Ch.6). With the context of these SCC and corrosion fatigue behaviors, it is also likely that these pores generally degrade the ductility of AM 17-4PH as evidenced by a correlation between ductile dimple and pore spacing (Ch.2).
- Under cathodic applied potentials, the sub-micrometer scale pores act as stress concentrators that expand and plastically deform the proximate microstructure during stress corrosion cracking. This plasticity is most pronounced in the overaged condition of AM 17-4PH (Ch.4). In the peak aged condition, pore plasticity is less pronounced with subtle indications of applied potential dependence (Ch.5).
- Inclusions of the same size as the porosity were present and likely contributed to the pore-enhanced fracture processes. The morphological similarity makes it difficult to pinpoint the particular contribution of each feature to the fracture process. It is postulated that porosity is more susceptible to

deformation and plays a more active role in fracture due to lack of constraint, but it is clear that either one or both (i.e., pores and/or inclusions) are contributing to the aforementioned AM 17-4PH fracture behaviors (Ch.4).

- Prior austenite grain boundaries in AM 17-4PH are more susceptible to SCC at cathodic applied potentials than wrought 17-4PH. This boundary deficit is critical for peak aged AM 17-4PH as evidenced by uniquely intergranular fracture, the fastest growth rates, and larger E_{app} susceptibility ranges than wrought in 0.6M NaCl (Ch.3,5).
- Residual stress can play a significant role in the fatigue crack growth of wrought 17-4PH. The additional stress can (1) modify crack growth rate through superposition with applied loads, (2) modify the fatigue crack path, and (3) induce secondary fatigue cracking mechanisms like closure through crack path topography modifications (Ch.7).

8.2 Recommendations for Future Work

- The primary contribution of this dissertation is the problem identified in Chapter 4: sub-micrometer porosity. The persistence and impact of this porosity poses a key challenge for the additive manufacturing community. Based on this work, sub-micrometer porosity negatively impacts the ductility, fatigue crack growth, and environmentally assisted cracking behavior of AM 17-4PH. Simply, this microstructural feature is a key barrier to achieving wrought-level AM 17-4PH performance. The likely source for this porosity is insoluble Ar gas introduced during the powder atomization process and from the build atmosphere. Future efforts should focus on understanding and/or attenuating this microstructural feature if AM 17-4PH performance is to be improved.
- In a similar manner to the porosity, oxide inclusions should receive additional study. Currently, it is unclear whether porosity or inclusions are the primary contributors to the degradation of AM 17-4PH. Future work could focus on making this differentiation. If oxide inclusions are indeed critical, then the powder atomization process needs to be improved to reduce the inherent oxygen content in AM 17-4PH powder.
- A key unanswered question in this work is the origin of preferential intergranular cracking along AM 17-4PH prior austenite grain boundaries. These boundaries were responsible for the increased SCC susceptibility and fast crack growth of peak aged AM 17-4PH. It is unclear whether there was an intrinsic problem with the boundary itself, or if other factors were contributing to this behavior. Future work might explore this issue by using Chapter 5 as a guide.

- Hydrogen-metal interactions (e.g., diffusivity, trapping, solubility, diffusible hydrogen) play a key role in the regime where AM and wrought 17-4PH SCC differences were maximal (i.e., at cathodic applied potentials). Study of H-metal interaction differences between AM and wrought 17-4PH is beyond the scope of the current work, but is critical future work for understanding the mechanisms driving their SCC behavior differences.
- Work is required to determine improved HIP processing parameters for AM 17-4PH. The current work has shown that (1) slow cooling during HIP degrades AM 17-4PH performance and (2) sub-micrometer pores persist at 100 MPa. Future work could explore the HIP cooling profiles and pressures required to address these problems.
- AM 17-4PH was notably less ductile when loaded in the Z direction indicating mechanical anisotropy. Conversely, fatigue and stress corrosion cracking evaluations showed no indications of anisotropy. This indicates an interesting difference in global (i.e., bulk mechanical) versus local (i.e., crack tip controlled) fracture processes. Future work might investigate the origins of this behavior.